University Of St Andrews

School Of Physics and Astronomy

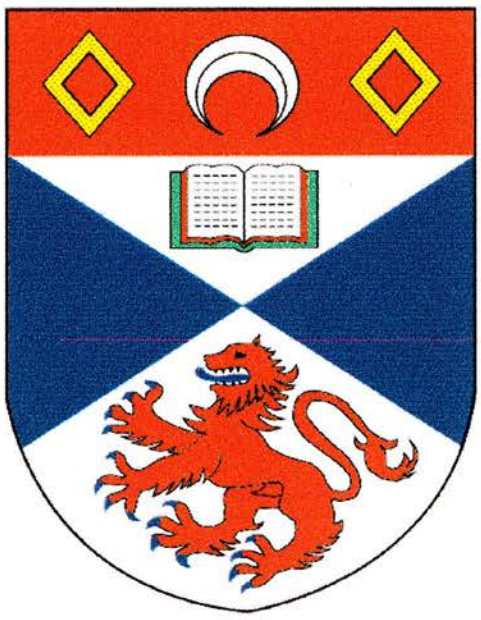

Moment Localisation in β-$Mn_{1-x}Al_x$

Thesis submitted for the degree of Doctor of Philosophy

by

J R Stewart

July 1998

Abstract

Despite the fact that β-Mn is paramagnetic at all temperatures, recent investigations have shown that it is a metal on the verge of antiferromagnetic order. Dilute substitution of various transition metal (Fe and Co) and non-transition metal (Al, Sn and In) atoms in the β-Mn lattice results in the stabilisation of short-range magnetic order at low temperatures. However, geometrical frustration inherent in the β-Mn lattice inhibits long-range magnetic order in β-Mn alloys.

In this thesis, the structural and magnetic properties of pure β-Mn and β-$Mn_{1-x}Al_x$ in the concentration range $0.03 \leq x \leq 0.2$ have been investigated in order to gain an understanding of the nature of the spin dynamics and magnetic ground states of these systems. To achieve this, various experimental techniques have been employed; in particular, neutron polarisation analysis , inelastic neutron scattering and muon spin relaxation. The results of these measurements show that β-Mn is an archetypal nearly antiferromagnetic metal, while β-$Mn_{1-x}Al_x$ displays magnetic properties consistent with the formation of partially localised moments. Our measurements reveal a dramatic and abrupt change in the fundamental nature of the spin dynamics in β-$Mn_{1-x}Al_x$ at a concentration of $x = 0.09$.

A novel reverse Monté-Carlo modelling procedure has been developed as part of this thesis in order to analyse the nuclear and magnetic short-range order present in the crystallographically complex β-Mn structure.

The entire β-$Mn_{1-x}Al_x$ series is characterised in terms of the temperature dependent amplitude of the spin fluctuations in the material according to the self-consistent renormalisation (SCR) theory.

I, John Ross Stewart, hereby certify that this thesis, which is approximately 50,000 words in length, has been written by me, that it is a record of work carried out by me and that it has not been submitted in any previous application for a higher degree.

date 21/7/98 signature of candidate

I was admitted as a research student in October 1996 and as a candidate for the degree of Doctor of Philosophy in October 1995; the higher study for which this is a record was carried out in the University of St Andrews between 1995 and 1998.

date 21/7/98 signature of candidate

I hereby certify that the candidate has fulfilled the conditions of the Resolution and Regulations appropriate for the degree of Doctor of Philosophy in the University of St Andrews and that the candidate is qualified to submit this thesis in application for that degree.

date 21/7/98 signature of supervisor

In submitting this thesis to the University of St Andrews I understand that I am giving permission for it to be made available for use in accordance with the regulations of the University Library for the time being in force, subject to any copyright vested in the work not being affected thereby. I also understand that the title and abstract will be published, and that a copy of the work may be made and supplied to any bona fide library or research worker.

date 21/7/98 signature of candidate

Acknowledgements

Enormous thanks go to my supervisor, Professor Bob Cywinski, for his constant encouragement and support. No amount of Oasis tickets could possibly repay my debt of gratitude to him.

Thanks also go to my colleagues at St Andrews – past and present, Dr Sue Kilcoyne, Dr Steve Lee, Mr Adrian Hillier, Mr Pascal Manuel, Dr Rob Bewley and Dr Mark Telling, and for technical support thanks go to Mr Reg Gavine. I would like to thank the School of Physics and Astronomy at the University of St. Andrews and especially to Professor Peter Riedi for providing my EPSRC postgraduate studentship.

I would also like to thank the following collaborators and local contacts:

Neutron Powder Diffraction	Dr Richard Ibberson and Dr Dave Keen of ISIS. Thanks also to Dr Clemens Ritter of the ILL for valuable discussions and spotting impurity phases.
μSR	Dr Steve Cottrell and Dr Francis Pratt of ISIS.
Neutron Polarisation Analysis	Dr Ken Andersen, Dr Amir Murani and Dr Otto Schärpf of the ILL.
Inelastic Neutron Scattering	Dr Wolfgang Hahn, Dr Chris Frost and Dr Roger Eccleston of ISIS.

Huge thanks also go to Professor Brian Rainford of the University of Southampton for his help and advice, as well as his seemingly infinite patience.

Thanks go to the Engineering and Physical Sciences Research Council, The Institute of Physics and The Stewart Society for their financial support.

Finally, I would like to thank my wife Mhairi, without whom it would not have been possible for me to complete either my undergraduate or postgraduate degrees. This thesis is dedicated to her. (I just hope she reads it)

Contents

1 Physical Properties of β-Mn Alloys

1.1 Introduction

Over the past few decades, considerable attention has been devoted to the investigation of the physical and magnetic properties of the 3d transition metals. The 3d ferromagnets Fe, Co and Ni, and the spin-density wave antiferromagnet Cr, have all been extensively studied. Relatively little attention has however been devoted to the magnetic and physical properties of elemental Mn.

Mn exists in four allotropic modifications at ambient pressure. The body centred cubic (bcc) α-Mn phase is stable at ambient pressure to a temperature of 1000K. α-Mn forms with space group $I\bar{4}3m$ with 58 atoms per unit cell and four non-equivalent crystallographic sites at Wyckoff positions 2a, 8c, and two sets at 24g [1]. The α-Mn structure is depicted in figure 1.1. Between 1000K and 1370K, the simple cubic β-Mn phase forms with space group $P4_132$ containing 20 atoms shared between two inequivalent crystallographic sites at Wyckoff positions 8c and 12d [2] (see figures 1.3, 1,4 and 1.5). For the next 40K between 1370K and 1410K, face centred cubic (fcc) γ-Mn is formed, and from 1410K up to the melting point of Mn at 1517K, we find bcc δ-Mn. The phase diagram of Mn is shown in figure 1.2 [3]. The β-phase of elemental Mn can be retained at room temperature by rapid quenching from the high temperature β-phase. γ-Mn undergoes a martensitic transition to a metastable face-centred tetragonal (fct) structure on quenching to room temperature. Attempts to obtain metastable δ-Mn by quenching various Mn alloys have all proved unsuccessful [4].

β-Mn does not order magnetically down to the lowest temperatures, unlike both α-Mn and γ-Mn, which show antiferromagnetic order at $T_N = 95K$ and 511K respectively.

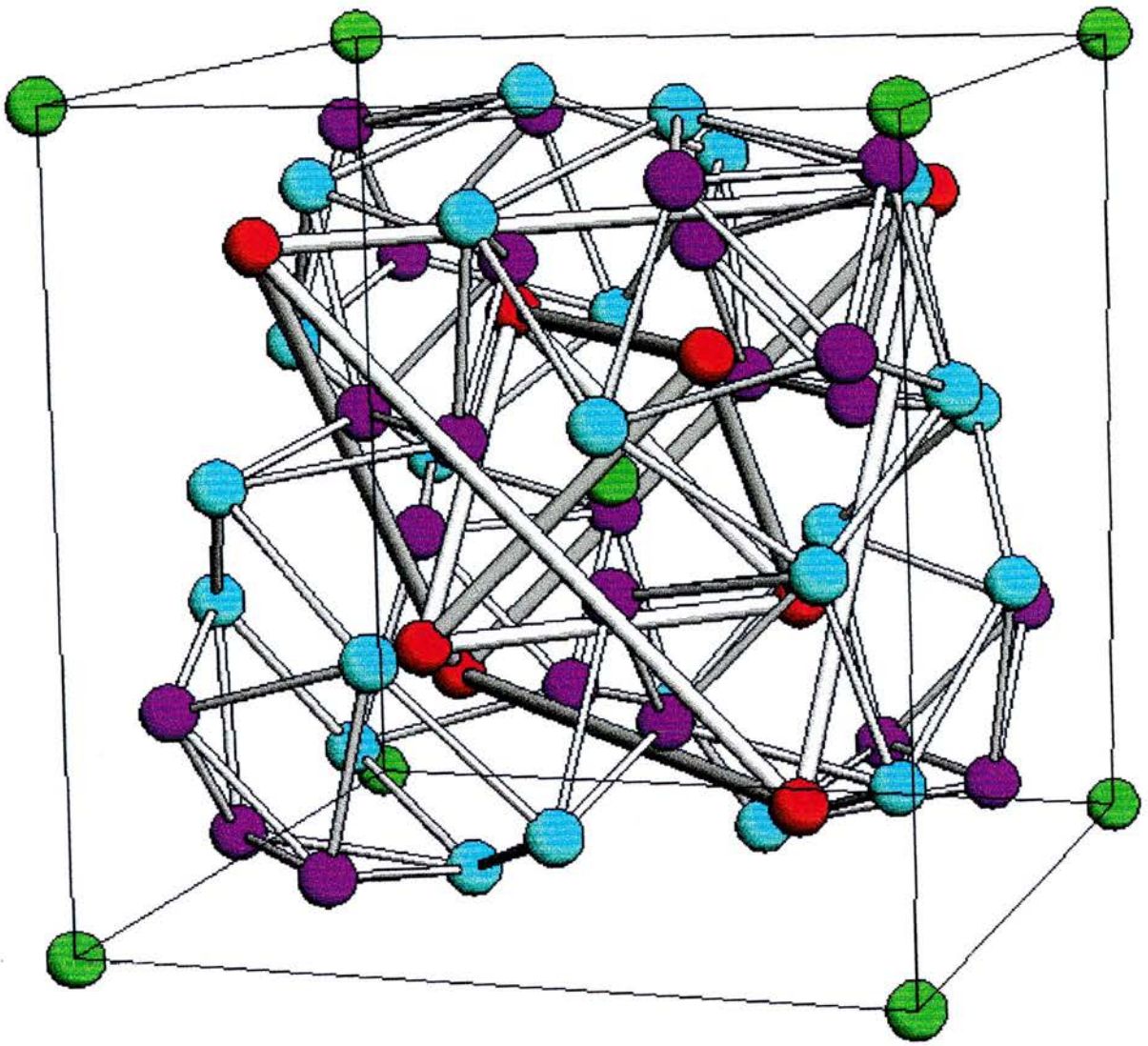

Figure 1.1

The crystal structure of α-Mn. Site I, II, III and IV Mn atoms are shown in green, red light blue and dark blue respectively.

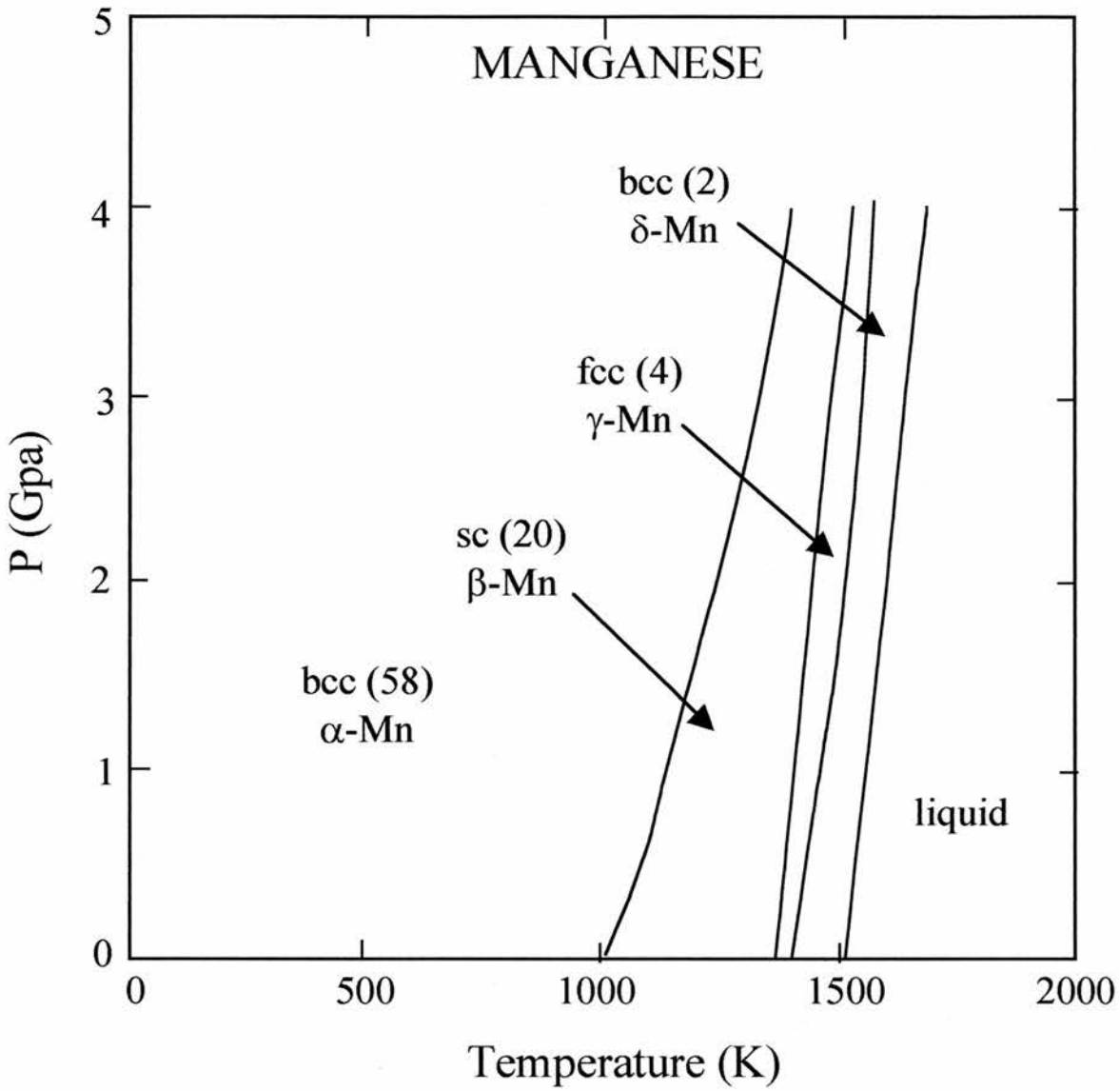

Figure 1.2

The phase diagram of manganese [3].

Despite the absence of magnetic order in β-Mn, a number of recent studies of pure β-Mn and β-Mn alloys have revealed some fascinating physical and magnetic properties, which are detailed in this chapter.

1.2 The Crystal Structure of β-Mn

The $P4_132$ simple cubic structure of β-Mn is unique in nature. Site I Mn atoms occupy position 8c with <111> rotational symmetry and site II Mn atoms occupy position 12d with <110> rotational symmetry. The crystallographic structure of β-Mn, based on the study of Kripyakevich [2] is summarised in table 1.1 and depicted in figures 1.2, 1.3 and 1.4.

Table 1.1 A summary of the β-Mn structure based on the study of Kripyakevich [2].

Space group	Atom Site	coordinates	
$P4_132$	8c	x,x,x	$x=0.061$
		$\bar{x}+\frac{1}{2},\bar{x},x+\frac{1}{2}$	
		$\bar{x},x+\frac{1}{2},\bar{x}+\frac{1}{2}$	
		$x+\frac{1}{2},\bar{x}+\frac{1}{2},\bar{x}$	
		$x+\frac{3}{4},x+\frac{1}{4},\bar{x}+\frac{1}{4}$	
		$\bar{x}+\frac{3}{4},\bar{x}+\frac{3}{4},\bar{x}+\frac{3}{4}$	
		$x+\frac{1}{4},\bar{x}+\frac{1}{4},x+\frac{3}{4}$	
		$\bar{x}+\frac{1}{4},x+\frac{3}{4},x+\frac{1}{4}$	
	12d	$\frac{1}{8},y,y+\frac{1}{4}$	$y = 0.206$
		$\frac{3}{8},\bar{y},y+\frac{3}{4}$	
		$\frac{7}{8},y+\frac{1}{2},\bar{y}+\frac{1}{4}$	
		$\frac{5}{8},\bar{y}+\frac{1}{2},\bar{y}+\frac{3}{4}$	
		$y+\frac{1}{4},\frac{1}{8},y$	
		$y+\frac{3}{4},\frac{3}{8},\bar{y}$	
		$\bar{y}+\frac{1}{4},\frac{7}{8},y+\frac{1}{2}$	
		$\bar{y}+\frac{3}{4},\frac{5}{8},\bar{y}+\frac{1}{2}$	
		$y,y+\frac{1}{4},\frac{1}{8}$	
		$\bar{y},y+\frac{3}{4},\frac{3}{8}$	
		$y+\frac{1}{2},\bar{y}+\frac{1}{4},\frac{7}{8}$	
		$\bar{y}+\frac{1}{2},\bar{y}+\frac{3}{4},\frac{5}{8}$	

As can be seen in figure 1.3, the site II β-Mn atoms form a distorted lattice of corner sharing triangles. This is known as the "distorted windmill" arrangement, and was first highlighted by Nakamura and co-workers [5].

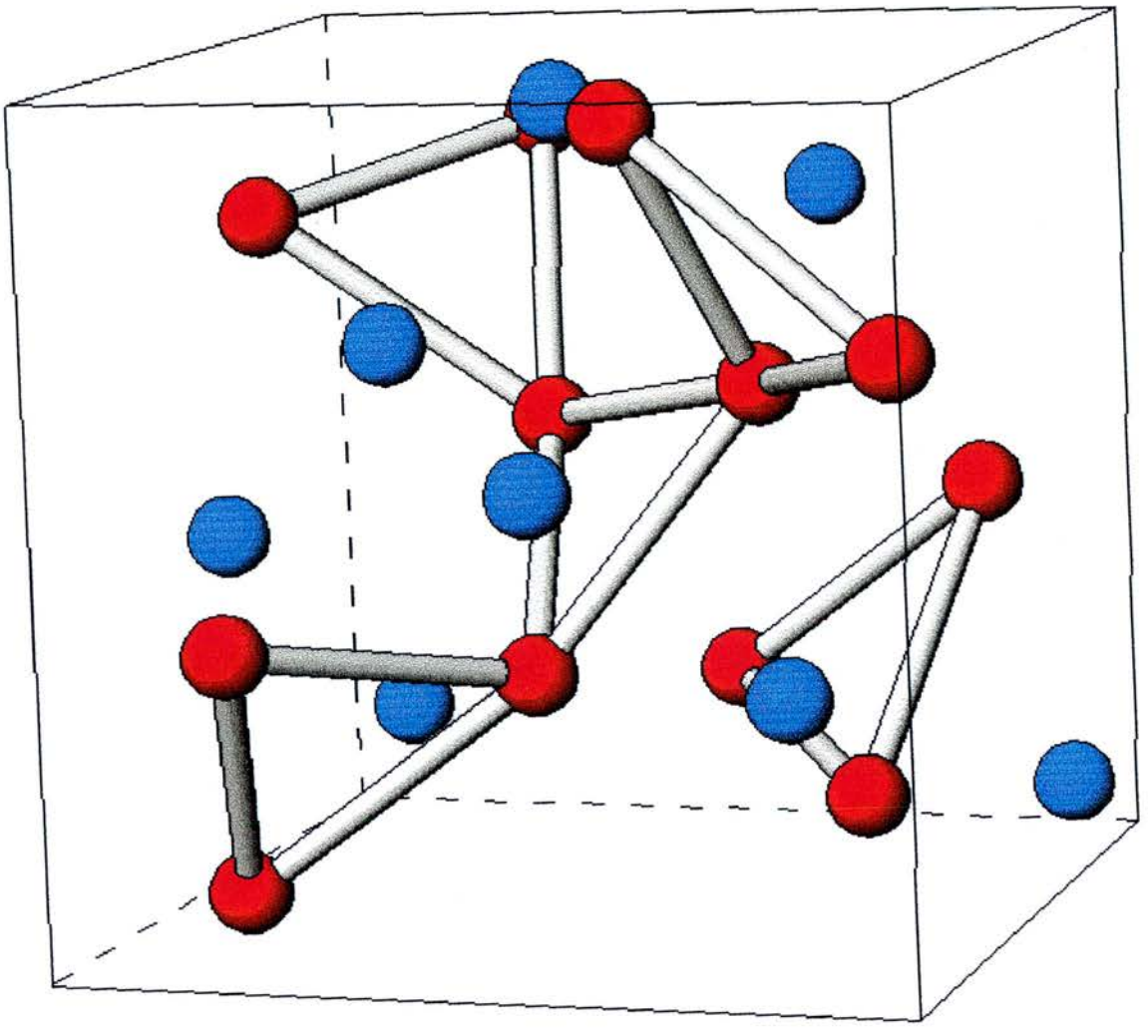

Figure 1.3

The β-Mn crystal structure. Site 1 Mn atoms are shown in blue, site II Mn atoms in red. The site II atoms are shown as a network of corner sharing triangles, with the triangle planes normal to the <1 1 1> direction.

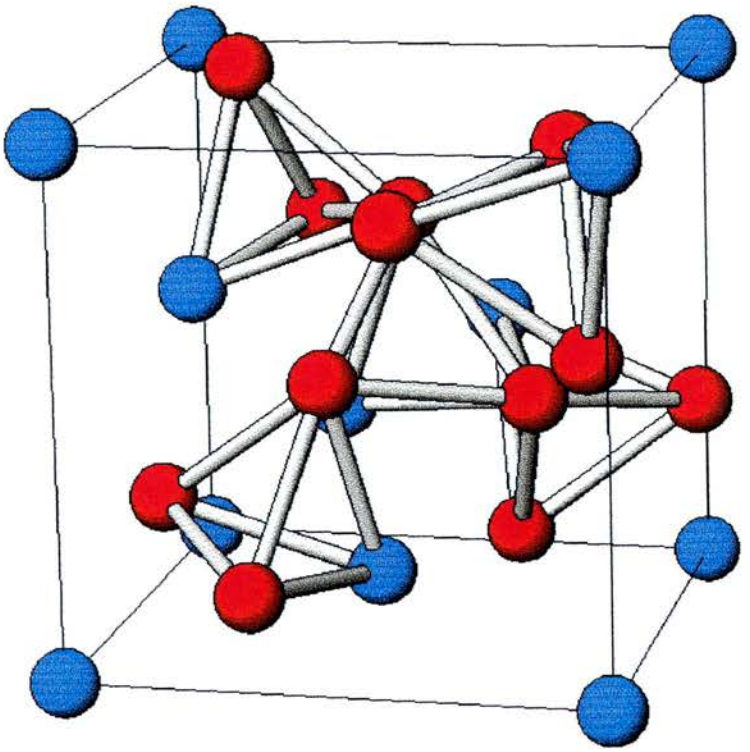

Figure 1.4

The β-Mn structure with a site I atom at the unit cell corner. The site I and II Mn atoms are shown forming a distorted lattice of corner sharing tetrahedra.

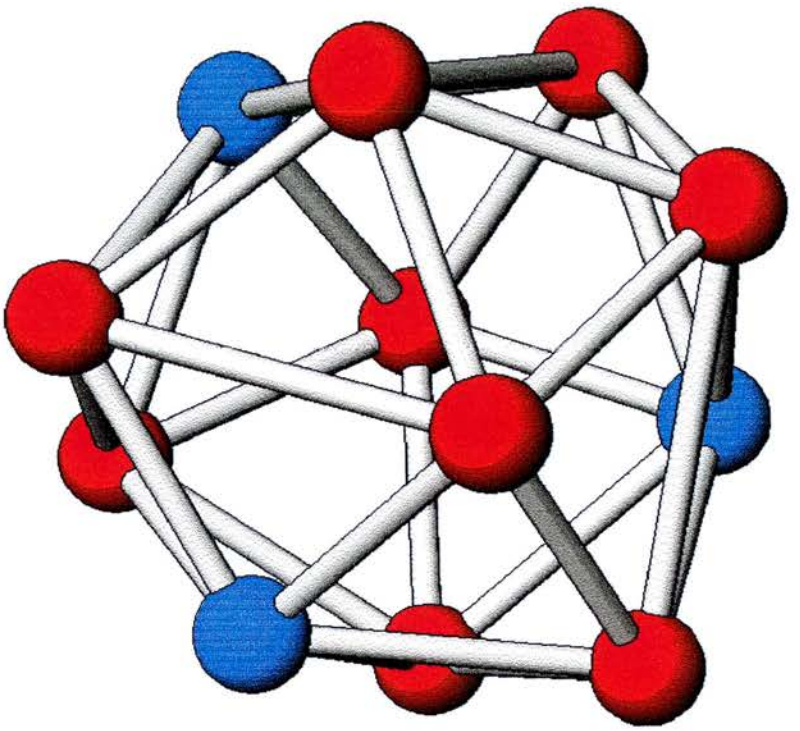

Figure 1.5

The first near-neighbour shell of a site I Mn atom in β-Mn (the central site I atom is not shown). This shell forms a distorted icosahedron with 3 site I and 9 site II Mn atoms [2,6].

Figures 1.3, 1.4 and 1.5 depict three possible descriptions of the local coordination of site I and site II Mn atoms in the β-Mn matrix. The icosahedral coordination of the site I Mn atoms is most unusual, and is the basis of a centre of *pseudo five-fold symmetry* similar to that observed in quasicrystal structures, many of which are Mn alloys [6].

It has been pointed out by O'Keefe and Andersson [7] that if the site II Mn positions are given by the coordinates in table 1.1 with,

$$y = \frac{9-\sqrt{33}}{16} = 0.20346....$$

then the triangular lattice formed by the site II Mn atoms, becomes a lattice of equilateral triangles with each triangle the same size. The reported value of y is 0.206 according to Kripyakevich [2] or 0.2022 according to Shoemaker and co-workers [8]. In chapter 5, I shall show that the value of y in β-MnAl alloys is very close to the critical value given above.

The various local coordinations of β-Mn shown above have been discussed by several authors in terms of the possible existence of *geometrical frustration* between Mn moments in the β-Mn lattice [5,9]. The concept of geometrical frustration and its impact on the magnetic ground state will be fully discussed in section 2.5.

1.3 Previous Studies of β-Mn and β-MnAl

1.3.1 Introduction

It has long been known that the introduction of dilute quantities of various transition metal and non-transition metal impurities into pure β-Mn stabilises a static ordered magnetic ground state in these alloys. One of the first investigations of this phenomenon was by Kohara and Asayama, who used zero-field NMR to examine the hyperfine fields in various β-Mn alloys [10]. They showed the existence of some form of static magnetic ground state (which they assumed to be antiferromagnetic) for β-Mn alloys with impurity concentrations greater than; 3at% Al, 2at% Fe, 0.7at% Co, 0.5at% Ni, 5at% Zn, 3at% In and 1at% Sb. Kohara and Asayama identified two possible

mechanisms for the formation of an ordered magnetic ground state. The first mechanism involved the donation of d-electrons to the conduction band by Fe, Co, Ni and Zn impurities. It was noticeable in Kohara's study that β-Mn alloys with Ti, V and Cr, which are situated to the left of Mn in the periodic table, did not exhibit magnetic order. Substitution of these transition metals into β-Mn causes a depletion in the d-electron number, whereas substitution of Fe, Co, Ni and Zn into β-Mn increases the d-electron number. An alternative mechanism for the formation of an ordered magnetic ground state in β-Mn alloys with Al, Sb and In impurities is an expansion of the β-Mn lattice due to inverse chemical pressure. This followed the work of Moriya [11] who showed that the appearance of magnetic order in metals was related to the interatomic spacing of the material. The concept of moment localisation due to lattice expansion in metals will be further discussed in section 2.4.3.1.

1.3.2 Mössbauer Spectroscopy Measurements

Several Mössbauer spectroscopy measurements have been performed on β-Mn alloys [12,13,14,15]. The study of Nishihara [15] showed that the hyperfine field at site I in β-Mn alloys with Fe, Co and Ni is dependent only on the excess of d-electrons donated to the band, as shown in figure 1.6. This result showed that β-Mn alloys are weak itinerant electron antiferromagnets in which the value of the Mn moment is dependent on the details of the conduction band. The contribution to the hyperfine field from the lattice expansion is depicted in figure 1.7. The value of the hyperfine field increases with increasing lattice expansion for small d-electron excess Δn_d.

The Mössbauer measurements of Nishihara broadly confirm the NMR study of Kohara and Asayama. Since the lattice expansion is small in β-Mn alloys with 3d-transition metal impurities, the magnetic ground state is determined by the excess of d-electrons donated to the conduction band. With non-magnetic and 4d transition metals, the effects of lattice expansion become important.

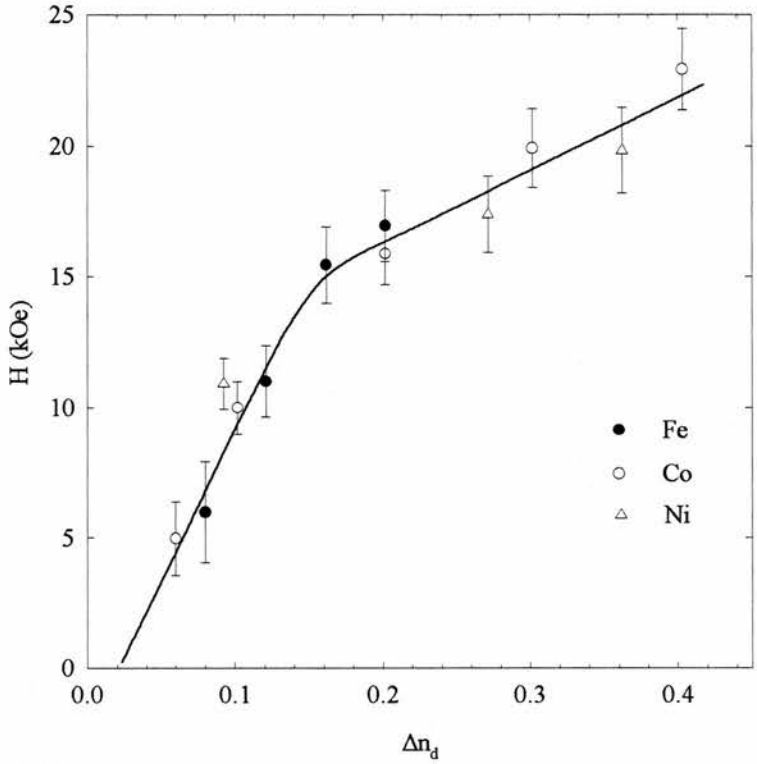

Figure 1.6

Variation of internal field with excess d-electron number in β-MnFe, β-MnCo and β-MnNi measured by Fe Mössbauer spectroscopy [15].

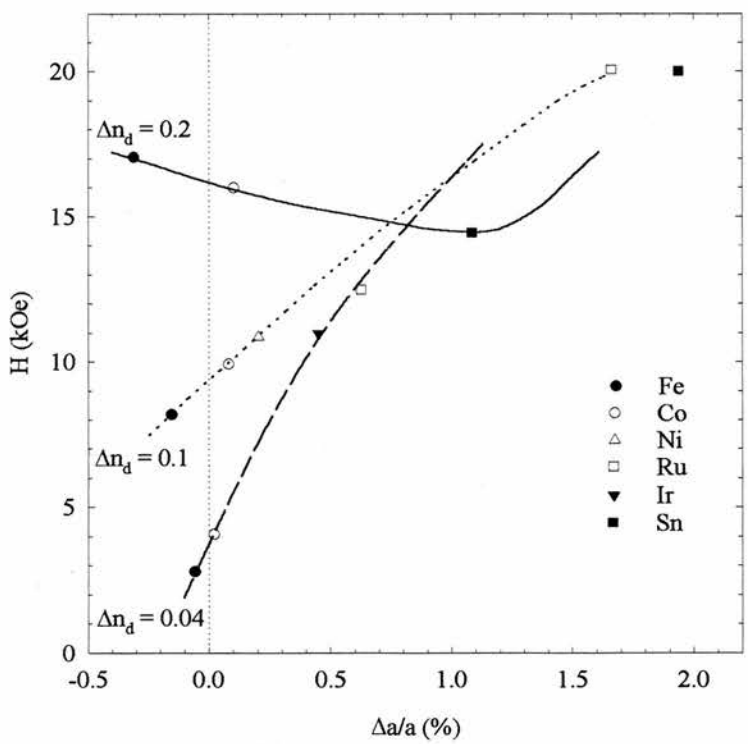

Figure 1.7

Effect of lattice expansion on internal field for 3 values of Δn_d measured by Fe Mössbauer spectroscopy [15].

1.3.3 Specific Heat Measurements

In the 1970s and 1980s, the self-consistent renormalisation (SCR) theory of itinerant electron magnetism was developed by Moriya [16]. This theory attempts to describe metallic magnets by considering the effects of longitudinal amplitude spin fluctuations, and orientational transverse spin fluctuations. Details of SCR theory will be given in section 2.4. Using SCR theory, Hasegawa predicted that spin fluctuations in metals on the verge of antiferromagnetic order would cause a strongly enhanced electronic coefficient of the specific heat γ [17]. In a normal metal the specific heat is given by,

$$C = \gamma T + \beta T^3, \qquad (1.1)$$

where γ and β are the electronic and lattice coefficients. The specific heat study of β-Mn and β-Mn alloys by Shinkoda and co-workers [18] found a strongly enhanced value of γ in pure β-Mn. A plot of γ versus the change in d-electron number Δn_d in various β-Mn alloys is shown in figure 1.8.

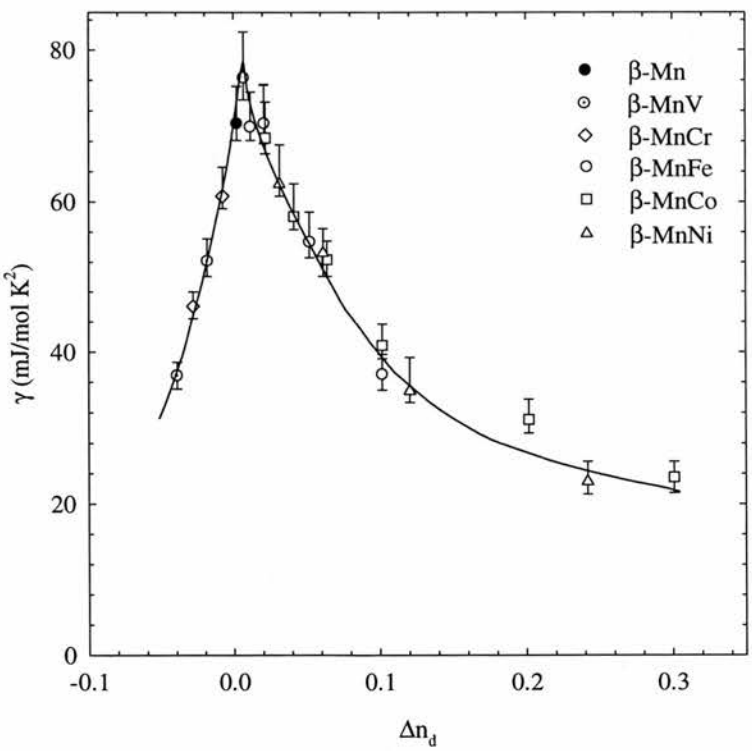

Figure 1.8

The dependence of the electronic coefficient of specific heat γ on excess d-electron number Δn_d. The solid line shows the functional dependence of the change in γ given by equation 1.2 [18].

Figure 1.8 shows that the change in γ throughout the series of β-Mn alloys studied is expressed by one line, irrespective of the impurity species. Starting from $\Delta n_d = -0.04$ for β-MnV, γ increases rapidly and peaks at $\Delta n_d = 0.005$. According to the SCR theory the position of the peak in γ is the critical point for the onset of antiferromagnetism, corresponding to the value of the Stoner parameter, $\alpha = 1$ (see section 2.3.2.3). The position of pure β-Mn slightly to the left of the peak suggests that α is slightly less than unity in the pure metal. The decrease in γ follows the functional dependence

$$|\Delta n_d - 0.005|^{1/2}, \tag{1.2}$$

where $\Delta n_d = 0.005$ has been taken as the position of the peak in γ corresponding to $\alpha = 1$. Hasegawa and Moriya have shown that the Néel temperature of weakly antiferromagnetic metals is related to γ by the relation,

$$\gamma = A - BT_N^{3/4}, \tag{1.3}$$

where A and B are constants [19]. Figure 1.9 shows that this relation holds for the β-Mn alloys studied by Shinkoda [18].

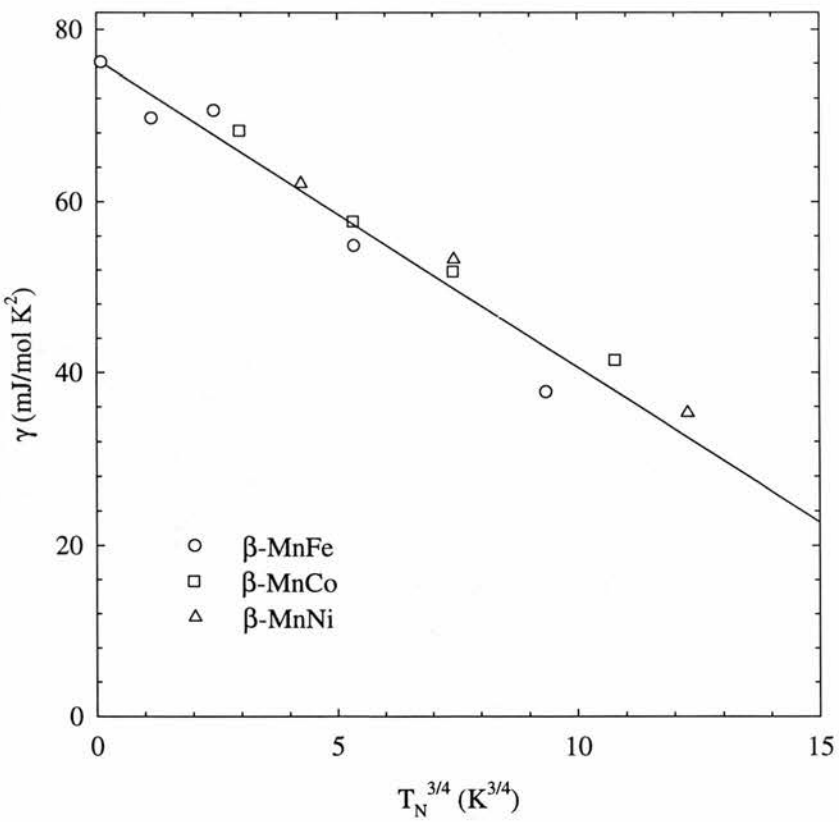

Figure 1.9

γ versus $T_N^{3/4}$ for antiferromagnetic β-Mn alloys, β-MnFe, β-MnCo and β-MnNi from the specific heat study of Shinkoda [18].

In demonstrating that the functional dependence of the electronic component of specific heat closely follows the predictions of the SCR theory, this study of β-Mn was the first to point out the crucial rôle played by spin fluctuations in β-Mn alloys. Although SCR theory up to this point had successfully described the physical properties of many itinerant electron ferromagnets such as MnSi and Sc_3In [20,21], this study was the first to provide support for the SCR theory of antiferromagnetic metals.

1.3.4 NMR Measurements of Spin Dynamics

There have been several NMR studies of spin dynamics in β-Mn. [22,23,24]. Figure 1.10 shows a plot of the nuclear spin lattice relaxation time $1/T_1$ for site I and Site II Mn atoms measured by Kohori and co-workers [24].

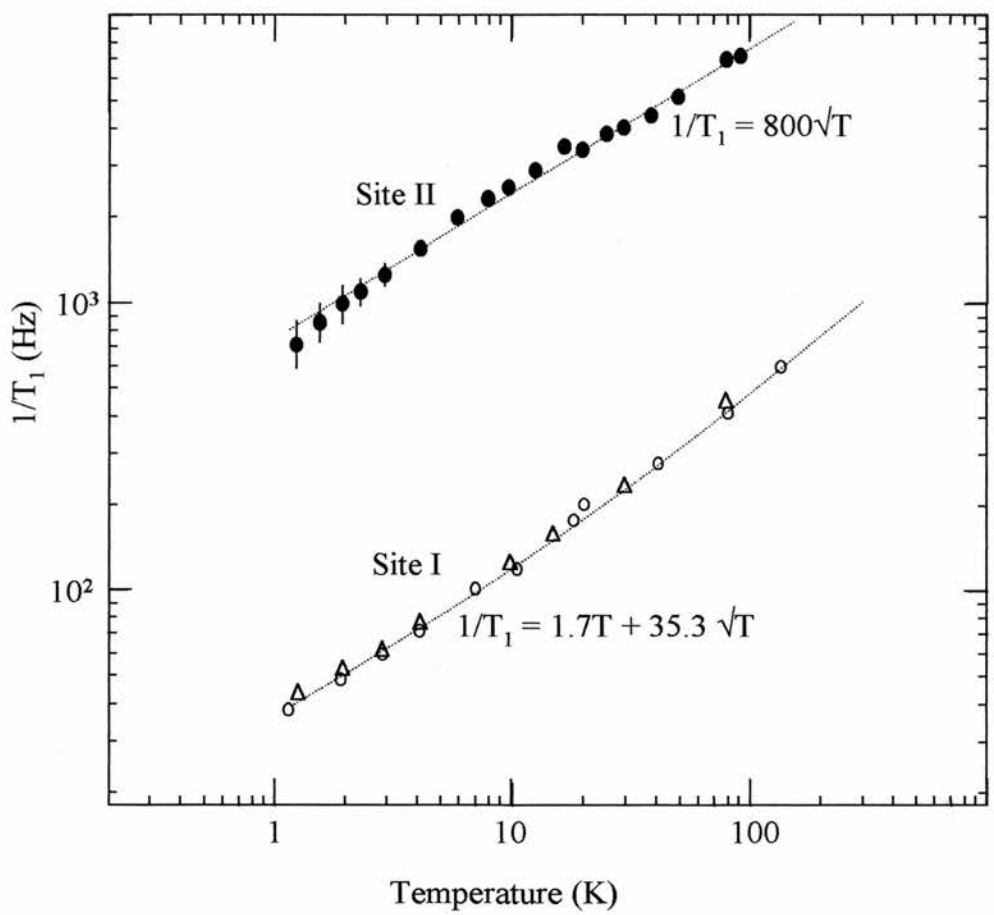

Figure 1.10

Temperature dependence of the nuclear spin-lattice relaxation rate $1/T_1$ for sites I and II in pure β-Mn measured by Kohori and co-workers [24].

The observed temperature dependence of the $1/T_1$ is well described by the equation,

$$\frac{1}{T_1} = aT + b\sqrt{T}, \tag{1.4}$$

where the coefficients a and b describe the interactions between the nuclear spin and the d-orbital and electron spin respectively [24]. The temperature dependence of $1/T_1$ given by eq. (1.4) was predicted by Moriya and Ueda using SCR theory [25] for systems on the verge of antiferromagnetic order. This measurement provides further confirmation that the physical properties of β-Mn are well described by the predictions of SCR theory. The values of the coefficient b = 800 for site II and b = 35.3 for site I indicate that the magnetic moment of the site II Mn atoms is much larger than that of the Site I Mn atoms. This result is supported by the band structure calculations of Sliwko and co-workers [26] which are depicted in figure 1.11.

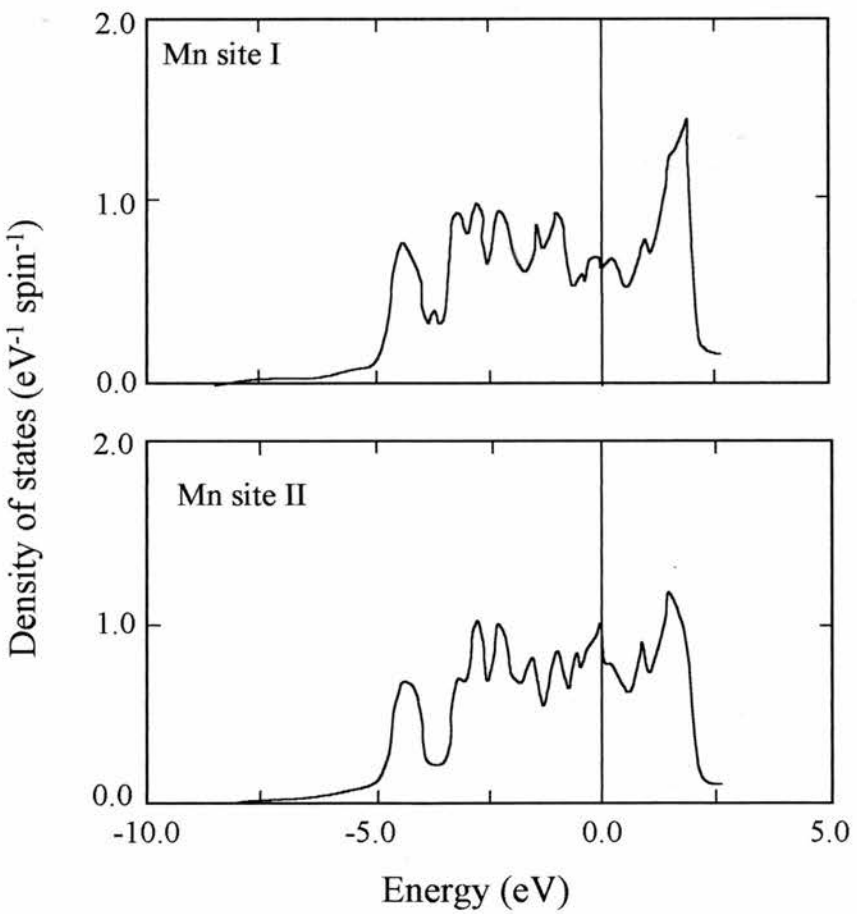

Figure 1.11

The spin dependent density of electron states for site I and Site II Mn atoms in β-Mn calculated by Sliwko et. al. [26].

The density of states at the Fermi energy ε_F (given by E = 0 in figure 1.11) is shown to be a minimum at site I and maximum at site II. The calculations of Sliwko confirm that the Stoner parameter α is only slightly less than unity for site II showing that the site II Mn atoms are on the verge of magnetic order [26].

A NMR study of the spin dynamics in β-MnAl has recently been performed by Nakamura and co-workers [5]. Figure 1.12 shows the temperature dependence of $1/T_1$ for β-$Mn_{0.97}Al_{0.03}$ and β-$Mn_{0.9}Al_{0.1}$.

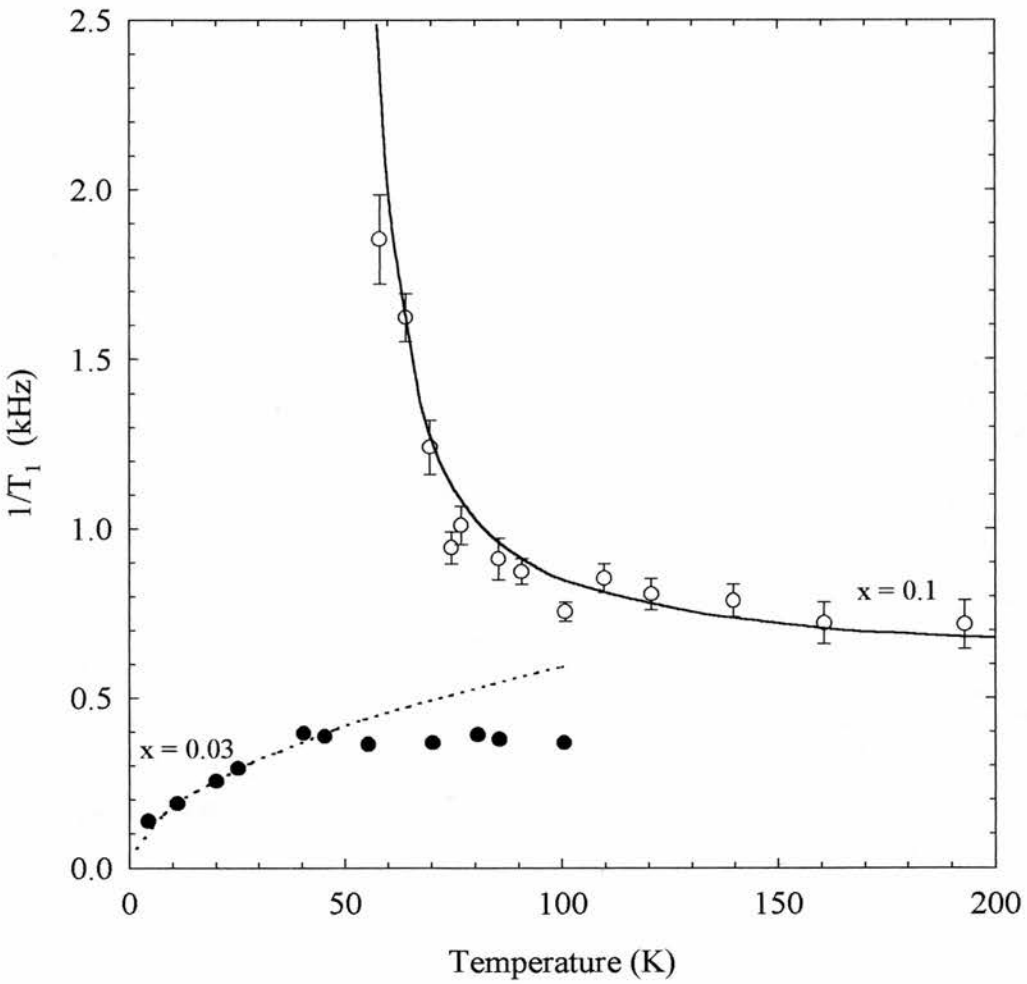

Figure 1.12

The temperature dependence of $1/T_1$ for β-$Mn_{1-x}Al_x$ with x = 0.03 and 0.1 measured by Nakamura et. al. [5]. The broken curve indicates a $T^{1/2}$ dependence of $1/T_1$ for β-$Mn_{0.97}Al_{0.03}$.

While $1/T_1$ in β-$Mn_{0.97}Al_{0.03}$ is found to obey a $T^{1/2}$ temperature dependence in accordance with SCR theory, $1/T_1$ in β-$Mn_{0.9}Al_{0.1}$ is found to diverge at around 50K. This behaviour is commonly seen in local moment systems undergoing a magnetic transition. This result is an indication that there may be a crossover from purely itinerant moments in pure β-Mn, to partially localised moments in β-MnAl.

1.3.5 Magnetic Susceptibility Measurements of β-MnAl

Magnetic susceptibility measurements taken by Nakamura and co-workers [5] are shown in figure 1.13.

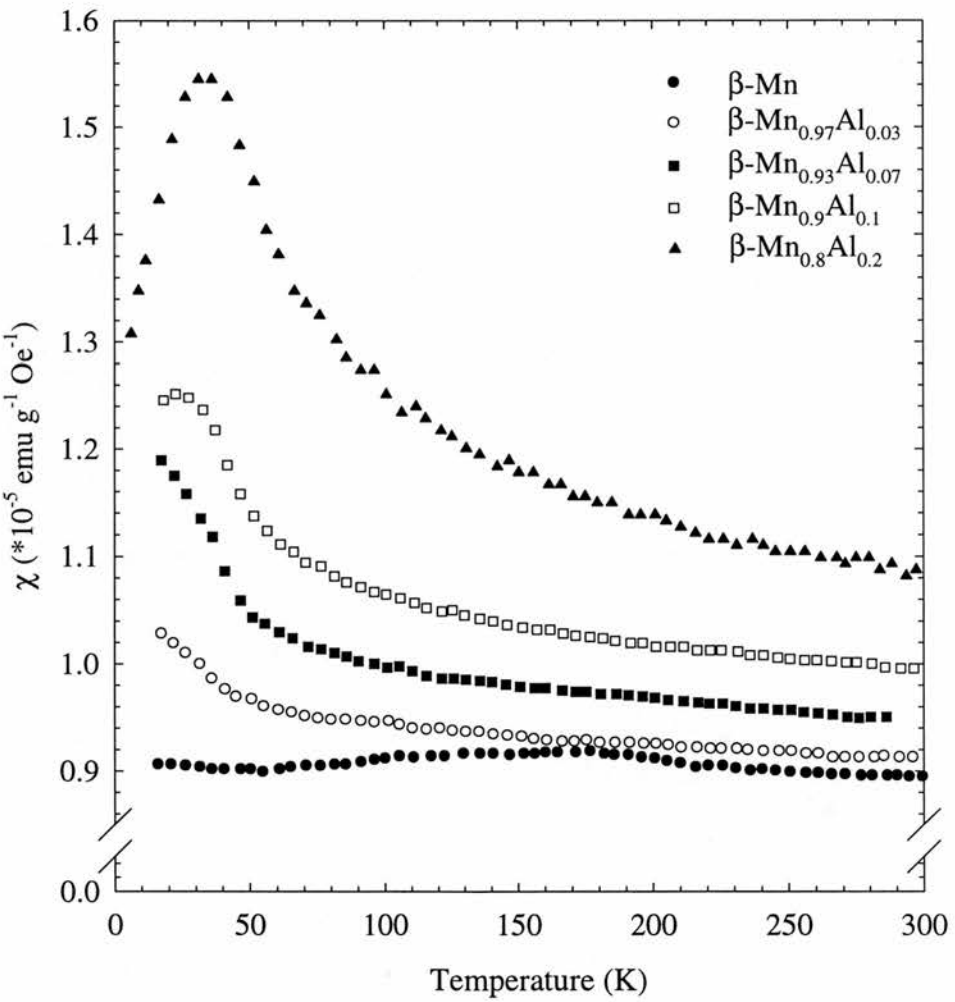

Figure 1.13

Temperature dependence of the zero field cooled magnetic susceptibilities of the β-MnAl concentrations shown, measured by Nakamura et. al. [5].

Figure 1.13 shows that the magnetic susceptibility of pure β-Mn is almost constant with temperature, implying a Pauli paramagnetic susceptibility of the conduction electrons (see section 2.3.1). With increasing Al concentration, the susceptibility becomes progressively larger and more temperature dependent, despite the fact that non-magnetic Al atoms are being substituted for magnetic Mn atoms. For β-$Mn_{0.9}Al_{0.1}$ and β-$Mn_{0.8}Al_{0.2}$ a peak in the susceptibility is observed. This data indicates that β-MnAl displays magnetic properties normally associated with a system of local magnetic moments. The peak in the susceptibility was interpreted by Nakamura as an indication of *spin glass* order in concentrated β-MnAl alloys (see section 2.5). In chapter 4, our own susceptibility measurements, broadly confirming Nakamura's measurements, will be presented and discussed.

1.3.6 Thermal Expansion Measurements of β-MnAl

Thermal expansion measurements of the β-MnAl series taken by Nakamura and co-workers [5] are shown in figure 1.14.

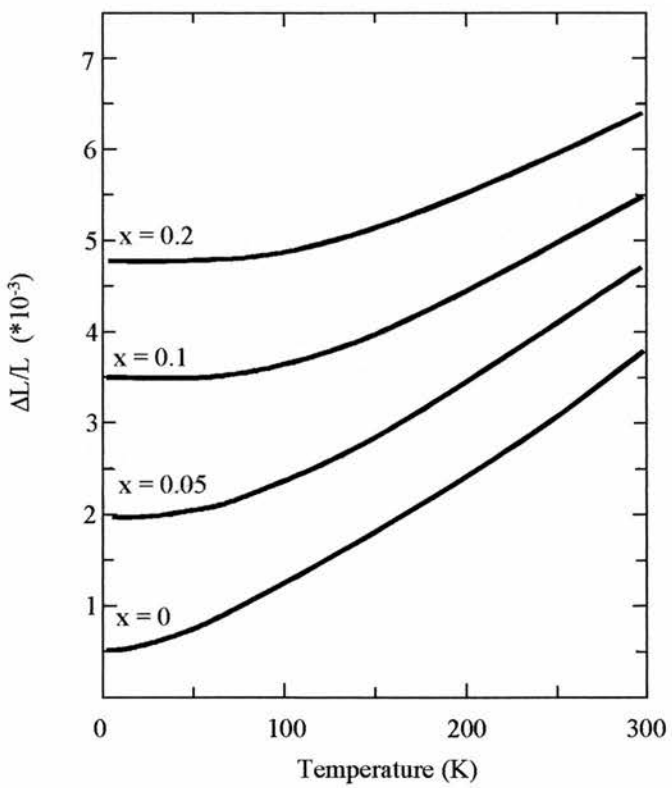

Figure 1.14

The temperature dependence of linear thermal expansion for β-$Mn_{1-x}Al_x$ alloys with x=0, 0.05, 0.1 and 0.2 measured by Nakamura and co-workers [5].

In pure β-Mn, the unit cell volume is found to increase steadily with increasing temperature. For β-$Mn_{1-x}Al_x$ alloys with $x \geq 0.05$ there is a temperature independent region in the thermal expansion curve at low temperatures. The width of this temperature independent region increases with increasing Al concentration. The origin of this temperature independence at low temperatures has been attributed to spontaneous volume magnetostriction in these alloys, and therefore an increasing magnetic contribution to the thermal expansion. The influence of spin fluctuations and moment formation on thermal expansion will be fully discussed in section 2.4.2.1. The coefficient of linear thermal expansion deduced from these measurements is large for pure β-Mn, with a value of $\kappa = 30 \times 10^{-6}\ K^{-1}$, and decreases linearly with increasing Al concentration, to a value of $\kappa = 18 \times 10^{-6}\ K^{-1}$.

1.3.7 Inelastic Neutron Scattering Measurements of β-MnAl

An inelastic polarised neutron scattering study of pure β-Mn and β-$Mn_{0.9}Al_{0.1}$ was recently undertaken by Shiga and co-workers [9]. Analysis of the initial and final neutron spin states enables the separation of the magnetic and nuclear contributions to the measured neutron cross-section (see section 7.2). Figure 1.15 shows the Q-dependence of the measured squared magnetisation density $M^2(Q)$ multiplied by the squared Mn magnetic form factor $f^2(Q)$ measured at the elastic line ($\Delta E = 0$). $f^2(Q)M^2(Q)$ is directly proportional to the measured magnetic neutron cross-section (see sections 3.2.2 and 7.7.1).

The shape of $f^2(Q)M^2(Q)$ is similar for both β-Mn and β-$Mn_{0.9}Al_{0.1}$, with a maximum at around $Q = 1.5 Å^{-1}$, corresponding to approximately twice the Mn-Mn near neighbour distance. This indicates dominant antiferromagnetic correlations between Mn spins in both β-Mn and β-$Mn_{0.9}Al_{0.1}$. The amplitude of the magnetisation density given in figure 1.15 is likely to be significantly less than the true value since these measurements were taken at high temperatures where spin fluctuations are likely to spread the magnetic intensity over a wide energy range, and outside the energy window available in Shiga's measurement.

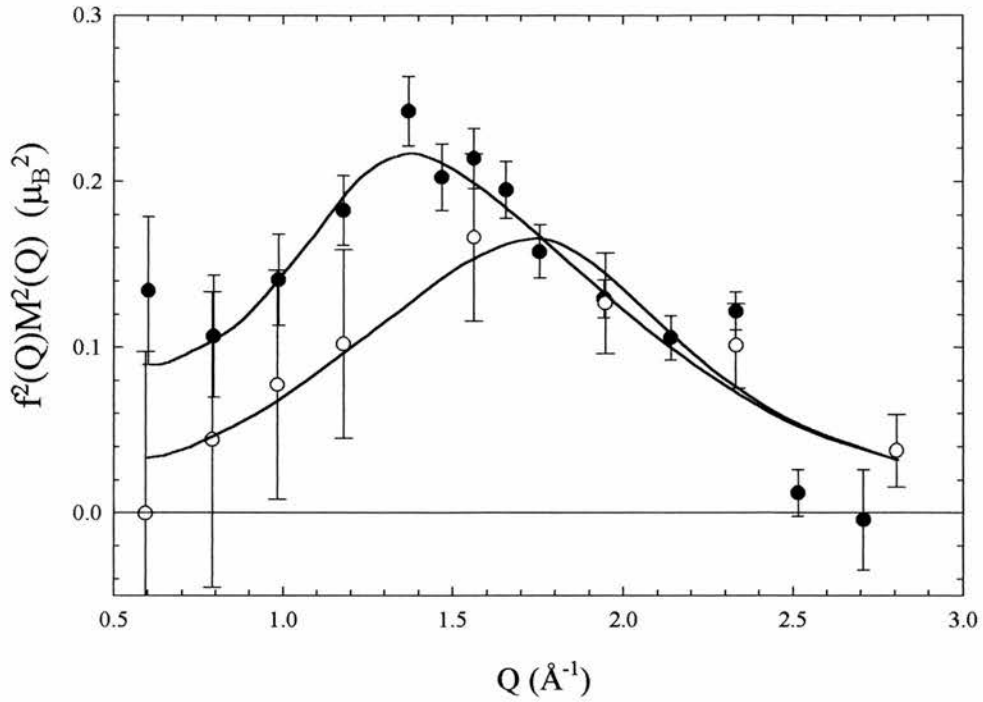

Figure 1.15

The Q-dependence of $f^2(Q)M^2(Q)$ of β-Mn (●) and β-$Mn_{0.9}Al_{0.1}$ (○) measured at the elastic line, $\Delta E = 0$, at a temperature of 290K by Shiga and co-workers [9].

The inelastic linewidth Γ, which is proportional to the spectral width of the spin fluctuations in the material, was measured by Shiga for β-Mn and β-$Mn_{0.9}Al_{0.1}$. The measured inelastic neutron linewidths of β-$Mn_{0.9}Al_{0.1}$ are shown as a function of temperature in figure 1.16. The inelastic linewidth Γ for β-Mn was found to vary only weakly with temperature with Γ falling from ~30meV at 290K to ~20meV at 7K. This result shows that strong spin fluctuations persist in β-Mn down to very low temperatures. The temperature dependence of Γ in β-$Mn_{0.9}Al_{0.1}$ is markedly different to that of pure β-Mn, with Γ falling steadily from ~10meV at 290K to ~0.7meV at 7K. This indicates that the spin fluctuations in β-Mn are substantially damped by the introduction of Al. This has led Shiga to characterise the transition from the dynamic β-Mn system to the largely static β-$Mn_{0.9}Al_{0.1}$ as a so-called *quantum spin liquid (QSL) to spin glass* transition [9]. In this model the replacement of magnetic Mn atoms by non-magnetic Al impurities, reduces the geometrical magnetic frustration between the Mn spins, caused by their triangular coordination. In the frustrated β-Mn lattice there are likely to be several degenerate allowed spin configurations, with zero-point fluctuations being sufficient to allow the spins to move between these configurations.

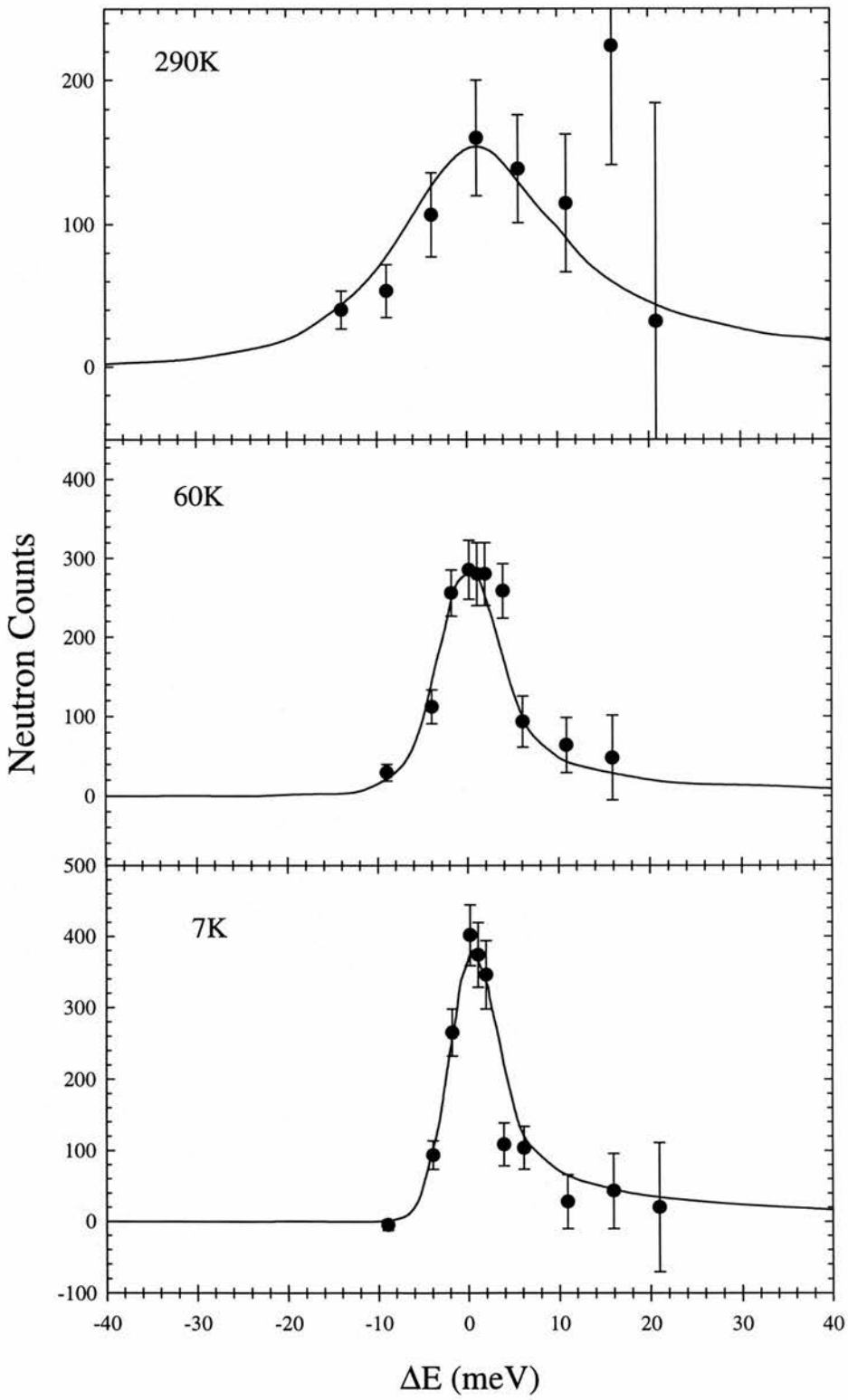

Figure 1.16

The temperature dependence of the inelastic neutron linewidth Γ for β-$Mn_{0.9}Al_{0.1}$ measured by Shiga and co-workers [9]. The solid lines are fits to a Lorentzian lineshape.

This dynamic magnetic ground state is termed a *quantum spin liquid* ground state. If the frustration is relieved by the introduction of the Al atoms then the degeneracy of the ground state spin configurations is gradually lifted until zero-point motions are not sufficient to alter the ground state spin configuration.

1.4 Outline of this Thesis

In this thesis, I will investigate the magnetic and structural properties of pure β-Mn and β-MnAl alloys, addressing three main questions:

i) Why is β-Mn non-magnetic when both α-Mn and γ-Mn are strongly antiferromagnetic?

ii) By what mechanism does the inclusion of Al impurities in pure β-Mn stabilise magnetic order?

iii) What is the nature of the spin dynamics and magnetic ground state observed in β-MnAl alloys?

- In chapters 2 and 3, the basic theoretical concepts of metallic magnetism and neutron scattering will be introduced.
- In chapter 4, details of the preparation and initial structural and magnetic characterisation of β-Mn and β-MnAl will be presented.
- In chapter 5, I will present an investigation of the structural properties of β-Mn and β-MnAl. The nature of the transition from α-Mn to β-Mn will be investigated using high resolution neutron powder diffraction. The site occupancies of β-Mn with various impurities will also be presented. This study will show that the nature of the magnetic ground state of β-Mn alloys is crucially dependent on whether the impurity atoms replace the magnetic site II Mn atoms, or the non-magnetic site I Mn atoms.
- In chapter 6, I will present a muon spin relaxation study which will provide the first magnetic phase diagram of the β-MnAl system, and will highlight an abrupt change in the nature of the spin dynamics as Al is added to pure β-Mn.
- In chapter 7, the nuclear short-range order and the quasi-static magnetic correlations in β-MnAl will be investigated using XYZ neutron polarisation analysis. The

nature of the nuclear short-range order and the magnetic correlations will be modelled by a Reverse Monte-Carlo method developed as part of this thesis.

- In chapter 8, I will present an inelastic neutron scattering study of the evolution of the spin dynamics in β-Mn and β-$Mn_{0.8}Al_{0.2}$. This study will show that the spin fluctuation width in β-Mn and β-$Mn_{0.8}Al_{0.2}$ is much greater than the measurements of Shiga have suggested [9]. These measurements will also provide evidence of a crossover from purely itinerant moments in β-Mn to partially localised moments in β-$Mn_{0.8}Al_{0.2}$.

1.5 References

[1] A J Bradley and J Thewlis, Proc. Roy. Soc. **A115** (1927) 456

[2] P I Kripyakevich, Sov. Phys.-Cryst **5** (1960) 253

Y Nakai, H Oyamatsu and N Kunitomi, J. Phys. Soc. Japan **58** (1989) 2805

[3] D A Young, *Phase Diagrams of the Elements*, (University of California Press, 1991)

[4] Z S Basinski and J W Christian, Proc. Roy. Soc. London **223 (A)**, 554

[5] H Nakamura, K Yoshimoto, M Shiga, M Nishi and K Kakurai, J. Phys. Cond. Matter **9** (1997) 4701

[6] Y Nakai, H Oyamatsu and N Kunitomi, J. Phys. Soc. Japan **58** (1989) 2805

[7] M O'Keefe and S Andersson, Acta Cryst., **A33** (1977) 914

[8] C B Shoemaker, D P Shoemaker, T E Hopkins, and S Yindepit, Acta Cryst. **B34** 3573

[9] M Shiga, H Nakamura, M Nishi and K Kakurai, J. Phys. Soc. Japan, **63** (1994) 1656

[10] T Kohara and K Asayama, J. Phys. Soc. Japan **37** (1974) 401

[11] T Moriya, Progr. Theor. Phys. **33** (1965) 157

[12] C W Kimball and L R Sill, Phys. Rev. **B1** (1970) 3953

[13] Y Nakai, J. Phys. Soc. Japan, **63** (1994) 775

[14] Y Nakai, J. Phys. Soc. Japan **65** (1996) 1787

[15] Y Nishihara, S Ogawa and S Waki, J. Phys. Soc. Japan, **42** (1977) 845

[16] T Moriya, *Spin Fluctuations in Itinerant Electron Magnetism*, (Springer 1985)

[17] H Hasegawa, J. Phys. Soc. Japan, **38** (1975) 107

[18] T Shinkoda, K Kumagai and K Asayama, J. Phys. Soc. Japan **46** (1979) 1754

[19] H Hasegawa and T Moriya, J. Phys. Soc. Japan **38** (1975) 107

[20] M Kontani, T Hioki, Y Masuda, Solid State Comm. **18** (1975) 1251

[21] R S Hayano, Y J Uemura, J Imazato, N Nishida, H Yasuoka, T Yamazaki and Y Ishikawa, Phys. Rev. Lett. **41** (1978) 1743

[22] S Akimoto, T Kohara and K Asayama, Solid State Comm **16** (1975) 1227

[23] M Katayama, S Akimoto and K Asayama, J. Phys. Soc. Japan **42** (1977) 97

[24] Y Kohori, Y Noguchi and T Kohara, J. Phys. Soc. Japan **62** (1993) 447

[25] T Moriya and K Ueda, Solid State Comm. **15** (1974) 169

[26] V Sliwko, P Hohn and K Schwarz, J. Phys. Cond. Matter **6** (1994) 6557

2 Metallic Magnetism

2.1 Introduction

Traditionally the theoretical description of metallic magnets is divided into two distinct models. The *Local Moment Model* assumes the existence of well localised magnetic moments in a metal. This model is particularly effective in describing the rare-earth metals and alloys, but it has proved inadequate in describing metallic 3d transition elements and alloys. The *Itinerant Electron Model* attempts to describe magnetic metals where the unfilled electron orbitals form a conduction band, as is the case for the 3d transition metal elements. This model, however, has had only limited success in accounting for the observed magnetic properties of the transition metals. Over the last thirty years, a new theory has been developed which has proved very successful in accounting for the observed physical properties of itinerant electron metallic magnets. This is the *Self-Consistent Renormalisation (SCR) Theory*, originally developed by Moriya and Kawabata in 1973 [1]. In this theory it is postulated that the magnetic properties of itinerant electron systems are governed by coupled transverse and longitudinal spin fluctuations which are localised in reciprocal space. This is regarded as the opposite limit to the local moment model, where the spin fluctuations are localised in *real* space. The fact that these two limiting cases exist has led to the postulation of a unified model of magnetism based on the nature of magnetic spin fluctuations, which interpolates between the opposite extremes of the local moment and itinerant electron models.

In this chapter the predictions and shortcomings of the local moment and itinerant electron models will be highlighted. SCR theory will then be introduced and finally, the notion of magnetic frustration and spin glass magnetic order will be discussed in terms of its pertinence to the β-$Mn_{1-x}Al_x$ system.

2.2 The Local Moment Model

In the local moment model, atoms in a magnetic material carry a magnetic moment of fixed size. According to quantum mechanics, an atom occupies a particular eigenstate having quantised spin and orbital angular momenta, $\hbar\mathbf{S} = \sum\hbar\mathbf{s}$ and $\hbar\mathbf{L} = \sum\hbar\mathbf{l}$, where **s** and **l** are the spin and orbital quantum numbers of each electron in the atom. The magnetic moment of each atom is also found to be quantised in units of $\mu_B = e\hbar/2m$, known as the Bohr Magneton, and is given by

$$\mathbf{m} = \mu_B(\mathbf{L} + 2\mathbf{S}) = g_J\mu_B\mathbf{J}, \tag{2.1}$$

where the total angular momentum $\mathbf{J} = \mathbf{L} + \mathbf{S}$, and g_J is the Landé g-factor. If the energy of the (2J+1)-fold degenerate eigenstate given by a particular value of J is well separated from other states given by different J values, we can regard the atom as possessing a fixed magnetic moment.

2.2.1 Non-Interacting Local Moments

When a magnetic field, B, is applied to a system of local moments, each atom in that system will posses a potential energy $U = m_J g_J \mu_B B$. Assuming that the probability of an atom being in a state with energy U is proportional to $\exp(-U/k_BT)$, and that the atomic moments in the magnetic material are completely uncoupled, the magnetic susceptibility, χ, is given by the Curie Law,

$$\chi = \frac{\mu_0 M}{B} = \frac{\mu_0 N g_J^{\,2} \mu_B^{\,2} J(J+1)}{3k_B T} = \frac{C}{T}, \tag{2.2}$$

where,

$$C = \frac{\mu_0 N g_J^{\,2} \mu_B^{\,2} J(J+1)}{3k_B}. \tag{2.3}$$

2.2.2 Interacting Local Moments

Atomic magnetic moments may be coupled via direct or indirect exchange interactions, in addition to the much smaller dipole-dipole and quadrupolar interactions. The energy of a system of magnetic moments interacting via direct exchange is given by the familiar Heisenberg Hamiltonian,

$$H_{ex} = -\sum_{i,j \neq i} J_{i,j} (\mathbf{S}_i . \mathbf{S}_j) \tag{2.4}$$

where J is the interatomic exchange constant and i, j specify atomic sites over the crystal. Weiss found that the existence of a spontaneous internal mean magnetic field, $\mathbf{B}_{int}$, proportional to the mean magnetisation, may be used to represent the sum of the exchange forces present in a magnetic material. In this case the magnetic susceptibility follows the Curie-Weiss Law,

$$\chi = \frac{C}{T - \theta_{CW}}, \tag{2.5}$$

where θ_{CW} is the so-called Weiss constant,

$$\theta_{CW} = \frac{JC}{g_J^{\,2} \mu_B^{\,2}}. \tag{2.6}$$

2.2.3 Wavevector Dependent Exchange

While Heisenberg initially assumed that the exchange constant J was positive and explained ferromagnetic materials, we now know that the sign, size and range of the exchange interaction may be generalised to account for antiferromagnetic, ferrimagnetic and helimagnetic systems. In these cases the exchange interaction can be expressed as,

$$J(q) = \sum_{q} J_{ij} e^{iq.(\mathbf{R}_i - \mathbf{R}_j)}, \tag{2.7}$$

where J(q) is a wavevector dependent exchange parameter, which reflects the real space variation of the exchange interactions within the material with a modulation wavevector of **q**. Replacing J by J(q) in eq. (2.6), we can write the wavevector dependent susceptibility as,

$$\chi(q) = \frac{C}{T - \frac{J(q)C}{g_J^{\,2} \mu_B^{\,2}}}, \tag{2.8}$$

where we have implicitly invoked the so-called *Random Phase Approximation* (RPA) in assuming that each of the Fourier components in the wavevector dependent exchange field is independent [2]. The ferro- or antiferromagnetic transition temperature $T_{C/N}$ will occur at the temperature given by the divergence of $\chi(q)$, at

$$T_{C/N} = \frac{J(q)C}{g_J^{\,2} \mu_B^{\,2}}. \tag{2.9}$$

Figure 2.1 shows $1/\chi(q)$ plotted as a function of temperature for various cases of **q**-vector in the case of a simple cubic structure.

From figure 2.1 we can see that substitution of $\mathbf{q} = (\pi/a,0,0)$ into eq. (2.7) leads to a negative exchange interaction constant, and hence antiferromagnetic order, with neighbouring spins lying anti-parallel with one another. The Néel temperature T_N, is given by the intercept on the negative temperature-axis. More complicated magnetic structures are fully determined by the precise nature of $J(q)$, which may be peaked at **q**-vectors incommensurate with the lattice, or may exhibit complex "triple-q" (q_x, q_y and q_z) dependence, leading to a diverse range of magnetic structures.

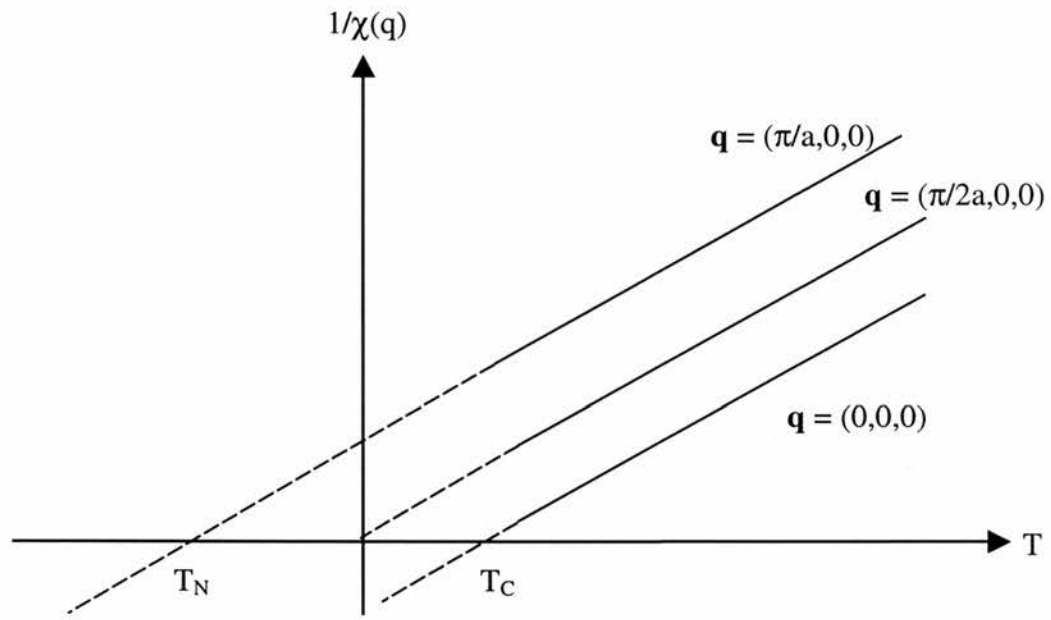

Figure 2.1

*Temperature dependence of the inverse wavevector dependent susceptibility $1/\chi(q)$ for various values of **q**, assuming a simple cubic crystal structure.*[2]

The Local Moment model has been well justified in magnetic systems where a well defined and stable magnetic moment can be said to exist, as is the case in magnetic insulators and rare-earth metals. However, direct Heisenberg exchange is relatively uncommon in these materials; "superexchange", mediated by a non-magnetic ligand, is the dominant exchange interaction in the insulators, while the conduction electron mediated RKKY interaction prevails in the rare-earth metals [2]. However the

observation in many magnetic metals of magnetic moments having values which are non-integer multiples of μ_B, is not consistent with the local moment model. In particular the observation of extremely small magnetisations in the weak ferromagnets $ZrZn_2$ and Sc_3In ($0.12\mu_B$ and $0.04\mu_B$ per atom respectively), cannot be explained by the local moment model, despite the fact that these metals obey the Curie-Weiss Law very closely for $T > T_C$, albeit with an effective moment far greater than that found in the ordered state.

2.3 The Itinerant Electron Model

2.3.1 Non-Interacting Itinerant Electrons

According to the nearly-free electron model, the eigenstates occupied by itinerant conduction electrons in a metal are characterised by their wavevectors, **k**. These states are occupied in accordance with the Pauli Exclusion Principle, with the k^{th} state occupied with a probability given by the Fermi-Dirac function,

$$f_k = \frac{1}{\exp\left[\frac{(\varepsilon_k - \varepsilon_F)}{k_B T}\right] - 1}, \tag{2.10}$$

where ε_k is the energy of the kth state and ε_F is the Fermi energy. In the absence of an applied or spontaneous magnetic field, each eigenstate is 2-fold degenerate with respect to electron spin. In the presence of a magnetic field, B, this degeneracy is lifted, with the energy of each spin eigenstate being given by,

$$\varepsilon = \begin{cases} \varepsilon_k - m_s g_s \mu_B B, & \text{for antiparallel spins} \\ \varepsilon_k + m_s g_s \mu_B B, & \text{for parallel spins.} \end{cases} \tag{2.11}$$

We can visualise this situation as in figure 2.2 where the electron density of states is split into a parallel and an antiparallel spin band.

After the electrons in the parallel band change their spin-state to equalise their potential energies at the Fermi level, there is a surplus, ΔN, of antiparallel electrons,

$$\begin{aligned} \Delta N &= 2\frac{D(\varepsilon_F)}{2} dE \\ &= D(\varepsilon_F) m_s g_s \mu_B B \end{aligned}, \tag{2.12}$$

leading to a magnetisation per unit volume of $M=\Delta N\mu_B$ in the same direction as the applied field, due to the negative gyromagnetic ratio of the electron. Taking the electronic Landé g-factor $g_s = 2$ and the magnetic spin quantum number $m_s = ½$, we arrive at the expression for the Pauli paramagnetic susceptibility,

$$\chi = \frac{\mu_0 M}{B} = \mu_0 \mu_B{}^2 D(\varepsilon_F), \tag{2.13}$$

which is independent of temperature. This expression successfully describes simple metals, such as the alkali metals, where the conduction electrons follow the free electron gas model (see figure 2.3).

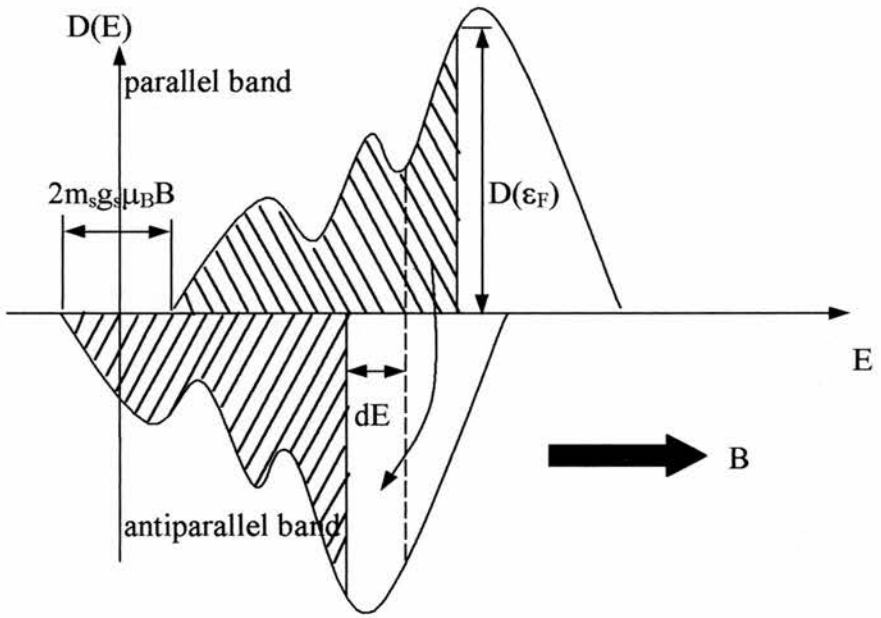

Figure 2.2

A schematic representation of Pauli paramagnetism at absolute zero. Electron states in the shaded regions are initially occupied. On application of an external field B, the band splits and the "up" and "down" electrons rearrange themselves to make their potential energies equal at the Fermi level, ε_F. This results in an net excess of spin "up" electrons in a magnetic field.

In the presence of a spatially varying mean molecular field of the form, **H**cos(**q.r**) the q-dependent paramagnetic susceptibility is given by the Lindhard function [4],

$$\chi(\mathbf{q}) = \frac{12\mu_0\mu_B{}^2 N}{16\varepsilon_F}\left[1+\frac{4k_F{}^2-q^2}{4k_Fq}\ln\left|\frac{2k_F+q}{2k_F-q}\right|\right], \tag{2.14}$$

where k_F is the Fermi wavevector given by $\varepsilon_F = \hbar^2 k_F^2/2m$. In the free electron approximation the density of electrons states at the Fermi energy is given by $D(\varepsilon_F) = 3N/2\varepsilon_F$, and we can combine eqs. (2.13) and (2.14) to obtain,

$$\chi(\mathbf{q}) = \chi_{\text{Pauli}}\left[\frac{1}{2} + \frac{4k_F^{\,2} - q^2}{8k_F q}\ln\left|\frac{2k_F + q}{2k_F - q}\right|\right], \tag{2.15}$$

where the term in brackets approaches unity as q tends to zero, as required.

2.3.2 Interacting Itinerant Electrons

2.3.2.1 The Hartree-Fock Model

Given a system of N electrons, the variational principle asserts that the n-electron wavefunction, Ψ, will be a solution to the Schrödinger equation, $H\Psi = E\Psi$, if it minimises the quantity,

$$\langle H \rangle_\Psi = \frac{(\Psi, H, \Psi)}{(\Psi, \Psi)}. \tag{2.16}$$

One trial wavefunction is that given by factorising Ψ into a product of N one-electron wavefunctions of the form,

$$\Psi(\mathbf{r}_1,s_1,\ \mathbf{r}_2,s_2,\ \mathbf{r}_3,s_3,\ldots..,\ \mathbf{r}_N,s_N) = \psi_1(\mathbf{r}_1,s_1)\psi_2(\mathbf{r}_2,s_2)\psi_3(\mathbf{r}_3,s_3)\ldots..\psi_N(\mathbf{r}_N,s_N). \tag{2.17}$$

However, this wavefunction does not obey the Pauli Exclusion Principle, which requires that the sign of Ψ changes whenever two of its arguments are interchanged. In order to overcome this problem, we replace Ψ given by eq. (2.17) by a *Slater Determinant* of one electron wavefunctions, which is a linear combination of the product of eq. (2.17) and all other possible permutations.

$$\Psi(\mathbf{r}_1,s_1,\mathbf{r}_2,s_2,\ldots..\mathbf{r}_N,s_N) = \begin{vmatrix} \psi_1(\mathbf{r}_1,s_1) & \psi_1(\mathbf{r}_2,s_2) & \ldots & \psi_1(\mathbf{r}_N,s_N) \\ \psi_2(\mathbf{r}_1,s_1) & \psi_2(\mathbf{r}_2,s_2) & \ldots & \psi_2(\mathbf{r}_N,s_N) \\ \vdots & \vdots & & \vdots \\ \psi_N(\mathbf{r}_1,s_1) & \psi_N(\mathbf{r}_2,s_2) & \ldots & \psi_N(\mathbf{r}_N,s_N) \end{vmatrix} \tag{2.18}$$

Substituting this wavefunction into the Schrödinger equation leads to the *Hartree-Fock equation*,

$$-\frac{\hbar^2}{2m}\nabla^2\psi_i(\mathbf{r})+U^{ion}(\mathbf{r})\psi_i(\mathbf{r})+U^{electron}(\mathbf{r})\psi_i(\mathbf{r}) \\ -\sum_j\int d\mathbf{r}'\frac{e^2}{|\mathbf{r}-\mathbf{r}'|}\psi_j^*(\mathbf{r}')\psi_i(\mathbf{r}')\psi_j(\mathbf{r})\delta_{s_is_j}=\varepsilon_i\psi_i(\mathbf{r}) \tag{2.19}$$

where $U^{ion}(\mathbf{r})$ is the potential due to the nuclei and $U^{electron}(r)$ is a potential due to the sum of all other electrons in the material. The last term on the left hand side is known as the *exchange term*, which results in a state of lower energy for parallel electron spins s_i and s_j. Thus, consideration of electron-electron exchange interactions leads to a substantially altered band structure from that predicted by the free-electron model. However, the Hartree-Fock model only describes electronic states in terms of one-electron wavefunctions, ψ_i, which are affected by interactions.

2.3.2.2 The Fermi-Liquid Model

The Fermi-Liquid model takes the proposition laid out in the Hartree-Fock model one stage further. It asserts that in addition to modified one-electron energies due to interactions, electron-electron scattering processes will occur. However, the requirement that an electron can only be scattered into unoccupied states according to the Pauli exclusion principle means that at a finite temperature, only electrons within k_BT of the Fermi energy, ε_F, are available to be scattered. This leads to a temperature dependence of the scattering rate;

$$\frac{1}{\tau}=A+B(k_BT)^2, \tag{2.20}$$

where A is the scattering rate at T=0, and the coefficient B is independent of temperature. This implies a temperature dependence of the electronic resistivity, $\rho(T) \propto T^2$ at low temperatures, when phonon contributions to electron scattering are small. (see section 4.5)

If an electron is excited above the Fermi energy, then Hartree-Fock type electron-electron interactions increase the amount of energy required to complete this process. This increase in energy is characterised by the effective mass, m^*, of the excited electron or *quasi-electron*. The energy of this quasi-electron state will be given by,

$$\varepsilon(\mathbf{k}) = \varepsilon_F + \frac{\hbar^2 k_F}{m^*}\left|k - k_F\right|, \tag{2.21}$$

where k_F is the Fermi wavevector. The energies associated with quasi-electrons created above the Fermi surface will affect the number of occupied quasi-electron states created in the presence of an applied magnetic field, and hence the value of the paramagnetic susceptibility. The resulting uniform susceptibility of a Fermi liquid is of the form [5]

$$\chi = \frac{1 + \frac{1}{3}A_1}{1 + B_0}\chi_{\text{Pauli}}\ , \tag{2.22}$$

where the parameter A_1 depends on the quasi-electron effective mass, and B_0 depends on the nature of the quasi-electron distribution in k-space. Notice that if B_0 falls from 0 to –1 as the electron interactions become stronger, the susceptibility becomes large, displaying so-called *exchange enhancement.* The susceptibility for various metals is shown in figure 2.3 [3]. The high values for the transition metals and Pd compared with the alkali metals indicates the presence of exchange enhancement. If B_0 = -1, the susceptibility diverges, implying a transition to a ferromagnetic state.

2.3.2.3 The Stoner/Hubbard Model

The Stoner/Hubbard model [6] assumes an electron-electron exchange interaction of the Hartree-Fock type, within the tight binding approximation. In this model, the exchange interaction is significant only for itinerant d-electrons on the same ionic site. Within the confines of this assumption, Stoner was able to describe the electron exchange interactions by a mean molecular field, analogous to the Weiss molecular field description of local moment exchange interactions. This molecular field takes the form,

$$H_m = \gamma M, \tag{2.23}$$

where γ is the molecular field constant. Referring to figure 2.2, if this field arises spontaneously the "up" and "down" electron spin bands will split, leading to a transfer of Δn electrons per unit volume from the "up" to the "down" spin states. The net magnetisation, M, is then,

$$M = 2\Delta n\mu_B = (n\downarrow - n\uparrow)\mu_B. \tag{2.24}$$

The increase in the number of parallel electron spins *decreases* the total exchange energy in the material according to the Hartree-Fock equation (2.17), which can be

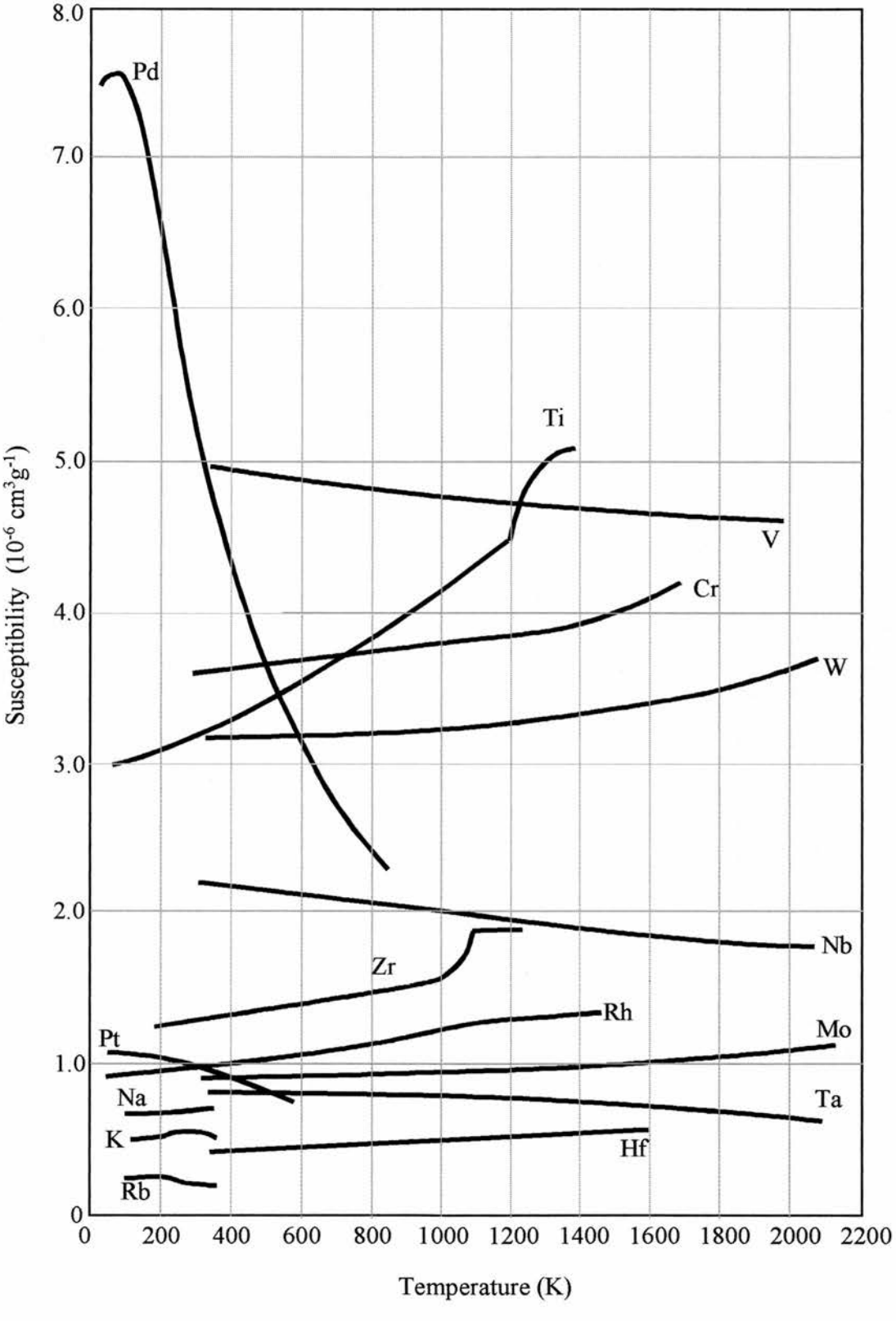

Figure 2.3

Temperature dependence of the paramagnetic mass susceptibility of metals. The large values associated with the transition metals and Pd indicate the presence of exchange enhancement (from Kittel, [3]).

equated to a decrease in the effective magnetostatic energy density within the molecular exchange field, H_m, given by,

$$\Delta E_{ex} = -\int_0^M H_m dM = -\gamma \int_0^M M dM = -\frac{1}{2}\gamma (n_\downarrow - n_\uparrow)^2 \mu_B{}^2 . \qquad (2.25)$$

This value is exactly half the relative displacement of the exchange split bands. If we restrict our attention to conditions at absolute zero, where the electron states are filled exactly to the Fermi energy, the kinetic energy of each electron transferred between the spin-dependent bands must increase, since each flipped electron will be lifted into an unoccupied state of higher energy. This increase in kinetic energy ΔE_k will be given by,

$$\Delta E_k = \frac{\Delta N}{\Delta N/\Delta E_k} = \frac{\frac{1}{2}(n_\downarrow - n_\uparrow)}{D(\varepsilon_F)/2} . \qquad (2.26)$$

If the net change is a decrease in total energy, the electron transfer between the spin dependent bands will take place spontaneously, resulting in an excess population in the spin "down" band. The condition for the appearance of spontaneous magnetisation is therefore,

$$\begin{aligned} \Delta E_{ex} > \Delta E_k &\Rightarrow \frac{1}{2}\gamma (n_\downarrow - n_\uparrow)\mu_B{}^2 D(\varepsilon_F) > 1 \\ &\Rightarrow ID(\varepsilon_F) > 1 \end{aligned} , \qquad (2.27)$$

where, $I = \frac{1}{2}\gamma(n\downarrow - n\uparrow)\mu_B{}^2$, termed the Stoner parameter, is a measure of the mean exchange energy per electron. Figure 2.4 shows the theoretically calculated values of $D(\varepsilon_F)$ and I and their product for various metals across the periodic table [7]. Eq. (2.27) is known as the *Stoner Criterion*. From this equation it can be seen that the occurrence of ferromagnetism in itinerant electron systems is closely related to the band structure in the vicinity of the Fermi energy. The Stoner Criterion is likely to be satisfied for a narrow, peaked electron density of states at the Fermi level, which is a characteristic feature of the d-electron transition metals.

If the Stoner criterion is not satisfied, the molecular exchange field will nonetheless affect the relative energy splitting of the spin-dependent bands in the presence of a magnetic field. dE in eq. (2.12) will become,

$$dE = m_s g_s \mu_B B + I \Delta N, \qquad (2.28)$$

leading to a paramagnetic susceptibility of the form,

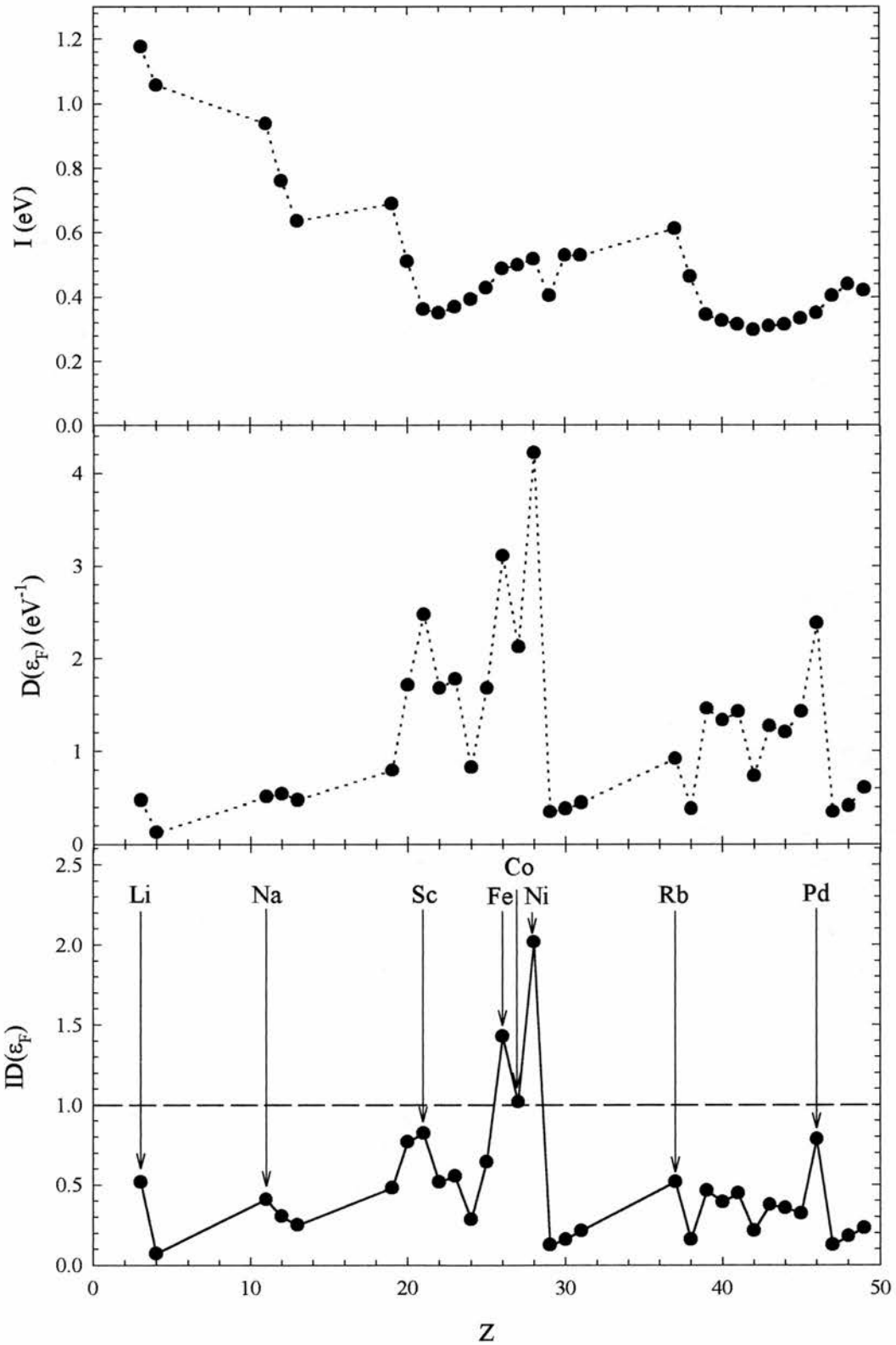

Figure 2.4

a) The Stoner exchange parameter, I, b) the density of states per atom at the Fermi energy, $D(\varepsilon_F)$, and c) the product of I and $D(\varepsilon_F)$, as a function of atomic number, z, at room temperature [7]. Fe, Co and Ni satisfy the Stoner Criterion and display ferromagnetism, while Sc and Pd, display strong exchange enhancement.

$$\chi = \frac{\chi_{\text{Pauli}}}{1 - \text{ID}(\varepsilon_F)}. \tag{2.29}$$

This form of the susceptibility was first predicted by Hubbard, and is of the same form as the Fermi liquid prediction of the exchange enhanced susceptibility (see figure 2.3).

The exact shape of the Fermi surface in a metal may cause the mean electron exchange interaction to be q-dependent, leading to a spatially varying mean molecular exchange field. Assuming that the Fourier components of this exchange field are independent (RPA) we can write the wavevector dependent susceptibility [8] as,

$$\chi(\mathbf{q}) = \frac{\chi_0(\mathbf{q})}{1 - \dfrac{2I\chi_0(\mathbf{q})}{Ng_s{}^2\mu_B{}^2}} = \frac{\chi_0(\mathbf{q})}{1 - \alpha\chi_0(\mathbf{q})}, \tag{2.30}$$

where $\chi_0(\mathbf{q})$ is the non-interacting susceptibility given by eq. (2.15).

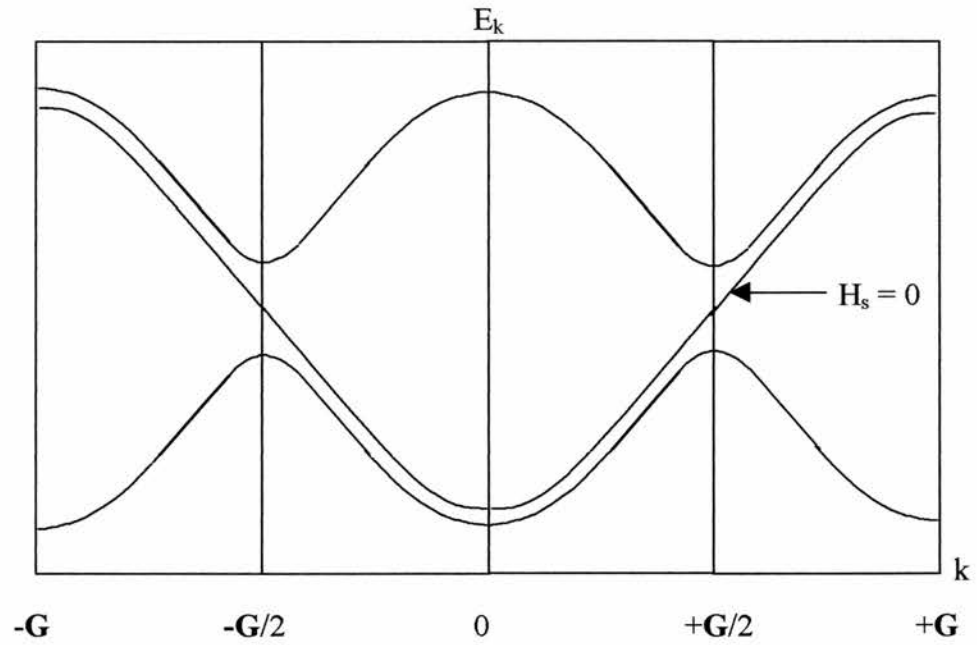

Figure 2.5

Electron energy dispersion arising from an antiferromagnetically correlated exchange field, H_s. The corresponding relation for H_s = 0 (paramagnetism) is also shown. Characteristic energy gaps are formed at the antiferromagnetic wavevector $\boldsymbol{Q} = \boldsymbol{G}/2$ where $\boldsymbol{G}$ is the reciprocal lattice vector. To minimise energy, electrons reside below the energy gaps, heaped up around the antiferromagnetic zone boundary.

For antiferromagnetic exchange, where the first divergence of $\chi(\mathbf{q})$ occurs at $\mathbf{q} = \mathbf{G}/2$, we define the so-called staggered magnetisation, $M_s = M_a - M_b$, where M_a and M_b are sublattice magnetisations,

$$M_a = \tfrac{1}{2} \sum_j (n_{j\downarrow} - n_{j\uparrow})$$

$$M_b = \tfrac{1}{2} \sum_i (n_{i\downarrow} - n_{i\uparrow}), \qquad (2.31)$$

where i and j are sublattice points which may or may not be associated with nuclear positions in the lattice. The staggered exchange field is then defined as, $H_s = \gamma M_s$. It can be shown [9] that the Hamiltonian constructed according to the Hartree-Fock approximation for antiferromagnetic exchange, leads to an electron energy dispersion of the form shown in figure 2.5

Defining the staggered susceptibility, $\chi_s = \chi(\mathbf{q} = \mathbf{G}/2)$, the condition for the appearance of antiferromagnetism is, $\alpha\chi_s > 1$, with the Néel Temperature T_N given by,

$$\alpha\chi_s(T_N) = 1. \qquad (2.32)$$

2.3.3 The Dynamical Susceptibility

Further development of the Stoner Model was attempted by Izuyama [10], in which the effects of fluctuations of the spin density in itinerant electron magnets were taken into account. Making use of the random phase approximation, the frequency dependent dynamical susceptibility of an interacting electron system under the influence of a spatially and time varying applied field of the form $\mathbf{H}\cos(\mathbf{q}.\mathbf{r} - \omega t)$ takes the form,

$$\chi(\mathbf{q},\omega) = \frac{\chi_0(\mathbf{q},\omega)}{1 - \dfrac{2I\chi_0(\mathbf{q},\omega)}{Ng_s^{\,2}\mu_B^{\,2}}} = \frac{\chi_0(\mathbf{q},\omega)}{1 - \alpha\chi_0(\mathbf{q},\omega)}, \qquad (2.33)$$

where $\chi_0(\mathbf{q},\omega)$ is the non-interacting frequency dependent susceptibility, given by a dynamical generalisation of the Lindhard function (2.14). In the random phase approximation, the dynamical susceptibility can be expressed in terms of the frequency distribution of spin fluctuations, $\Gamma(\mathbf{q})$, as

$$\chi(\mathbf{q},\omega) = \frac{\chi(\mathbf{q})}{1 - \dfrac{i\omega}{\Gamma(\mathbf{q})}}. \qquad (2.34)$$

Taking the imaginary part of the dynamical susceptibility given by eq (2.34), we find,

$$\frac{1}{\omega}\chi''(\mathbf{q},\omega) = \frac{\chi(\mathbf{q})\Gamma(\mathbf{q})}{\Gamma(\mathbf{q})^2 + \omega^2}, \qquad (2.35)$$

which is a Lorentzian form, of width $\Gamma(\mathbf{q})$ and area $\chi(\mathbf{q})$, centred at zero frequency. This quantity can be directly measured using inelastic neutron scattering (see section 3.2.3).

Stoner calculated the contribution to the dynamical susceptibility from excitations of quasi-electrons moving across the Fermi surface and changing their spin states. Such excitations contribute to the dynamical susceptibility as a function of their wavevector transfers, $\mathbf{q}$ and energy transfers, $\hbar\omega$. In the absence of exchange interactions these single particle excitations are termed *Stoner excitations*. When exchange interactions between quasi-electron and quasi-hole excitations and are taken into account, the spatial and temporal fluctuations of the electron spin density may form co-operative normal modes or *spin waves*.

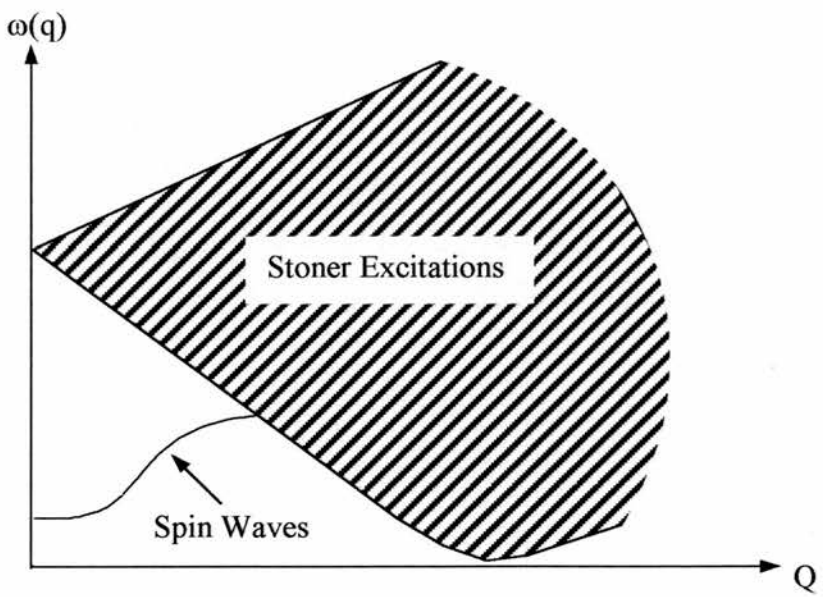

Figure 2.6

Theoretical prediction of the magnetic excitation spectrum for an itinerant ferromagnet [11].

This occurs when the second term in the denominator of eq. (2.33), $\alpha\chi_0(\mathbf{q},\omega) = 1$, resulting in a singularity of the dynamical susceptibility. The predicted excitation spectrum for a ferromagnetically correlated electron gas is shown in figure 2.6. The spin wave branch calculated using the dynamical Lindhard equation is found to be quadratic in $\mathbf{q}$.

2.3.4 The Validity of the Itinerant Electron Model

The itinerant electron model is able to explain the observed ordered moment per atom of materials such as Fe, Co and Ni which are not integral multiples of the Bohr magneton. Support for this model is also provided by the observation of narrow d-electron bands in the 3d ferromagnets which are well described by the tight-binding model, and which are consistent with the requirements of the Stoner Criterion for the appearance of ferromagnetism. However, the itinerant electron model fails to explain the observed susceptibility in the transition metals at finite temperatures, and predicts magnetic transition temperatures of at least an order of magnitude too high when compared with experiment. Most strikingly, it cannot account for the observed Curie-Weiss susceptibility for $T > T_C$ in the 3d ferromagnets. The failure of the Stoner Model has been attributed to the invalidity of the random phase approximation at high temperatures. According to the RPA spin fluctuations in the electron bands involve excited quasi-electron states moving independently of each other, with only bound quasi-electron-hole states undergoing electron exchange interactions. This model, however, neglects the quasi-electron interaction with the quasi-hole created by the excitation at high temperatures. When the quasi-electron-hole pair forms a bound state it corresponds to a spin wave excitation. When a bound state is not formed the excitation is of a unbound or dissipative nature, but nevertheless is an exchange enhanced mode of the spin fluctuations. Thus, while the appearance of spin waves at low temperatures is predicted, the failure of the Stoner model to include exchange enhancement at high temperatures results in its inability to account for the paramagnetic behaviour of the 3d ferromagnets, and the dramatic overestimation of the transition temperatures. To refine the description of itinerant electron magnets then, one must include the interaction of both collective and dissipative spin fluctuation components at high temperatures.

2.4 The Self-Consistent Renormalisation Theory

In the Self-Consistent Renormalisation (SCR) theory [9], the free energy of an itinerant electron system is calculated from the Hartree-Fock Hamiltonian, plus an additional potential which includes a spin-correlation term included to take account of coupled

exchange enhanced spin fluctuations. The inclusion of this potential represents the *renormalisation* of the equilibrium state. Using the fluctuation dissipation theorem [12], the spin correlation term, $S(\mathbf{q},\omega)$, can be expressed in terms of the imaginary part of the dynamical susceptibility, $\chi''(q,\omega)$,

$$S(\mathbf{q},\omega) = \frac{N\hbar}{\pi(g_s\mu_B)^2} \cdot \frac{1}{1-\exp(-\hbar\omega/k_BT)} \cdot \chi''(\mathbf{q},\omega) . \qquad (2.36)$$

The spin correlation term in the Hamiltonian is determined using an assumed form of the dynamical susceptibility, and correspondingly, the static susceptibility is evaluated from the form of the renormalised free energy of the system, as determined by this Hamiltonian. Taking the RPA expression for $\chi''(\mathbf{q},\omega)$ given by eq (2.35), the static susceptibility inferred by this method is found to be inconsistent with the original RPA form of $\chi''(\mathbf{q},\omega)$ at finite temperatures [9]. The task of SCR theory is to find an appropriate spin-correlation term for the Hamiltonian of the spin fluctuating system which can then be solved in a *self-consistent* fashion. Moriya and Kawabata [13] showed that in order to obtain a self-consistent solution of the renormalised free energy, the dynamical susceptibility must be of the form,

$$\chi(\mathbf{q},\omega) = \frac{\chi_0(\mathbf{q},\omega)}{1-\alpha\chi_0(\mathbf{q},\omega)+\lambda(\mathbf{q},\omega)}, \qquad (2.37)$$

where $\lambda(\mathbf{q},\omega)$ is the so-called renormalisation term. The detailed form of $\lambda(\mathbf{q},\omega)$ depends on the exact nature of the assumed spin fluctuation correlations.

2.4.1 Curie-Weiss Susceptibility in Itinerant Electron Magnets

Perhaps the most remarkable result of SCR theory is that even the assumption of a non-interacting electron gas with parabolic bands in the determination of the form of $\lambda(\mathbf{q},\omega)$, leads to an approximate Curie-Weiss temperature dependence of the inverse static susceptibility. Moriya, has used mode-mode coupling theory [14] to express $\lambda(\mathbf{q},\omega)$ in terms of the thermal averages of the *longitudinal spin density amplitude* fluctuations and *transverse spin density orientational* fluctuations.

2.4.1.1 Itinerant Electron Ferromagnets

For a system of ferromagnetically correlated spin fluctuations, $\lambda(\mathbf{q},\omega)$ is given by,

$$\frac{\lambda(\mathbf{q},\omega)}{\chi_0(\mathbf{q},\omega)} = \frac{5}{3}F_1 S_L{}^2(\mathbf{q},\omega), \tag{2.38}$$

where, $\chi_0(\mathbf{q},\omega)$ is the non-interacting susceptibility, F_1 is the mode-mode coupling constant and $S_L(\mathbf{q},\omega)$ is the thermal average of the local longitudinal and transverse spin density fluctuations. $S_L{}^2$ can be determined by the fluctuation-dissipation theorem, and is of the form [15],

$$< S_L{}^2 >= \frac{3k_B T}{g_s{}^2 \mu_B{}^2 N^2} \sum_q \chi(\mathbf{q}). \tag{2.39}$$

If we define the *local susceptibility* as the sum over $\mathbf{q}$ of $\chi(\mathbf{q})$,

$$\chi_L = \frac{1}{N}\sum_q \chi(\mathbf{q}), \tag{2.40}$$

then we can rearrange eq. (2.39) to give,

$$\chi_L(T) = \frac{N g_s{}^2 \mu_B{}^2 S_L(T)^2}{3k_B T}, \tag{2.41}$$

which is the form of the Curie Law. If we now substitute eq. (2.38) into the dynamical susceptibility given by eq. (2.37), sum over all spin fluctuation energies and take the inverse, we find that the $\mathbf{q} = 0$ component of the susceptibility, $\chi(0)$, can be expressed by,

$$\begin{aligned} &\frac{\chi_0}{\chi(0)} = (1 - \alpha\chi_0(0)) + \frac{5}{3}F_1 S_L{}^2 \\ &\Rightarrow \frac{1}{\chi(0)} = \frac{1}{\chi_{HF}(0)} + \frac{5}{3}F_1 S_L{}^2 \end{aligned}, \tag{2.42}$$

where χ_{HF} is the Hartree-Fock susceptibility given by eq. (2.30).

This equation follows a Curie-Weiss form of the susceptibility assuming $S_L{}^2$ rises linearly with T. It should be emphasised that the magnetic transition temperature, given by eq (2.42) when $1/\chi(0)=0$, will be a positive value only if the Stoner criterion, $\alpha\chi_0(0) > 1$, is satisfied. Figure 2.7 shows a number of numerical simulations of $\chi_0/\chi(T)$ given by eq (2.42) for various values of $\alpha\chi_0$, compared with the Stoner prediction for a system with $T_C = 0.01K$ [16].

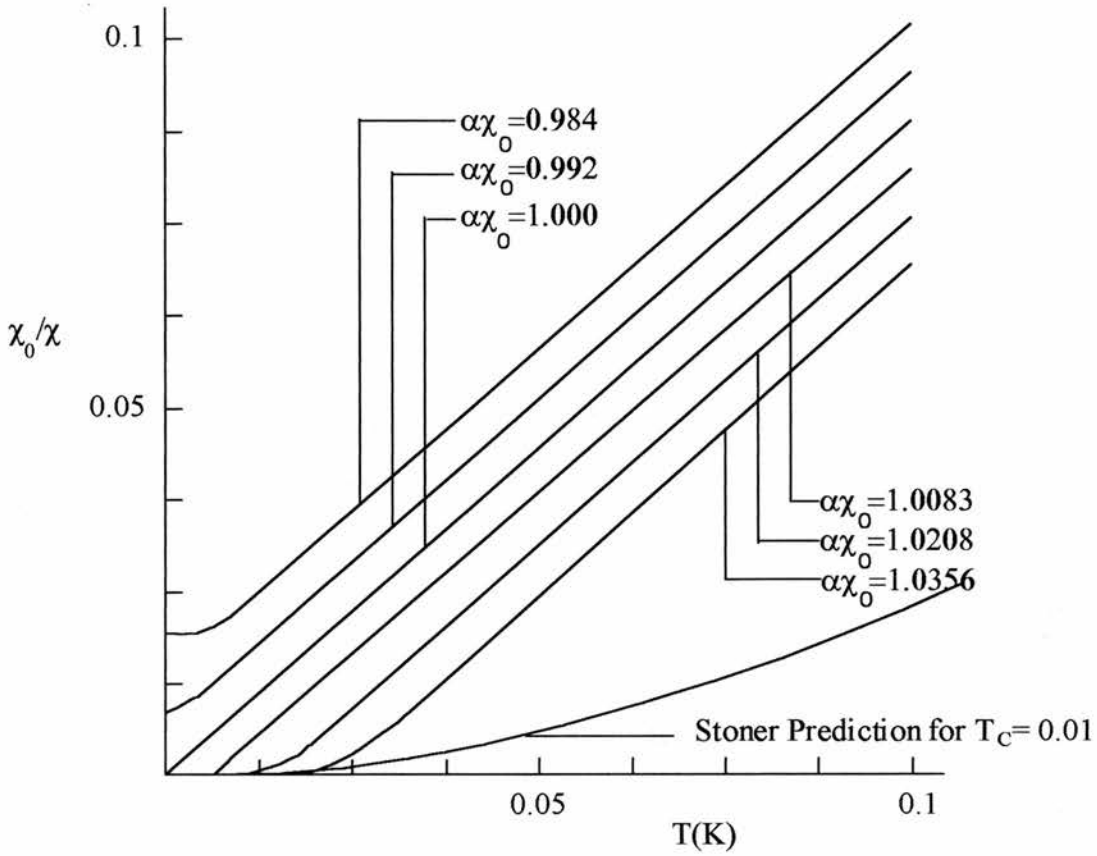

Figure 2.7

Temperature dependence of the inverse magnetic susceptibility from numerical simulations of a free electron gas, following eq (2.42). The Stoner prediction is also shown for comparison[16].

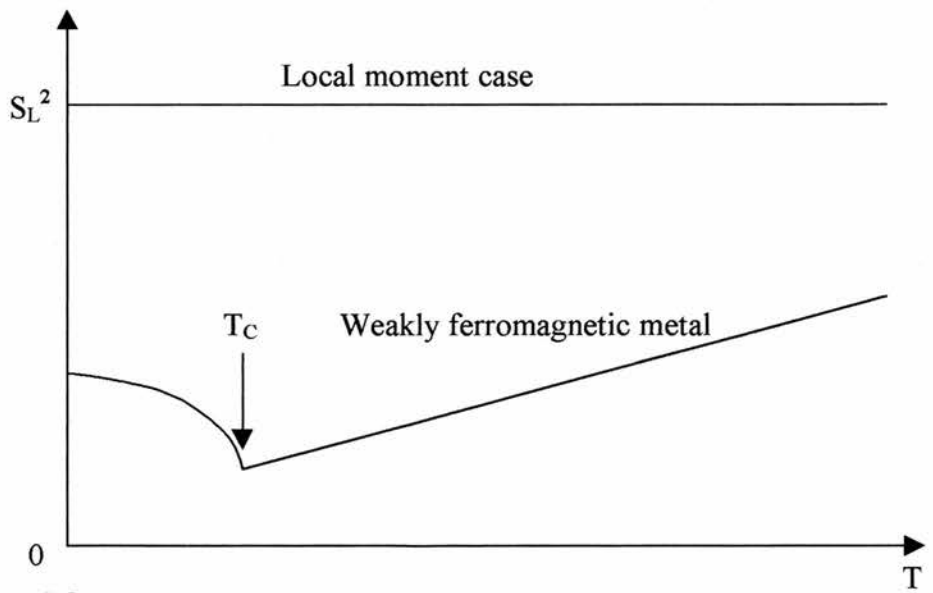

Figure 2.8

Temperature dependence of the squared local spin density amplitude S_L^2 for a weakly ferromagnetic metal and a local moment system [9].

The spin density fluctuation amplitude S_L^2 at T_C is given by,

$$S_L^2(T_C) = 3/5\ (M(0)/N)^2, \tag{2.43}$$

where M(0) is the magnetisation at T=0K. This implies that S_L^2 will initially decrease with increasing temperature, until it reaches 3/5 of its initial value at T_C, and then rises linearly above T_C. This temperature dependence of S_L^2 is shown in figure 2.8, compared with the local moment case.

2.4.1.2 Itinerant Electron Antiferromagnets

For antiferromagnetically correlated spin fluctuations, $\lambda(Q)$ is given by,

$$\frac{\lambda(\mathbf{Q})}{\chi_0(\mathbf{Q})} = F_s(\frac{5}{3}S_L^{\ 2} + M_s^{\ 2}(0)), \tag{2.44}$$

where, F_s is the mode-mode coupling constant for the Fourier components of the spin density around the antiferromagnetic wavevector Q, and $M_s(0)$ is the staggered magnetisation per magnetic atom at T=0K. The magnetic susceptibility at $\mathbf{q} = Q$ will then be [17,18],

$$\frac{1}{\chi(Q)} = \frac{1}{\chi_{HF}(Q)} + \frac{5}{3}F_sS_L^{\ 2} + F_sM_s^{\ 2}(0). \tag{2.45}$$

Eq. (2.45) is once again of a Curie-Weiss form with the intercept at $1/\chi(Q) = 0$ taking a negative value when,

$$\frac{1}{\chi_{HF}(Q)} + F_sM_s^{\ 2}(0) > 0. \tag{2.46}$$

Since this condition can be satisfied even when $\alpha\chi_0(Q) < 1$, eq. (2.46) applies to both antiferromagnetic metals and antiferromagnetically correlated paramagnetic metals (known as *nearly* antiferromagnetic metals).

2.4.2 Physical Properties of Itinerant Electron Antiferromagnets

The SCR theory has been applied to discuss various physical properties in addition to the magnetic susceptibility discussed in the preceding section. Good agreement between theory and experiment for itinerant electron ferromagnets has been demonstrated in a number of systems, including MnSi, Sc_3In and $ZrZn_2$ [19,20,21]. There has been much less attention devoted to the itinerant electron antiferromagnets, with the notable exception of the C15 cubic Laves phase compound YMn_2 and related

alloys [22,23]. The predicted physical properties of itinerant electron antiferromagnetic systems are summarised below.

2.4.2.1 Thermal Expansion

Since the squared spin density fluctuation amplitude S_L^2 increases with increasing temperature, the magnetovolume of the system should also increase. This is expressed in terms of SCR theory as,

$$\Omega_m = \sum_q \left(\frac{D_q}{B} \right) \left(S_q^2(T) - S_q^2(0) \right), \tag{2.47}$$

where Ω_m is the magnetic volume strain, B is the Bulk modulus, and D_q is the q-dependent magnetovolume coupling constant. For antiferromagnetic metals, it can be assumed that $\sum_q D_q \sim D_Q$ where Q is the antiferromagnetic ordering wavevector. Therefore, summing over the Brillouin zone we have,

$$\Omega_m(T) = N^2 \frac{D_Q}{B} \left(S_L^2(T) - S_L^2(0) \right). \tag{2.48}$$

This suggests that the temperature dependence of Ω_m is the same as that of S_L^2. However, this effect is extremely difficult to test, unless one can isolate and subtract out non-magnetic contributions to the thermal expansion. A study of the thermal expansion of pure Cr and CrV alloys, by Roberts and co- workers, seems to support the SCR prediction of an increase in S_L^2 with increasing temperature, in the paramagnetic regime [24]. The SCR theory also provides a qualitative explanation of the *invar* phenomenon, in which ferromagnetic metals such as Fe_3Pt and some Fe-Ni alloys display nearly vanishing thermal expansion coefficients [25]. This effect arises due to the compensation of non magnetic thermal expansion by a negative (constrictive) magnetic contribution given by eq. (2.48). A negative contribution will occur when S_L^2 decreases with increasing temperature as it approaches T_C from below, causing a reduction in the magnetostriction.

2.4.2.2 Specific Heat

SCR theory predicts that the electronic coefficient of the specific heat for weakly antiferromagnetic metals is proportional to $|\alpha - 1|^{1/2}$ [26]. This leads to a relation of the form,

$$\gamma = \gamma_0 - \nu T_N^{4/3} \tag{2.49}$$

where ν is a constant. This relation has been supported by measurements on various β-Mn alloys by Shinkoda and co-workers [27]. (see chapter 1)

2.4.2.3 Nuclear Spin Relaxation

Assuming a dominating Fermi-contact type interaction between nuclear and electronic spins, and a Curie-Weiss temperature dependence of the staggered susceptibility, SCR theory predicts a nuclear spin relaxation rate $1/T_1$ of the form [28].

$$\frac{1}{T_1} \propto \frac{T}{(T-T_N)^{1/2}}, \tag{2.50}$$

This prediction has been supported by NMR studies of β-Mn and β-MnAl [29,30,31]. (see chapter 1)

2.4.2.4 Electrical Resistivity

The SCR theory predicts a contribution to the electrical resistivity from antiferromagnetically correlated spin fluctuations of the form,

$$\rho \propto T^{3/2}, \tag{2.51}$$

for metals close to the Stoner critical boundary, $\alpha\chi_0(Q) \sim 1$. In chapter 4 of this study, it will be shown that the temperature dependence of the electrical resistivity of β-Mn follows this prediction.

2.4.3 The SCR Unified Theory

Two theories of magnetism have now been introduced which apply to two mutually opposite limiting cases: the local moment limit and the itinerant moment limit. We now need to generalise the SCR theory to take account of the possible existence and formation of local moments in metals.

Figure 2.9 shows the so-called Rhodes-Wohlfarth plot [32], in which p_C/p_s is plotted against T_C for various ferromagnets, where p_C is the effective magnetic moment per atom as deduced from the Curie constant [eq. (2.3)] and p_s is the saturation moment per magnetic atom. In the local moment limit the ratio $p_C/p_s = 1$, whereas in the itinerant electron limit $p_C/p_s >> 1$, since the saturation moment is independent of the Curie constant.

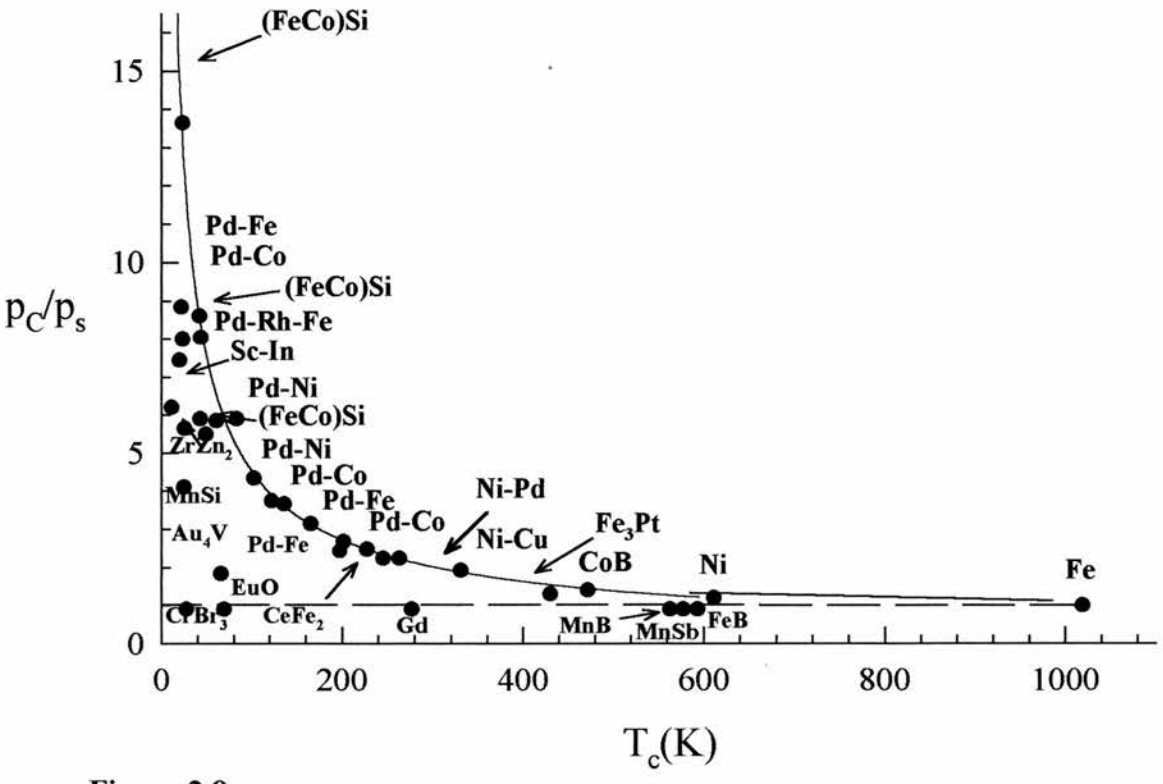

Figure 2.9

The Rhodes-Wohlfarth plot [32].

It is instructive to note that the values of p_C/p_s are distributed very evenly between these two extremes, suggesting the simultaneous existence of both local and itinerant moments in many metallic magnets. This observation highlights the need for a unifying theory which is able to interpolate between the local moment and itinerant electron limits.

According to SCR theory the physical properties of local moment and itinerant systems are determined purely by the nature of their spin density fluctuations. In local moment systems the spin density fluctuation amplitude is fixed, implying magnetic moments localised in real space. In itinerant electron systems, the spin fluctuation amplitude varies with temperature, and is generally small compared with local moment systems. Since these fluctuations are correlated in time as well as space they can only be regarded as localised in reciprocal space and therefore, infinitely extended in real space. It follows that all magnetic materials may be classified according to the amplitude, and spatial extent of their spin fluctuations. Figure 2.10 shows Moriya's classification

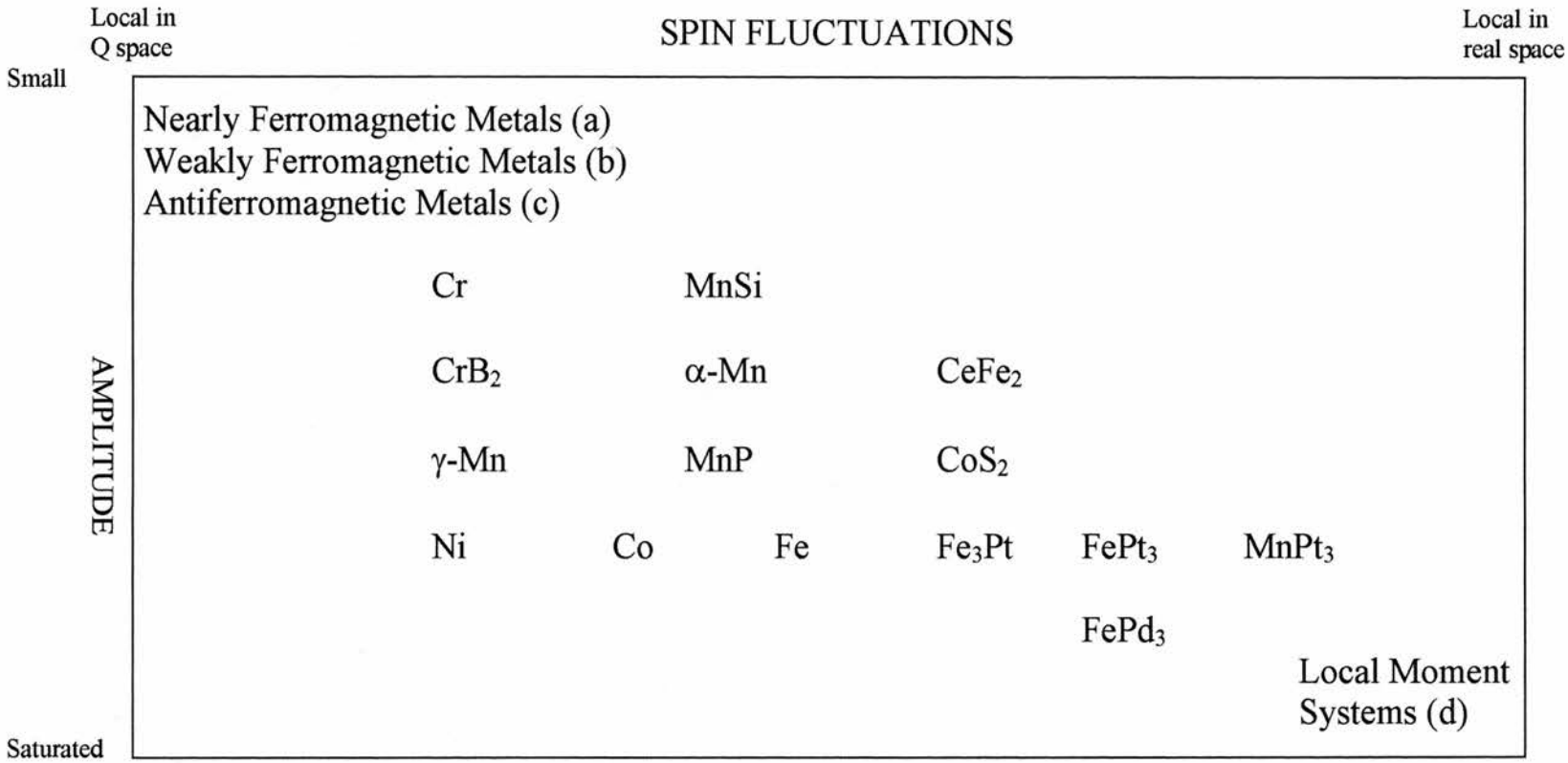

(a) Pd, $HfZn_2$, $TiBe_2$, YCo_2, YRh_6B_4, Ni-Pt alloys, etc.

(b) Sc_3In, $ZrZn_2$, YNi_3, Ni_3Al, $FeCoSi_2$, $LaRh_6B_4$, etc.

(c) β-Mn, V_3Se_4, CrMo alloys, etc.

(d) Magnetic Insulator compounds, Rare-earths, Heusler alloys, etc.

Figure 2.10

Moriya's classification of magnetic materials according to their spin fluctuation properties. [33]

diagram in which various magnetic materials are arranged according to the above criteria [33].

2.4.3.1 Moment Localisation in Metals

A description of the formation of a local magnetic moment in a metal was given by Anderson in 1961 [34], to account for the observation of localised magnetic moments on transition metal impurity atoms in non-magnetic, metallic hosts. The Hamiltonian describing a 3d impurity in a metallic host will take the form,

$$H = H_{s\text{-band}} + H_{d\text{-band}} + H_{impurity} + H_{hopping} + H_{exhange}. \quad (2.52)$$

We can represent this situation schematically, as shown in figure 2.11 [35].

The hopping term $H_{hopping} = V$ (also known as the sd mixing term) arises from the hopping of electrons from the localised d-orbital to the conduction band. This term will depend on the lattice constant of the host metal, with the hopping energy increasing as the atoms become progressively more localised. The $H_{impurity}$ term is simply,

$$H_{impurity} = U n_{d\uparrow} n_{d\downarrow}, \quad (2.53)$$

where U is the intra-atomic Coulomb repulsion between opposite spins in the localised orbital, and $n_{d\uparrow}$ and $n_{d\downarrow}$ are the numbers of spin "up" and spin "down" electrons in the localised orbital.

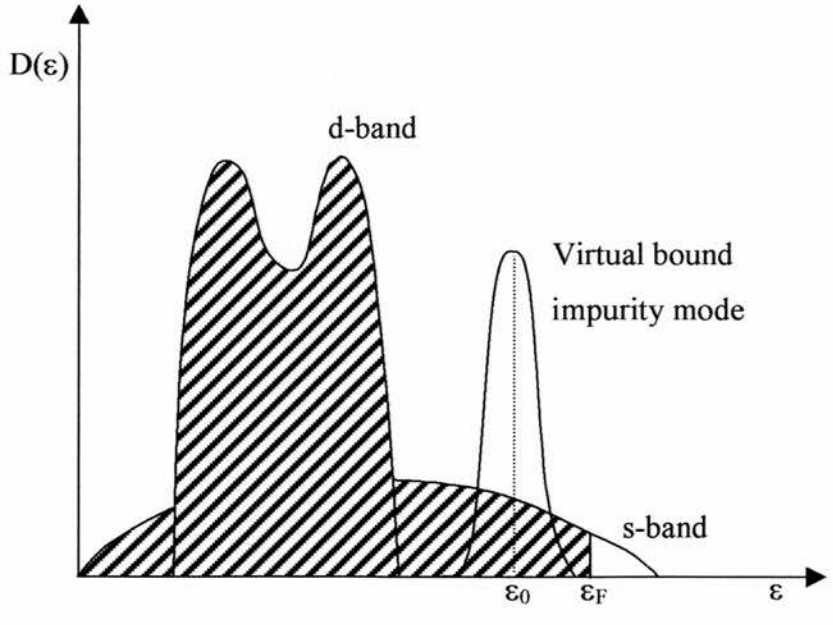

Figure 2.11

Density of states of a d-band material, containing an impurity atom [35].

Anderson showed that the condition for the appearance of a local atomic moment, with electrons bound to the impurity d-state energy mode, is

$$U\,\rho_d(\varepsilon_F) > 1, \tag{2.54}$$

where $\rho_d(\varepsilon_F)$ is the density of the virtual bound impurity d-states at the Fermi-energy. For large $\rho_d(\varepsilon_F)$, the hopping term V should be small, since the presence of hopping will serve to enhance the conduction band density of states, and deplete the impurity density of states. If the presence of exchange between two localised bound states is taken into account, then Moriya has shown [36] that the condition for the appearance of a localised magnetic moments with antiferromagnetic coupling is,

$$\frac{(U+4J)}{\Delta} > \pi\left\{\frac{\left(\frac{V}{\Delta}\right)}{\tan^{-1}\left(\frac{V}{\Delta}\right)}\right\}, \tag{2.55}$$

where Δ is the width of the virtual bound impurity state and J is interatomic exchange energy.

In summary, favourable conditions for local moment formation in metals are, large intra-atomic Coulomb and exchange energies, small energy width Δ, and small hopping term V. The condition of eq. (2.55) is vital to the understanding of the pressure dependence of the magnetic moment in many metallic antiferromagnets. In particular, only 3kbar of external pressure are required to completely suppress moment formation and antiferromagnetic order in YMn_2. Assuming that U, Δ and J remain constant with increasing pressure, one can see that the existence of a magnetic moment is crucially dependent of the hopping term V, and hence the lattice constant of the metal.

2.4.3.2 Unified Susceptibility and Local Spin Density

In the unified SCR theory, there are two possible mechanisms for the appearance of a Curie-Weiss susceptibility: the Heisenberg molecular field approximation for local moments and the SCR form of the susceptibility given by equations (2.42) and (2.45). Moriya has derived a single equation in which the susceptibility is consistent with both the local moment and itinerant electron models [37]. This equation for ferromagnetic coupling is,

$$\frac{1}{\chi(0)} = \frac{4k_B I^2}{T_0 N\mu_B} \sum_q \left(\frac{T}{1/\chi(0) + 2V(0) - 2V(q)} - \frac{T_C}{2V(0) - 2V(q)} \right), \qquad (2.56)$$

where, T_0, is the *longitudinal stiffness constant*, and,

$$V(q) = I / S_L^2(q). \qquad (2.57)$$

The dominant contribution to eq.(2.56) will depend on the longitudinal stiffness constant, which is a measure of the "stiffness" against a change of the spin fluctuation amplitude. If $T_0 \rightarrow 0$, giving maximum longitudinal stiffness and representing the local moment regime, eq. (2.56) reduces to

$$\chi_0 = \frac{N\mu_B{}^2 S_L{}^2}{3k_B(T - T_C)}, \qquad (2.58)$$

which is the familiar molecular field approximation for the Heisenberg model. In the limit of large T_0 and therefore small longitudinal stiffness, eq. (2.56) becomes,

$$\frac{1}{\chi_0} = \frac{4NI^2\mu_B{}^2 S_L{}^2(T)(T - T_C)}{3k_B T_0 T_C}. \qquad (2.59)$$

In eq. (2.59) the Curie-Weiss susceptibility arises solely due to the T-linear increase of $S_L^2(T)$, we can see that this contribution will become progressively smaller as T_0 becomes small and the longitudinal spin density fluctuations are dampened out.

Figure 2.12 depicts the predicted temperature variation of S_L^2 (T) for systems with varying longitudinal stiffness constants and degrees of moment localisation.

When T_0 is small, $S_L^2(T)$ will rapidly increase with temperature until it reaches a limit determined by the electron concentration and d-band structure. This is the phenomenon of temperature induced local moment formation, and is expected in magnetic metals in the intermediate regime between local and itinerant magnetic order. Favourable conditions for the formation of temperature induced local moments are: a large $\rho(\varepsilon_F)$ satisfying eq.(2.54), a small longitudinal stiffness constant and large exchange enhancement.

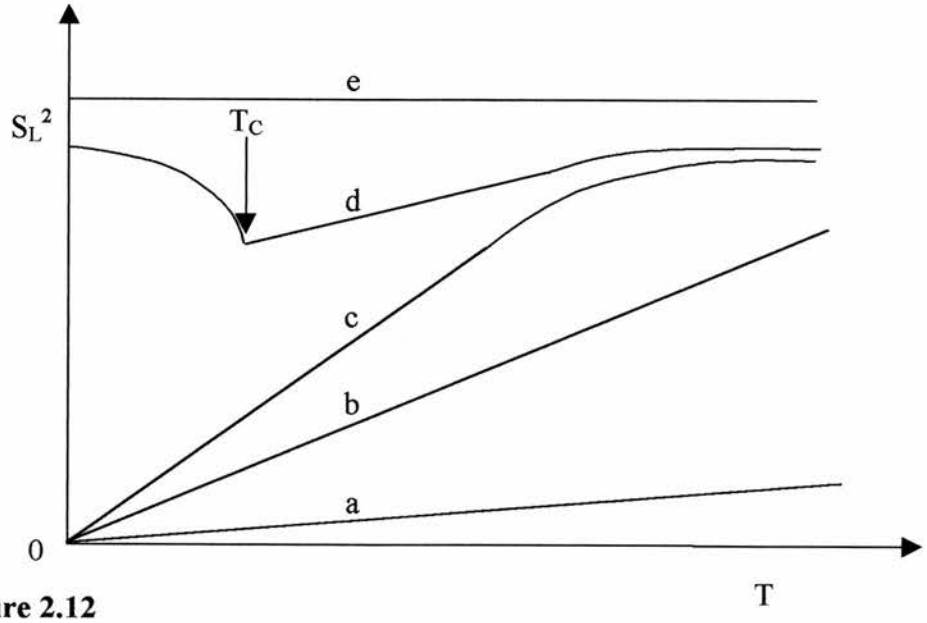

Figure 2.12

SCR theory predictions of the temperature dependence of S_L^2 for various magnetic metals.
a) Pauli paramagnet (large T0)
b) Nearly antiferromagnetic metal
c) Nearly antiferromagnetic metal with temperature induced local moments
d) Antiferromagnetic metal with temperature induced local moments (small T0)
e) Local moment system

2.5 Magnetic Frustration and Spin-Glass Order

A magnetic material whose low-temperature state is a static but disordered system of moments, rather than a long-range periodic spin structure is termed a *spin-glass*. In order to achieve a spin-glass magnetic ground state, the magnetic interactions between the spins must compete with one another, so that no single spin configuration exists which is uniquely favoured by the interactions. The first systems to be characterised as spin-glasses consisted of dilute transition metal impurities in noble metal hosts, and included, AuFe and AgMn. In these systems the magnetic exchange between the impurity ions is of the RKKY type, where the impurity moment polarises the surrounding conduction electrons, in such a way that the sign of the electron polarisation changes with distance from the impurity atom. The coupling between impurities then depends on their separation, and since they are placed randomly in the host matrix, the near neighbour interactions compete with one another and a spin-glass state is formed. There are other types of interaction which can cause spin-glass like magnetic order, including ferromagnetic coupling in the presence of large single ion

anisotropy. However, the mechanism behind spin-glass order which is pertinent to β-Mn and β-MnAl is that of *topological frustration* of antiferromagnetically coupled magnetic moments, and I shall limit my discussion of spin-glasses to this phenomenon.

2.5.1 Topological Frustration

There are several lattice types in which the site symmetry of localised spins in the matrix, causes them to be frustrated. Two of these are the pyrochlore lattice [38,39] and the kagomé lattice shown in figure 2.13. The pyrochlore lattice consists of a network of corner sharing regular tetrahedra, while the kagomé lattice is a 2-dimensional lattice of corner sharing triangles. Figure 2.13 b) demonstrates the existence of topological frustration in the triangular lattice caused by near neighbour antiferromagnetic coupling. Similarly, it is impossible for antiferromagnetic coupling to exist between a spin and each of its nearest neighbours in the 3-dimensional pyrochlore lattice.

2.5.2 The Quantum Spin-Liquid to Spin-Glass Phase Transition

Numerical simulations of antiferromagnetically coupled spin configurations on the perfect pyrochlore-type lattice have shown that spin-glass order should not occur in these materials down to zero temperature [39]. Zero-point amplitude and orientational spin fluctuations in these systems are sufficient to allow the ground state spin configurations to vary, and prevent spin-glass freezing. These systems, which display dynamic, short range, antiferromagnetic spin correlations down to zero temperature have been termed *quantum spin-liquids* (QSL), due to the quantum origin of their spin fluctuations. Experimental studies have shown that pyrochlore-type lattices are extremely sensitive to chemical disorder, where the substitution of non-magnetic impurities into the lattice quickly transforms the QSL into a spin-glass at low temperatures. Intuitively, one can see that the replacement of a magnetic ion by a non-magnetic impurity in a frustrated lattice, will lift the spin configurational frustration of the neighbouring spins. Therefore, the ground state spin configurational degeneracy is at least partially removed and the spins become frozen at low temperatures. Recent studies of the C15 cubic Laves phase compound, $Y_{0.93}Sc_{0.3}(Mn_{1-x}Al_x)_2$ have provided broad support for the QSL model. In this system , itinerant Mn moments form on a pyrochlore-like sublattice. With zero Al substitution, the system behaves like a quantum spin-liquid, with a broad spectral width of spin fluctuations persisting to the

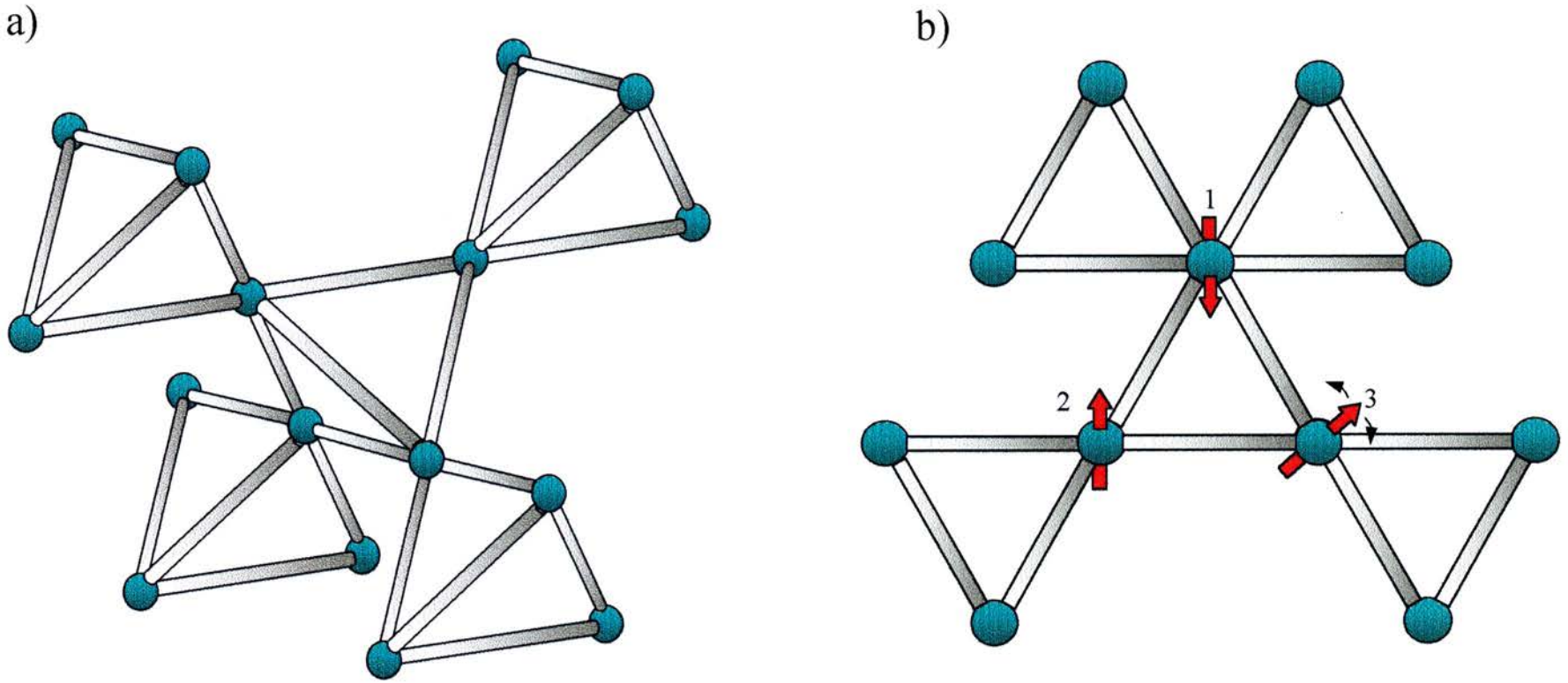

Figure 2.13

The a) pyrochlore and b) kagomé lattices. If neighbouring antiferromagnetic correlations are assumed, then spins 1 and 2 frustrate spin 3 and so on, leaving the lattice frustrated by the competing interactions.

lowest temperatures. The substitution of 5at% Al (x=0.05) is sufficient to relieve the topological frustration in the Mn sublattice, the spin fluctuation spectral width narrows and a spin-glass like magnetic ground state is formed at low temperatures. It is unclear, however, whether the Mn spins are truly static in this system, as there is evidence of residual spin fluctuations below the supposed freezing temperature [40].

Recent studies of the pyrochlore antiferromagnet $Y_2Mo_2O_7$ have indicated that spin-glass order can also can occur in pyrochlore lattices without the presence of chemical disorder [41].

It is an open question whether the observation of spin-glass freezing in topologically frustrated systems is due to an underlying thermodynamic phase transition characterised by a truly divergent correlation time, or to the characteristic spin relaxation time of the system exceeding the time window set by the experimental technique. A suitable order parameter for the characterisation of spin-glass phase transitions is the Edwards-Anderson order parameter [42], defined as,

$$q_{EA} = \lim_{t\to\infty} \lim_{N\to\infty} [\langle \mathbf{S}_i(0).\mathbf{S}_i(t) \rangle]_{av}, \qquad (2.60)$$

where $\mathbf{S}_i(t)$ is the local spin number at time t, and $\langle \mathbf{S}_i(0).\mathbf{S}_i(t) \rangle$ is the spin-spin autocorrelation function. The "av" subscript denotes the mean autocorrelation function over the crystal. q_{EA} will have a finite value when the spin-spin autocorrelation function is finite as $t \to \infty$, that is, the characteristic spin relaxation time in infinite, and therefore the spins are static. If the transition to the spin-glass state represents a thermodynamical phase transition, then we would expect q_{EA} to follow the scaling relationship,

$$q_{EA} \propto (T_f - T)^{\beta}, \qquad (2.61)$$

where β is the critical exponent for the spin-glass transition. In addition, there are critical exponents for the magnetic susceptibility and correlation length.

A recent study by Gingras and co-workers [41] has provided evidence of universal critical exponents for both q_{EA} and magnetic susceptibility, with β in the range 0.6 to 0.9. These values of β are consistent with those found in conventional spin-glasses.

2.5.3 Spin Dynamics of Spin Glasses

In conventional magnetic systems, magnetic spin relaxation from a non-equilibrium state to a state of thermal equilibrium is assumed to occur exponentially. Suppose a sample is placed in an external field, producing a net magnetisation component M in the sample. When the external field is removed, the sample, which is not in thermal equilibrium, will approach its equilibrium magnetisation M_0 at a rate proportional to its departure from the equilibrium value. We can write this as,

$$\frac{dM}{dt} = \omega(M_0 - M), \tag{2.62}$$

where ω is a constant of proportionality. Integrating eq. (2.62) between 0 and t, we find that,

$$M(t) = M_0(1 - e^{-\omega t}). \tag{2.63}$$

Eq. (2.63) indicates that the spins relax exponentially to their equilibrium state with a time constant of ω.

Computer simulations of the decay of the spin-spin autocorrelation function,

$$q(t) = \overline{\langle \mathbf{S}_i(0).\mathbf{S}_i(t) \rangle}, \tag{2.64}$$

in +/-J Ising spin glasses [43] showed that the time evolution of the spins was strongly non-exponential. It was found that in the paramagnetic regime at temperatures close to T_g, the time evolution of the autocorrelation function was given by,

$$q(t) = c\, t^{-x} \exp(-\omega t^{\beta}), \tag{2.65}$$

where the exponent β was found to increase from $\beta=1/3$ at $T=T_g$ to $\beta=1$ at temperatures greater than $\sim 4T_g$. At $T < T_g$, q(t) was found to decay algebraically as,

$$q(t) = c\, t^{-x}. \tag{2.66}$$

The appearance of non-exponential or *Kohlrausch* relaxation in these computer simulations was accounted for by the presence of a distribution of spin correlation times $P(\tau)$. The non-exponential relaxation then results from summing over individual exponential contributions to the spin relaxation from uncorrelated localised spin fluctuations weighted by $P(\tau)$.

Recent muon spin relaxation [44] and neutron spin echo [45]studies have directly observed non-exponential relaxation in spin glasses.

2.6 References

[1] T Moriya and A Kawabata, J. Phys. Soc. Japan **34** (1973) 639

[2] R M White, *Quantum Theory of Magnetism*, (McGraw-Hill, 1970), pp 92-95

[3] from C Kittel, *Introduction to Solid State Physics*, (6^{th} ed. Wiley, 1986) p 417

[4] R M White, ibid., pp 81-82

[5] R M White, ibid., pp 109-111

[6] E C Stoner, Acta Metal. **2** (1954) 260

J Hubbard, Proc. Roy. Soc. (London), **276A** (1963) 238

R M White, ibid., pp 111-115

[7] H Ibach and H Luth, *Solid State Physics*, (Springer-Verlag 1990) p138

J F Janak, Phys. Rev. **B 16** (1977) 255

[8] R M White, ibid., pp 113

[9] T Moriya, *Spin Fluctuations in Itinerant Electron Magnetism* (Springer-Verlag, 1985)

[10] T Izuyama, D J Kim, and R Kubo, J. Phys. Soc. Japan **18** (1963) 1025

[11] H Ibach and H Luth, ibid., p150

[12] R M White, ibid., pp15-20

[13] T Moriya and A Kawabata, J. Phys. Soc. Japan **34** (1973) 639

[14] T Moriya, *Spin Fluctuations in Itinerant Electron Magnetism* (Springer-Verlag, 1985) ch. 4

[15] T Moriya, *Spin Fluctuations in Itinerant Electron Magnetism* (Springer-Verlag, 1985), 68-69

[16] T Moriya, J. Mag. Magn. Mater. **14** (1979) 1

[17] T Moriya, Y Takahashi and K Ueda, J. Phys. Soc. Japan **59** (1990) 2905

[18] K Nakayama and T Moriya, J. Phys. Soc. Japan **56** (1987) 2918

[19] Y Ishikawa, Y Uemura, C F Majzak, G Shirane and Y Noda, Phys. Rev. **B 31** (1985) 5884

R S Hayano, Y Uemura, J Imazato, N Nishida, H Yasuoka, T Yamazaki and Y Ishikawa, Phys. Rev. Lett. **41** (1978) 1743

[20] K Ikeda and K A Gschneidner Jr., J. Mag. Magn. Mater. **30** (1983) 273

Y Masuda, T Hioki and A Oota, Physica **B 91** (1977) 291

[21] M Kontani, T Hioki and Y Masuda, Physica **B 86** (1977) 399
T Hioki and Y Masuda, J. Phys. Soc. Japan **43** (1977) 1200

[22] T Freltoft, P Böni, G Shirane and K Motoya, Phys. Rev. **B 37** (1988) 3454

[23] R Cywinski and B D Rainford, Hyperfine Inter., **64** (1994) 215

[24] S Roberts, G K White and E Fawcett, Physica **B119** (1983) 63

[25] M Shiga and Y Nakamura, J. Phys. Soc. Japan **26** (1969) 24

[26] H Hasegawa, J. Phys. Soc. Japan **38** (1975) 107

[27] J Shinkoda, K Kumagai and K Asayama, J. Phys. Soc. Japan **46** (1979)

[28] K Ueda and T Moriya, J. Phys. Soc. Japan **38** (1975) 32

[29] S Akimoto, T Kohara and K Asayama, Solid State, Comm. **16** (1975) 1227

[30] Y Nakamura, K Yoshimoto, M Shiga, M Nishi and K Kakurai, J. Phys. Cond. Matter **9** (1997) 4701

[31] Y Kohori, Y Iwamoto, Y Muro and T Kohara, Physica **B 237** (1997) 455

[32] P R Rhodes and E P Wohlfarth, Proc. Roy. Soc. (London) **273** (1963) 247

[33] T Moriya, *Spin Fluctuations in Itinerant Electron Magnetism,* (Springer-Verlag, 1985) 130

[34] P W Anderson, Phys. Rev., **124** (1961) 41

[35] R M White, *Quantum Theory of Magnetism*, (McGraw – Hill, 1970) 194

[36] T Moriya, Progr. Theor. Phys., **33** (1965) 157

[37] T Moriya, *Spin Fluctuations in Itinerant Electron Magnetism,* (Springer-Verlag, 1985) ch. 7

[38] M P Zinkin, M J Harris and T Zeiske, Phys. Rev. **B 56** (1997) 11 786

[39] B Canals and C Lacroix, Phys. Rev. Lett. **80** (1998) 2933

[40] H Nakamura, F Takayanigi, M Shiga, M Nishi and K Kakurai, J. Phys. Soc. Japan. **65** (1996) 2779

[41] M J P Gingras, C V Stager, N P Raju, B D Gaulin and J E Greedan, Phys. Rev. Lett. **78** (1997) 947

[42] S F Edwards and P W Anderson, J. Phys. F **5** (1975) 965

[43] A T Ogielski, Phys. Rev. **B32** (1985) 7384

[44] I A Campbell, A Amato, F N Gygax, D Herlach, A Schenck, R Cywinski and S H Kilcoyne, Phys. Rev. Lett. **72** (1994) 1291

[45] R I Bewley, J R Stewart, C Ritter, P Schleger and R Cywinski, Physica **B234** (1997) 762

3 Neutron Scattering

3.1 Introduction

The neutron is an electrically neutral particle, with a magnetic moment of $\gamma = 1.913\mu_N$, where the nuclear magneton $\mu_N = e\hbar/2m_p = 5.051 \times 10^{-27}\ JT^{-1}$.

The energy of a neutron is related to its wavevector **k** by the equation,

$$E_k = \frac{\hbar^2 k^2}{2m_n} = \frac{81.72}{\lambda^2}, \qquad (3.1)$$

where E is in units of meV and λ in units of Å. Thermal neutrons at ~300K have a wavelength, λ ~1.7Å, which is comparable to the interatomic spacing in solids, thus allowing diffraction and interference effects to occur. There are two types of interaction between the neutron and matter in a scattering experiment.

i) Neutrons and nuclei interact at a range of between 10^{-14}m and 10^{-15}m. This interaction range is much smaller than the thermal neutron wavelength implying that the neutron is scattered isotropically by a nucleus (S-wave scattering).

ii) The neutron magnetic moment interacts with the magnetic field due to unpaired electronic spins via a $\boldsymbol{\mu}.\mathbf{B}$ interaction. The range of this interaction is approximately the radius of the unpaired electron orbit, and thus comparable to the thermal neutron wavelength. Neutrons scattered from different points of the electron cloud are phase shifted with respect to one another and therefore interfere, implying that magnetic scattering is non-isotropic (non-S-wave scattering).

This chapter is a brief introduction to the basic concepts underlying the neutron scattering studies of β-MnAl presented in chapters 5, 7 and 8.

3.2 The Neutron Scattering Experiment

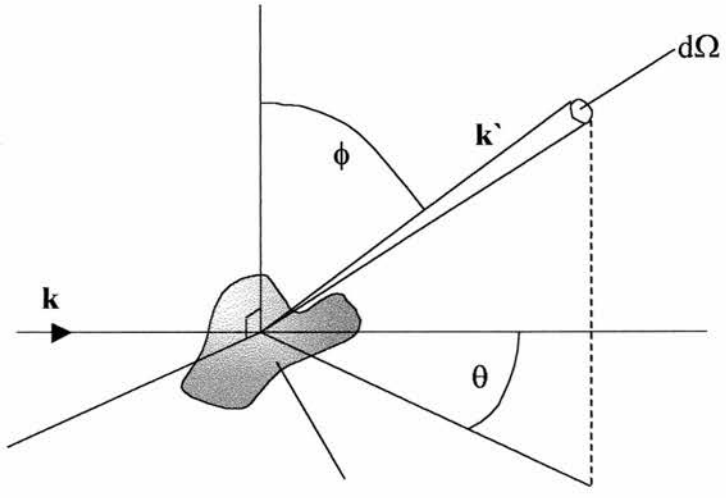

Figure 3.1

Geometry of a typical neutron scattering experiment.[1]

Figure 3.1 shows a typical scattering experiment in which neutrons of wavevector **k** and energy E are scattered by a target sample. The scattered neutrons of wavevector **k`** and energy E` are counted by a neutron detector subtending a solid-angle element dΩ. The detector is placed along the direction defined by the unit vector $\Omega = \mathbf{k}`/k`$, specified by the polar angles (θ,ϕ) relative to the incident beam, and can only count neutrons within an energy element dE` of E`. The *partial differential cross-section*, is defined as the neutron counting rate at the detector per energy interval, normalised by the incident neutron flux.

$$\frac{d^2\sigma}{d\Omega dE`} = \frac{\text{neutrons/sec in } d\Omega \text{ between } E` \text{ and } E`+dE`}{\Phi d\Omega dE`}, \tag{3.2}$$

where Φ is the incident neutron flux. Integrating over all energy, we obtain the *differential cross-section*,

$$\frac{d\sigma}{d\Omega} = \int_{E`} \frac{d^2\sigma}{d\Omega dE`} dE`. \tag{3.3}$$

Finally, the *total cross-section* is obtained by integrating with respect to Ω over 4π steradians,

$$\sigma = \iint_{\Omega,E`} \frac{d^2\sigma}{d\Omega dE`} d\Omega dE`. \tag{3.4}$$

The total cross section has the dimensions of area and is usually expressed in *barns* (b),

$$1 \text{ barn} = 10^{-24} \text{ m}^2.$$

Assuming the *Born approximation* [2] in which the incident and scattered neutrons are described by plane waves of the form $e^{i(\mathbf{k}.\mathbf{r})}$, the partial differential cross-section is given by,

$$\frac{d^2\sigma}{d\Omega dE`} = \frac{k`}{k}\frac{m_n^{\,2}}{(2\pi\hbar^2)^2}\sum_{\Lambda,\Lambda`,s,s`} p_\Lambda p_s \left|\langle \mathbf{k}s\Lambda|V|\mathbf{k}`s`\Lambda`\rangle\right|^2 \delta(E_\Lambda - E_{\Lambda`} + \hbar\omega), \qquad (3.5)$$

where V is the interaction potential between the neutron and the sample resulting in a transition of neutron wavevector **k** to **k`**, and neutron spin s to s`. The target sample undergoes a transition from an initial state Λ to final state $\Lambda`$, with the delta-function ensuring conservation of energy. The partial differential cross-section is then obtained by summing over all possible initial and final neutron spin states s and target sample states Λ, weighted by their probability of occurrence, p_Λ and p_s

3.2.1 Elastic Nuclear Scattering

The isotropic nature of the neutron-nucleus interaction implies that the interaction strength may be characterised by a single parameter; the so-called *scattering length* b, which will in general be a complex quantity depending on the particular nuclear isotope and its spin-state. A suitable potential representing scattering from a rigid array of nuclei with scattering lengths b_i and positions R_i is the Fermi pseudopotential [2],

$$V(r) = \frac{2\pi\hbar^2}{m_n}\sum_i b_i \delta(r - R_i) \cdot \qquad (3.6)$$

The differential cross-section resulting from the assumption of the Fermi pseudopotential, and obtained by integrating eq. (3.5) over all energies may be written as the sum of two contributions,

$$\left.\frac{d\sigma}{d\Omega}\right|_{\text{Total}} = \left.\frac{d\sigma}{d\Omega}\right|_{\text{coherent}} + \left.\frac{d\sigma}{d\Omega}\right|_{\text{incoherent}} . \qquad (3.7)$$

The coherent differential cross-section which arises due to interference effects between the scattered neutrons from each nucleus is given by,

$$\left.\frac{d\sigma}{d\Omega}\right|_{coherent} = \left|\overline{b}^2\right| \left|\sum_i e^{i(\mathbf{Q}.\mathbf{r}_i)}\right|^2, \qquad (3.8)$$

where $\mathbf{Q} = \mathbf{k_f} - \mathbf{k_i}$ is the neutron wavevector transfer and the sum is over all nuclei in the lattice. The coherent differential cross-section representing the scattering from a single unit cell of volume V can be obtained by factorising eq. (3.8) to obtain,

$$\left.\frac{d\sigma}{d\Omega}\right|_{coherent} = \frac{(2\pi)^3}{V} \sum_{h,k,l} \delta(\mathbf{Q} - \mathbf{G}_{hkl}) \left|F(\mathbf{G}_{hkl})\right|^2, \qquad (3.9)$$

where $\mathbf{G}_{hkl}$ is the reciprocal lattice vector for the (h k l) family of lattice planes and $F(\mathbf{G}_{hkl})$ is the *nuclear structure factor* [3]. The delta-function in eq. (3.9) represents the Bragg peak for the (h k l) reflection which is located at wavevector transfers given by *Bragg's Law*,

$$\mathbf{Q} = \mathbf{G}_{hkl}. \qquad (3.10)$$

The intensity of the Bragg reflection in eq. (3.9) is proportional to the square of the nuclear structure factor,

$$\left|F(\mathbf{G}_{hkl})\right|^2 = \sum_{R_0} b_{R_0} e^{i(\mathbf{G}.\mathbf{R}_0)}, \qquad (3.11)$$

where R_0 represents the position of each nucleus of scattering length b_{R_0} within the unit cell.

In a neutron powder diffraction measurement, a collimated neutron beam is incident upon a finely powered crystalline sample, all crystal planes being presented to the neutron beam simultaneously. For a given neutron wavelength, neutrons which satisfy the Bragg condition of eq. (3.10) will be diffracted through an angle $2\theta_{hkl}$ and will be located on the surface of a Debye-Scherrer cone (see figure 3.2).

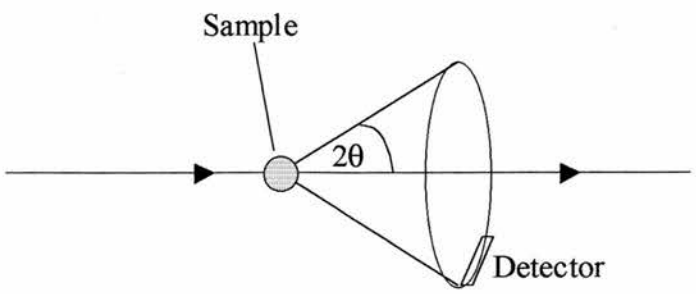

Figure 3.2

A Debye-Scherrer cone in a powder diffraction measurement.

The integrated cross section for a Bragg reflection of multiplicity j into the Debye-Scherrer cone is given by [3],

$$\sigma_{hkl} = \frac{\lambda^3 j}{4V \sin\theta} |F(G_{hkl})|^2 . \qquad (3.12)$$

The coherent differential cross-section may also exhibit evidence of *short-range order* in systems such as liquids and glasses where there are no coherent Bragg peaks. Nuclear short-range order can also arise due to short-range correlations between nuclear species in binary alloys and compounds, and nuclear displacement disorder.

The incoherent contribution to the elastic differential cross-section contains no interference term between neutrons scattered from different nuclear sites, and is therefore isotropic, giving a constant background to the elastic scattering. This contribution is given by,

$$\left.\frac{d\sigma}{d\Omega}\right|_{incoherent} = N(\overline{b^2} - (\overline{b})^2) . \qquad (3.13)$$

This term is commonly known as the *isotope incoherent* differential cross-section.

So far we have considered elastic scattering from a rigid lattice. However, at finite temperatures thermal vibrations in the lattice induce a phase mismatch between neutrons scattered from different nuclear sites. To take account of this we must replace the structure factor in eq. (3.11) by,

$$|F(\mathbf{G}_{hkl})|^2 \rightarrow |F(\mathbf{G}_{hkl})|^2 e^{-2W} , \qquad (3.14)$$

where e^{-2W} is the *Debye-Waller Factor*,

$$e^{-2W} = e^{-PQ^2T} . \qquad (3.15)$$

The Debye-Waller factor thus reduces the scattering intensity with increasing wavevector transfer.

Neutron diffraction studies of β-Mn alloys shall be presented in chapter 5. In chapter 7, nuclear short-range order in β-MnAl alloys will be investigated.

3.2.2 Elastic Magnetic Scattering

Assuming a magnetic dipole-dipole interaction between the neutron spin and the magnetic moments in the target sample, we can write the elastic magnetic differential cross-section as,

$$\left.\frac{d\sigma}{d\Omega}\right|_{Magnetic} = (\gamma r_0)^2 \left|\frac{1}{2} g f(Q)\right|^2 \sum_{\alpha,\beta}(\delta_{\alpha\beta} - Q_\alpha Q_\beta)\sum_{i,j} e^{iQ.(R_i - R_j)} < S_i^{\alpha} >< S_j^{\beta} >, \quad (3.16)$$

in which the sum is over all lattice sites i and j and over all Cartesian directions, $\alpha,\beta = x,y,z$. γ is the neutron magnetic moment and r_0 is the classical electron radius,

$$r_0 = \frac{e^2}{m_e} (\text{SI units}) = 2.818 \times 10^{-15} \text{m}. \quad (3.17)$$

$<S_i^{\alpha}>$ and $<S_j^{\beta}>$ are the time averaged spin components on sites i and j. f(Q) is the *magnetic form factor* and is the Fourier transform of the magnetisation density around the magnetic ion. The form factor represents the non-isotropic scattering from magnetic ions caused by the spatial extent of the electron distribution mentioned in section 3.1. The effect of the magnetic form factor is to reduce the magnetic scattering intensity with increasing Q. The form factors of many rare-earth and transition metal elements have been parameterised by Brown [4] as a function of S where,

$$S = \sin\theta/\lambda = Q/4\pi. \quad (3.18)$$

For Mn ions the magnetic form factor my be written as,

$$f(S)=A \exp(-aS^2) + B \exp(-bS^2) + C \exp(-cS^2) + D. \quad (3.19)$$

The parameters for the Mn^{2+}, Mn^{3+} and free Mn ions are given in table 3.1, and the form factors for these ions are plotted in figure 3.3.

Table 3.1 Parameters for the free Mn, Mn^{2+} and Mn^{3+} form factors [4].

	A	a	B	b	C	c	D
free Mn	0.2438	24.963	0.1472	15.673	0.6189	6.54	-0.0105
Mn^{2+}	0.4220	17.684	0.5948	6.005	0.0043	-0.609	-0.0219
Mn^{3+}	0.4198	14.283	0.6054	5.469	0.9241	-0.009	-0.9468

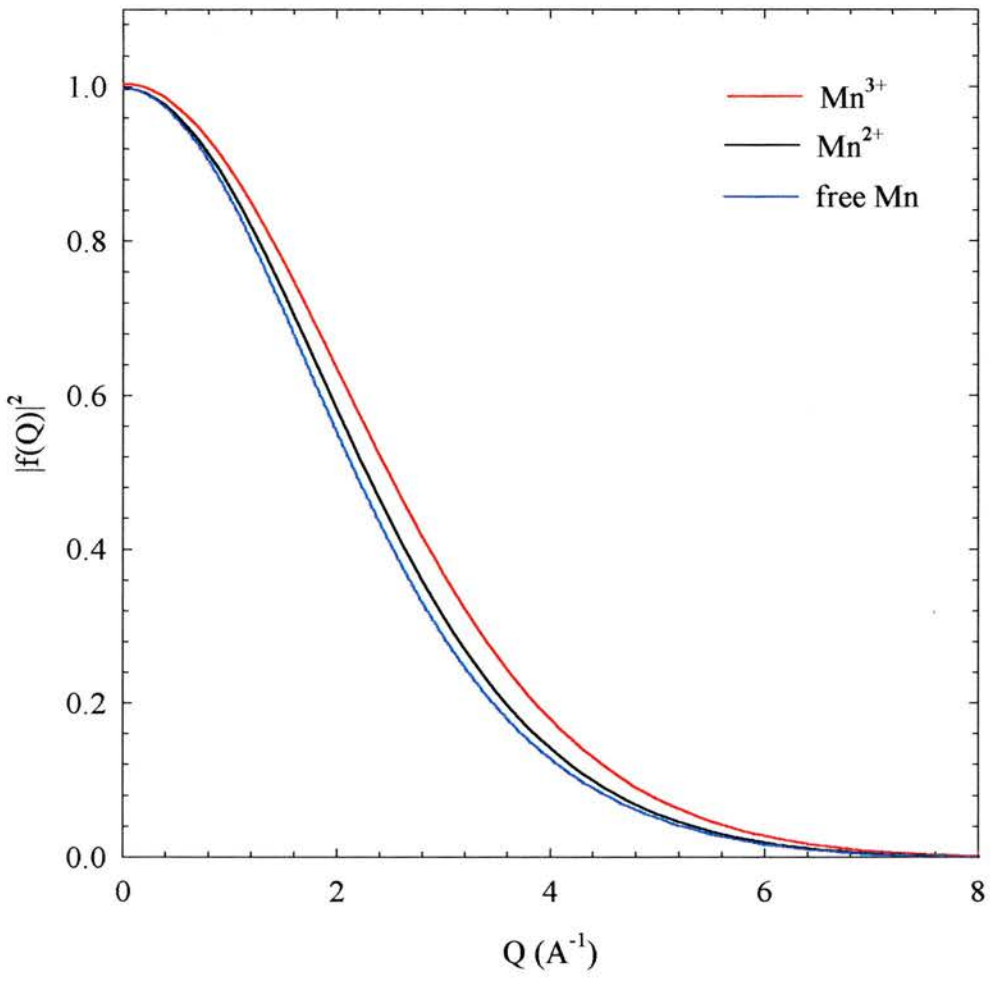

Figure 3.3

The squared form factor of the free Mn, Mn^{2+} and Mn^{3+} ions derived from the parameterisation of Brown [4]

For a single free atom, the differential scattering cross-section is obtained by integrating over all energy in eq. (3.16) to obtain,

$$\left.\frac{d\sigma}{d\Omega}\right|_{Magnetic} = (\gamma r_0)^2 \frac{1}{4} g_S{}^2 |f(Q)|^2 \langle \mathbf{S}_\perp . \mathbf{S}_\perp \rangle , \qquad (3.20)$$

where $\mathbf{S}_\perp = \hat{\mathbf{Q}} \wedge (\mathbf{S} \wedge \hat{\mathbf{Q}})$ **[7]**. Using the rule for the triple product: **a∧(b∧c) = (a.c)b – (a.b)c**, we can show that,

$$\langle \mathbf{S}_\perp . \mathbf{S}_\perp \rangle = \left\langle S^2 - (\hat{\mathbf{Q}}.\mathbf{S}) \right\rangle^2 = \frac{2}{3} S(S+1) . \qquad (3.21)$$

We can therefore write eq. (3.20) as,

$$\left.\frac{d\sigma}{d\Omega}\right|_{Magnetic} = \frac{2}{3} \left(\frac{\gamma r_0}{2} \right)^2 g_S{}^2 |f(Q)|^2 S(S+1) , \qquad (3.22)$$

where the factor,

$$\left(\frac{\gamma r_0}{2}\right)^2 = 0.073 \text{ barns}. \tag{3.23}$$

In chapter 7, the elastic magnetic scattering from β-MnAl alloys will be investigated using neutron polarisation analysis.

3.2.3 Inelastic Neutron Scattering

In an inelastic neutron scattering experiment, the neutron either gains an energy transfer ΔE from the sample, or it loses ΔE to the sample. This can occur through the creation or annihilation of a coherent excitation such as a phonon or spin wave, with ΔE centred at the characteristic energy of the excitation. Neutrons can also gain or lose energy via incoherent magnetic spin-fluctuations centred around the elastic line at ΔE = 0 (quasi-elastic scattering). The total inelastic cross section measured in an neutron experiment given by eq.(3.5) will, in general, include the inelastic magnetic response due to coherent and incoherent magnetic excitations, and the phonon scattering response from the coherent vibrational excitations in the crystal. To reveal information about the magnetic spin-dynamics of the target sample, the phonon scattering has to be subtracted from the measured partial differential cross-section.

The magnetic partial differential cross-section can be written as,

$$\left.\frac{d^2\sigma}{d\Omega dE`}\right|_{\text{Magnetic}} = \frac{k`}{k}\frac{(\gamma r_0)^2}{\hbar}\left[\frac{1}{2}g_s f(Q)\right]^2 S(Q,\omega), \tag{3.24}$$

where S(Q,ω) is the *dynamical structure factor* which provides information on the spatial and temporal magnetic correlations in the sample. Using the *fluctuation-dissipation theorem*, S(Q,ω) can be related to the imaginary part of the dynamical susceptibility of the system. The fluctuation-dissipation theorem states that the frequency dependent correlation function S(Q,ω) is proportional to the imaginary part of the response function of the system, which in this case is the dynamical susceptibility [5]. We can thus write the dynamical structure factor as,

$$S(Q,\omega) = \frac{N\hbar}{(g\mu_B)^2}[1+n(\omega)]\frac{1}{\pi}\chi''(Q,\omega), \tag{3.25}$$

where $[1+n(\omega)]$ is the so-called *detailed balance factor*. This factor is introduced to take account of the fact that the relative thermal population of energy gain and energy loss processes will depend on the temperature of the system [6]. At low temperatures neutrons will predominantly lose energy to the sample by exciting it from the ground state to an excited state. The detailed balance factor may be expressed as,

$$[1+n(\omega)] = \frac{1}{1-\exp\left(\frac{-\hbar\omega}{k_B T}\right)}. \tag{3.26}$$

The imaginary part of the dynamical susceptibility of a magnetic system is thus directly observable in an inelastic neutron scattering experiment. Using the *Kramers-Kronig Relation* [7] we can relate $\chi''(Q,\omega)$ to the static wavevector dependent susceptibility $\chi(Q)$, as

$$\chi(Q) = \frac{1}{\pi}\int_{-\infty}^{\infty}\frac{\chi''(Q,\omega)}{\omega}d\omega. \tag{3.27}$$

In chapter 8 I shall present an inelastic neutron scattering study of β-MnAl alloys.

3.3 References

[1] P M Chaikin and T C Lubensky, *Principles of Condensed Matter Physics*, (Cambridge University Press, 1995) p400

[2] S W Lovesey, *Theory of Neutron Scattering from Condensed Matter*, (Clarendon Press, 1984), p12

[3] G L Squires, *Introduction to Thermal Neutron Scattering*, (Cambridge University Press, 1978)

[4] P J Brown, *International Tables of Crystallography*, Vol III, p391

[5] P M Chaikin and T C Lubensky, op. cit., chapter 7

[6] S W Lovesey, op. cit., p175

[7] B D Rainford, *Magnetism and Neutron Scattering*, in "Neutron Scattering on a Pulsed Source", ed. B D Rainford, R Cywinski and R J Newport, p354

4 Preparation and Initial Characterisation of β-MnAl

4.1 Introduction

All of the samples used in this study were prepared by the argon arc-melting technique, in which appropriate amounts of the constituent metals are melted together using a high current electric arc in a low pressure, pure argon atmosphere. β-$Mn_{1-x}Al_x$ samples with Al concentrations in the range $0 \leq x \leq 0.2$ were formed from high purity starting materials; these being, electrolytically produced pure Mn flake with a purity of 99.98% and Al ingot with a purity of 99.99%. After melting, the β-phase was stabilised in these materials by annealing under a low pressure argon atmosphere in quartz ampoules at a temperature of between 900C and 950C for at least 24 hours. The exact temperature chosen was determined by the MnAl phase diagram presented by Hansen [1]. The β- phase was retained at room temperature by quenching the samples in water.

X-ray diffraction spectra of the β-$Mn_{1-x}Al_x$ samples were taken on a Philips reflection geometry X-ray diffractometer. The use of reflection geometry X-ray diffraction was found to be much more reliable than transmission geometry X-ray diffraction, which produced a large background and low signal to noise ratio caused by the high degree of X-ray fluorescence exhibited by Mn atoms. The samples were further characterised "in-house" by dc susceptibility and electrical resistivity studies. The larger samples required for neutron and muon measurements were prepared as separate ingots of around 10g each, and then broken up, mixed and re-melted in order to ensure sample homogeneity.

4.2 Sample Preparation Procedure

Appropriate quantities of the constituent elements were weighed to within an accuracy of ± 0.1 mg using a *Sartorius* electronic balance. The surface oxide layer on both the Mn flakes and Al ingots was removed by etching in a dilute (~5%) solution of Nitric

Acid. The argon arc-furnace was flushed prior to melting with pure argon at least three times, after which any remaining impurities were removed by melting a titanium "getter" ingot. Great care was taken not to thermally shock the samples during the melting process. Mn is an extremely brittle metal, and goes through three structural phase transitions before it reaches the melting point (1470K). Because of this, Mn is prone to shatter if heated or cooled too rapidly. Accordingly, the samples were heated using a small current, and cooled as slowly as possible by ensuring that the water coolant flow through the furnace hearth was reduced to the minimum possible level. The existence of gaseous impurities in the Mn flakes caused them to shatter on heating. The Mn flakes were therefore melted repeatedly in order to remove these impurities. Only after a solid pure Mn ingot was obtained was the Al added. The MnAl ingots were turned and melted at least five times to ensure homogeneity. Re-weighing the ingots after melting revealed high mass losses in the β-MnAl ingots, typically of around 2.5%. This mass loss is mainly due to the low heat of sublimation of Mn, and it was assumed that Mn mass loss accounted for all of the mass lost in the melting procedure. Consequently, the constituent elements were weighed in such a way as to allow for this mass loss.

After annealing and quenching the ingots to produce the β-phase, X-ray, neutron scattering, μSR and dc susceptibility samples were prepared by finely powdering the samples. Both X-ray and neutron diffraction measurements demonstrated that minimal strain is produced by the powdering process in these samples. The dc magnetisation samples were made by combining a small quantity (typically ~0.5g) of powder with some *Araldite* epoxy resin, and fashioning into a sphere. It is highly desirable in electrical resistivity measurements to have solid samples of uniform cross-sectional area. This was achieved by cutting cuboid shaped samples of typical dimensions: 1.5mm × 1.5mm × 10mm, from the MnAl ingots with a spark eroder. The resistivity samples were then annealed and quenched as described above.

4.3 X-Ray Diffraction measurements

of The β-MnAl samples studied in this investigation were all initially characterised by X-ray diffraction, in reflection geometry, on finely powdered samples. Figure 4.1 shows a typical room temperature X-ray diffraction pattern, in this case for β-$Mn_{0.9}Al_{0.1}$. All of the samples studied were found to be single phase with the simple cubic β-Mn structure (see section 1.2). The results of our X-ray diffraction studies are summarised in table 4.1, which shows the calculated lattice constants, the value of χ^2 given by the least-squares fit, and the R-factors for the refinements (see section 5.3). The high values of both χ^2 and the R-factors given in table 4.1 are symptomatic of the poor quality of the X-ray data, which were affected by the high degree of Mn X-ray fluorescence and the presence of preferred orientation in the samples studied. The Reitveld analyses of the measured X-ray diffraction spectra suggested that the Al atoms showed a strong occupational preference for site II in the β-Mn structure. However, since this observation was complicated by the presence of preferred orientation, the site occupation factors were varied in the analysis, with the Al atoms constrained to sit on site II of the β-Mn matrix. I shall present a neutron diffraction study of β-Mn with various impurity atom substitutions in chapter 5, which confirms that Al atoms preferentially occupy site II.

Table 4.1: Lattice parameters, $\chi 2$ and R-factors of the β-$Mn_{1-x}Al_x$ series deduced from Reitveld analysis of our X-ray diffraction measurements.

X	a (Å)	χ^2	R-Factor
0	6.316(2)	2.06	0.043
0.03	6.330(1)	1.44	0.015
0.06	6.333(1)	2.54	0.062
0.08	6.342(1)	3.21	0.23
0.09	6.343(1)	1.56	0.025
0.1	6.351(1)	1.96	0.19
0.15	6.376(1)	2.99	0.63
0.2	6.388(1)	4.11	0.19

Figure 4.2 shows the Al concentration dependence of the lattice constant of our β-$Mn_{1-x}Al_x$ samples, which clearly demonstrates the uniform expansion of the β-Mn lattice on increasing Al concentration, rising from a = 6.316Å in pure β-Mn to a = 6.388Å in β-$Mn_{0.8}Al_{0.2}$.

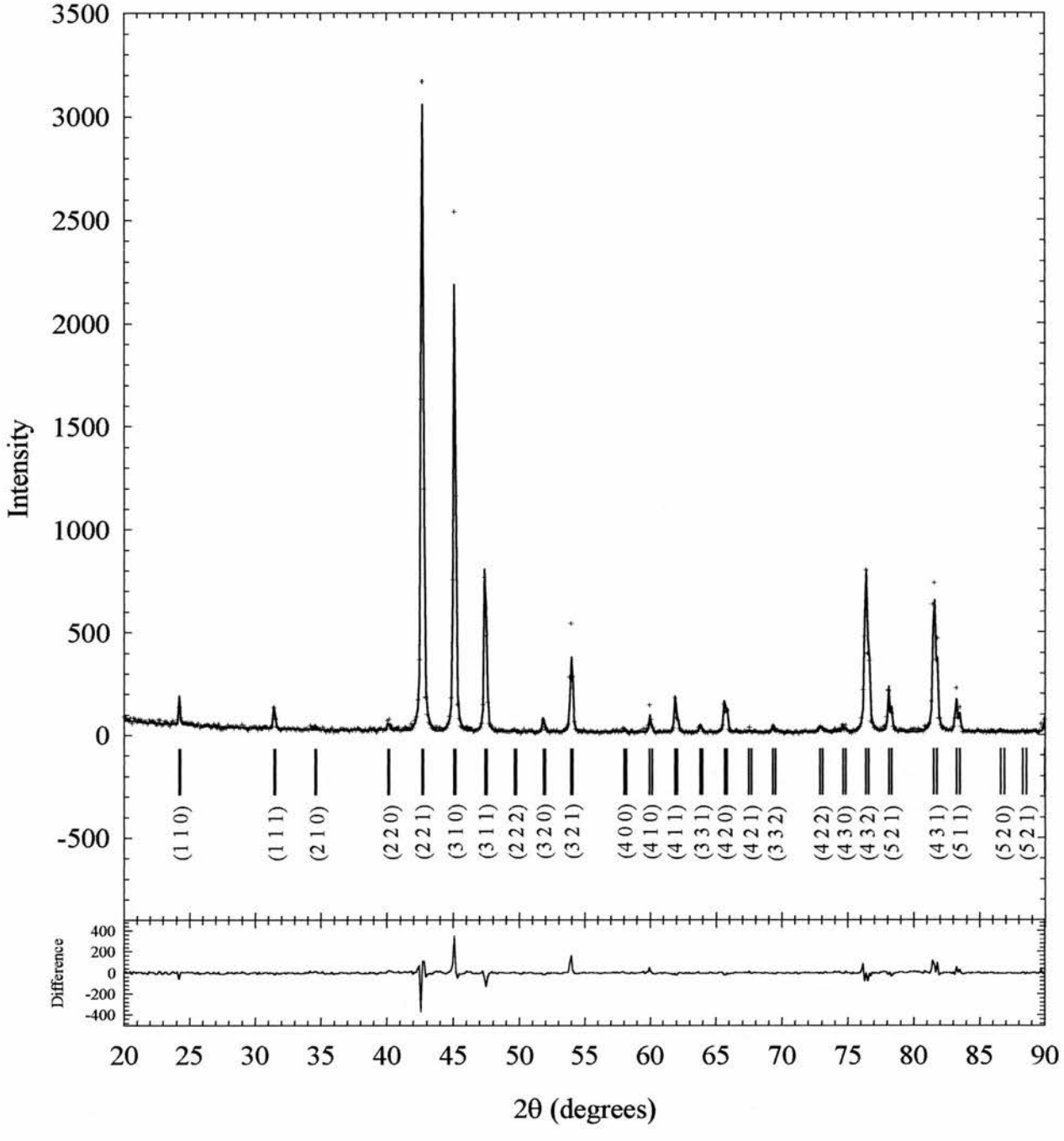

Figure 4.1

Room temperature Cu K_α X-ray powder diffraction pattern of β-$Mn_{0.9}Al_{0.1}$ with Reitveld profile refinement and difference pattern. The solid line is the calculated diffraction pattern from a full Reitveld profile refinement of the data, produced by the FullProf *suite of programs.*

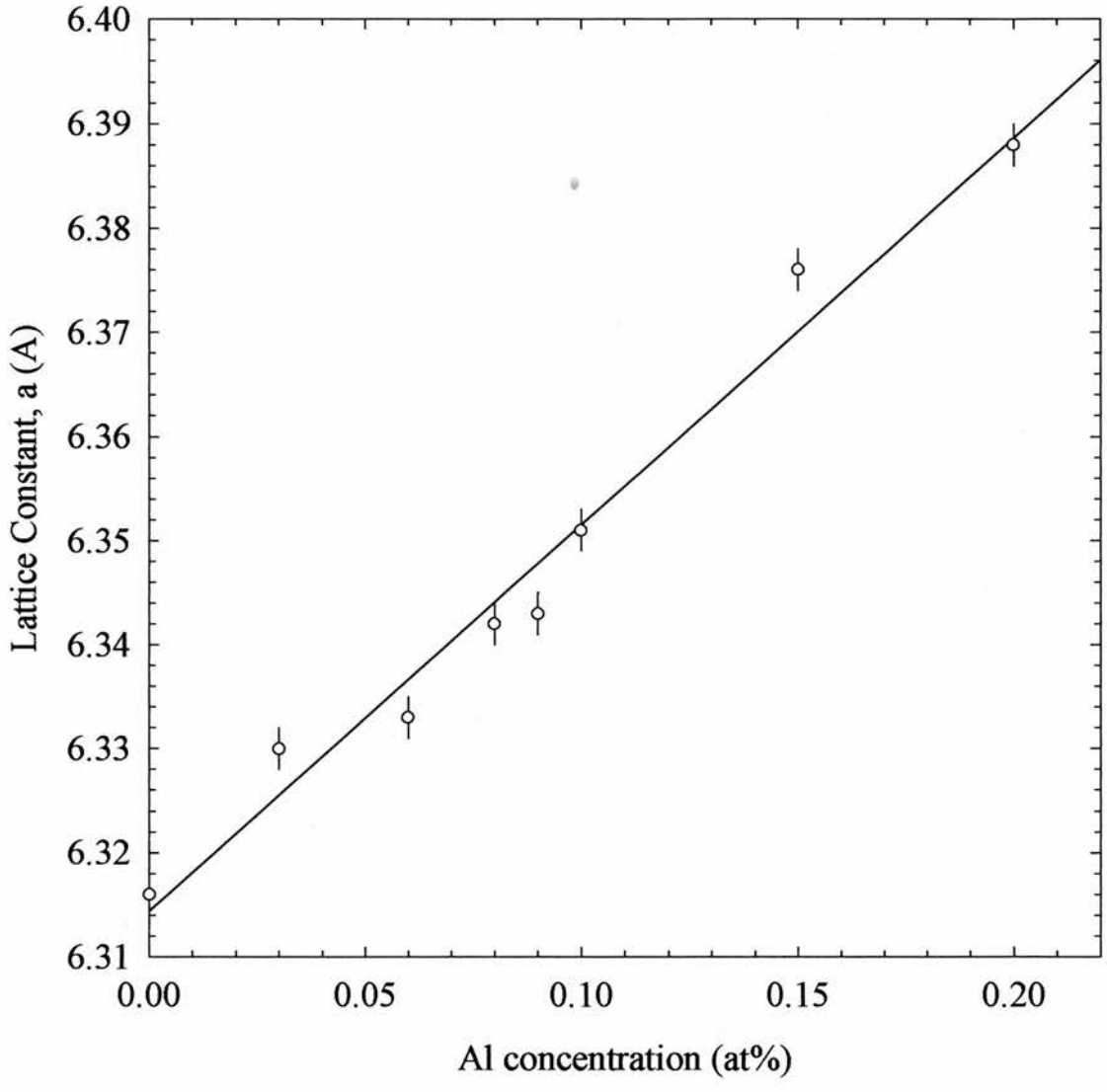

Figure 4.2

Concentration dependence of the lattice constant of β-MnAl alloys, measured by X-ray diffraction. The solid line is a guide to the eye.

4.4 Magnetometry

4.4.1 Introduction

The magnetic volume susceptibility of a material is defined as the ratio of the magnetisation per unit volume acquired in some steady applied magnetic field to the applied magnetic field strength.

$$\chi_{dc} = \frac{M}{H}, \tag{4.1}$$

where the "dc" subscript implies the use of a dc applied magnetic field. Most methods of measuring susceptibility (e.g. Vibrating Sample Magnetometry or SQUID magnetometry) are indirect in that they measure the magnetisation of the sample and then calculate the susceptibility using the above formula, assuming that M is proportional to H. However, if a small amplitude ac magnetic field is applied, then one can measure the modulation of the magnetisation of a sample to find the so called ac susceptibility,

$$\chi_{ac} = \frac{dM}{dH_{ac}} \tag{4.2}$$

This technique assumes linearity between M and H only in the region of dH_{ac}, and is extremely useful for studying dynamical magnetic processes. ac susceptibility measurements of the β-MnAl samples were attempted; however, no signal above background was observed. Linearity between M and H was found to hold for all β-MnAl samples up to H = 12T.

Since conventional magnetometry techniques measure the bulk magnetisation of a material, they are only sensitive to magnetic materials with a non-zero wavevector dependent susceptibility $\chi(Q)$ at $Q = 0$. Magnetic materials with well localised moments will in general posses a non-zero $\chi(Q = 0)$ in the presence of a external magnetic field. This is not, however, the case for antiferromagnetically correlated itinerant electron systems.

4.4.2 The Demagnetisation Factor

When a magnetic material is placed in an applied magnetic field $\mathbf{H_a}$, magnetic poles are set up on the surface of the material, which arise due to its magnetisation **M**. These poles create a demagnetising field $\mathbf{H_d}$, opposed to the applied field, and result in an internal magnetic field $\mathbf{H_i}$ which is in general different to $\mathbf{H_a}$. For elliptically shaped samples it can be shown that,

$$\mathbf{H_i} = \mathbf{H_a} - \mathbf{H_d} = \mathbf{H_a} - D\mathbf{M} \tag{4.3}$$

where D is the so-called demagnetising factor and is dependent on the shape of the material. The components of D for a spherical material are $D_x = D_y = D_z = 1/3$, while for a flat plate in the xy-plane, $D_x = D_y = 0$ and $D_z = 1$. The components of D always satisfy the requirement that that $D_x + D_y + D_z = 1$. The magnetic susceptibility is then given by,

$$\chi_i = \frac{\mathbf{M}}{\mathbf{H_i}} = \frac{\mathbf{M}}{\mathbf{H_a} - D\mathbf{M}}. \tag{4.4}$$

Therefore, since the measured susceptibility χ_m is given by

$$\chi_m = \frac{\mathbf{M}}{\mathbf{H_a}}, \tag{4.5}$$

we can combine equations (4.4) and (4.5) to obtain,

$$\chi_i = \frac{\chi_m}{1 - D\chi_m}. \tag{4.6}$$

4.4.3 Vibrating Sample Magnetometer Apparatus

The dc susceptibility measurements presented in this study were all carried out on a Oxford Instruments 3001 Vibrating Sample Magnetometer (VSM). The material under investigation is mounted in a delrin sample holder at the end of a carbon fibre rod and inserted into an Oxford Instruments CF1200 continuous flow Helium Cryostat, which is mounted in the bore of a 12 Tesla superconducting magnet. The sample is then vibrated with an amplitude of ~1.5mm along the vertical axis in a uniform applied field. The motion of the sample induces an emf in two detector coils, which is proportional to the rate of change of the magnetic flux through them (Faraday's Law). The vibration frequency is set at 66Hz, to avoid any interference from 50Hz mains supply noise. The centre of vibration of the sample can be positioned at the exact centre of the sense coil

arrangement, to within an accuracy of ± 10μm, in order to achieve the maximum output signal. The induced emf, which is proportional to the magnetic susceptibility of the sample, goes through a two-stage amplification process and is monitored by the VSM electronics and recorded on a computer.

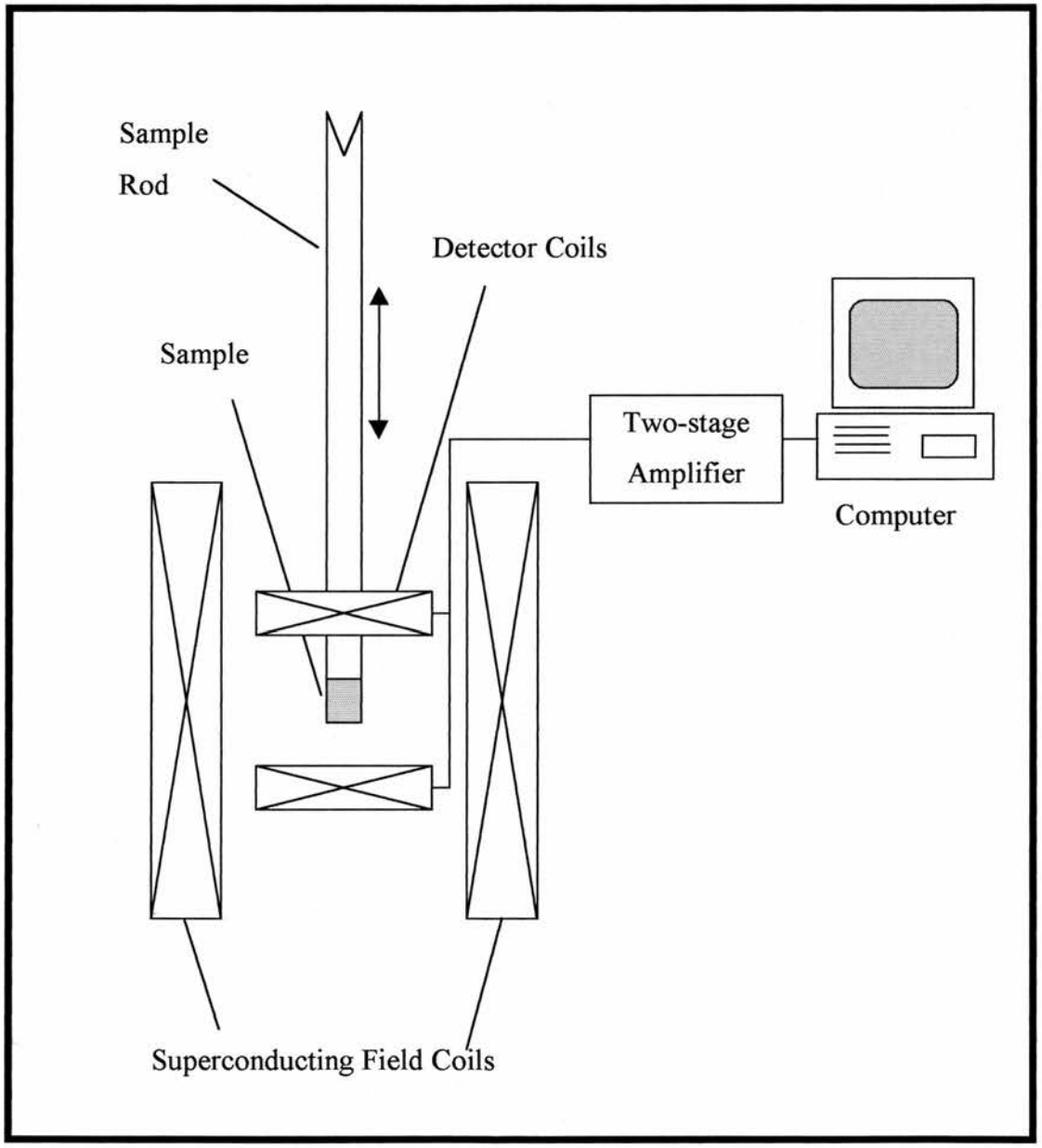

Figure 4.3

Schematic layout of the vibrating sample magnetometer (VSM)

The sample temperature is measured by a AuFe/Chromel thermocouple in direct contact with a copper heat exchanger situated below the sample. Temperature control is maintained by an Oxford Instruments ITC4 temperature controller. The VSM system is fully computer controlled. A diagram of the VSM system is shown in figure 4.3.

4.4.4 Calibration of the VSM

The VSM is calibrated by adjusting the gain of the second amplifier stage while measuring the saturation magnetisation of a Ni sphere of known mass. When performing the calibration, it is helpful to use a Ni standard of a similar magnetic dipole moment to the sample which is to be measured, so that the primary stage amplifier gain remains the same. In our magnetisation measurements, we have used the value of the Ni magnetic dipole moment per unit mass given by Aldred [2] of 54.85 $emug^{-1}$ at 300K.

4.4.5 Magnetisation Measurements of β-MnAl

Magnetisation measurements were carried out on β-$Mn_{1-x}Al_x$ alloys with compositions, x=0, 0.03, 0.06, 0.1 and 0.2. The measured magnetisation per unit mass in units of emu g^{-1} was converted to dc susceptibility in units of emu g^{-1} Oe^{-1} using eqs. (4.5) and (4.6). The *volume* susceptibility in SI units (dimensionless) was obtained using the following formula,

$$\chi_V(SI) = \chi_m\,(CGS) \times 4\pi \times \rho\,(CGS), \qquad (4.7)$$

where ρ (CGS) is the sample density in units of g cm^{-3}.

The temperature dependence of χ_V (SI) for β-Mn, β-$Mn_{0.96}Al_{0.06}$, β-$Mn_{0.9}Al_{0.1}$ and β-$Mn_{0.8}Al_{0.2}$ is shown in figure 4.4. These results are in broad agreement with those of Nakamura and co-workers presented in chapter 1 [3].

The temperature dependence of the dc susceptibility for β-Mn and β-$Mn_{0.94}Al_{0.06}$ is relatively weak, with a small rise being observed at around 40K. The feature at 40K was observed to a greater or lesser extent in all the β-MnAl alloys studied, and was attributed to the presence of Mn_3O_4 or *Haussmannite* as a surface oxide impurity in the powdered β-MnAl samples.

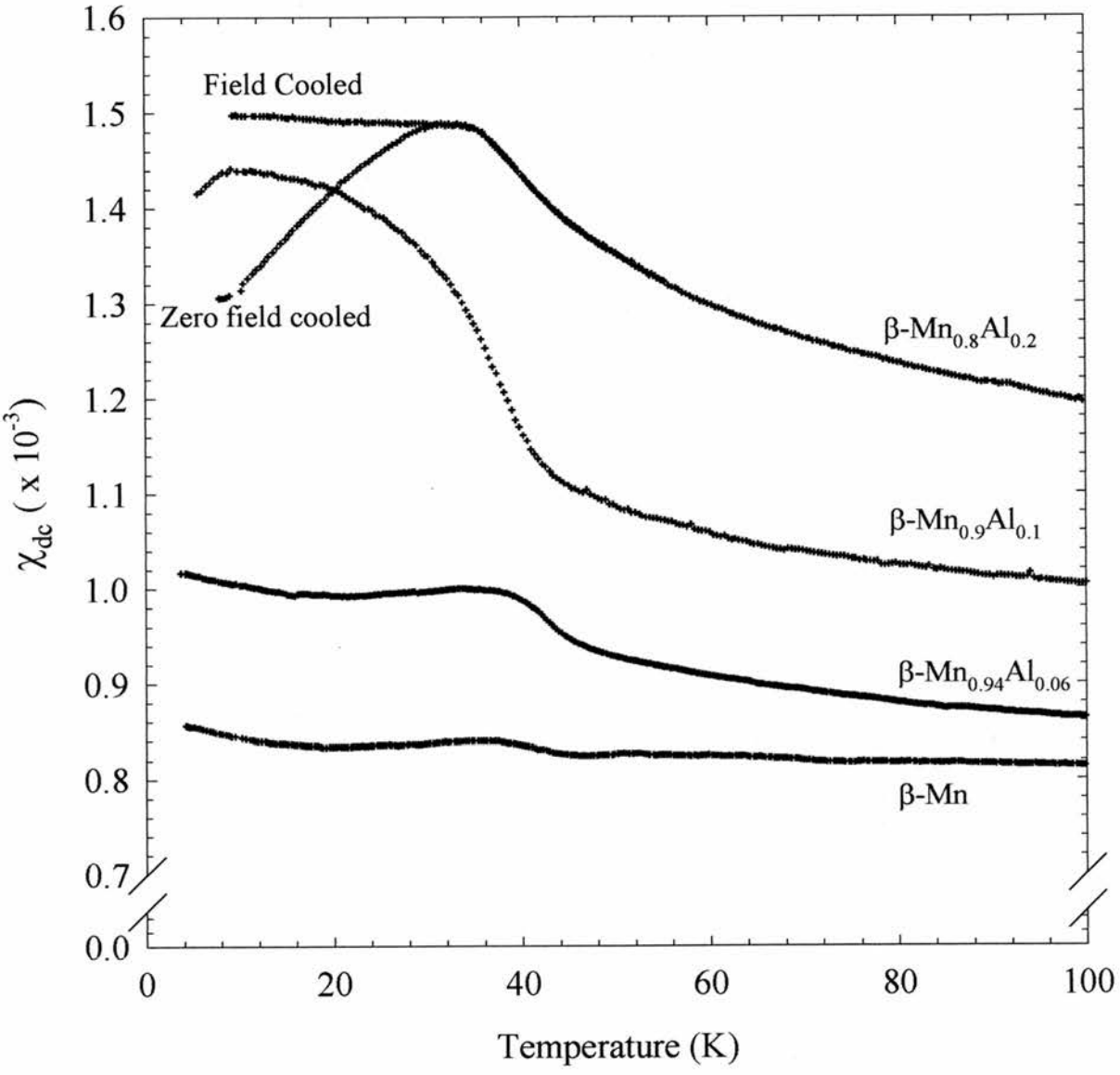

Figure 4.4

The temperature dependence of the dc susceptibility of β-MnAl alloys cooled in zero field. A peak in χ_V is exhibited by the β-$Mn_{0.9}Al_{0.1}$ and β-$Mn_{0.8}Al_{0.2}$ concentrations. The field cooled branch of the susceptibility is also shown for β-$Mn_{0.8}Al_{0.2}$ indicating spin glass behaviour for this composition.

Mn readily oxidises in air to produce mainly MnO and Mn_3O_4. MnO is probably the world's most famous antiferromagnet (T_N = 120K) [4] and Mn_3O_4, which is a cubic spinel material, becomes ferrimagnetic at a temperature of 42K [5].

The β-$Mn_{0.9}Al_{0.1}$ and β-$Mn_{0.8}Al_{0.2}$ compositions display a much stronger temperature dependence of χ_V, with a peak in the susceptibility being observed at low temperatures. This peak occurs at ~10K in β-$Mn_{0.9}Al_{0.1}$ and ~34K in β-$Mn_{0.8}Al_{0.2}$. At temperatures greater than the peak temperature, the susceptibility shows a steady decrease with increasing temperature.

The temperature dependence of χ_V for β-$Mn_{0.8}Al_{0.2}$ displays history dependent behaviour below T ~ 34K. This history dependence is an indication of spin glass freezing at a temperature T_g. Mean-field theories have identified critical lines in H-T space (de Almeida-Thouless lines) below which history dependent behaviour is expected in spin glasses [6]. In the ZFC branch, when the field is turned on at $T < T_g$ the frozen spins will slowly start to turn towards the direction of the applied field as the temperature increases, and thermal energy is supplied to the system. The susceptibility will therefore increase until the thermal fluctuations in the system are sufficient to ensure that the spins no longer follow the field, and are therefore in the paramagnetic state. This is the origin of the familiar cusp in the susceptibility of spin-glasses. In the FC branch, the field is turned on at $T > T_g$, when all of the spins can respond to it, and are frozen completely at T_g. The susceptibility, therefore, flattens out at low temperatures. Although this description seems appropriate to the explanation of the temperature dependence of χ_V for β-$Mn_{0.8}Al_{0.2}$, the peak in the ZFC branch is not a classical spin glass cusp in the susceptibility, but instead, a broad maximum.

In conclusion, these magnetisation measurements provide evidence for spin glass *like* behaviour in β-MnAl alloys at Al concentrations > 10at%. The observation of a temperature dependent bulk susceptibility in β-$Mn_{0.9}Al_{0.1}$ and β-$Mn_{0.8}Al_{0.2}$, in contrast to the weak temperature dependence observed in β-Mn, is indicative of the formation of at least partially localised moments in these alloys. The neutron scattering studies of Shiga presented in chapter 1 [7] showed that the Mn moments in both β-Mn and

β-$Mn_{0.9}Al_{0.1}$ were antiferromagnetically correlated; the wavevector dependent susceptibility $\chi(Q)$ displaying a maximum at the antiferromagnetic wavevector, $Q \sim 1.4 Å^{-1}$, and falling away towards zero at low Q. If β-$Mn_{0.9}Al_{0.1}$ were a purely itinerant magnet, our magnetisation measurements of the bulk (Q = 0) susceptibility in β-$Mn_{0.9}Al_{0.1}$ would display only the temperature independent Pauli susceptibility due to the conduction electrons. The formation of at least partially localised moments however would explain our results, since the application of an external field to a system of localised moments partially aligns these moments in the direction of the applied field, and hence contributes to the bulk magnetisation of the sample, even when these moments are antiferromagnetically correlated.

4.5 Electrical Resistivity

4.5.1 Introduction

Measurement of the temperature dependence of the electrical resistivity of a magnetic material, can often provide a valuable insight into its structural and magnetic properties. The functional form of the temperature dependence of the resistivity often provides information on dominant electron scattering processes in the material of interest. This technique is particularly useful in the study of itinerant electron magnets, where the changes in the distribution of electron spin density at a magnetic phase transition will affect the measured resistivity.

4.5.2 Contributions to the electrical resistivity

The temperature dependence of the phonon contribution to the electrical resistivity, $\rho(T)$ takes the form of the Grueneisen equation,

$$\rho(T) \approx 4\left(\frac{T}{\theta_D}\right)^5 \int_0^{\theta_D/T} \frac{e^x x^5}{\left(e^x - 1\right)^2} dx, \qquad (4.8)$$

where θ_D is the Debye temperature of the crystal, and is a measure of the phonon stiffness. For low and high temperature regions eq. (4.8) reduces to,

$$\rho_{ph}(T) = \begin{cases} \propto T^5 & \text{for } T << \theta_D \\ \propto T & \text{for } T >> \theta_D \end{cases} \qquad (4.9)$$

In a system of uncorrelated local moments in the absence of any crystal electric field, there will be a contribution to the resistivity ρ_{lm} caused by the scattering of the conduction electrons by these disordered localised spins. This contribution is temperature independent and takes the form,

$$\rho_{lm} = \frac{3\pi N m^*}{2\hbar e^2 E_F} |J|^2 (g_J - 1)^2 J(J+1), \qquad (4.10)$$

where m* is the effective mass of the conduction electrons, J is the Heisenberg exchange constant and $(g_J\text{-}1)^2J(J+1)$ is the de-Gennes factor.

Many metallic systems are well described by the Fermi-Liquid model outlined in section (2.3.2.3), where quasi-electrons and holes occupying states within k_BT of the Fermi energy, may collide with each other, and are subject to changes in their effective masses as result of electron-electron interactions. The Fermi-Liquid model predicts a contribution to the resistivity $\rho_{fl}(T)$, at low temperatures, of the form

$$\rho_{fl}(T) = BT^2, \qquad (4.11)$$

where B is a constant, with a value which depends on the Fermi energy and the electron-electron interaction cross section, σ_0. The presence of spin fluctuations in a magnetic material will also contribute to the electrical resistivity since they scatter conduction electrons via the so-called s-d exchange interaction [8]. In this model the d-electrons (which may be either localised or itinerant) contribute to the spin fluctuations which then scatter the s-band conduction electrons. Ueda has shown [9] that in weakly antiferromagnetic metals, $\rho(T)$ obeys eq. (4.11), and that the coefficient, B, tends to diverge as it approaches the critical boundary, as

$$B \propto |\alpha - 1|^{-1/2}, \qquad (4.12)$$

for both weakly and nearly antiferromagnetic metals. At the critical boundary, $\alpha = 1$, $\rho(T)$ no longer follows the Fermi-Liquid model given by eq. (4.11). Instead, the theory predicts,

$$\rho_{nfl}(T) \propto T^{3/2}, \qquad (4.13)$$

where the subscript "nfl" signifies this non Fermi-Liquid scaling.

In general, at the lowest temperatures, where there are no phonons present and the spin fluctuations have been reduced to zero point motions, the resistivity of a material tends toward a constant value known as the residual resistivity, ρ_0. This will include the local moment contribution ρ_{lm}, but will also be affected by lattice imperfections, grain boundaries and chemical impurities.

If the individual electron scattering processes are independent of one another, the total measured resistivity will obey Matthiessen's Rule, where the total resistivity is given by the sum of the individual contributions.

$$\rho(T) = \rho_0 + \rho_{ph}(T) + \rho_{lm}(T) + \rho_{fl}(T) + \ldots\ldots \qquad (4.14)$$

4.5.3 Electrical Resistivity Apparatus

The apparatus used to measure the electrical resistivity of β-MnAl samples in this study, is based on a standard *four probe* method shown in figure 4.5. A known current density is driven through the sample between probes 1 and 4 and the voltage dropped between points 2 and 3 separated by distance, l, is measured. The resistivity is then calculated from the equation,

$$\rho(T) = \frac{V(T)}{J \times l}. \qquad (4.15)$$

The advantage of this method is that contact resistance and the impedance of the contact leads can be neglected.

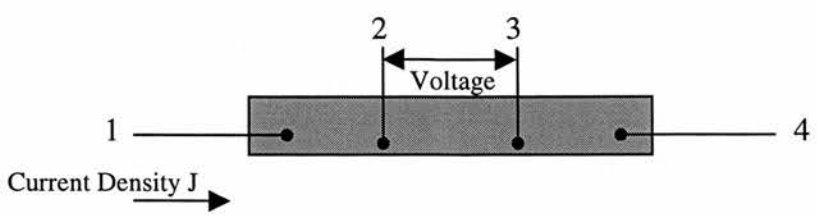

Figure 4.5

Standard arrangement for a four probe measurement of the electrical resistivity of a sample with known cross-sectional area A.

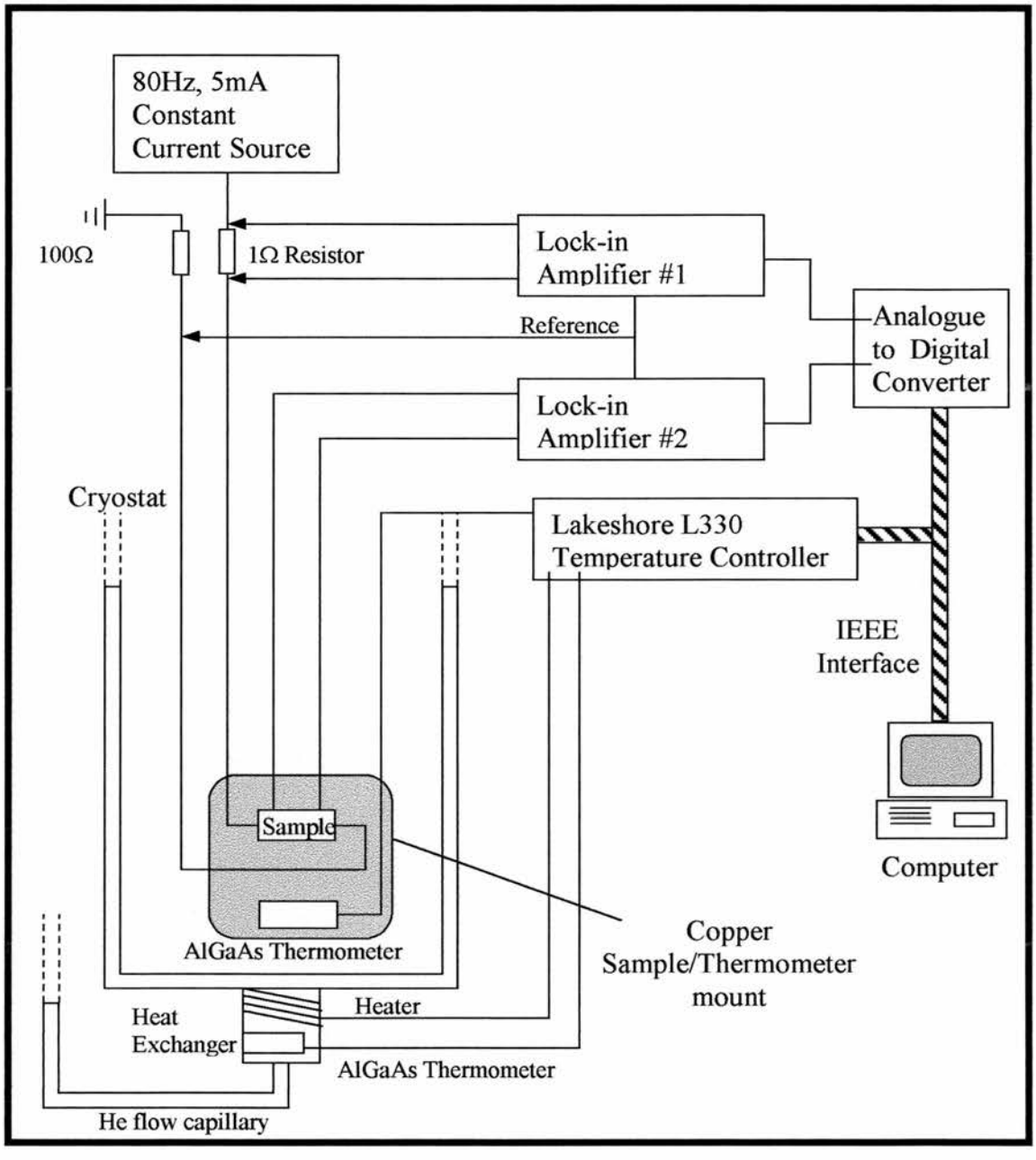

Figure 4.6

A schematic diagram of the electrical resistivity apparatus

We employ an ac technique in which a low frequency (80Hz) square-wave constant ac current is used, in conjunction with phase sensitive detection of the measured voltage. This ac technique allows the elimination of thermal and contact emfs, since they do not depend on the current direction and are averaged out to zero over a measuring cycle.

A schematic diagram of the electrical resistivity apparatus is shown in figure 4.6. A constant ac current generator supplies a 5mA current. This is passed to earth through a 100Ω reference resistor and the sample. The sample is mounted in a copper sample block together with an AlGaAs diode thermometer. Measurements can be taken over the temperature range 2K to 330K by cooling the sample in a Janis "Supervaritemp" continuous flow He cryostat. Temperature measurement and control is maintained by a Lakeshore L330 temperature controller, connected to the AlGaAs diode sample thermometer, and a control AlGaAs thermometer and copper wire heater which are attached to the heat exchanger of the cryostat. The voltages across the sample and a 1Ω resistor are monitored by two Brookdeal lock-in Amplifiers. Operation of the system and data collection are fully computer controlled. A typical measurement takes of the order of 18 hours, depending on the warming rate of the cryostat and the time constant of the lock-in amplifiers. This enables the collection of several hundred data points at a particular temperature. The data collection program includes an algorithm for the removal of data points lying outside one standard deviation of the data set at each temperature, before the final averaging takes place. This greatly reduces the signal to noise ratio of the measurement.

4.5.4 Resistivity Measurements of β-Mn and β-$Mn_{0.9}Al_{0.1}$

Electrical resistivity measurements were successfully carried out on β-Mn and β-$Mn_{0.9}Al_{0.1}$. Resistivity measurements of many other concentrations were attempted. However these samples were found to contain many cracks and defects, especially at high Al concentrations, and many broke or crumbled during the measurements.

Figure 4.7 shows plots of ρ(T) for β-Mn and β-$Mn_{0.9}Al_{0.1}$. The residual resistivity ρ_0, was found to be large in these samples, with $\rho_0 \sim 81.2$ μΩcm for β-Mn and $\rho_0 \sim 147.4$ μΩcm for β-$Mn_{0.9}Al_{0.1}$. The high temperature resistivity above ~120K is very similar in the two samples, being roughly proportional to T in accordance with the

high temperature phonon contribution given by eq.(4.9). Below, 110K, $\rho(T)$ continues to fall steadily in β-Mn, but in the β-$Mn_{0.9}Al_{0.1}$ sample, $\rho(T)$ reaches a minimum at ~95K and then starts to increase with decreasing temperature. The appearance of a resistivity minimum, followed by a negative temperature coefficient of resistivity is consistent with the formation of local moments in β-$Mn_{0.9}Al_{0.1}$ (see section 2.4.3.1). If local moments are being stabilised with decreasing temperature in this system, then electrons removed from the conduction band will increase the resistivity of the material. This observation of a negative temperature coefficient in β-$Mn_{0.9}Al_{0.1}$ is in agreement with the measurements of Nakamura and co-workers. [3]. The appearance of a negative temperature coefficient has been observed in several disordered binary alloys such as $Ti_{0.67}Al_{0.33}$, $Ti_{0.8}V_{0.2}$ and $Ni_{0.8}Cr_{0.2}$ [10].

In order to obtain the functional form of $\rho(T)$ in β-Mn, a log-log plot of $\rho(T) - \rho_0$ is presented in figure 4.8. The low temperature region of the data below 20K is fitted to a straight line, revealing the power law,

$$\rho(T) - \rho_0 = BT^{\gamma}, \tag{4.16}$$

where γ and B are found to be 1.503 and 0.056 respectively.

The value, $\gamma = 1.503$, of the power coefficient shows that the functional form of $\rho(T)$ for β-Mn is in good agreement with Moriya's prediction of $\rho(T)$ for nearly and weakly antiferromagnetic metals on the edge of the magnetic non-magnetic instability, given in eq. (4.13).

In conclusion, our resistivity measurements show that β-Mn exhibits non-Fermi liquid scaling, consistent with the SCR theory prediction for nearly antiferromagnetic metals. To our knowledge, this is the first observation of non-Fermi liquid scaling in a paramagnetic elemental metal. The addition of 10at%Al to β-Mn causes a drastic change in $\rho(T)$ with a minimum at ~95K followed by a region where $\rho(T)$ contains a negative temperature coefficient. This observation, which is in qualitative agreement with previous measurements [3] is consistent with the temperature induced formation of local moments in the system.

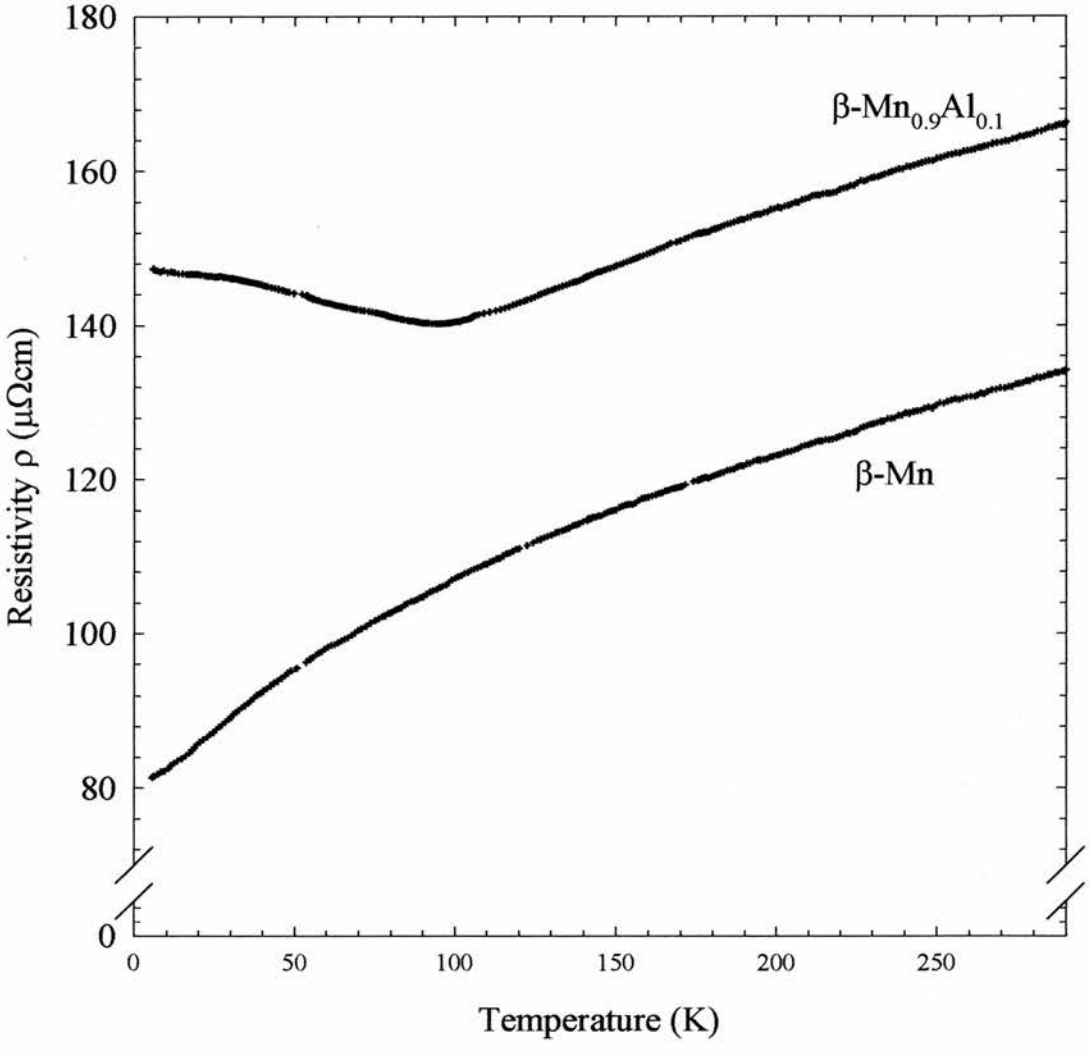

Figure 4.7

Temperature dependence of the electrical resistivity $\rho(T)$ of β-Mn and β-$Mn_{0.9}Al_{0.1}$. $\rho(T)$ of both β-Mn and β-$Mn_{0.9}Al_{0.1}$ in the high temperature region at $T > 120K$ is proportional to T indicating dominant phonon scattering of the conduction electrons. A minimum in $\rho(T)$ is observed at $T \sim 100K$ in β-$Mn_{0.9}Al_{0.1}$, followed by a region where $\rho(T)$ has a negative temperature coefficient.

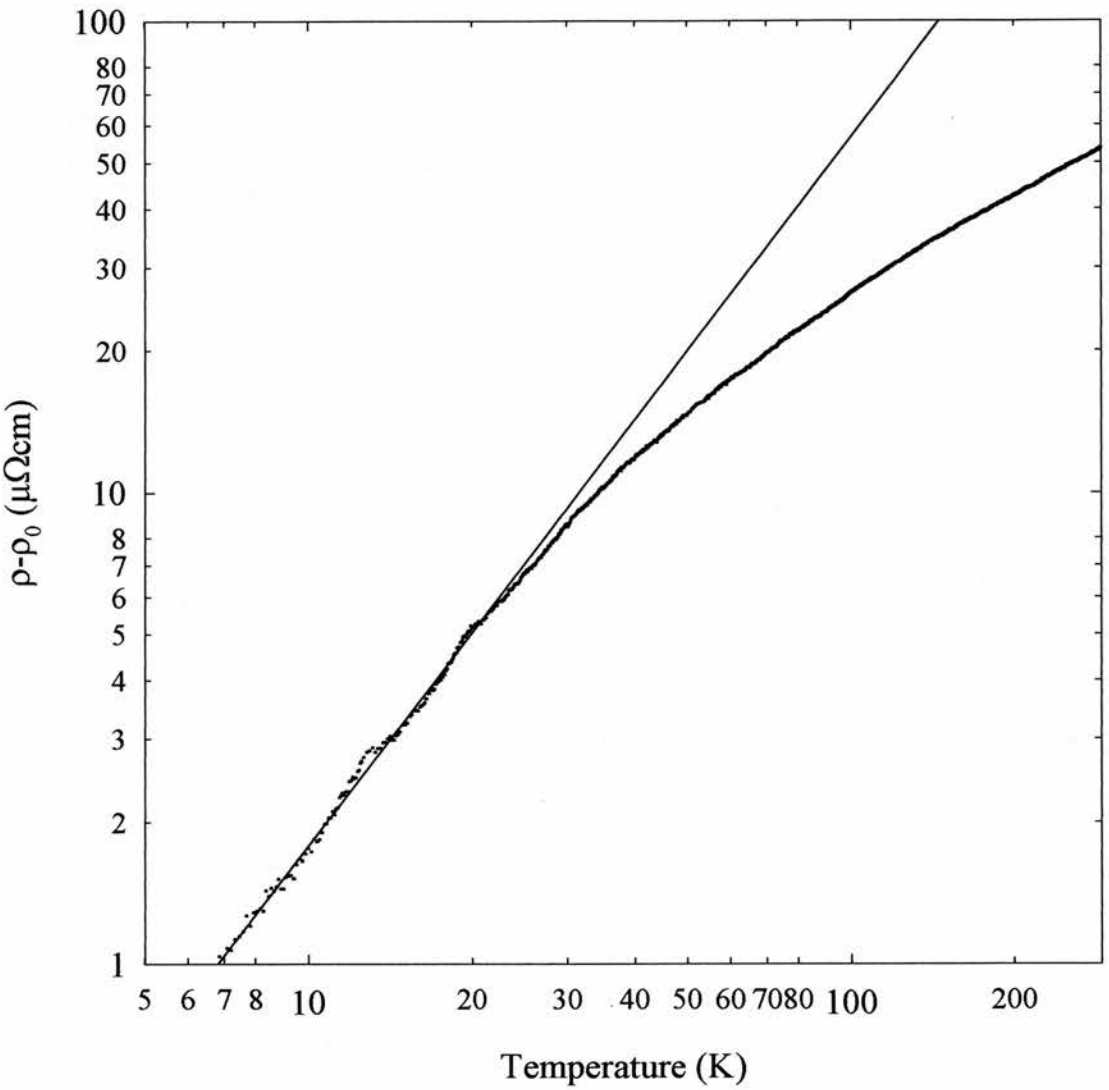

Figure 4.8

Log-log plot of $\rho(T) - \rho_0$ for β-Mn. The fit to a straight line of the form given by eq. (4.16) shows that $\rho(T) \propto T^{3/2}$ at low temperatures in agreement with the SCR prediction for nearly antiferromagnetic metals on edge of the magnetic non-magnetic boundary where $\alpha\chi_0 \sim 1$.

4.6 References

[1] Hansen, *Phase diagrams of Binary Alloys*, (McGraw Hill, New York, 1958)

[2] A T Aldred, Phys. Rev. B **11** (1975) 2597

[3] H Nakamura, K Yoshimoto, M Shiga, M Nishi and K Kakurai, J. Phys. Cond. Matter **9** (1997) 4701

[4] C G Shull, W A Strauser and E O Wollan, Phys. Rev. **76** (1949) 1256

[5] Jensen and Nielsen, J. Phys. C **7** (1974) 409

[6] J R De Almeida and D J Thouless, J. Phys, A**11** (1978) 983

[7] M Shiga, H Nakamura, M Nishi and K Kakurai, J. Phys. Soc. Japan **63** (1994) 1656

[8] T Moriya, *Spin Fluctuations in Itinerant Electron Magnetism*, Springer-Verlag 1995

[9] K Ueda, J. Phys. Soc. Japan **43** (1977) 1497

[10] J H Mooij, Phys. Stat. Sol (a) **17** (1973) 521

5 Neutron Powder Diffraction Studies

5.1 Introduction

Two neutron diffraction studies have been undertaken as part of this thesis. Firstly, the nature of the α-Mn to β-Mn phase transition has been investigated using real time kinetic neutron diffraction. This study was undertaken in order to gain an insight into the structural properties inherent in α-Mn and β-Mn, which support the formation of an antiferromagnetic ground state in α-Mn and prevent long-range magnetic order in β-Mn.

Secondly, we have investigated the site occupancy and structural properties of dilute β-Mn alloys with Al, In, Sn, Co and Fe. These alloys have been shown to possess a static magnetic ground state by the NMR studies of Kohara and Asayama [1] and the Mössbauer spectroscopy studies of Nishihara [2] (see chapter 1). We have identified the lattice site in the β-Mn structure which is preferentially occupied by the impurity atoms in order to gain further understanding of the mechanisms behind the formation of a static magnetic ground state in these alloys.

5.2 Time of Flight Neutron Powder Diffraction

In a time of flight neutron diffraction experiment a pulse of neutrons having a distribution of wavelengths n(λ) is scattered by a powdered sample. The neutron pulse will contain a Maxwellian distribution of neutron speeds, the width of which is determined by a neutron moderator situated in front of the neutron source. The wavelength of a neutron of velocity v within the pulse is given by the de Broglie equation,

$$\lambda = \frac{h}{mv}. \qquad (5.1)$$

The speed of the neutron is determined by the time of flight t over the length of the neutron flight path L, giving [3]

$$\lambda = \frac{ht}{mL}; \quad \lambda(A) = 3.956\frac{t(ms)}{L(m)}. \tag{5.2}$$

For elastic scattering the incident and scattered neutron wavevectors are such that $|\mathbf{k}_i| = |\mathbf{k}`|$, so that the scattering triangle shown in figure 5.1 is isosceles with the wavevector transfer given by,

$$Q = \frac{4\pi \sin\theta}{\lambda}. \tag{5.3}$$

Figure 5.2 shows the Q values available from eq (5.3) for a given scattering angle and incident wavelength.

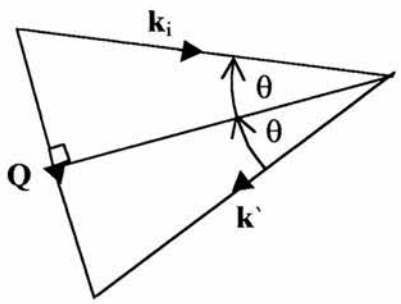

Figure 5.1

Elastic scattering triangle in a neutron diffraction measurement with $|\boldsymbol{k}_i| = |\boldsymbol{k}`|$.

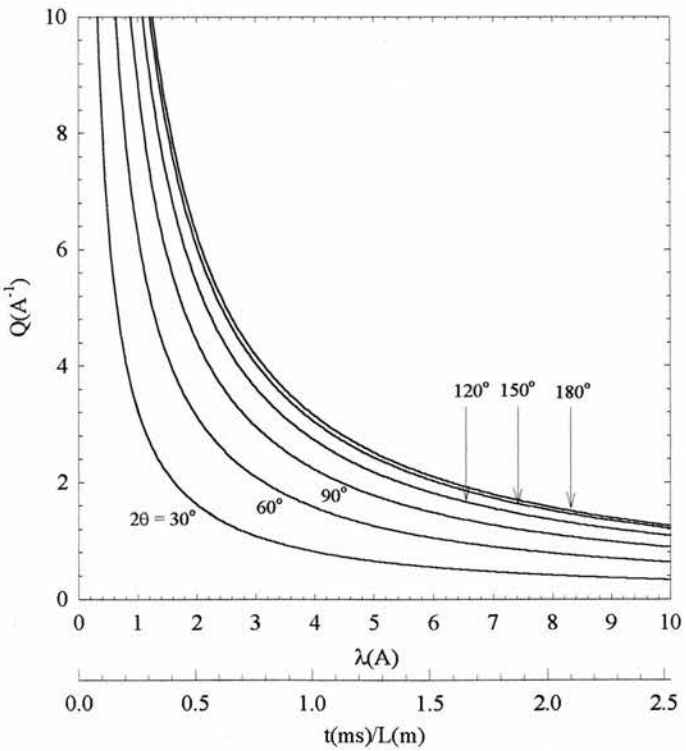

Figure 5.2

Q values available for a time of flight neutron diffraction measurement for a given scattering angle. The time of flight axis from which the wavelengths are found is shown.

Combining eqs. (5.2) and (5.3) we can write the Bragg condition for a time of flight diffraction measurement,

$$\frac{4\pi \sin\theta mL}{ht} = G_{hkl} = \frac{2\pi}{d_{hkl}}$$
$$\therefore d_{hkl} = \frac{ht}{2mL\sin\theta} \qquad (5.4)$$

The resolution of the observed d spacing is obtained by partial differentiation of eq. (5.4) with respect to the three experimental degrees of freedom; θ, t and L. If these variables are assumed to be independent, then the uncertainties add in quadrature so that the resolution is given by,

$$R = \frac{\Delta d}{d} = \left[\Delta\theta^2 \cot^2\theta + \left(\frac{\Delta t}{t}\right)^2 + \left(\frac{\Delta L}{L}\right)^2 \right]^{1/2} . \qquad (5.5)$$

High resolution is therefore achieved at high scattering angles and long flight paths and times of flight. It can be shown that for a neutron diffraction experiment with the three degrees of freedom in present in eq. (5.5) the experimental resolution is depends mainly on the flight path with, $R = 3\delta/L$, where δ depends on the time spread of the neutron pulse caused by the moderator [3].

5.3 Reitveld Refinement of Powder Diffraction Data

In the Reitveld refinement method, a structural model of the crystal structure is assumed and the neutron intensities expected from the model are calculated using eqs. (3.11) and (3.12). The model is iteratively adjusted and the calculated powder pattern is compared with the measured powder pattern using a least-squares refinement procedure. The quality of the fit is quantified by the following "R-factors".

a) The Bragg R-factor R_B, is the sum of the magnitude of the residuals for each Bragg reflection, normalised to the total observed intensity of all the Bragg reflections.

b) The profile R-factor R_p, is the sum of the magnitude of the residuals for each point in the powder pattern, normalised to the total integrated intensity of the pattern.

c) The weighted profile R-factor R_{wp}, is similar to R_p but the residual of each point is squared and weighted , the square-root being taken after the summation, i.e.,

$$R_{wp} = \left(\frac{\sum_n w_n \left| I_{n,obs} - I_{n,calc} \right|^2}{\sum_n w_n I_{n,obs}^2} \right)^{\frac{1}{2}}, \qquad (5.6)$$

where the weighting factor $w_n = 1/I_{n,obs}$, n is the number of points in the pattern and $I_{n,obs}$ and $I_{n,calc}$ are the observed and calculated intensities respectively.

d) The expected R-Factor R_{exp}, is defined such that $(R_{wp}/R_{exp})^2 = \chi^2$, where χ^2 is the standard measure of the quality of a least-squares fit [4].

The model from which the theoretical intensity is calculated contains up to 400 independent parameters which may be adjusted during a Reitveld refinement. The most important factors to be taken into account in a Reitveld refinement are outlined below.

a) *The scale factor* accounts for the measured integrated neutron intensity.

b) *The background* is usually fitted to a polynomial function.

c) *The unit cell constants and atomic coordinates* define the contents of the assumed unit cell and hence the location and intensities of the Bragg reflections from eq (3.12).

d) *The zero shift* adjusts the zero point of the measurement (often this value is determined by independent calibration of the particular diffractometer and should not be varied in the refinement).

e) *The isotropic temperature factors* U_{iso} in units of $Å^2$ adjust the Bragg intensities according to the Debye-Waller factor [eq. (3.15)].

f) *The absorption correction* accounts for the reduction in the observed intensity of a Bragg reflection due to the attenuation of neutrons passing through the sample. This correction is dependent on neutron wavelength and scattering angle. In the backscattering limit ($2\theta \sim 180°$) the intensity is given by

$$I_B = \frac{I_0}{2\mu T}(1 - e^{-2\mu T}), \qquad (5.7)$$

where μ is the linear absorption coefficient.

g) *The peak shape* is determined by the intrinsic instrumental lineshape and powder particle size and strain effects. In a time of flight neutron diffractometer, the intrinsic lineshape is described by the Ikeda-Carpenter function [3,5] which

represents the combination of a Gaussian lineshape determined by the instrumental resolution convoluted with a pulse shape represented by a sharp rise, followed by a "fast" exponential decay arising from the slowing down of epithermal neutrons and a "slow" exponential decay representing the thermal neutrons. Broadening effects due to the sample are taken into account by convolving the Ikeda-Carpenter function with a Lorentzian lineshape.

5.4 The α-Mn to β-Mn Phase Transition

5.4.1 Introduction

When a physical system is brought to a non-equilibrium state by a sudden change of temperature the system will transform to the equilibrium state at a rate dependent on the difference in Gibbs free energy between the initial and final states. The manner in which the transformation proceeds will depend upon random fluctuations from the initial state and whether these fluctuations raise or lower the free energy of the system. A metastable system is resistant to all possible fluctuations.

In a *heterogeneous* phase transformation, the system can be separated into distinct regions some of which have transformed and others which have not. The transformation begins from nucleation centres and then spreads throughout the system in a manner depending on the topology of the free energy surface. In forming a nucleation centre, the stable region within the nucleus will decrease the free energy of the system while the interface between the nucleus and the initial phase will, in general, increase the free energy. The rate of creation and growth of the nucleation centres therefore depends upon the ratio between these surface and volume contributions to the free energy. For instance, if the increase in free energy at the surface of the nucleation centre is small, more nuclei will be formed in a given volume and a given time. In the limit that the surface free energy disappears altogether, all parts of the system will nucleate simultaneously, in which case the phase transition is *homogeneous*.

Heterogeneous phase transformations can be subdivided into the following two types.

a) *Nucleation and growth transformations.* Nucleation centres are formed when a thermal activation energy barrier determined by the free energy of the system is overcome. The new phase grows at the expense of the initial phase by atoms migrating across the interface between the nucleation centre and the initial phase. The atoms move independently at a rate determined by the temperature of the system and the free energy difference between the initial and final states.

b) *Martensitic transformations.* These transformations do not involve atomic diffusion but a co-operative movement of several thousand atoms occurring at very high velocity. Such a phase transformation is often called a "shear transformation". While a martensitic phase transformation occurs at a particular temperature, the rate of the transformation is independent of the transition temperature. This phenomenon cannot be explained by processes of thermal activation such as those which occur in nucleation and growth transformations.

5.4.2 Isothermal Transformation Curves

The nature of a phase transformation may be investigated by examining the time dependence of the volume of the transformed region at a constant temperature. This time dependent behaviour is known as the isothermal transformation curve.

In a homogeneous transformation, all regions of the system have an equal probability of transforming in a given time which is proportional to the untransformed volume remaining at that time. A transformation from state α to state β can thus be expressed in terms of the differential rate equation,

$$\frac{dV_\beta}{dt} = k(V - V_\beta), \tag{5.8}$$

where V_β is the volume of the transformed region, V is the total volume of the system and k is the rate constant. Defining the β-phase fraction $S_\beta = V_\beta/V$ eq. (5.8) can be solved to obtain,

$$S_\beta = 1 - \exp(-t/\tau), \tag{5.9}$$

where $\tau = 1/k$ is the time constant of the phase transformation.

In nucleation and growth transformations it is assumed that a nucleation centre is formed at a time t_0 called the *induction period*. It is found experimentally that any dimension of the transformed region increases linearly with time, until the transformed regions impinge on each other, thereby interfering with each other's growth rate. This problem is essentially geometrical and was first addressed by Johnson and Mehl [6], and later by Avrami [7,8,9]. Avrami proposed that growth and nucleation transformations may be described in terms of the general equation,

$$S_\beta = 1 - \exp[-(t/\tau)^n], \qquad (5.10)$$

where the exponent n represents the dimensionality of the growth of the nucleated regions as shown in table 5.1. Eq.(5.10) is known as the Avrami-Johnson-Mehl (AJM) equation. If the exponent n = 1 the AJM equation reduces to eq. (5.9) and the transformation is homogeneous.

Table 5.1 Type of growth process indicated by the exponent n in the AJM equation.

exponent n	Type of growth
1	homogeneous
$1 \leq n \leq 2$	1 dimensional – "*dendritic*"
$2 \leq n \leq 3$	2 dimensional – "*plate like*"
$3 \leq n \leq 4$	3 dimensional

5.4.3 The High Resolution Powder Diffractometer (HRPD)

The HRPD diffractometer at the ISIS pulsed neutron facility is the highest resolution neutron powder diffractometer in the world, with a resolution $R = \Delta d/d \sim 4 \times 10^{-4}$ in the backscattering detector bank used in these measurements. HRPD is therefore ideal for the study of phase transformations which may involve subtle changes in the dimensions of the unit cell of the material under investigation. The incident neutron pulse is moderated by methane at 100K, providing HRPD with a wavelength range of $0.5\text{Å} \leq \lambda \leq 12\text{Å}$, with the peak flux at $\lambda = 2\text{Å}$. The high resolution on HRPD results from an extremely long flight path of almost 100m from the target station at ISIS together with optimal use of backscattering geometry. These two features minimise the $\Delta t/t$, $\Delta L/L$ and $\cot^2\theta$ contributions to the resolution function given by eq. (5.5). Since this flight

path entails extremely long times of flight of the incident neutrons, a chopper is placed in the beam line which admits 1 out of every 5 neutron pulses available at ISIS at a repetition rate of 10Hz, in order to avoid pulse overlap. Our measurements were taken using the backscattering ZnS scintillator detector on HRPD covering a scattering angle range of $160° \leq 2\theta \leq 176°$.

5.4.4 Experimental Procedure

The finely powdered Mn samples were placed in a vanadium sample can of 12mm diameter and inserted into a standard ISIS furnace covering a temperature range of 300K to 1200K. The Mn samples were held at a temperature of 500C for at least 1hr before the temperature was raised rapidly at time $t = 0$ to the desired temperature required for the measurement of the isothermal transformation curve. This ensured that the sample was phase pure α-Mn at $t = 0$. Raising the temperature from 500C to slightly above the phase transition temperature (~700C) took approximately 5 minutes. The excellent temperature control of the sample furnace on HRPD ensured minimum overshoot of the desired temperature. Real time diffraction patterns were obtained in time slices of between 5 and 15 minutes depending on the rate of the phase transformation. A 5 minute measurement was found to be the shortest practical time slice on HRPD.

5.4.5 Results

Figure 5.3 shows a typical measurement of the α-β Mn phase transition. The observed diffraction patterns are shown as a function of time at a constant temperature of 710K. Four such measurements were performed at temperatures of 700K, 705K, 710K and 715K. The β-Mn phase fraction S_β at each time interval was obtained by full two-phase Reitveld refinement of the measured diffraction patterns using the "General Structure Analysis System" (GSAS) suite of programs [10]. A typical GSAS refinement is shown in figure 5.4. The time dependence of S_β at each temperature is shown in figure 5.5. The solid lines shown in figure 5.5 are fits of the data to the AJM equation (5.8). The time constant and exponent found by fitting the data are presented in table 5.1.

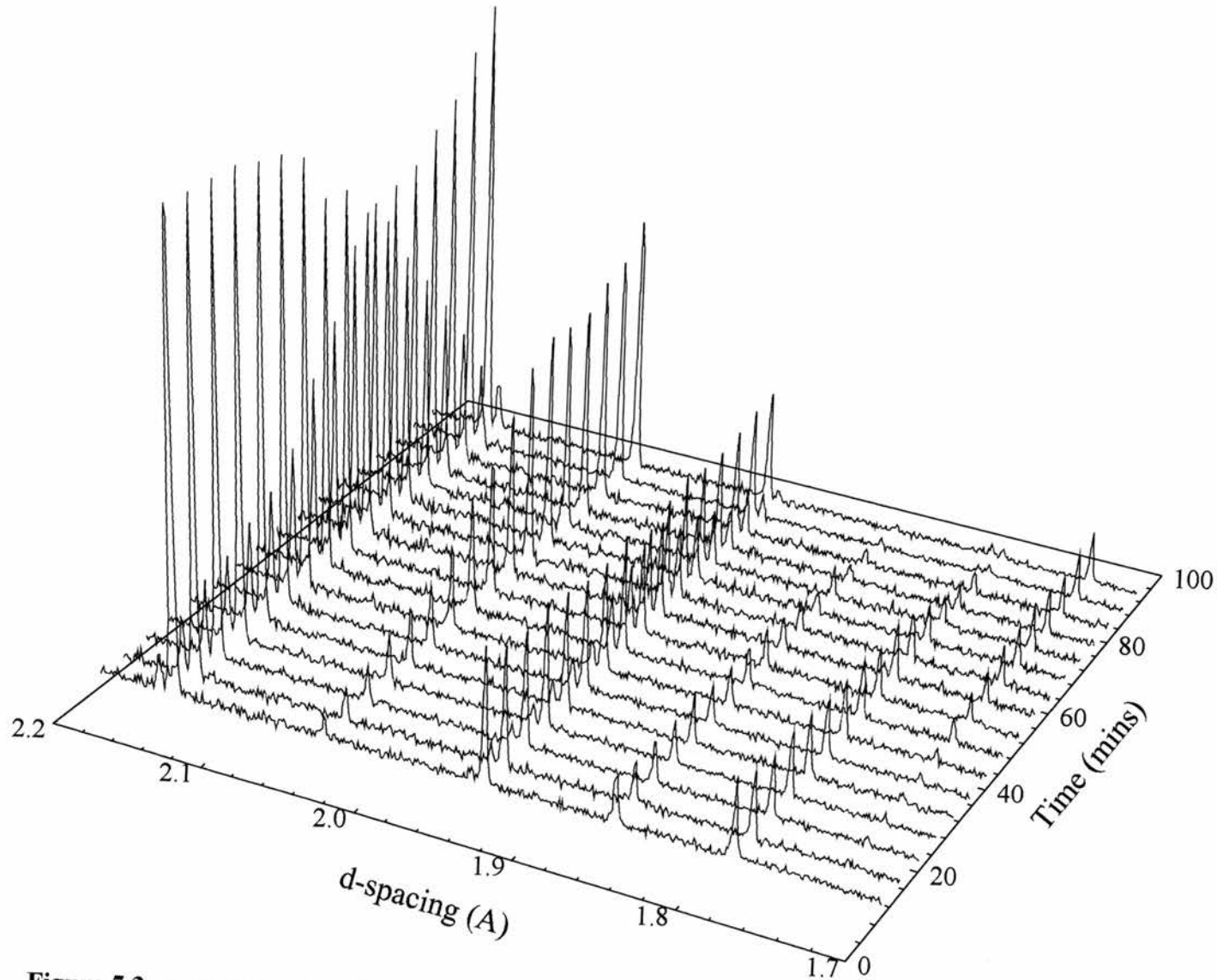

Figure 5.3 *α–βMn phase transformation at a temperature of 710K. The spectra shown represent 10 minute time slices.*

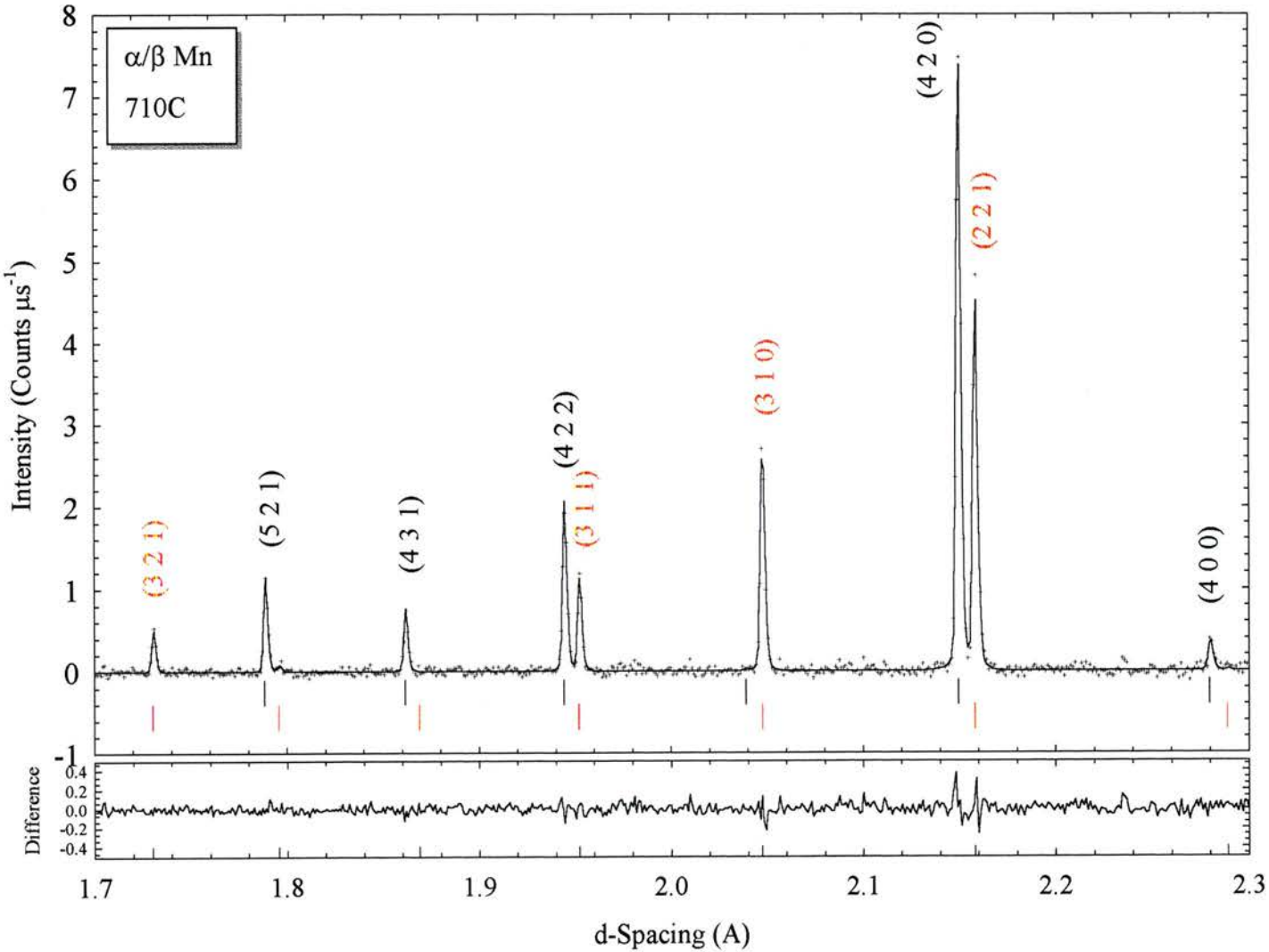

Figure 5.4 *Typical two-phase Reitveld refinement of α/βMn at 710C, 50 minutes into the measurement. The diffraction pattern was collected in 10 minutes. α-Mn reflection positions are shown in black, while β-Mn reflection positions are shown in red.*

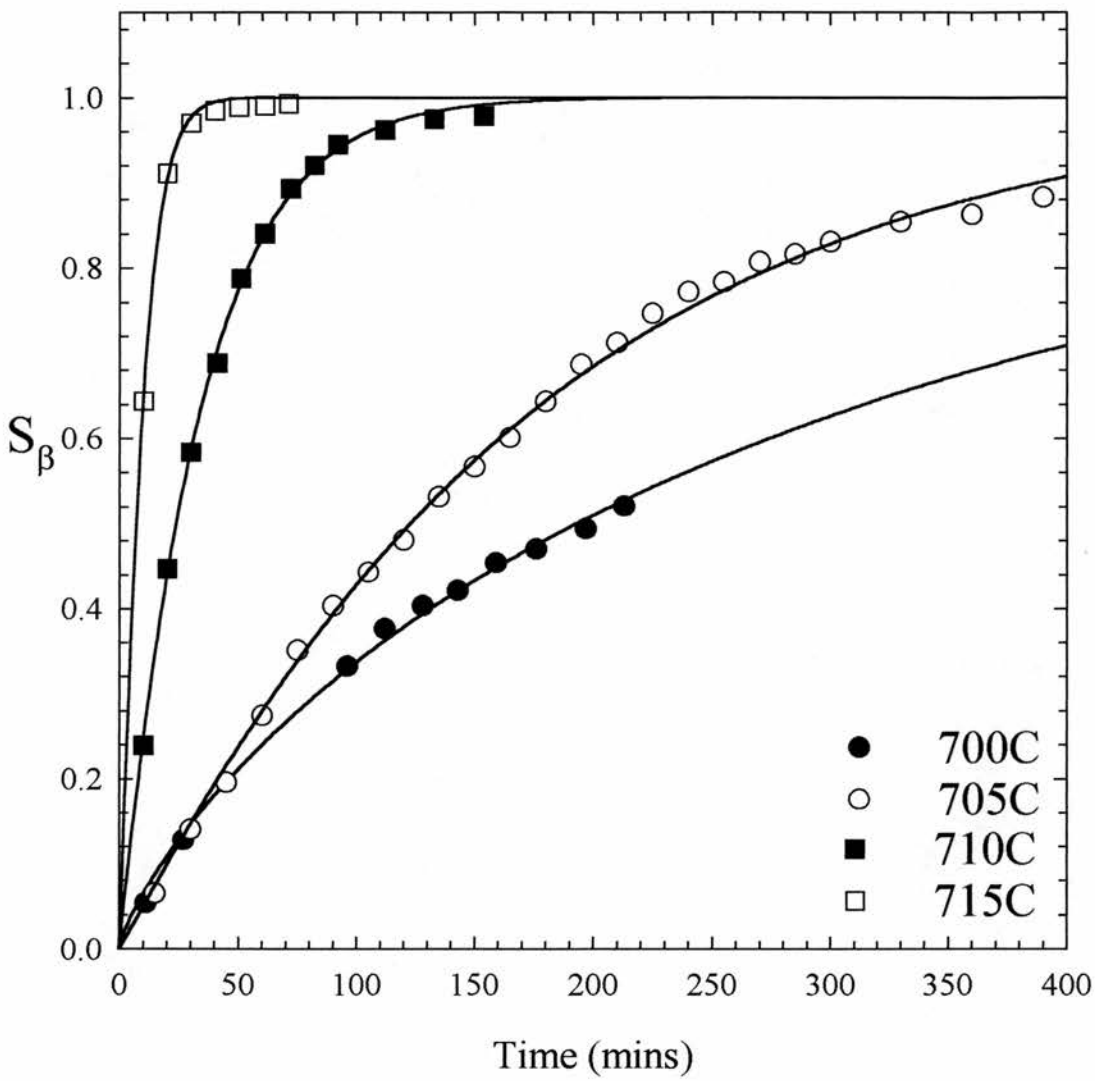

Figure 5.5

Measured time and temperature dependence of the β-Mn phase fraction S_β for the α to β Mn transition.

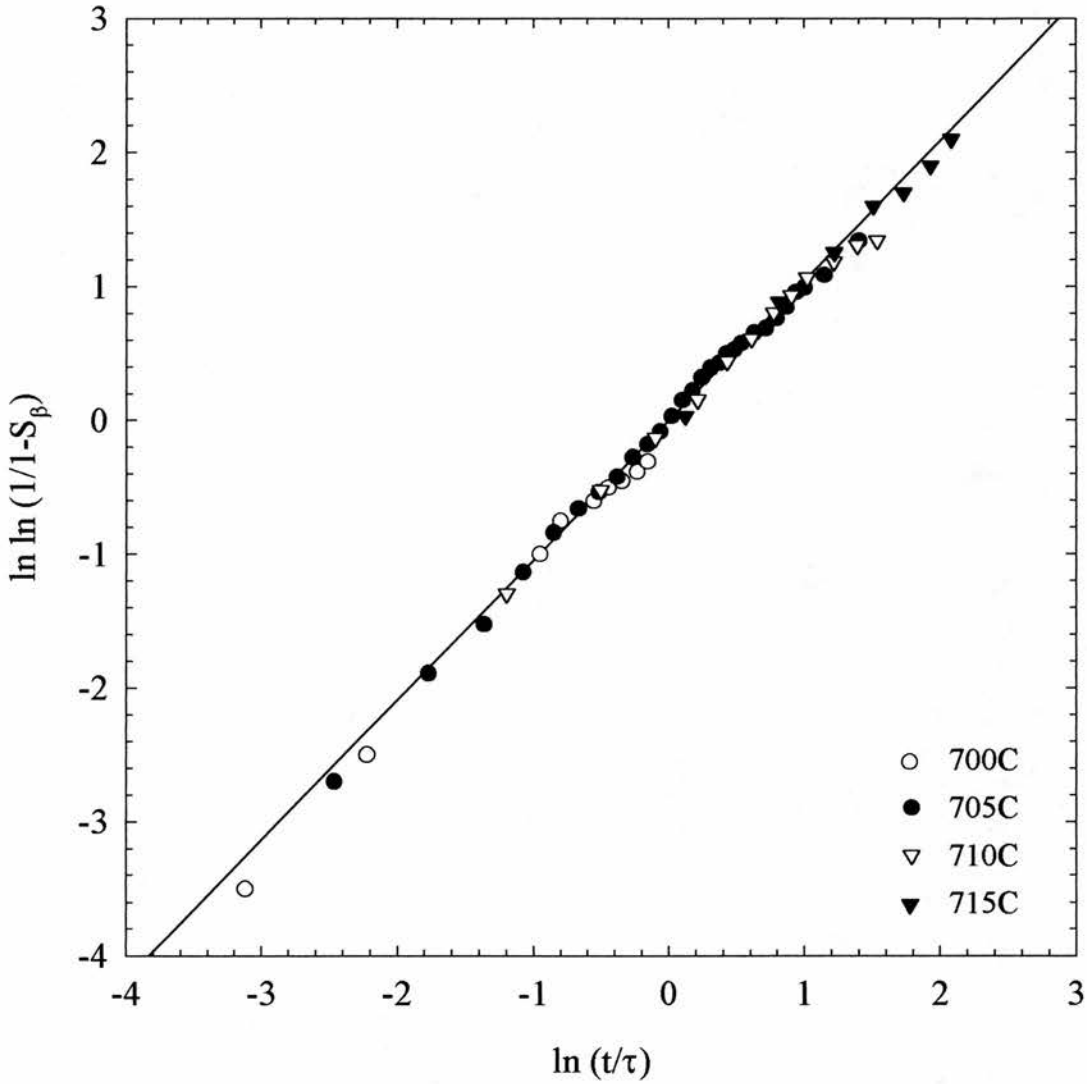

Figure 5.6

Graph of lnln(1/1-S_β) against ln(t/τ) demonstrating the scaling behaviour of the β-Mn phase fraction expressed in the form of a straight line of slope n. n is found to be 1.04 ± 0.02 for the α to β Mn phase transition.

Table 5.1 The time constant τ and exponent n for the α to β Mn phase transition at the temperatures shown, found by fitting the data shown in figure 5.5 to the AJM equation.

Temperature (C)	τ (minutes)	n
700 ± 0.5	310 ± 10	0.79 ± 0.03
705 ± 0.5	175 ± 2	1.05 ± 0.01
710 ± 0.5	34.0 ± 0.3	1.04 ± 0.02
715 ± 0.5	9.7 ± 0.2	1.17 ± 0.06

The form of the AJM equation implies that the α to β Mn isothermal transformation curves should scale with respect to time. This is demonstrated in figure 5.6 which shows the four isothermal transformation curves plotted in straight line form,

$$\ln\ln\left(\frac{1}{1-S_\beta}\right) = n\ln\left(\frac{t}{\tau}\right), \tag{5.11}$$

as a function of t/τ. The curves scale precisely with an average gradient of $n = 1.04 \pm 0.02$.

Figure 5.7 shows that the time constants measure for the α to β Mn phase transition are consistent with an Arrhenius process, of the form,

$$\ln(\tau) = E_a/k_BT + \ln(\tau_0), \tag{5.12}$$

where E_a is the activation energy of the transformation. E_a/k_B was found to be $(1.4 \pm 0.2)\times 10^5$ C.

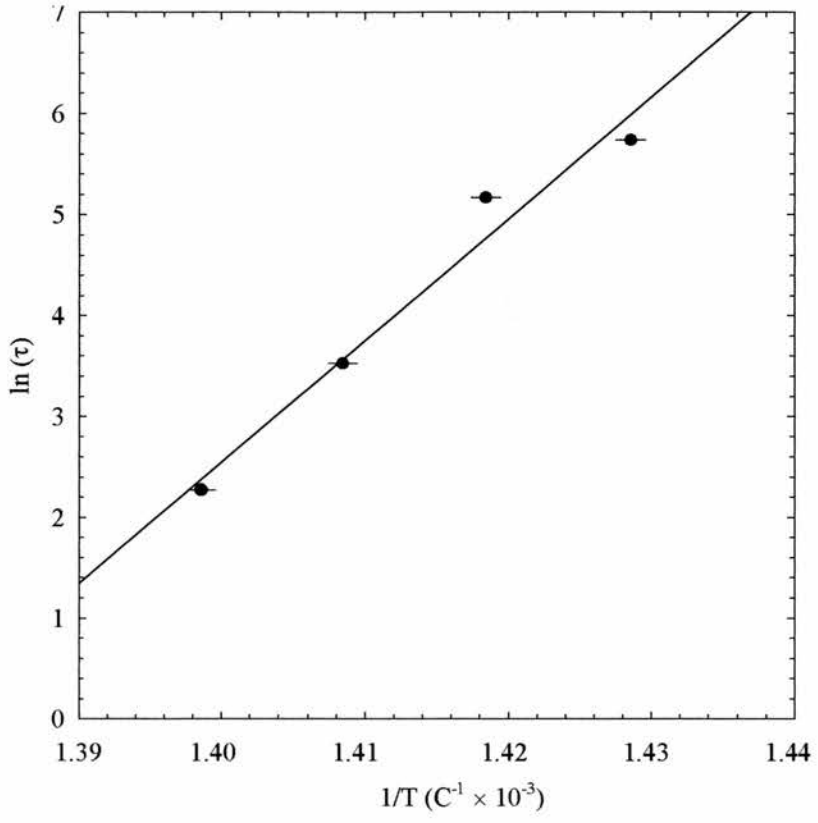

Figure 5.7

Arrhenius behaviour of the temperature dependence of the time constant τ plotted in terms of ln(τ) vs 1/T. The activation temperature was found to be (1.4 ± 0.2) × 10^5 C.

5.4.6 Discussion

The value of the exponent n = 1 found in this study implies that the α to β Mn phase transition is homogeneous throughout the sample. This is perhaps not surprising since the phase transformation is rather subtle, involving a very slight volume expansion with both phases displaying cubic symmetry as shown in figures 5.3 and 5.4. We might therefore expect that the free energy difference at the interface between the two phases is extremely small, leading to homogeneous nucleation of the β-Mn phase. The metastable β to α Mn phase transformation which occurs at ~230C has been shown by Husband and co-workers [11] to transform according to the AJM equation with an exponent of n = 4. This is thought to be due to the large drop in free energy from the local free energy minimum associated with the metastable β-Mn phase to the α-Mn free energy, leading to a large free energy barrier at the interface between the transformed

regions and nucleation centres. Similar behaviour has been observed in the α to β and β to α Sn transformations which have exponents of n = 2 and n = 5 respectively [12].

As can be seen from figure 5.4, the major peaks of α-Mn and β-Mn are very close in d-spacing. The transformation from a peak of index (4 2 0) in α-Mn to (2 2 1) in β-Mn corresponds to a subtle change of symmetry with the <1 0 0> planes of the α phase forming the <1 1 0> planes of the β phase. As a result, the room temperature lattice constants of α and β Mn (8.89Å and 6.32Å respectively) are such that,

$$a_\alpha \sim \sqrt{2}\, a_\beta. \qquad (5.13)$$

The change of symmetry is accompanied by an overall lattice expansion of $\Delta d/d = 4 \times 10^{-3}$.

5.4.7 Conclusions

We have investigated the transformation kinetics of the α to β Mn phase transformation using high resolution neutron powder diffraction.

The form of the observed isothermal α to β Mn transformation curves is well described by the Avrami-Johnson-Mehl (AJM) equation with an exponent n = 1, implying that the α to β Mn phase transition is homogeneous.

The α to β Mn phase transition involves a subtle change of symmetry with the <1 0 0> planes of the $I\bar{4}3m$ α-Mn phase forming the <1 1 0> planes of the $P4_132$ β-Mn phase, with an associated 0.4% linear expansion of the lattice.

While a net expansion of the lattice might be expected to result in a greater distance between neighbouring Mn atoms, and hence favour the formation of local magnetic moments (see section 2.4.3.1), analysis of the Mn-Mn near neighbour distances found in the current study and shown in table 5.2, reveals that β-Mn is a closer packed structure than α-Mn.

Table 5.2 α and β Mn near neighbour distances at 700C for each of the crystallographic sites shown.

Site	α-Mn NN distance (Å)	β-Mn NN distance (Å)
I	2.81	2.41
II	2.62	2.70
III	2.41	—
IV	2.41	—

In the antiferromagnetic state, α-Mn is thought to possess localised magnetic moments on site I, the most localised site in the matrix [13]. However, the Mn atoms are much more evenly distributed in the β-Mn structure with smaller Mn-Mn near neighbour distances than the site I near neighbour distance in α-Mn. The closer atomic packing in the β-Mn structure may therefore prevent moment localisation in the matrix. In addition, it is likely that frustration between the triangularly coordinated site II Mn atoms in the β-Mn structure will prevent long-range magnetic order.

5.5 Site Substitution in β-Mn Alloys

5.5.1 Introduction

The NMR studies of Kohara and Asayama [1] presented in chapter 1 show that a static magnetic ground state is often stabilised in dilute β-Mn alloys with transition metal and non-transition metal impurities.

Transition metal impurities are thought to occupy the non-magnetic site I in the β-Mn matrix, where they either donate 3d electrons to the band, or polarise the surrounding site II Mn spins (see chapter 1). Non-transition metal impurities are thought to preferentially occupy site II, where they may bring about magnetic order due to moment localisation through lattice expansion, or the removal of spin-configurational degeneracy brought about by possible geometrical frustration in the β-Mn lattice [1,14]. The evidence for site preference of impurities in the β-Mn lattice is however, mainly indirect (Mössbauer [2] and NMR [1,15]) and is still the subject of some debate.

We have carried out a comprehensive neutron diffraction study of the alloys, β-($Mn_{0.95}Sn_{0.05}$), β-($Mn_{0.98}In_{0.05}$), β-($Mn_{0.9}Fe_{0.1}$), β-($Mn_{0.9}Co_{0.1}$), and β-($Mn_{1-x}Al_x$) with x=0,0.03, 0.06, 0.08, 0.1, and 0.2, in order to determine their impurity site occupancies and lattice expansion properties. Determination of impurity site occupancy was facilitated by the large contrast exhibited between the Mn atoms and the impurity atoms, due to the negative scattering length of Mn. The measurements were performed using the LAD neutron diffractometer at the ISIS pulsed neutron facility, and were refined using the GSAS [10] suite of programs.

5.5.2 The Liquids and Amorphous Diffractometer (LAD)

The LAD diffractometer is optimised for high neutron flux and low resolution measurements of the structure factor S(Q) of liquid and amorphous materials. However, the backscattering detector on LAD at $2\theta = 148°$ and with a total flight path of L = 11.128m has a high enough resolution ($\Delta d/d = 6 \times 10^{-3}$) for powder diffraction measurements to be obtained. The incident neutron pulse is moderated by the same 100K methane moderator as HRPD.

5.5.3 Results

The measured diffraction patterns and Reitveld refinements of pure β-Mn, β-$Mn_{0.9}Co_{0.1}$ and β-$Mn_{0.8}Al_{0.2}$ are shown in figures 5.8, 5.9 and 5.10 respectively.

The relative peak intensities in figures 5.9 and 5.10 are significantly different to those observed in the pure β-Mn spectrum shown in figure 5.8, illustrating the effect of the high contrast in neutron scattering length between the Mn and impurity atoms. The fitting parameters obtained from Reitveld analysis of all the samples studied are presented in table 5.3. The occupation factors and site preferences found are presented in table 5.4.

Figure 5.11 shows the concentration dependence of the room temperature lattice constant for all samples studied. The concentration dependence of the near neighbour distances and lattice constants of the β-MnAl alloys studied in this investigation is shown in figure 5.12.

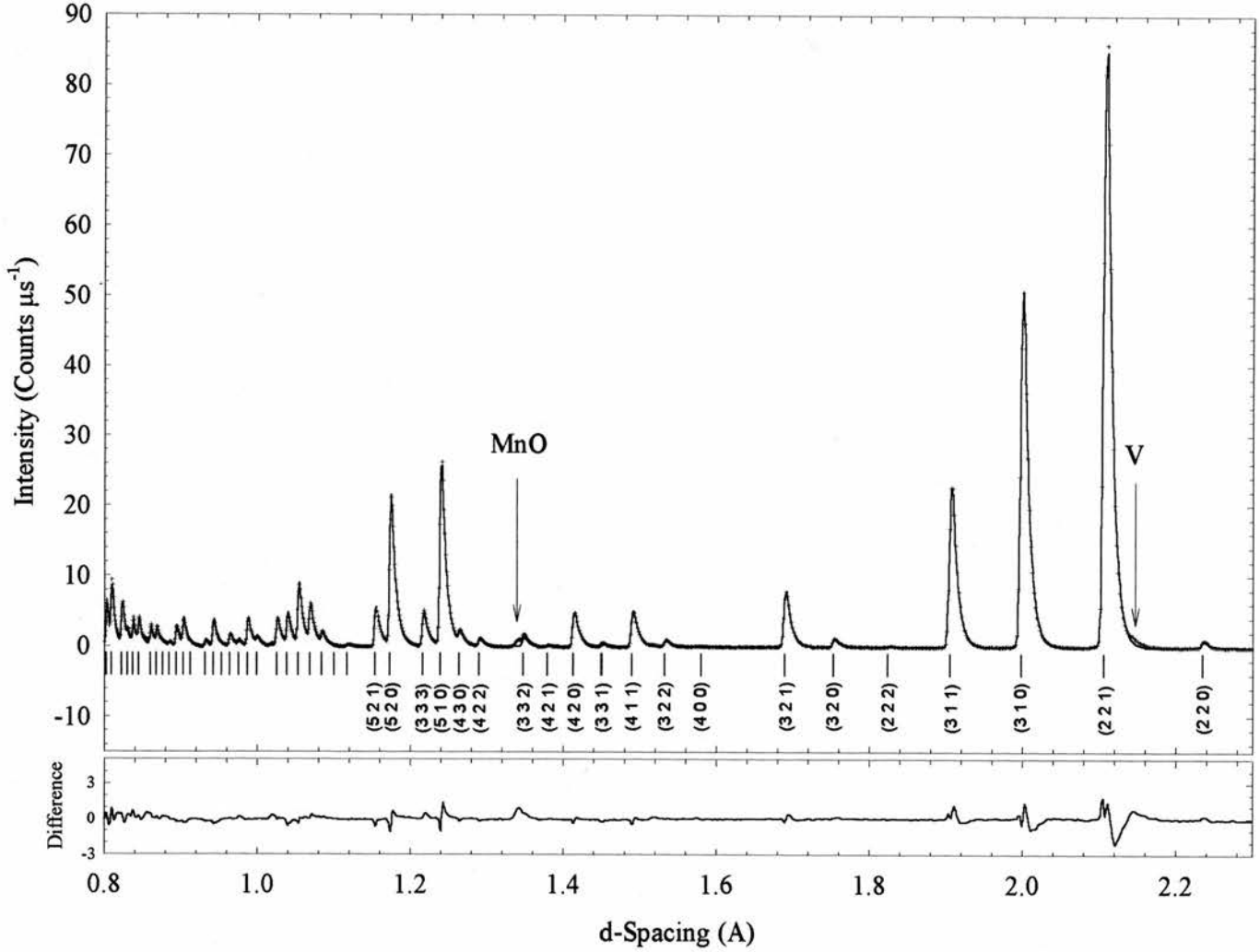

Figure 5.8

Powder diffraction pattern and GSAS Reitveld refinement of pure β-Mn at room temperature.

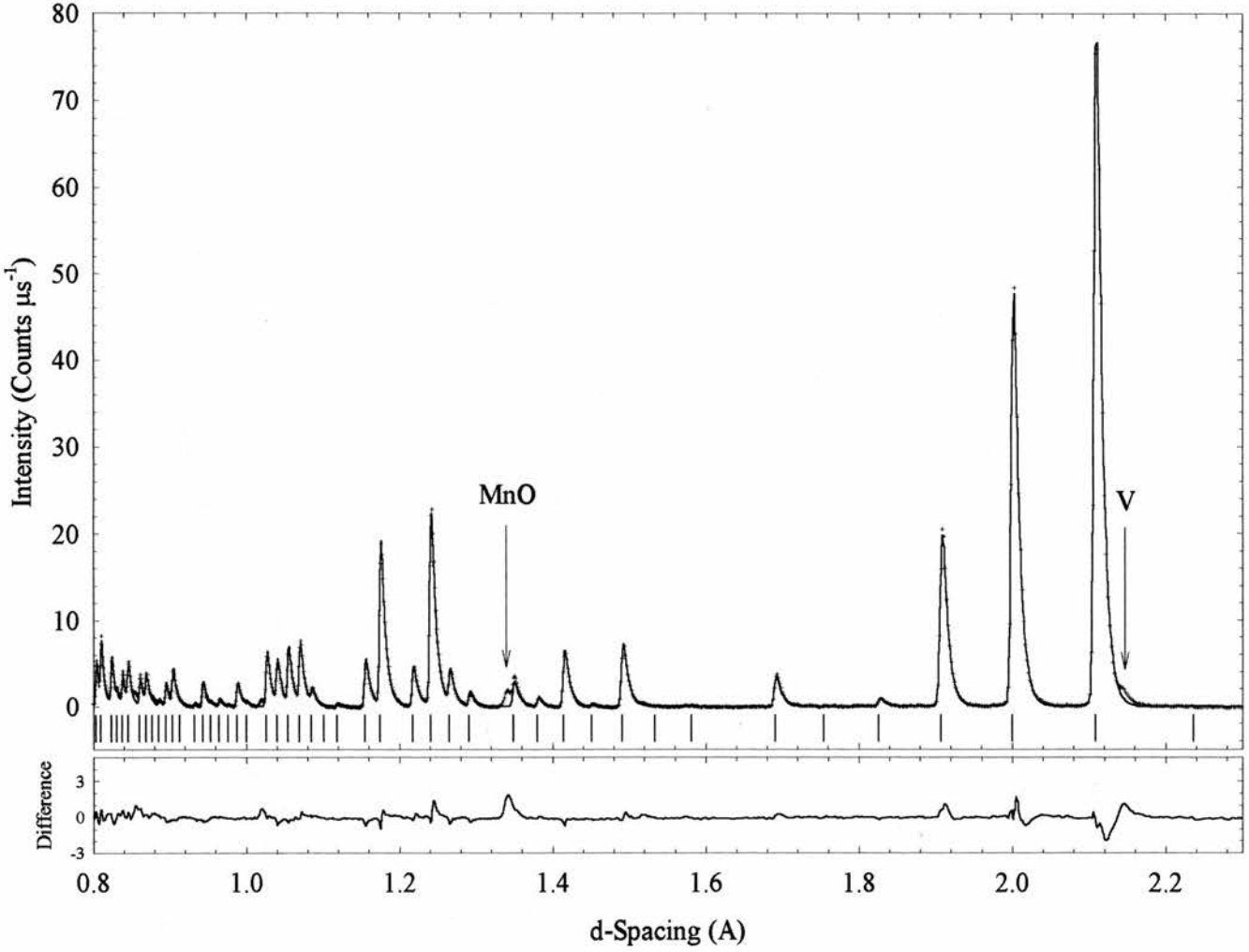

Figure 5.9

Powder diffraction pattern and GSAS Reitveld refinement of β-$Mn_{0.9}Co_{0.1}$ at room temperature.

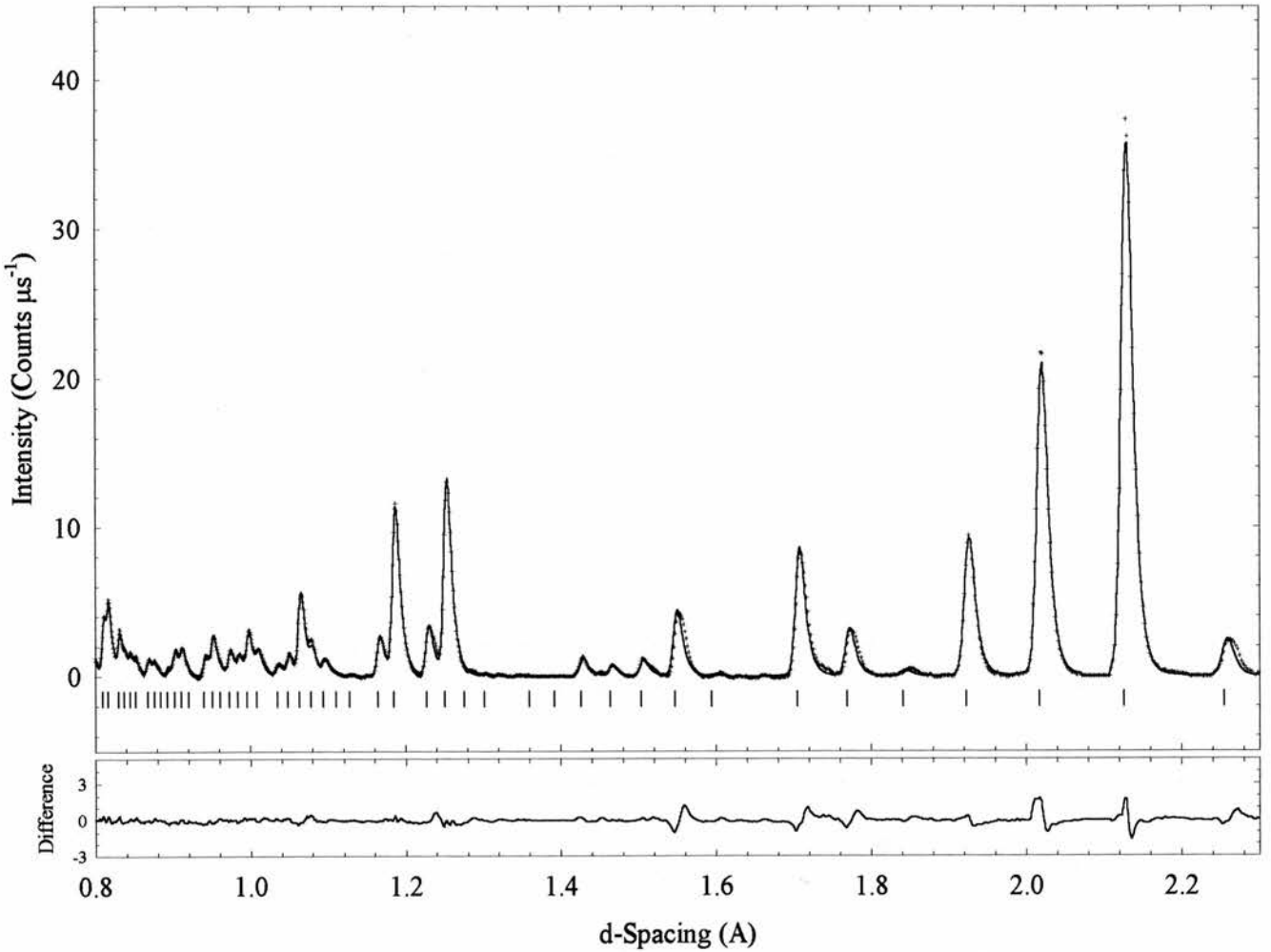

Figure 5.10

Powder diffraction pattern and GSAS Reitveld refinement of β-$Mn_{0.8}Al_{0.2}$ at room temperature.

Table 5.3 Parameters obtained by Reitveld refinement of the powder neutron diffraction patterns for the β-Mn alloys shown.

At% Impurity	*Lattice Constant (Å)*	*X*	*Y*	U_{iso} *site I*	U_{iso} *site II*	*Site I separation (Å)*	*Site II separation (Å)*	*R-Factor* R_{wp}
0at%	6.3203(2)	0.0632(2)	0.2019(1)	0.40(3)	0.64(3)	2.3669	2.6461	0.0395
3at% Al	6.3288(1)	0.0637(1)	0.2023(1)	0.39(3)	0.66(3)	2.3682	2.6521	0.0291
6at% Al	6.3350(2)	0.0641(1)	0.2025(1)	0.46(3)	0.72(4)	2.3685	2.6539	0.0419
8at% Al	6.3406(2)	0.0646(1)	0.2024(1)	0.42(3)	0.64(4)	2.3691	2.6576	0.0320
10at% Al	6.3500(3)	0.0651(1)	0.2026(1)	0.39(5)	0.65(5)	2.3704	2.6628	0.0407
20at% Al	6.3787(4)	0.0662(1)	0.2037(2)	0.26(5)	0.54(6)	2.3766	2.6816	0.0310
5at% In	6.4328(4)	0.0653(2)	0.2017(2)	0.25(5)	0.79(6)	2.4001	2.6919	0.0307
5at% Sn	6.4181(2)	0.0652(1)	0.2020(2)	0.29(4)	0.75(5)	2.3955	2.6876	0.0268
10at% Fe	6.3141(2)	0.0628(3)	0.2020(2)	0.29(4)	0.71(5)	2.3666	2.6441	0.0280
10at% Co	6.3259(2)	0.0632(2)	0.2024(1)	0.45(8)	0.76(4)	2.3692	2.6515	0.0315

Table 5.4 Site preferences and occupation factors of various impurity concentrations in β-Mn

at% Impurity	*Preferred Site*	*Occupation Factor*	*% Occupancy*
3at% Al	Site II	0.049(3)	99(1) %
6at% Al	Site II	0.060(4)	80(1) %
8at% Al	Site II	0.097(4)	86(1) %
10at% Al	Site II	0.122(5)	87(1) %
20at% Al	Site II	0.272(3)	91(1) %
5at% In	Site II	0.084(5)	100(1) %
5at% Sn	Site II	0.081(3)	99(1) %
10at% Fe	Site I	0.120(3)	74(1) %
10at% Co	Site I	0.235(5)	97(1) %

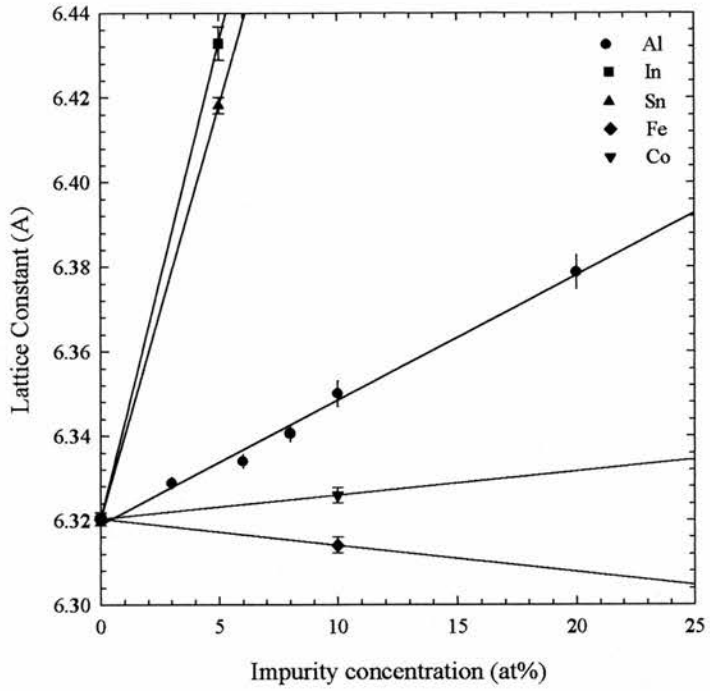

Figure 5.11

The impurity concentration dependence of the lattice constant in the β-Mn alloys studied in this investigation.

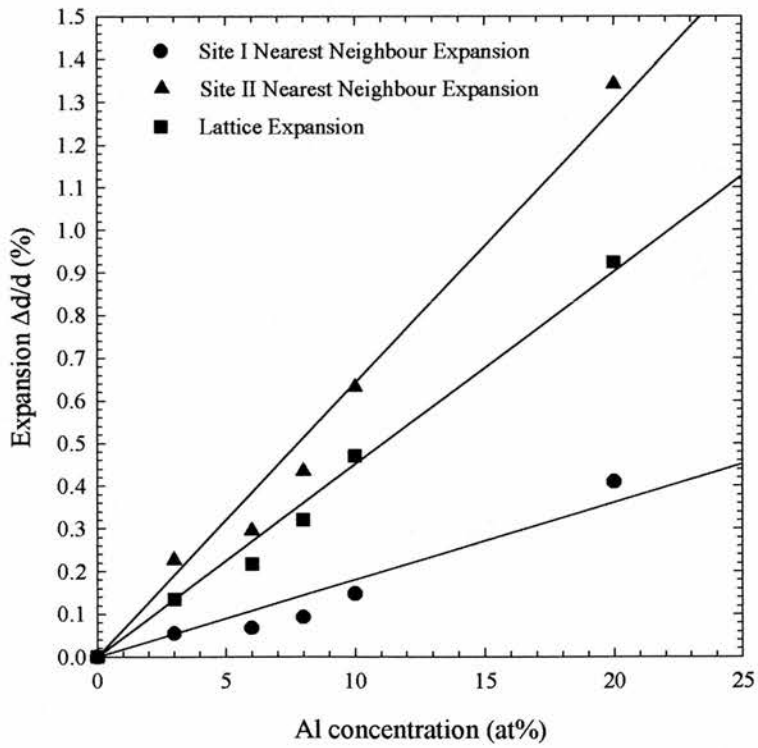

Figure 5.12

Expansion of the site I and site II near neighbour distance compared with the lattice expansion as a function of Al concentration in the β-MnAl alloys studied.

5.5.4 Conclusions

We have investigated the site preferences of various dilute impurities in β-Mn alloys.

- Our results show that the transition metal substituents Fe and Co preferentially occupy Site I in the β-Mn lattice, while the non-transition metal substituents occupy site II, thus confirming the previous Mössbauer [2] and NMR [15] studies.
- The substitution of non-transition metal Al, In and Sn into β-Mn causes expansion of the lattice (0.003 Å/at% Al, 0.020Å/at% Sn, and 0.023 Å/at% In), while substitution of the transition metals Fe and Co leaves the lattice constant almost unchanged.
- Moment localisation associated with site II Mn atoms in β-MnAl [14] may be associated with the Al concentration dependence of the site II near neighbour distance, which is found to increase at a higher rate than the lattice constant.

The observation that Al atoms strongly prefer site II in the β-Mn matrix is crucial to understanding the nature of the magnetic ground state in the β-MnAl alloys studied in this thesis. Since the site II Mn atoms have been shown to possess large magnetic moments [14,16] the substitution of non-magnetic Al atoms into the site II sublattice will introduce a magnetic defect in the matrix. This observation supports the suggestion of Nakamura et. al. [14] that Al substitution lifts the spin configurational degeneracy of the triangularly frustrated Mn atoms. Analysis of the static component of the β-MnAl magnetic ground state presented in chapter 7 will be greatly facilitated by the fact that both nuclear and magnetic disorder in β-MnAl resides solely on the site II sublattice.

5.6 References

[1] T Kohara and K Asayama, J. Phys. Soc. Japan **37** (1974) 401

[2] Y Nishihara, S Ogawa and S Waki, J. Phys. Soc. Japan **42** (1977) 845

[3] C G Windsor, *Pulsed Neutron Scattering* (Taylor and Francis 1981)

[4] P R Bevington, *Data Reduction and Error Analysis for the Physical Sciences*, (M^{c}Graw-Hill, 1969)

[5] S Ikeda and J M Carpenter, Nucl. Inst. Meth. **A235**, (1985) 553

[6] W A Johnson and R F Mehl, Trans. Am. Inst. Min. (Metall.) Engrs. **135** 416

[7] M Avrami, J. Chem. Phys. **7** (1939) 1103

[8] M Avrami, J. Chem. Phys. **8** (1940) 212

[9] M Avrami, J. Chem. Phys. **9** (1941) 177

[10] A C Larson and R B Von Dreele, *GSAS: General Structure Analysis System*, (Los Alamos National Laboratory Report LAUR 86-748, 1994)

[11] J N Husband, K L Mason and J W Christian, *unpublished work* (1959)

[12] M Iizumi, Physica **136B** (1986) 36

[13] P de Doncker et al, J de Physique **49** (1988) C8-81

[14] H Nakamura, K Yoshimoto, M Shiga, M Nishi and K Kakurai, J. Phys. Cond. Matter **9** (1997) 4701

[15] M Katayama, S Akimoto and K Asayama, J. Phys. Soc. Japan **42** (1977)97

[16] Y Kohori, Y Noguchi and T Kohara, J. Phys. Soc. Japan **62** (1993) 447

6 A Muon Spin Relaxation Study of β-MnAl

6.1 Introduction

From the description of the magnetic and physical properties of β-Mn presented in chapter 1, it is apparent that β-MnAl affords an ideal opportunity to investigate the processes of spin fluctuations, moment formation and frustration in a relatively simple, almost elemental, 3d transition metal system. Muon spin relaxation (μSR) has already proved a particularly powerful tool with which to study such phenomena, and previous studies have provided valuable insights into the nature of spin fluctuations in YMn_2, $Y(Mn_{1-x}Fe_x)_2$ and $Y(Mn_{1-x}Al_x)_2$ [1,2]. In this chapter, I shall present the results of a μSR study of the effects of Al substitution on the spin fluctuations and magnetic ground state of β-Mn.

6.2 Theory of Muon Spin Relaxation

6.2.1 The Properties of Positive Muons

Positive muons are unstable second generation leptons which decay with a lifetime of $\tau = 2.2$ μs into a positron, a μ-neutrino and a μ-antineutrino. The properties of the muon are summarised in table 6.1.

Table 6.1: The fundamental properties of the positive muon.

Mass	$208.6 \times m_e$
	$0.113 \times m_p$
Spin	$1/2\hbar$
Charge	$+e$
Magnetic Moment	$3.183\mu_N$
Gyromagnetic ratio $\gamma_\mu/2\pi$	135.5 MHz T^{-1}
Lifetime	2.197 μs

In the muon decay process, violation of parity causes the positrons to be emitted preferentially along the direction of the muon spin. The probability of detecting a positron as a function of the angle between the muon spin polarisation and the positron detector is given by,

$$P(\theta) = 1+a_0 \cos\theta, \qquad (6.1)$$

where a_0 is termed the initial muon asymmetry parameter which is determined by the kinetic energy of the muon, and varies between $-1/3$ and 1. The angular probability distributions $P(\theta)$ for $a_0 = 1/3$ and 1 are shown in figure 6.1.

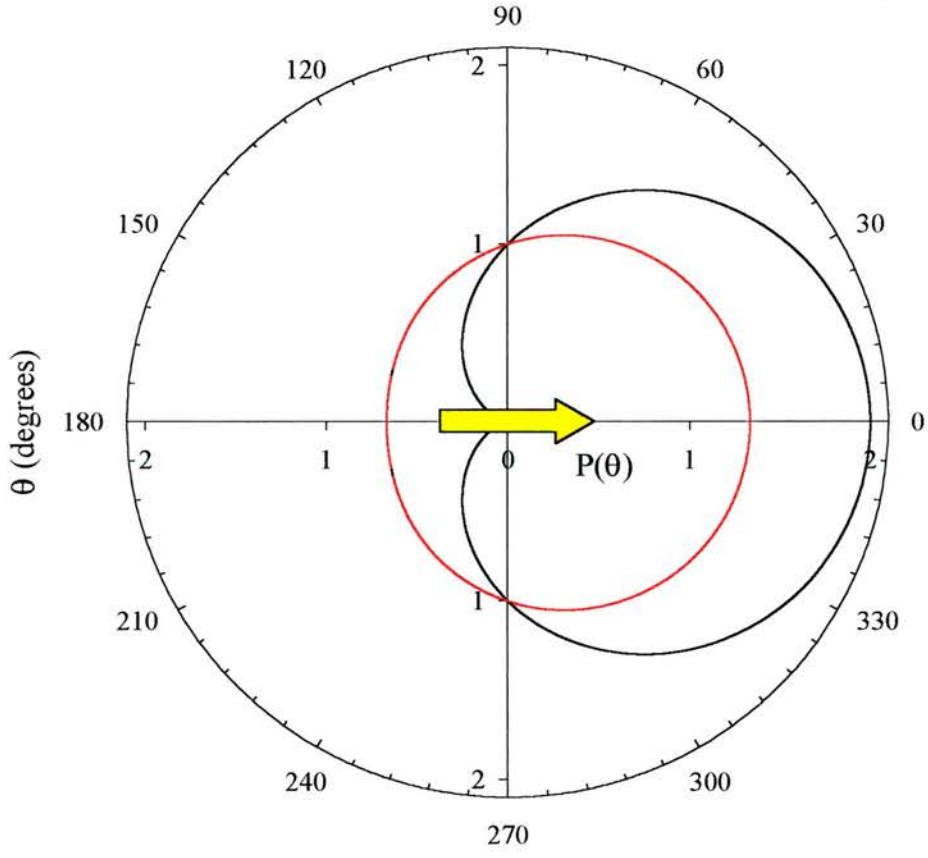

Figure 6.1

Polar plot of the angular probability distribution P(θ) for positron emission from positive muon decay. $a_0 = 1$ is shown in black and $a_0 = 1/3$ is shown in red.

6.2.2 The μSR Experiment

In a pulsed muon spin relaxation experiment, a pulse of muons which are spin polarised in their direction of motion is thermalised in the sample under investigation.

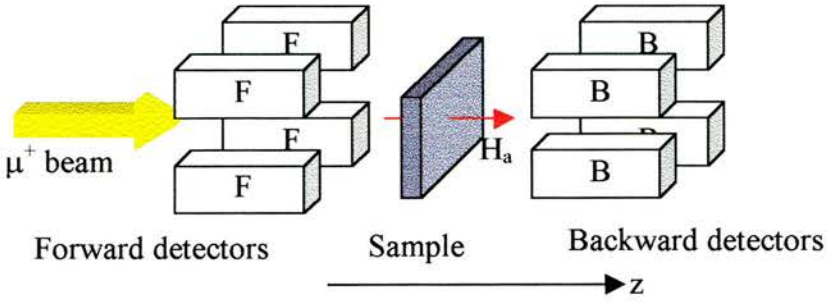

Figure 6.2

Schematic experimental arrangement for a muon spin relaxation (μSR) experiment. H_a shows the direction of the longitudinal field, which is turned off in a zero-field μSR experiment. The z-direction is defined by the direction of motion of the muons.

The angular distribution of positron decay products P(θ) leads to a spatial asymmetry in the number of positrons counted in detector bank arrays in the forward and back directions (see figure 6.2). The resulting positron count rates in the two detector banks are,

$$N_{F,B}(t) = N_{F,B}(0)\exp\left(-\frac{t}{\tau_\mu}\right)\left[1 \pm G_z(t)\right], \qquad (6.2)$$

where $G_z(t)$ is the longitudinal muon spin relaxation function.

$G_z(t)$ is extracted from the measured count rates by taking the ratio

$$R_z(t) = a_o G_z(t) = \frac{N_F(t) - \alpha N_B(t)}{N_F(t) + \alpha N_B(t)}, \qquad (6.3)$$

where α is a normalisation term which accounts for the relative efficiencies of the forward and backward detectors and the anisotropic absorption of positrons by the sample and surrounding ancillary equipment. α is determined for each sample by applying a field of 2mT perpendicular to the initial muon polarisation, in essence a *muon spin rotation* experiment. The muon spin polarisation precesses at the Larmor frequency, $\omega_L = \gamma_\mu B$, and thereby periodically intersects the forward and backward detector banks. Upon taking the ratio given by eq. (6.3) we expect the muon asymmetry plot to oscillate with frequency ω_L and to be modulated by a depolarisation envelope, $G_x(t)$.

$$R_x(t)=\frac{N_F(t)-\alpha N_B(t)}{N_F(t)+\alpha N_B(t)}=a_o G_x(t)\cos(\omega_L t), \qquad (6.4)$$

The value of α is assigned by inter-normalising the forward and backward detector banks until the measured asymmetry oscillates around zero. Figure 6.3 shows a typical uncorrected muon rotation spectrum of pure β-Mn in a transverse field of 2mT. The line is a least squares fit to the equation,

$$R_x(t) = a_0 G_x(t)\cos(\omega_L t) + a_{bg}\cos(\omega_L t) + k, \qquad (6.5)$$

where $R_x(t)$ is the measured spectrum, k is the offset, a_{bg} is a background asymmetry term arising from muons thermalised in the silver sample holder and $G_x(t)$ is a Gaussian decay function. The value of α is found by iteratively assigning values of α to eq. (6.4) until the measured value of k in eq (6.5) is equal to zero.

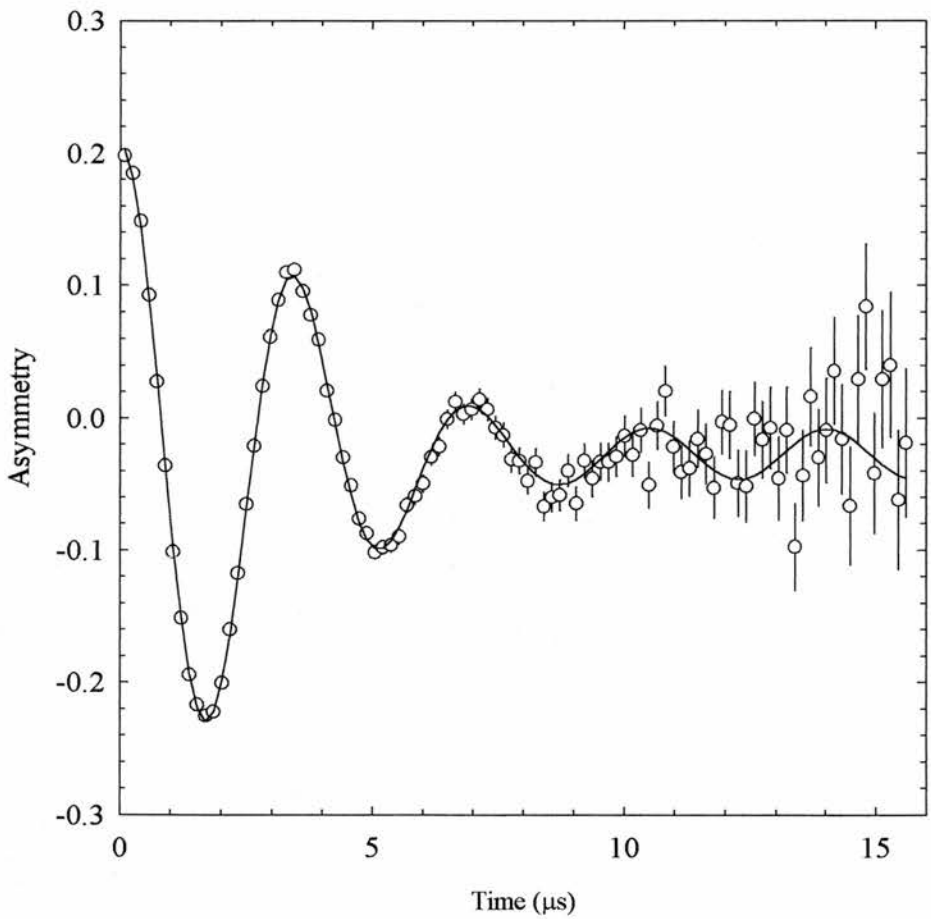

Figure 6.3

Muon spin rotation spectrum of pure β-Mn at 290K in a transverse magnetic field of 2mT obtained on the ARGUS spectrometer, used to obtain the calibration factor α. The solid line is a fit of eq. (6.5) to the data. α was found to be 1.132 for this measurement.

6.2.3 Dead Time Correction

After detecting a single positron, the detector becomes unable to register further events for a period τ_d known as the detector *dead time*. The measured positron count rate n_m is therefore less than the true count rate n_t. In the so-called non-paralysable model [3] positrons which hit the detector during the dead time will not extend the dead time further. The true number of counts N_t per detector in a time bin of width τ_b is $N_t = n_t\tau_b$. Similarly, $N_m = n_m\tau_b$ is the measured number of counts per detector. The number of counts which must be added to correct for detector dead time is $\Delta N = N_t - N_m$. Within the time bin τ_b the total dead time is $N_m\tau_d$ and therefore $\Delta N = n_t N_m \tau_b$. We can therefore write,

$$\begin{aligned} N_t - N_m &= n_t N_m \tau_b \\ &= N_t N_m \left(\frac{\tau_d}{\tau_b}\right) . \qquad (6.7) \\ \therefore \quad N_t &= \frac{N_m}{1 - N_m\left(\frac{\tau_d}{\tau_b}\right)} \end{aligned}$$

The true number of counts can be determined provided τ_d is known for each detector. To measure τ_d a measurement of the asymmetry of pure silver is performed.

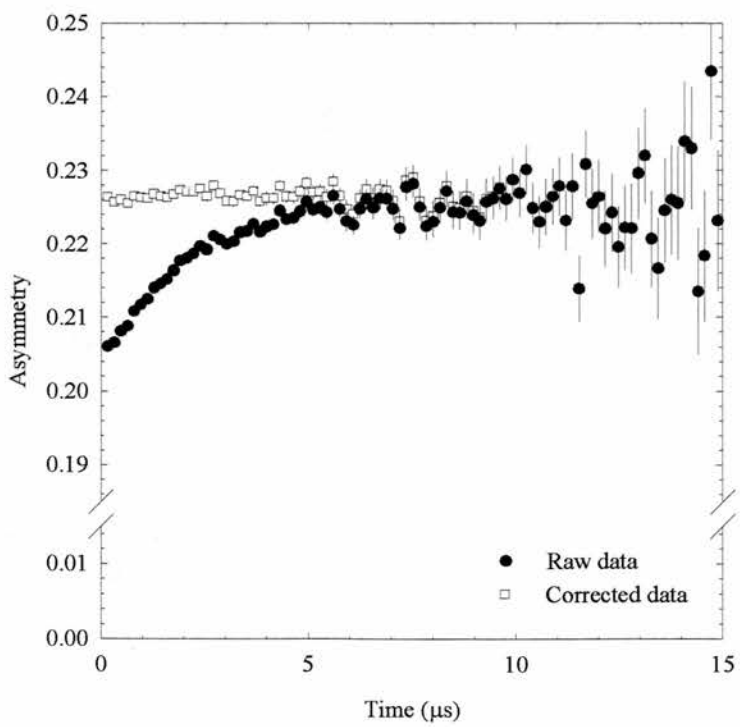

Figure 6.4

Longitudinal μSR spectrum of high purity silver before and after dead time correction.

Since silver does not depolarise the muon ensemble, $N_t = N_t(0)\exp(-t/\tau_\mu)$ from eq. (6.2). Substituting this expression into eq. (6.7) we obtain,

$$N_m \exp\left(-\frac{t}{\tau_\mu}\right) = -N_t(0)\left(\frac{\tau_d}{\tau_b}\right)N_m + N_t(0)\,. \qquad (6.8)$$

Therefore, plotting $N_m\exp(-t/\tau_\mu)$ against N_m one obtains a straight line of gradient, $m = -N_t(0)(\tau_d/\tau_b)$ from which τ_d may be calculated. Figure 6.4 shows both corrected and raw μSR spectra of high purity silver taken at room temperature. The fall off in the uncorrected spectrum at short times where the muon count rate is highest, is attributed to detector dead time effects. Detector dead times must be determined for each detector element individually before grouping into the forward and backward detector arrays and taking the asymmetry ratio of eq. (6.3).

6.2.4 Muon Depolarisation Functions

6.2.4.1 Muon Depolarisation Due to Static Dipolar Fields

For a concentrated randomly oriented system of magnetic moments, such as an array of nuclear dipoles which appear static on the timescale of the muon lifetime, the x, y and z components of the local magnetic field distribution may be represented by a Gaussian function. If the local random dipolar fields are also assumed to be isotropic, then each orthogonal field component is given by,

$$P(B_i) = \frac{1}{\Delta\sqrt{2\pi}}\exp\left(-\frac{B_i^{\,2}}{2\Delta^2}\right) \qquad (6.9)$$

where i= x, y, z and Δ is the Gaussian field distribution width. The second moment of the distribution is defined as,

$$M_2^{\,x,y,z} = \int_{-\infty}^{\infty} B_{x,y,z}^{\,2} P(B_{x,y,z})\,dB_{x,y,z}\,, \qquad (6.10)$$

so that for a Gaussian distribution where $P(B_{x,y,z})$ is given by eq. (6.9), the second moment is given by $M_2 = \Delta^2$.

If the muons are introduced into the sample at t = 0 with their spins aligned along the z-axis then the time evolution of the z-component of the muon spin m_z is given by,

$$m_z = \cos^2\theta + \sin^2\theta\cos(\gamma_\mu B t), \qquad (6.11)$$

where B is the magnitude of the field that a particular muon experiences and θ is the angle between B and the z-axis. The depolarisation function is given by the statistical average of m_z,

$$G_z(t) = \iiint m_z(t)P(B_x)P(B_y)P(B_z)dB_x dB_y dB_z \tag{6.12}$$

$$\therefore\ G^{GKT}{}_z(t) = \frac{1}{3} + \frac{2}{3}\left(1-\sigma^2t^2\right)e^{-\frac{\sigma^2t^2}{2}} \tag{6.13}$$

where the nuclear depolarisation rate, σ, is related to the second moment of the field distribution by,

$$\sigma^2 = \gamma_\mu{}^2\, M_2 = \gamma_\mu{}^2\, \Delta^2. \tag{6.14}$$

Eq. (6.13) is known as the *zero field static Gaussian Kubo-Toyabe function* [4].

In a longitudinal external magnetic field, B_i in eq. (6.9) where i = z, should be replaced by $B_z + B_{ext}$. Taking the average of eq. (6.12) then yields,

$$G^{GKT}{}_z(t,\omega_L) = 1 - \frac{2\sigma^2}{\omega_L{}^2}\left(1-\exp\left(-\frac{\sigma^2t^2}{2}\right)\cos\omega_L t\right) + \frac{2\sigma^4}{\omega_L{}^3}\int_0^t \exp\left(-\frac{\sigma^2\tau^2}{2}\right)\sin\omega_L\tau d\tau, \tag{6.15}$$

which is known as the *applied field static Gaussian Kubo-Toyabe function* [5]. As the longitudinal field is increased, the contribution to the muon depolarisation from the static dipoles, σ, is dominated by the contribution from the external field. In this way the application of an external magnetic field decouples the muon spin from the random internal fields, decreasing the time dependence of the depolarisation and restoring the asymmetry. Numerical solutions of eq. (6.15) have shown that in an applied longitudinal field $B_{ext} = 5\Delta$, which is typically around 3mT for a system of nuclear dipoles, the asymmetry is almost completely recovered.

If the system of static dipolar fields is sufficiently dilute, then one may assume a Lorentzian field distribution of the form,

$$P(B_i) = \frac{\gamma_\mu}{\pi}\frac{\Lambda}{(\Lambda^2 + \gamma_\mu{}^2 B_i{}^2)}, \tag{6.16}$$

where Λ is the Lorentzian field distribution width. Substituting this into eq. (6.12) gives,

$$G^{LKT}{}_z(t) = \frac{1}{3} + \frac{2}{3}(1-\Lambda t)e^{-\Lambda t}, \tag{6.17}$$

which is known as the *zero-field static Lorentzian Kubo-Toyabe function* [4].

6.2.4.2 Muon Diffusion in Static Spin Systems

The muon is assumed to jump between sites with a mean hopping frequency ν, within the strong collision model [6] which assumes that the muon experiences a sudden change in the value of the local field and that there is no correlation between the fields experienced by the muon before and after a jump. In this model, the evolution of the polarisation of a particular muon immediately following a jump is described by the static Kubo-Toyabe function [eq. (6.13)] with an initial amplitude determined by the muon polarisation vector immediately prior to the jump. The total muon polarisation at a time t is the superposition of the polarisation of each muon at that time. The probability that a muon has not experienced a jump is given by $e^{-\nu t}$, and therefore the contribution to the total polarisation from those muons which have not jumped is given by,

$$G^{(0)}{}_z(t) = G^{GKT}{}_z(t)e^{-\nu t}. \tag{6.18}$$

The probability that a muon has jumped once at time t` and thereafter has remained stationary is given by $e^{-\nu(t-t`)}$ and therefore its polarisation will be given by $(G^{GKT}{}_z(t`)\times e^{-\nu t`}) \times (G^{GKT}{}_z(t - t`)\times e^{-\nu(t-t`)})$. The total contribution to the muon polarisation from these muons is therefore [5],

$$G^{(1)}{}_z(t) = \nu\int_0^\infty G^{GKT}{}_z(t`)e^{-\nu t`}G^{GKT}{}_z(t-t`)e^{-\nu(t-t`)}dt`. \tag{6.19}$$

The higher order terms can be successively derived by the recurrence relation,

$$G^{(n)}{}_z(t) = \nu\int_0^t G^{(0)}{}_z(t`)G^{(n-1)}{}_z(t-t`)dt`, \tag{6.20}$$

and therefore the total relaxation function given by the sum of eq. (6.20) between $n = 0$ and $n = \infty$, $G^{DKT}{}_z(t) = \sum_n G^{(n)}{}_z(t)$, can be written as,

$$G^{DKT}{}_z(t) = G^{(0)}{}_z(t) + \nu\int_o^y G^{DKT}{}_z(t-t`)G^{(0)}{}_z(t`)dt`, \tag{6.21}$$

and is known as the *dynamic Kubo-Toyabe function*.

Eq. (6.21) can be solved by taking the Laplace transform to obtain $G^{DKT}{}_z(\omega)$, and using a numerical algorithm to take the inverse Laplace transform giving the time domain

depolarisation function. Alternatively eq.(6.21) can be solved by numerical methods directly. However, since numerical calculation of $G^{DKT}{}_z(t)$ requires considerable time and computing power, $G^{DKT}{}_z(t)$ may be tabulated and fitted to the experimental data using a linear interpolation routine [3].

An analytical expression for the dynamic Kubo-Toyabe has been derived [7] by applying a perturbation expansion [8] to the strong collision model. The expansion of (6.21) is performed on a time scale of $1/\nu$ and a field scale of σ, and is therefore expected to hold for $\sigma/\nu < 1$. The analytical approximation in zero longitudinal field is,

$$G^{DKT}{}_z(t) = \exp\left(\frac{2\sigma^2}{\nu^2}\left[e^{-\nu t} - 1 + \nu t\right]\right). \qquad (6.22)$$

This function is compared to a numerical solution of eq. (6.21) in figure 6.5 as a function of the dimensionless parameters $R = \nu/\sigma$ and $T = \sigma t$.

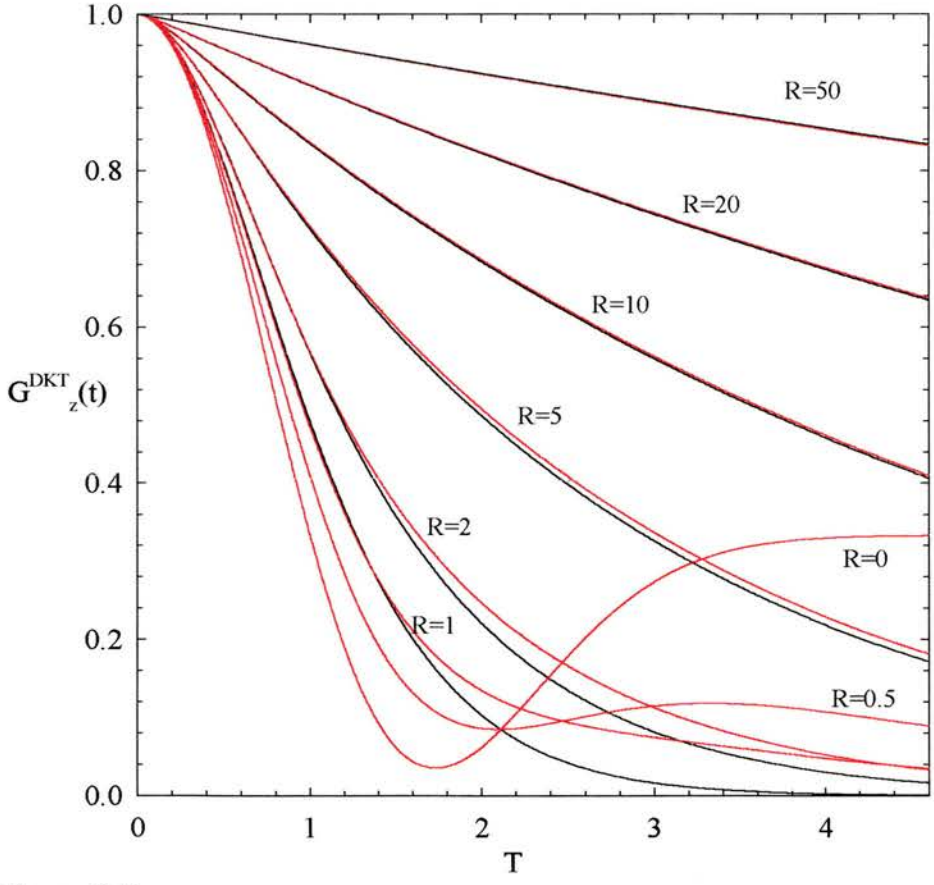

Figure 6.5

The dynamic Kubo-Toyabe function plotted as a function of the dimensionless parameters, $T=\sigma t$ and $R=\nu/\sigma$. The numerical calculation of eq (6.21) is shown in red and the analytical solution of eq. (6.22) in black. The analytical formula is shown to be a good approximation of $G^{DKT}{}_z(t)$ for $R > 1$.

6.2.4.3 Muon Depolarisation from Dynamic Spin Systems

If the magnetic field at the muon site is time dependent, the muon randomly samples many local fields, weighted by their probability distribution. In this way the muon will see a time average of the total field distribution, thereby effectively reducing the total width of the distribution. This is the familiar motional narrowing phenomenon.

Motional narrowing is seen clearly in the behaviour of the dynamic Kubo-Toyabe function, in which the effective depolarisation of the muons decreases as the muon hopping rate ν increases. Motional narrowing of the field distribution at the muon site is also caused by fluctuating atomic spins surrounding a static muon. Making a comparison between electronic and nuclear field widths Δ_a and Δ_n, we would expect Δ_a to be several orders of magnitude larger than Δ_n since $\mu_N \sim 10^{-3} \times \mu_B$. Despite this, for a wide range of atomic spin fluctuation rates ($10^8 Hz < \nu < 10^{13} Hz$) the parameter $R = \nu/\sigma$ is in the fast fluctuation limit ($R > 20$), and eq.(6.22) reduces to,

$$G_z(t) = \exp\left(-\frac{2\sigma^2 t}{\nu}\right), \tag{6.23}$$

indicating that the muon depolarisation is well described by an exponential form [9,7]. Unlike the case of a diffusing muon however, one cannot assume that the modulation of the field is sudden and uncorrelated in dynamic spin systems. The field modulation is more appropriately described by the autocorrelation function,

$$q_B(t) = \frac{\langle \mathbf{B}(0).\mathbf{B}(t) \rangle}{\langle \mathbf{B}(0)^2 \rangle}, \tag{6.24}$$

where the brackets denote statistical averages. In a conventional paramagnet for which there is no spin-spin correlation and a unique spin relaxation time at a particular temperature (see section 2.5 3), the spin autocorrelation function is given by a simple exponential,

$$q_s(t) = \exp(-\nu t), \tag{6.25}$$

where ν is the inverse of the spin relaxation time. The field autocorrelation function $q_B(t)$ is also expected to follow this form. Despite the fact that the strong-collision model can no longer be assumed, muon depolarisation is usually taken to be exponential in form. This is justified by the fact that Kubo and Toyabe originally assumed an exponential field autocorrelation of the form given by eq. (6.25) in the derivation of the

dynamic Kubo-Toyabe function, from which they obtained a depolarisation function which is not significantly different from that obtained using the strong collision model [10]. If one then assumes the spin autocorrelation function given by eq. (6.25), the muon depolarisation function due to fluctuating atomic spins in the fast fluctuation limit is given by,

$$G_z(t) = \exp(-\lambda t), \tag{6.26}$$

where λ is the atomic contribution to the muon depolarisation rate. This is related to the atomic field distribution width Δ and the characteristic spin fluctuation time τ_c by,

$$\lambda = \frac{\gamma_\mu{}^2 \Delta^2 \tau_c}{(1-\omega_0{}^2 \tau_c{}^2)} \tag{6.27}$$

where $\omega_0 = \gamma_\mu B_Z$, and B_Z is the applied longitudinal field. It follows that in zero applied field or in the limit of motional narrowing where $\omega_0{}^2\tau_c{}^2 << 1$, eq.(6.27) becomes,

$$\lambda = \gamma_\mu{}^2 \Delta^2 \tau_c . \tag{6.28}$$

Referring to eqs. (6.14) and (6.28), eq.(6.26) reduces to the expression given in eq. (6.23) where the fluctuation rate $\nu = 1/\tau_c$.

6.2.4.4 Muon Depolarisation from Spin Glasses

Muon depolarisation in conventional dilute spin glasses such as $Au_{0.99}Fe_{0.01}$ and $Cu_{0.97}Mn_{0.03}$ has been described by Uemura and co-workers [10,11]. In Uemura's model, it is assumed that fluctuation of magnetic impurity moments in dilute spin glasses leads to a time modulated field at the muon site. The dynamic range of this field modulation will depend on the proximity of the muon to its neighbouring spins, as illustrated in figure 6.6.

In Uemura's treatment, the dynamic variable range of the local fields at each muon site is approximated by a Gaussian distribution of width $\Delta = \sigma/\gamma_\mu$,

$$P^G(B_i) = \frac{\gamma_\mu}{\sigma\sqrt{2\pi}} \exp\left[-\frac{\gamma_\mu{}^2 B_i{}^2}{2\sigma^2}\right], \; i = x, y, z, \tag{6.29}$$

The probability of choosing a muon at a site of width σ is calculated to be,

$$\rho(\Delta) = \sqrt{\frac{2}{\pi}} \frac{a}{\sigma^2} \exp\left[-\frac{a}{2\sigma^2}\right], \tag{6.30}$$

so that the total field distribution obtained by summing over all muon sites weighted by their probabilities, is a Lorentzian distribution of width a/γ_μ given by,

$$P^L(B_i) = \int_0^\infty P^G(B_i)\rho(\sigma)d\sigma\,, \tag{6.31}$$

where the L superscript indicates a Lorentzian distribution.

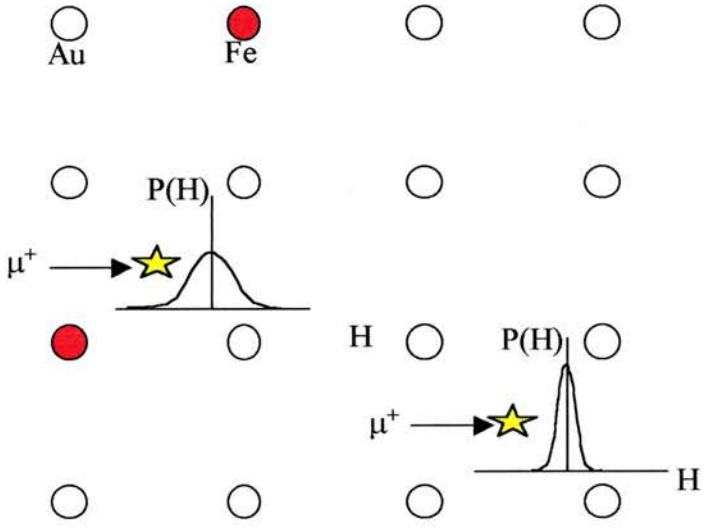

Figure 6.6

Schematic view of the different dynamic ranges of fields available at different muon sites in a dilute spin-glass. The fluctuation of the Fe moments causes a wider range of local fields available at muon sites closer to the magnetic atoms (taken from [11]).

If we now assume that we are in the fast fluctuation limit so that the muon depolarisation at each site of width σ is given by eq. (6.23), the total dynamic spin glass muon depolarisation function is given by,

$$\begin{aligned} G^{SG}{}_z(t) &= \int_0^\infty G_z(t,\sigma,\nu)\rho(\sigma)d\sigma \\ &= \exp\left[-\left(\frac{4a^2t}{\nu}\right)^{1/2}\right] \end{aligned} \tag{6.32}$$

This simple "root exponential" function has been shown to account for the observed zero-field muon response in several dilute spin systems [11] and recently in the dilute superparamagnetic cluster system $Cu_{0.98}Co_{0.02}$ [12].

In concentrated spin glasses every muon site will be situated next to a magnetic ion. Therefore it is expected that there will not be a wide variation of Gaussian field distributions between the muon sites. If one then assumes a spin autocorrelation function given by eq. (6.25) implying a unique spin relaxation time $\tau_c = 1/\nu$ at each temperature, one obtains a muon depolarisation function which is close to exponential in form. However, as was shown in section 2.5.3, the spin autocorrelation function in concentrated spin glasses was found to follow so-called "stretched exponential" or Kohlrausch relaxation given by eq. (2.65) [13],

$$q(t) = ct^{-x} \exp[-(t/\tau_c)^{\beta}], \tag{6.33}$$

with the stretched exponential exponent β having a value of around 1/3 at T_g rising towards the simple exponential value $\beta = 1$ at a temperature of around $4T_g$. It has been shown by Campbell and co-workers [14] that the form of the stretched exponential autocorrelation function and the muon depolarisation function are extremely similar, though not identical, to each other. For instance, if we assume a stretched exponential muon depolarisation function of the form,

$$G_z(t) = \exp\left[-(\lambda t)^{\beta}\right], \tag{6.34}$$

with $\beta = ½$, we can obtain the implied distribution of muon depolarisation rates λ_i proportional to the relaxation times τ_i, via an analytic Laplace transform, giving

$$P(\lambda_i) = \left[\frac{\lambda^2}{2\left(\pi\lambda_i^{\,3}\right)^{1/2}}\right] \exp\left(-\frac{\lambda^4}{4\lambda_i}\right). \tag{6.35}$$

If we further assume that the depolarisation of each muon is due to a local spin with a relaxation time τ_i, then the spin autocorrelation function will be given by,

$$q(t) = \int_0^{\infty} P(\lambda_i) \exp\left(-\frac{t}{\alpha\lambda_i}\right) d\lambda_i \,, \tag{6.36}$$

where $\tau_i = \alpha\lambda_i$. This is calculated to be,

$$q(t) = \left(1 + \frac{4t}{\alpha\lambda^4}\right)^{-1/2}. \tag{6.37}$$

If the calculated q(t) is compared with the assumed form of $G_z(t)$ it is found that the two curves are quite similar and that they correspond to very similar relaxation times. Numerical integrations of eq.(6.34) with β=1/3 and 2/3 performed by Campbell and co-workers have confirmed the result obtained analytically for $\beta = 1/2$. A comparison of

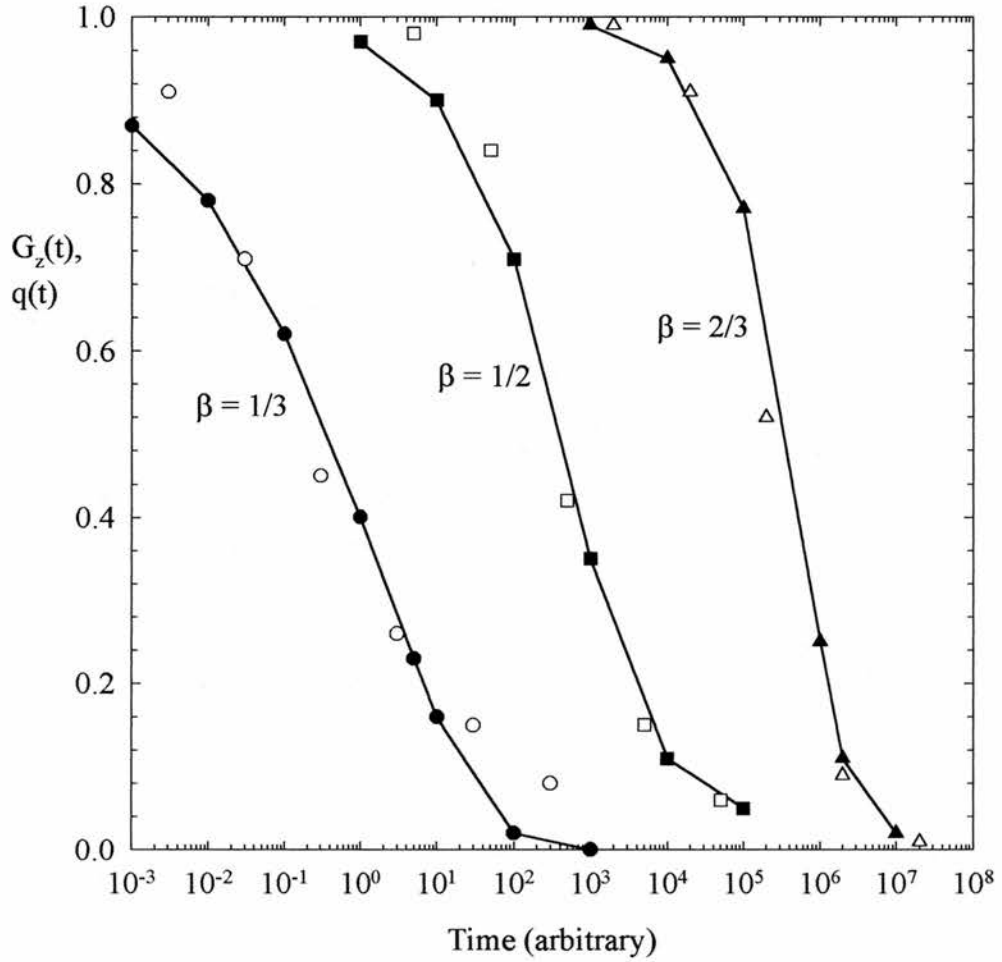

Figure 6.7

The comparison of the stretched exponential $G_z(t)$ shown in solid symbols, and the spin autocorrelation function (open symbols) calculated analytically for $\beta=1/2$ and numerically otherwise, presented by Campbell et. al. [14]. The curves have been arbitrarily shifted along the time axis as only their relative shapes are important.

the stretched exponential depolarisation function and the autocorrelation function calculated by Campbell et. al. is shown in figure 6.7.

The stretched exponential muon depolarisation function has been observed in many concentrated spin glass systems, such as $Ag_{0.9}Mn_{0.1}$ [14] and $Y(Mn_{0.9}Al_{0.1})_2$ [1,2]. However, the observation of stretched exponential muon depolarisation, while being consistent with concentrated spin glass spin dynamics, cannot be relied upon to show that the system under investigation is a spin glass. Stretched exponential muon depolarisation has recently been observed by Hillier et. al. [15] in long-range antiferromagnetically ordered $RENi_2B_2C$ compounds with RE = Er and Tb. This behaviour is thought to be due to a distribution of local relaxation times associated with rare-earth single ion anisotropy in these systems.

6.3 Experimental

6.3.1 The EMU and ARGUS Muon Spectrometers

Our muon spin relaxation measurements were carried out on the EMU and ARGUS spectrometers at the ISIS pulsed muon and neutron facility at the UK's Rutherford Appleton Laboratory. ISIS produces high intensity pulses of spin polarised muons of approximately 70ns FWHM at a repetition rate of 50Hz. Diagrams of the ARGUS and EMU spectrometers are shown in figures 6.8, and 6.9.

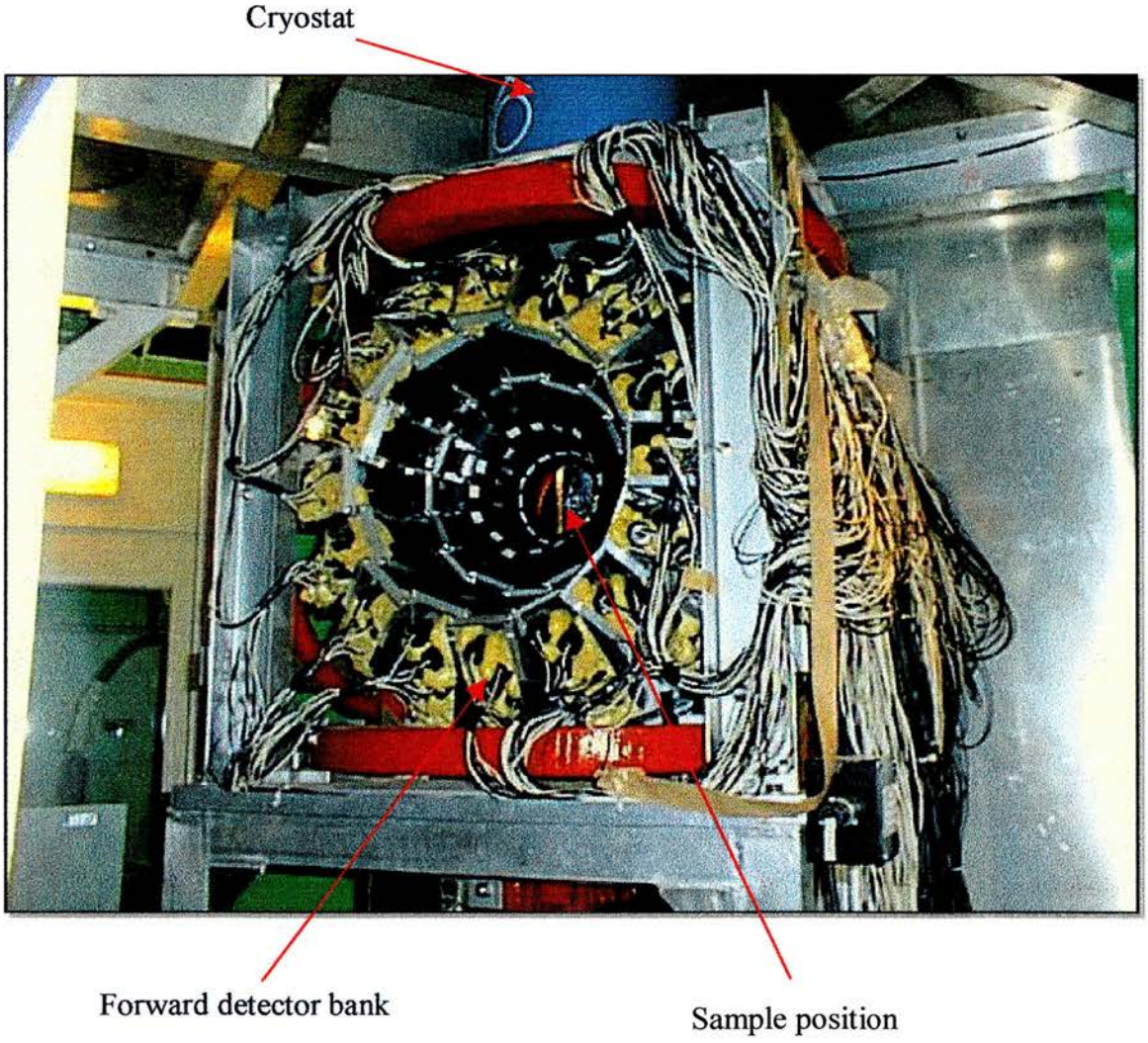

Figure 6.8

The ARGUS muon spectrometer located on the RIKEN-RAL muon facility at the Rutherford Appleton Laboratory. The forward and backward detector banks are each made up of 128 separate muon detectors.

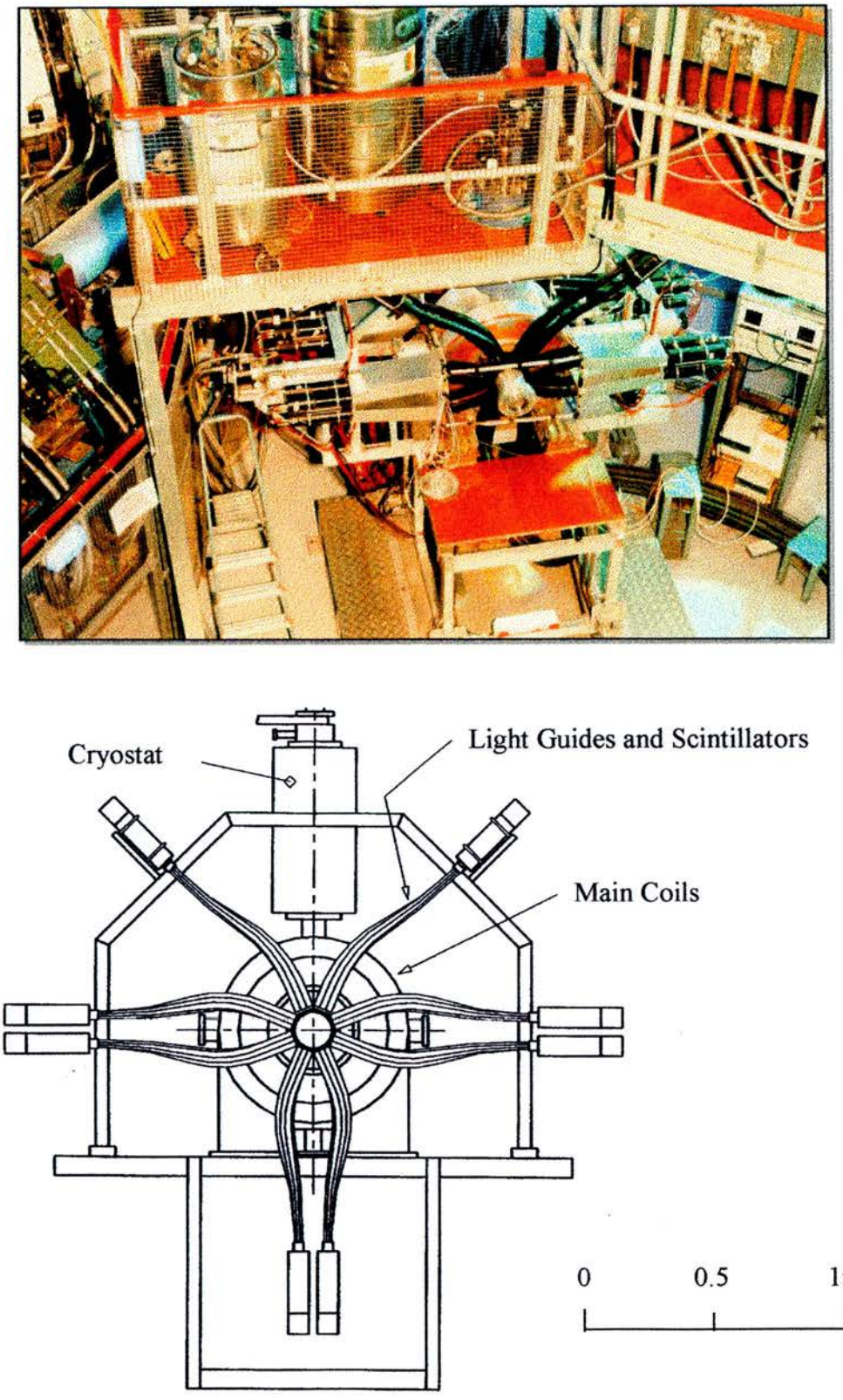

Figure 6.9

The EMU muon spectrometer located on the European Surface Muon facility at the Rutherford Appleton Laboratory. The forward and backward detector banks each consist of 16 muon detectors.

The forward and backward muon detector banks on the ARGUS and EMU spectrometers consist of a 128 and 32 positron scintillator counters respectively. The photons emitted when a positron is captured by a scintillator travels along a Plexiglas light guide to a photomultiplier tube where it is amplified and subsequently transmitted to the data acquisition electronics. The data for each scintillator is stored in the form of a time histogram with time bin widths of 16ns. The muon asymmetry spectrum is obtained by grouping the individual detectors into the forward and backward detector banks and taking the asymmetry ratio given in eq. (6.3). The EMU and ARGUS muon spectrometers are both optimised to work in longitudinal geometry with longitudinal fields of up to 0.4T and 0.35T available respectively. A set of 3 orthogonal Helmholtz coils at the sample position is used to cancel the Earth's magnetic field to within a few μT for precise zero-field μSR experiments.

The principal advantage of the pulsed μSR technique is that the intrinsic beam-borne background is extremely small, allowing reliable data to be collected to several muon lifetimes. Consequently even small muon depolarisation rates can be measured with some accuracy. However, the finite muon pulse width imposes constraints on the upper limit of the muon spin relaxation rates that can be extracted from the data. In particular the experimental convolution of the finite pulse width with the relaxation function precludes the observation of both high relaxation rates and coherent muon precession in transverse (internal or applied) fields exceeding 50mT. The onset of magnetic order is therefore often signalled by an apparent decrease of the initial asymmetry to one third of its high temperature value.

6.3.2 Background determination

The powdered β-$Mn_{1-x}Al_x$ alloys were mounted as disk shaped samples, 30mm in diameter and 2mm thick on silver sample holders. A gas flow (Oxford Instruments) cryostat enabled measurements to be made over the temperature range from 1.5K to 300K. The time independent background asymmetry arising from those muons in the beam penumbra which localise in the sample holder was determined by mounting Fe_2O_3 (haematite) at the sample position and performing a transverse field measurement at ambient temperature. Those muons implanted into the silver sample holder experience

negligible depolarisation and rotate at the Larmor frequency of 1.7MHz appropriate to a 2mT transverse field. Randomly oriented antiferromagnetic domains will immediately depolarise muons localising in the haematite by a factor of 2/3, representing the component of the muon polarisation transverse to the domain magnetisation. The remaining 1/3 component of the muon polarisation parallel to the domain magnetisation is lightly damped due to the presence of water in the haematite. The resulting asymmetry plot is shown in figure 6.10, where the solid line is a least squares fit of the data to the equation,

$$A(t) = a_{bg}\cos(2\pi\gamma_{\mu}Bt)\exp(-\lambda_{Ag}t) + a_{H}\exp(-\lambda_{H}t), \qquad (6.38)$$

where, a_{bg} is the background asymmetry, B is the applied transverse field, λ_{Ag} is the small depolarisation rate of muons thermalised in the silver sample holder, a_H is the 1/3 asymmetry component of the muons thermalised in the haematite and λ_H is the depolarisation rate of the 1/3 component. Background asymmetries were found to be of the order of $a_{bg} = 0.045$ on ARGUS and $a_{bg} = 0.035$ on EMU.

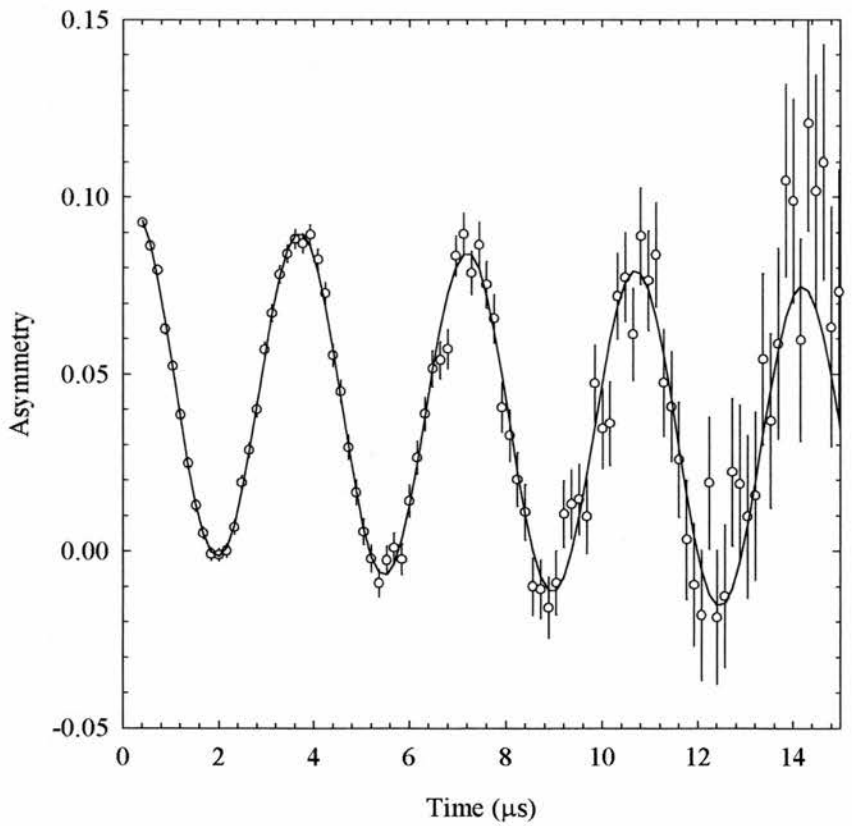

Figure 6.10

Transverse μSR spectra of haematite taken at ambient temperature on the ARGUS spectrometer, used to determine the background contribution to the total muon asymmetry due to muons implanted into the silver sample holder.

6.3.3 Muon Depolarisation Spectra of β-MnAl

Typical muon spectra obtained from the β-$Mn_{1-x}Al_x$ samples are shown in figure 6.11. It is possible to fit the background subtracted spectra from all samples at most temperatures with the relatively simple relaxation function:

$$a_0 G_z(t) = a_0 G^{GKT}{}_z(t) \exp[-(\lambda t)^{\beta}], \qquad (6.39)$$

in which $G^{GKT}{}_z(t)$ is the static Kubo-Toyabe function given by eq. (6.13), associated with a Gaussian distribution of local magnetic fields at the muon site arising from neighbouring nuclear spins. $G_{MAG}(t) = \exp[-(\lambda t)^{\beta}]$ represents the magnetic spin relaxation function arising from dynamic magnetic fields associated with the fluctuating atomic spins. The multiplicative combination of the nuclear and magnetic relaxation functions in eq. (6.39) is valid providing that the nuclear and atomic fields represent independent channels for muon depolarisation. For the most part this is the case in β-$Mn_{1-x}Al_x$, although there may be some evidence for "double relaxation" processes (see section 6.3.3.2).

Whereas the Kubo-Toyabe function, $G^{GKT}{}_z(t)$, provides direct information on the interstitial site occupancy of the muon, it is $G_{MAG}(t)$ which provides an insight into the spin fluctuations and moment localisation in β-$Mn_{1-x}Al_x$. Each of these terms will now be discussed in detail.

6.3.3.1 Muon Site Determination in β-MnAl

Figure 6.12 shows the background subtracted muon relaxation spectrum for pure β-Mn at a temperature of 5K in both zero field and a longitudinal field of 10mT. The solid lines represent best fits of eqs. (6.39) and (6.26) to the data. For the zero field spectrum the fitted nuclear depolarisation rate, σ, is $0.37\mu s^{-1}$, while the magnetic depolarisation rate, λ is $0.03\mu s^{-1}$. β = 1, implying simple exponential relaxation. As can be seen in figure 6.12, a 10mT longitudinal field is clearly sufficient to decouple fully the muon from the small static nuclear fields. The residual magnetic depolarisation in the 10mT applied field remains simple exponential in form, with $\lambda=0.03\mu s^{-1}$. Neither σ nor λ exhibit significant temperature dependence in β-Mn. Such an absence of temperature dependence in σ is a clear indication of a stationary muon.

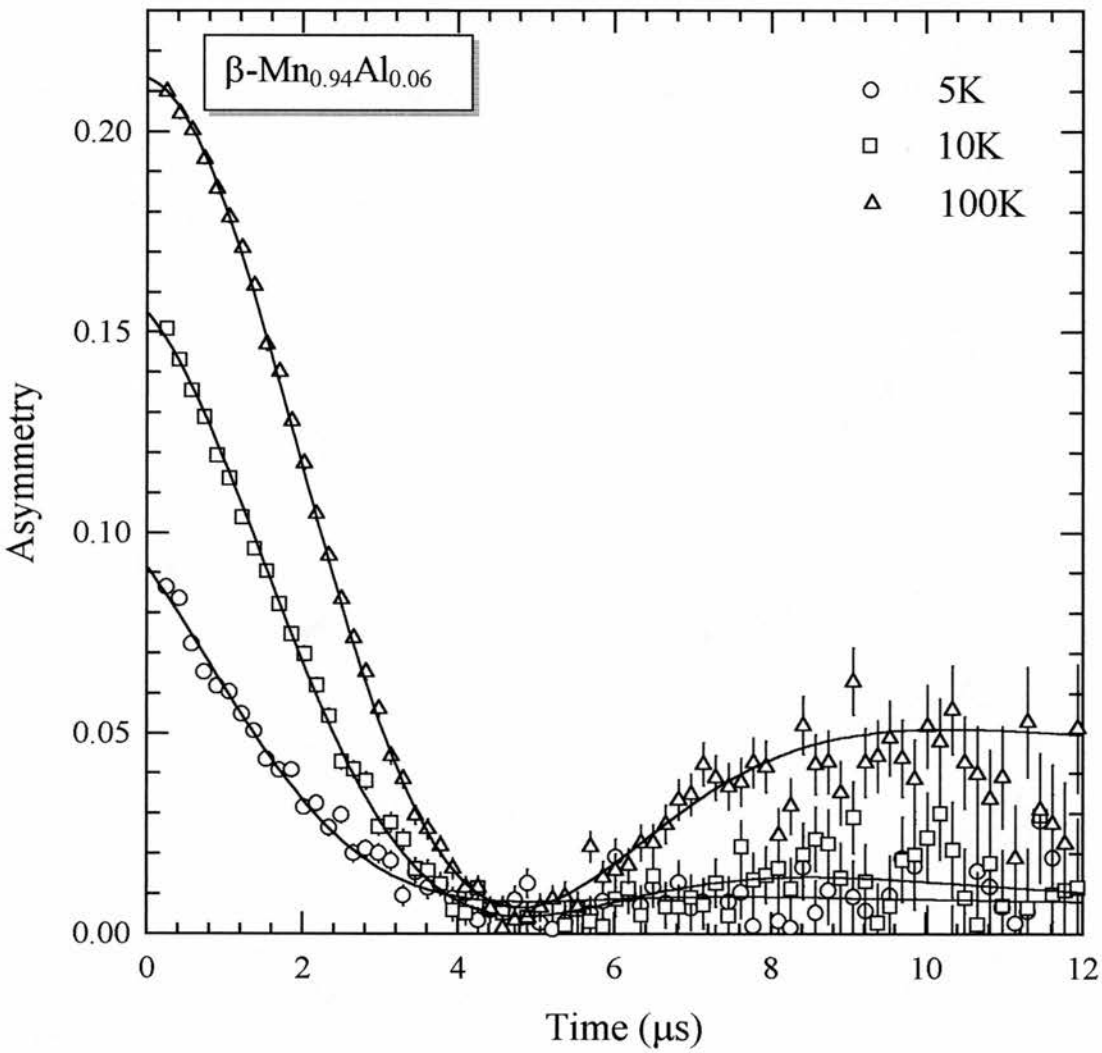

Figure 6.11a

Background subtracted muon depolarisation spectra of β-$Mn_{0.94}Al_{0.6}$ at 5K, 10K and 100K. Solid lines shown are fits to eq. (6.39) with $G_{MAG}(t)$ following a simple exponential form given by eq. (6.26).

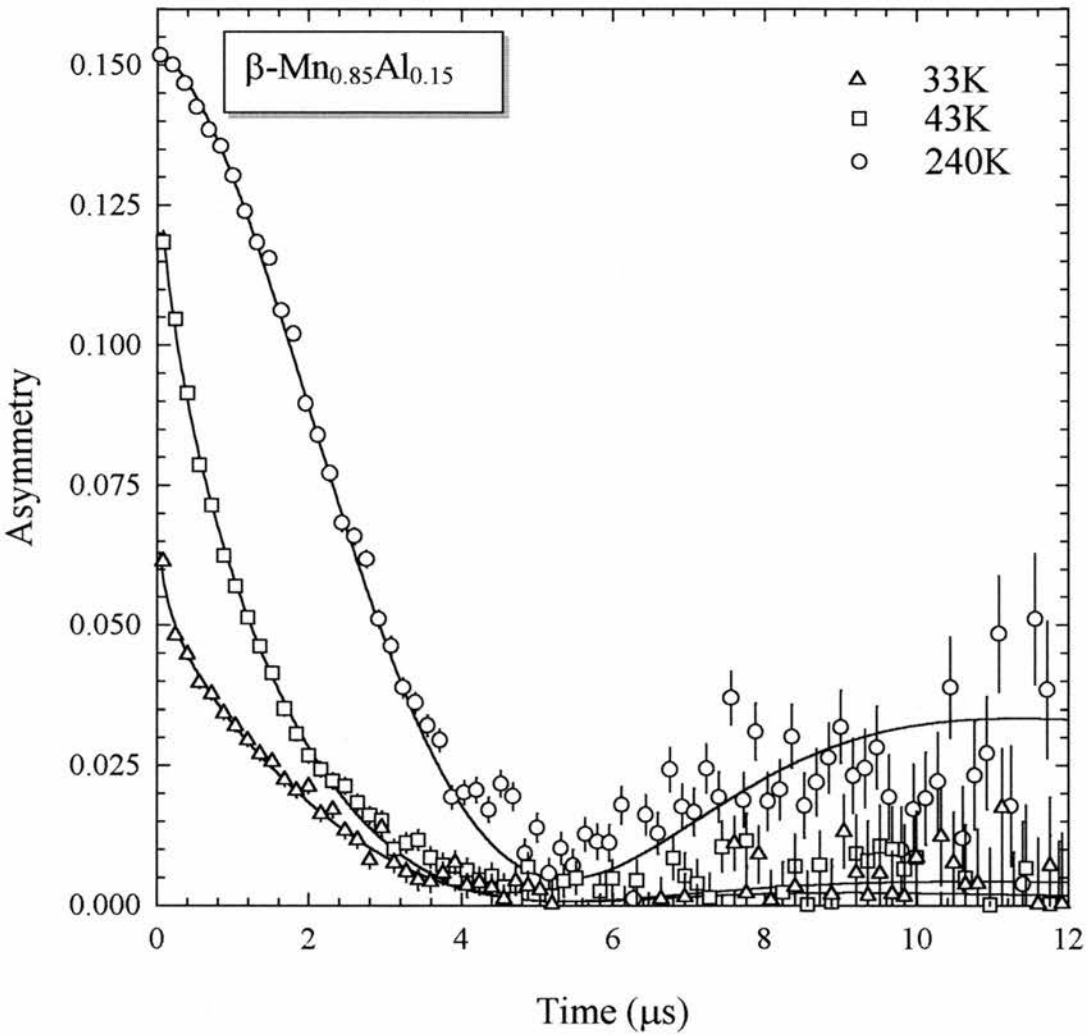

Figure 6.11b

Background subtracted muon depolarisation spectra of β-$Mn_{0.85}Al_{0.15}$ at 33K, 43K and 240K. Solid lines shown are fits to eq. (6.39) with $G_{MAG}(t)$ following a stretched exponential form given by eq. (6.34)

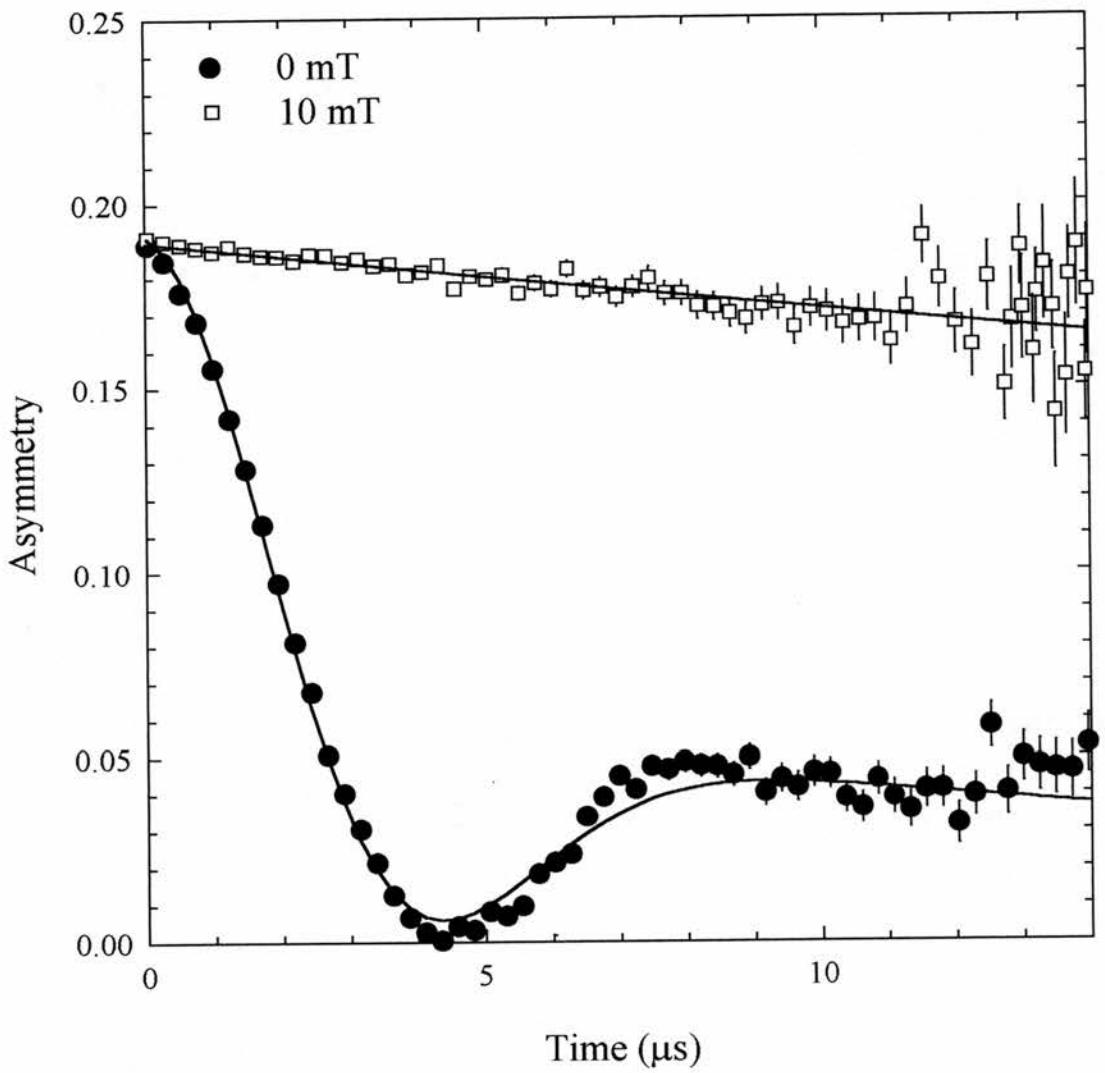

Figure 6.12

Background subtracted muon depolarisation spectra for pure β-Mn at 5K. Solid lines are fits to eq. (6.39) for the zero-field data and eq. (6.26) for the 10mT data.

Candidate interstitial sites for the muon in the β-Mn matrix can be established by using finite element analysis to determine the second moment of the Gaussian field distribution at all points within the unit cell. Δ^2, and hence σ^2, can be calculated for the case of odd half integer nuclear spins (such as Mn and Al for which I=5/2) using the relation [4,16]

$$\Delta^2 = \frac{\sigma^2}{\gamma_\mu^{\,2}} = \frac{1}{6} I(I+1) \frac{8}{3} \left(\frac{\mu_0 \hbar}{4\pi} \gamma_\mu \gamma_n \right)^2 \left\{ 1 + \frac{3}{8} \frac{I+\frac{1}{2}}{I(I+1)} \right\} \sum_{i=1}^{N} \frac{1}{r_i^{\,6}} \qquad (6.40)$$

When this calculation is performed for the β-Mn lattice, taking the sum to a radial distance of 12Å, the nuclear depolarisation rate associated with almost all the candidate muon sites within the cell is found to exceed greatly the experimentally determined value of σ=0.37μs^{-1}. Figure 6.13 shows a contour map of the calculated values of σ for the (1 1 0) and (3/8 0 0) crystal planes.

Only the four crystallographically equivalent interstitial sites at (3/8,3/8,3/8), (1/8,5/8,7/8), (5/8,7/8,1/8) and (7/8,1/8,5/8), for which σ is calculated to be 0.40μs^{-1}, can be accepted as viable muon sites. These sites have a distorted octahedral coordination, as shown in figure 6.14 with six site II Mn near neighbours at a distance of 1.97Å from the muon site.

In order to confirm our muon site determination calculations, we have used a Monte-Carlo simulation procedure to determine the nuclear dipolar field distribution at the (3/8,3/8,3/8) muon site in β-Mn. In this procedure, we randomly assign a nuclear spin direction to each Mn nucleus up to and including the 3rd near neighbour shell around the (3/8,3/8,3/8) site and calculate the resultant dipolar field. A field distribution in the x, y and z directions is built up by repeated iterations of this procedure. The calculated field distributions in the x, y and z directions were found to be isotropic and the field distribution in the x-direction $P(B_x)$ is plotted in figure 6.15a. The solid line is a fit to a Gaussian distribution given in eq. (6.9).

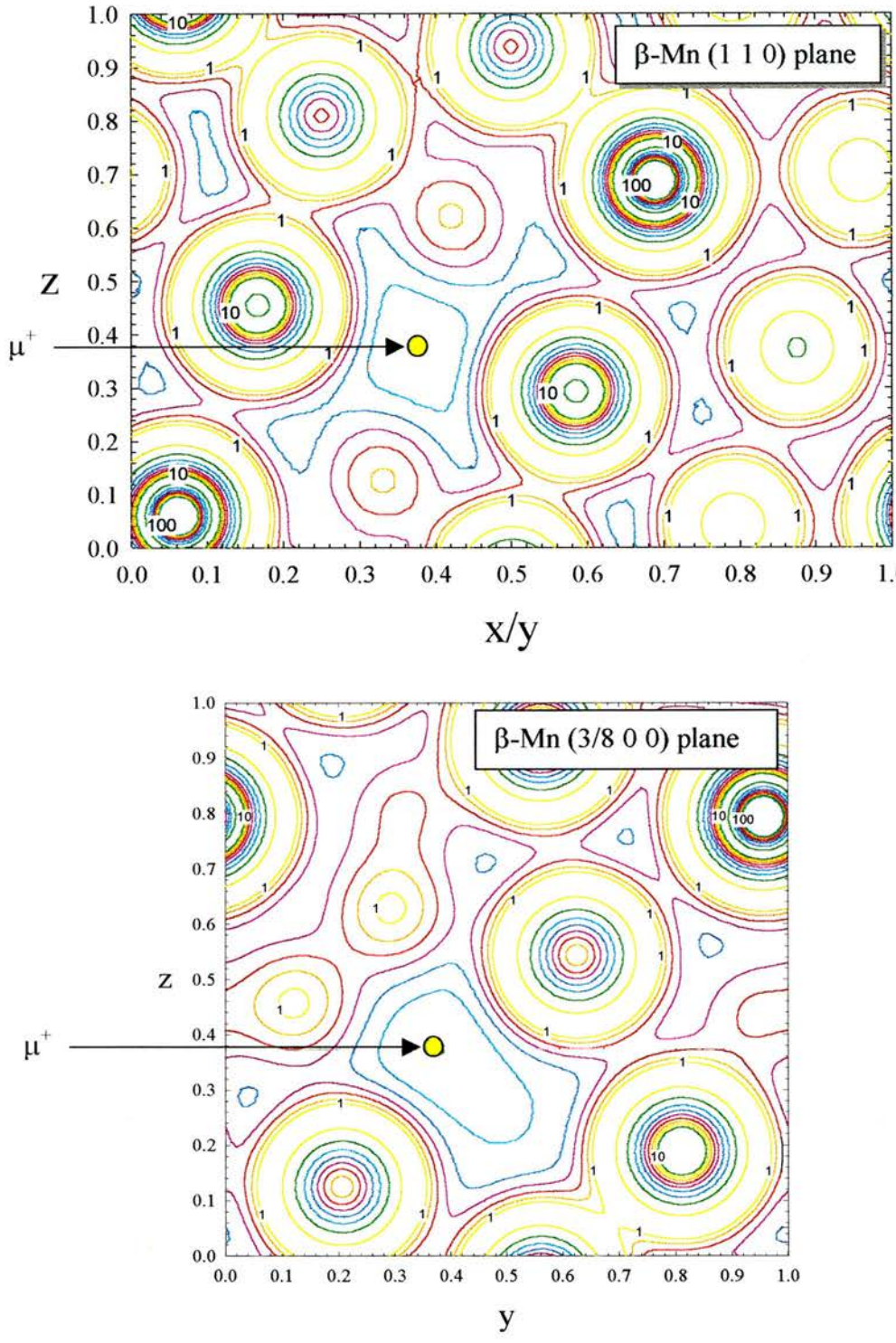

Figure 6.13

Contour maps of the calculated nuclear depolarisation rate σ for the β-Mn (1 1 0) and (3/8 0 0) crystal planes. A deep minimum is revealed at (3/8,3/8,3/8) where σ = 0.40μs^{-1}. This was found to be the only general interstitial lattice position with a value of σ consistent with the experimental data.

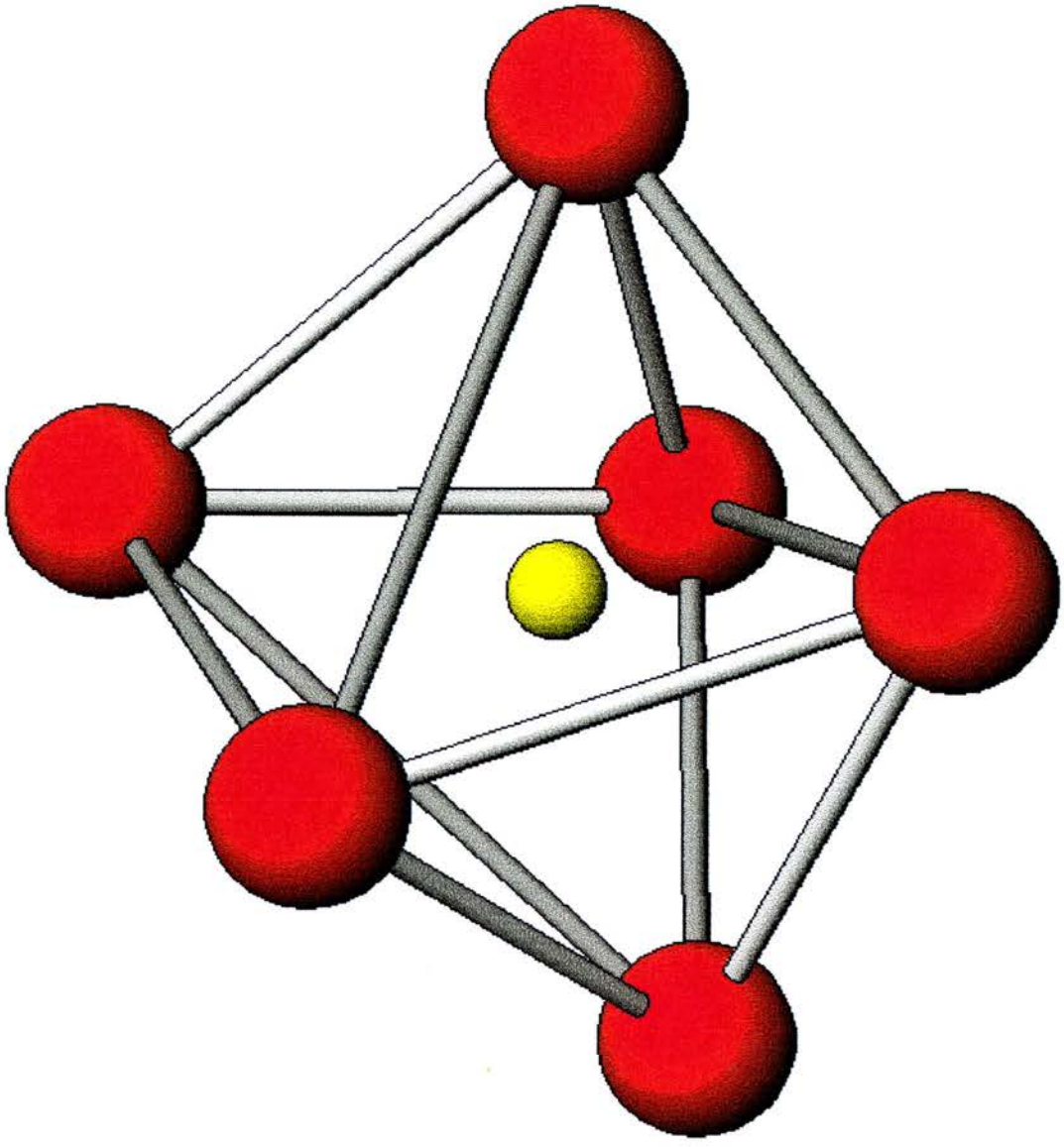

Figure 6.14

The (3/8,3/8,3/8) muon site in β-Mn. The muon is shown in yellow, surrounded by a distorted octahedron of site II Mn near neighbours.

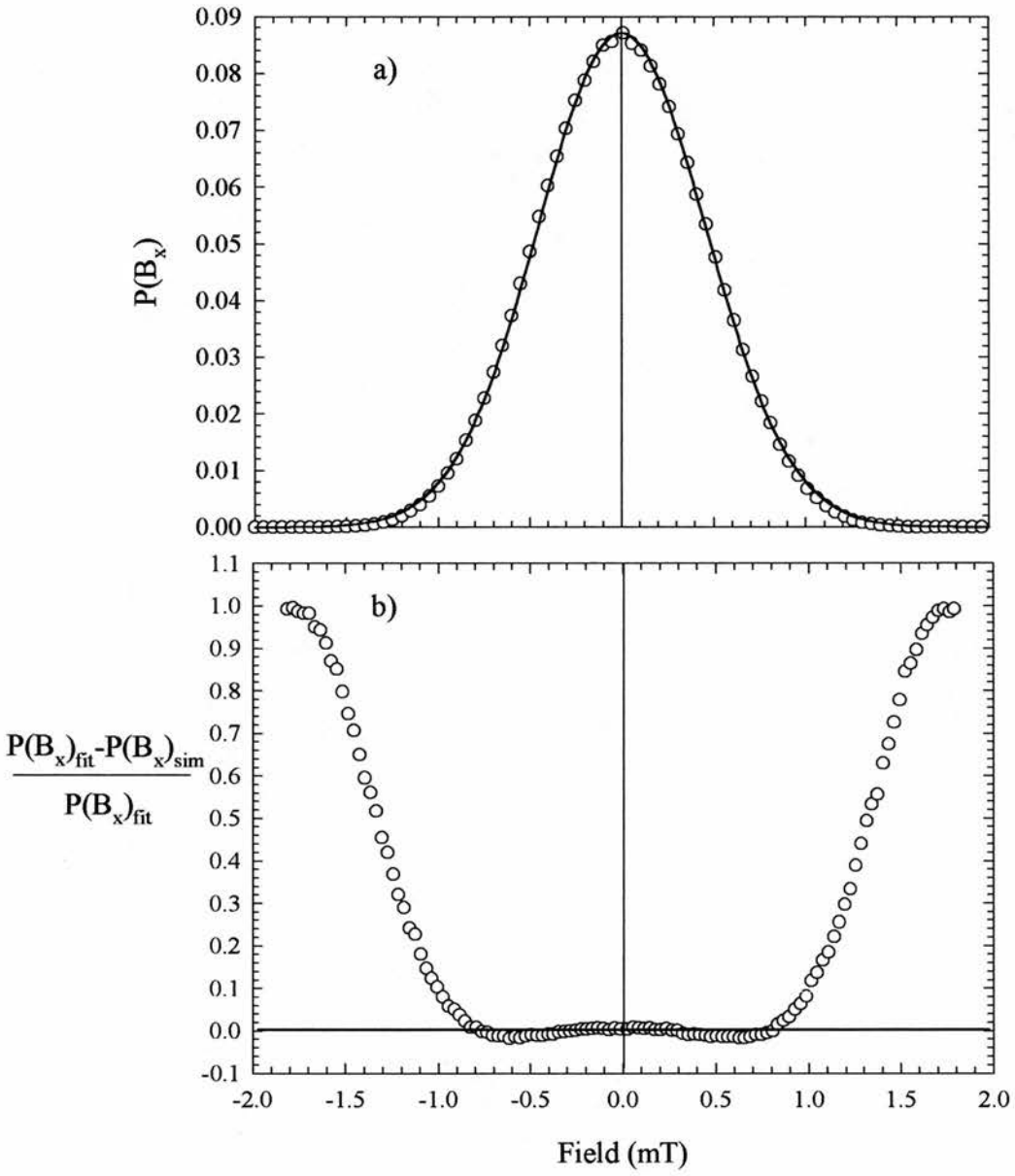

Figure 6.15

a) Calculated muon field distribution at the (3/8, 3/8, 3/8) muon site in pure β-Mn. The solid line is a fit to a Gaussian distribution function.

b) Fractional difference between Gaussian fit and calculated field distribution.

The second moment of the calculated distribution was derived numerically using eq. (6.10) and was found to be $M_2 = 1.95 \times 10^{-7}\ T^2$, while the Gaussian fit gave $M_2 = \Delta^2 = 1.98 \times 10^{-7}\ T^2$. These values of the second moment are both consistent with the data, giving $\sigma = 0.376\ \mu s^{-1}$ and $0.378\ \mu s^{-1}$ respectively. While at first glance, a Gaussian distribution appears to be a fair representation of the calculated field distribution at the (3/8,3/8,3/8) site, a plot of the fractional difference between the calculated distribution and the fit, shown in figure 6.15b, shows a significant deviation from the Gaussian form particularly within the wings of the distribution. Our calculated field distribution is in fact slightly narrower than a Gaussian. This point is more clearly demonstrated in figure 6.16a which shows the resultant field distribution P(B), where $B = \sqrt{(B_x^2 + B_y^2 + B_z^2)}$. If $P(B_{x,y,z})$ is Gaussian in form, then P(B) will be Maxwellian in form,

$$P(B) \propto B^2 \exp(-\frac{B^2}{2\Delta^2}), \qquad (6.41)$$

where $\Delta = \Delta_{x,y,z}$. However, the fractional difference between our calculated field distribution and a Maxwellian fit plotted in figure 6.16b, highlights the non-Gaussian nature of the field distributions in the x, y and z directions, with the resultant field distribution being much narrower than a Maxwellian, but peaked around the same field, $B_{peak} = \sqrt{2}\Delta = 0.62$ mT.

In order to simulate the muon depolarisation function expected at the (3/8,3/8,3/8) site in β-Mn, we have used Monte-Carlo μSR simulation techniques similar to those described by Crook and Cywinski [17], except that no assumptions have been made as to the nature of the nuclear field distribution. Instead we have used the calculated field distribution at the muon site in β-Mn explicitly in the simulation procedure. In figure 6.17 the zero-field muon depolarisation spectrum is shown, normalised to an initial asymmetry, $a_0 = 1$. The solid line is our simulated muon depolarisation spectrum multiplied by the exponential damping observed in pure β-Mn. Our simulation is in remarkable agreement with the measured μSR spectrum, especially around the area of the minimum between 3μs and 8μs, where the fit of the Kubo-Toyabe function shown in fig. 6.12, shows a significant deviation from the data. The dip in the measured spectrum at longer times may be attributed to quadrupolar coupling of the I = 5/2 Mn nuclei to a radial electric field gradient set up by the interstitial muon [18]

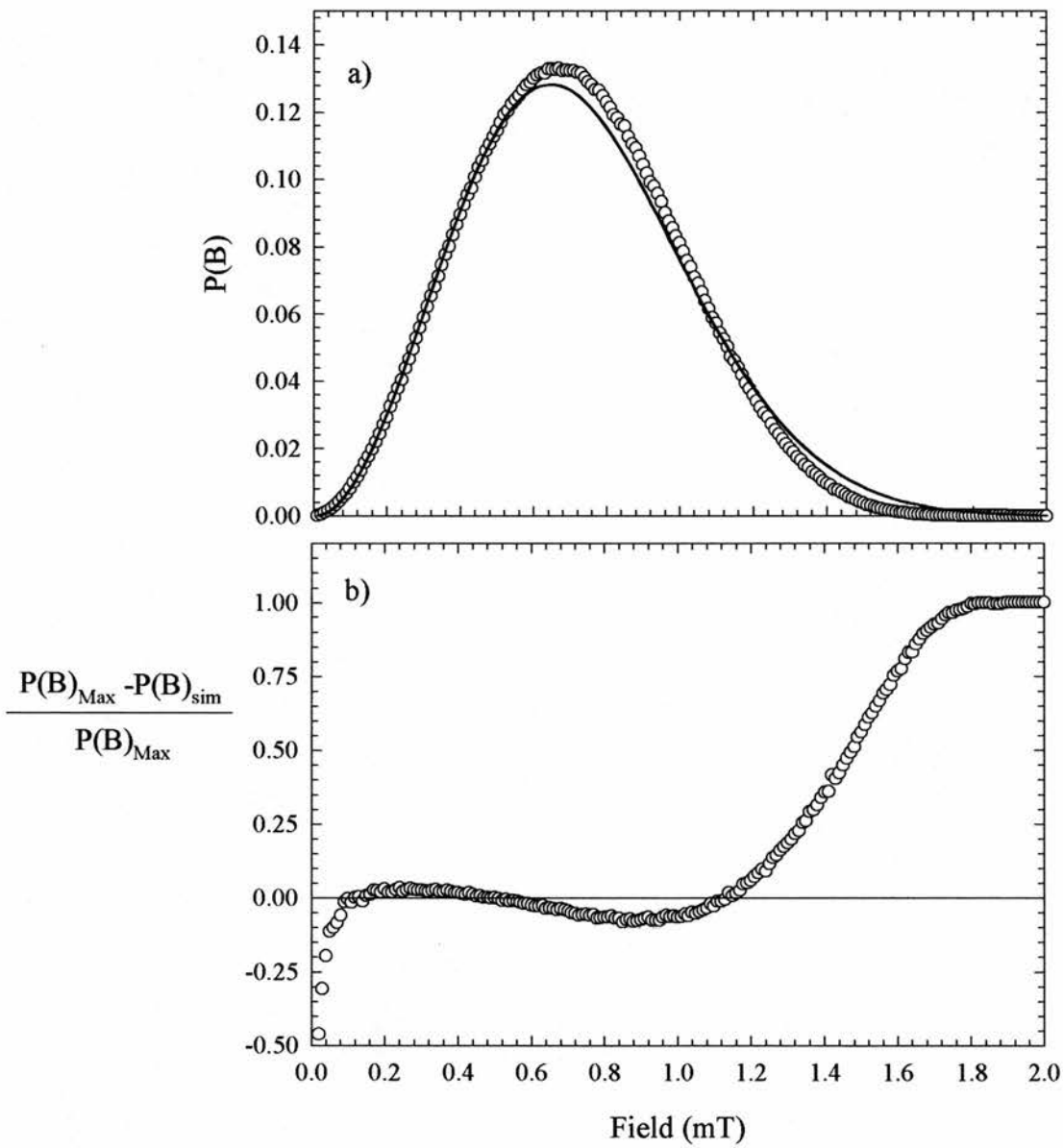

Figure 6.16

a) Calculated resultant muon field distribution at the (3/8, 3/8, 3/8) muon site in pure β-Mn. The solid line is a fit to a Maxwellian distribution function.

b) Fractional difference between the Maxwellian fit and calculated field distribution.

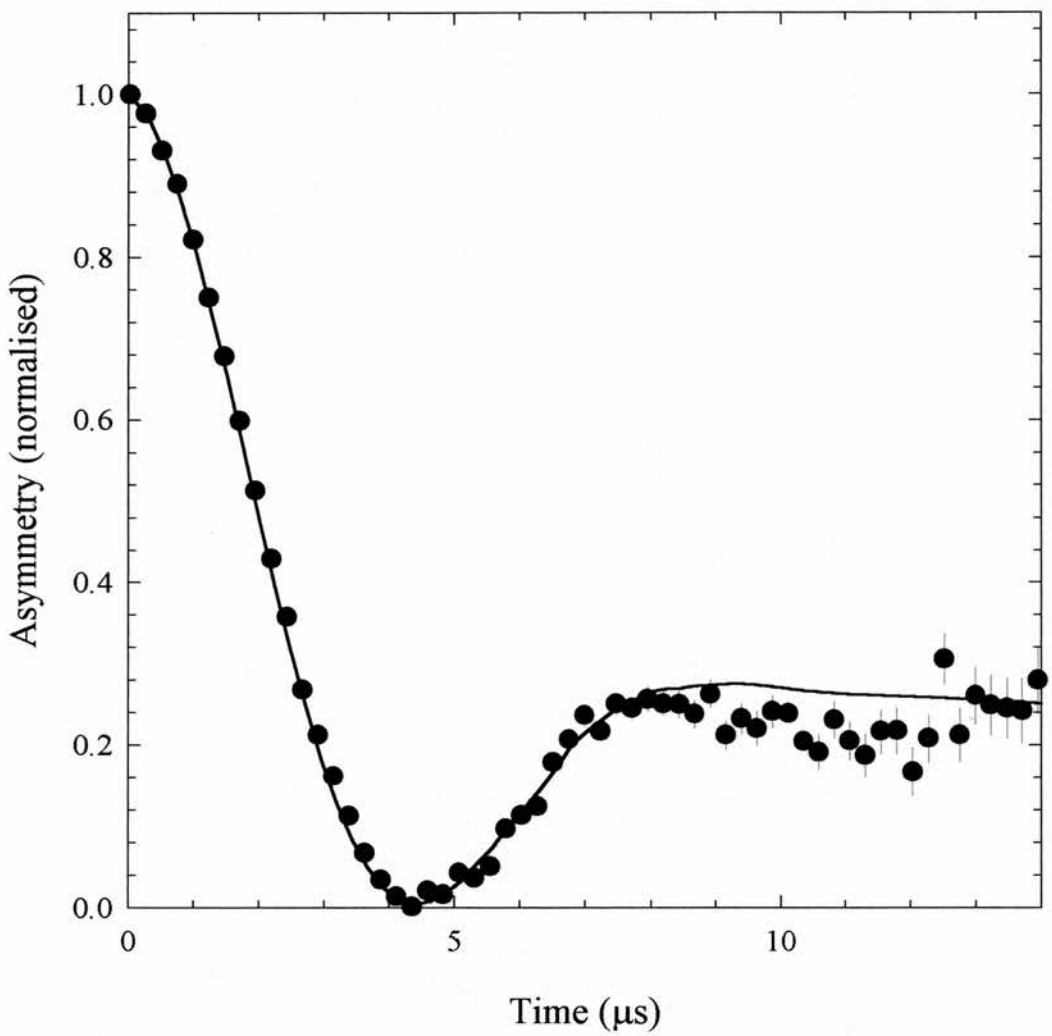

Figure 6.17

Background subtracted muon depolarisation spectrum for β-Mn at 5K, normalised to an initial asymmetry of 1. The solid line is the simulated depolarisation spectrum, using the theoretically calculated field distribution at the (3/8,3/8,3/8) muon site in β-Mn.

Our simulations then, provide an excellent description of the observed nuclear contribution to the muon relaxation, and confirm our muon site determination calculations. They also point out the tremendous sensitivity of the functional form of the muon depolarisation to the precise nature of the nuclear dipolar field distribution at the muon site [19].

However, while the field distribution at the muon site has been found to be non-Gaussian, the second moment of that distribution, and hence the muon depolarisation rate σ, are found to be almost identical to those found by fitting a conventional Kubo-Toyabe function to our data. Furthermore, the deviation from the Kubo-Toyabe form is only apparent in our depolarisation spectrum for β-Mn at 5K, shown in figures 6.12 and 6.17, which has on average, 3 times the counting statistics of our other μSR spectra taken during the course of this experiment. The remaining μSR spectra are therefore fitted to eq. (6.39), with the proviso that the nuclear field distributions are non-Gaussian in nature.

6.3.3.2 Concentration Dependence of the Nuclear depolarisation rate

The nuclear depolarisation rate has been extracted from the zero field μSR spectra of all seven β-$Mn_{1-x}Al_x$ samples at ambient temperature. As both Mn and Al are spin 5/2 nuclei it is expected that the principal contribution to the concentration dependence of σ will arise from the lattice expansion associated with Al substitution. However, the concentration dependence of σ, plotted in figure 6.18 shows a considerably more rapid decrease with increasing Al concentration than that expected from the lattice expansion alone. In addition a slight discontinuity in the monotonic decrease of σ with concentration is observed between x=0.09 and x=0.10.

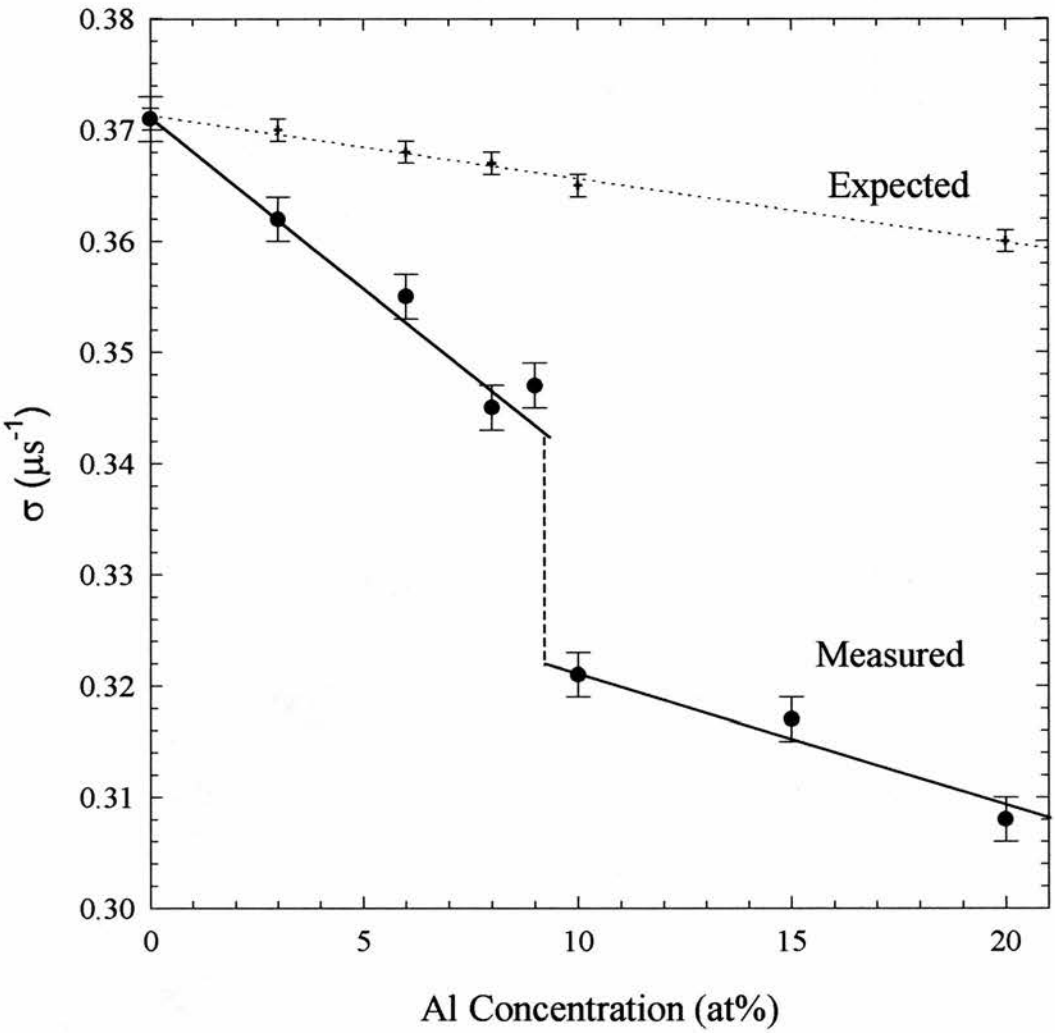

Figure 6.18

Plot of the nuclear depolarisation rate σ, vs. Al concentration. σ is seen to decrease in a roughly linear fashion, with a sharp drop around 10at% Al. The expected decrease in σ calculated using the neutron diffraction data presented in chapter 5 is also shown. The lines shown are guides to the eye.

It is tempting to account for the discrepancy between the calculated and observed values of σ by invoking a local distortion of the β-$Mn_{1-x}Al_x$ lattice around the muon site. Such a dilation of the host lattice is consistent with the so-called small polaron model, within which the muon exerts an electrostatic repulsion on the neighbouring nuclei [20,21,22]. This model, which is also used in the description of hydrogen in metals, predicts local displacements of up to a few per cent of the inter-atomic spacing, (for example, 5% in pure Copper [21]), while the lattice distortion falls off as a power law in distance for more distant neighbouring atomic shells. If the discrepancy between the measured and calculated values of σ is attributed entirely to a local distortion, over and above the concentration dependent expansion of the lattice, we estimate a local linear lattice distortion which rises from 2.9% in pure β-Mn to 8.2% in β-$Mn_{0.8}Al_{0.2}$. These values are of the same order as those observed in pure Cu [21]. The concentration dependence of the local lattice distortion shown in figure 6.19, emphasises the apparent change in behaviour between x=0.09 and x=0.1.

An alternative explanation for the apparent additional and excessive decrease in σ with increasing Al concentration may be provided by the phenomenon known as "muon-nuclear-spin double relaxation" [23] wherein the precession of nuclear dipoles in strong fluctuating atomic fields leads to motional narrowing of the nuclear dipolar field distribution. Within this model the increasing discrepancy between the measured and calculated σ is a consequence of the increasing localisation of atomic moments as Al is added to β-Mn and the lattice expands. The discontinuity in the concentration dependence of σ between x=0.09 and x=0.1 is then seen as evidence for a marked change in the nature of the Mn moments at this concentration.

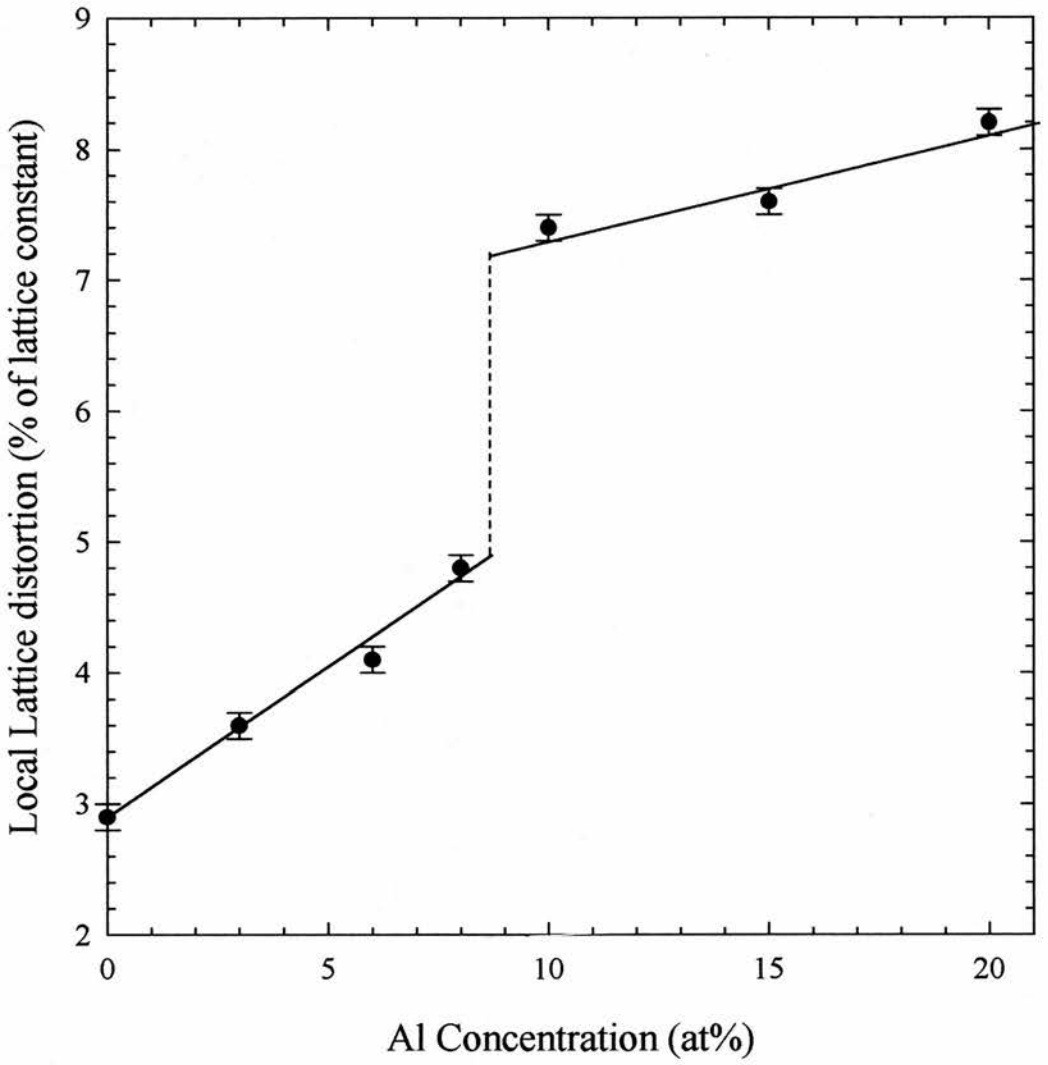

Figure 6.19

The calculated local lattice distortion around the interstitial muon site expressed as a percentage of the lattice constant, plotted against Al concentration. The lines shown are guides to the eye.

6.3.3.3 Spin Dynamics of β-MnAl

In section 6.3.3 it was shown that the muon spin relaxation spectra for all the β-$Mn_{1-x}Al_x$ alloys are well described by eq. (6.39),

$$a_0 G_z(t) = a_0 G^{GKT}{}_z(t) \exp[-(\lambda t)^{\beta}].$$

In fitting this relaxation function to the data the background contribution to the total initial asymmetry, a_{bg}, was fixed at the experimentally determined values. The initial asymmetry, a_0, the nuclear depolarisation rate σ, the magnetic depolarisation rate, λ, and the exponent β remain as free parameters. In all cases σ is found to be temperature independent, and remains within a few percent of the values extracted from the high temperature spectra of the respective alloys in which the contributions to the muon depolarisation from the atomic fields are extremely motionally narrowed. The temperature dependence of a_0, λ and β is shown in figures 6.20 and 6.21.

It is immediately apparent, even from a cursory inspection of figures 6.19 and 6.20, that the muon spin relaxation function, $G_{MAG}(t)$, changes dramatically and suddenly as the Al concentration increases beyond x=0.09.

A. β-$Mn_{1-x}Al_x$ with $0 < x \leq 0.09$

For β-$Mn_{1-x}Al_x$ alloys with $x \leq 0.09$ the relaxation function is simple exponential in form, with β in eq. (6.39) refining to unity at all temperatures. The temperature dependence of the initial asymmetry, a_0, shows clear evidence of the approach to a magnetic transition at low temperatures in all alloys. However the decrease in the initial asymmetry is gradual, indicating that this transition is essentially inhomogeneous in character. Moreover, at the lowest temperatures, a_0 falls below 1/3 of its high temperature value, indicating the persistence of residual atomic spin dynamics below the transition. While it is not possible to extract reliable transition temperatures from the temperature dependence of a_0, the relaxation rate, λ, shows a marked critical-like divergence at low temperatures.

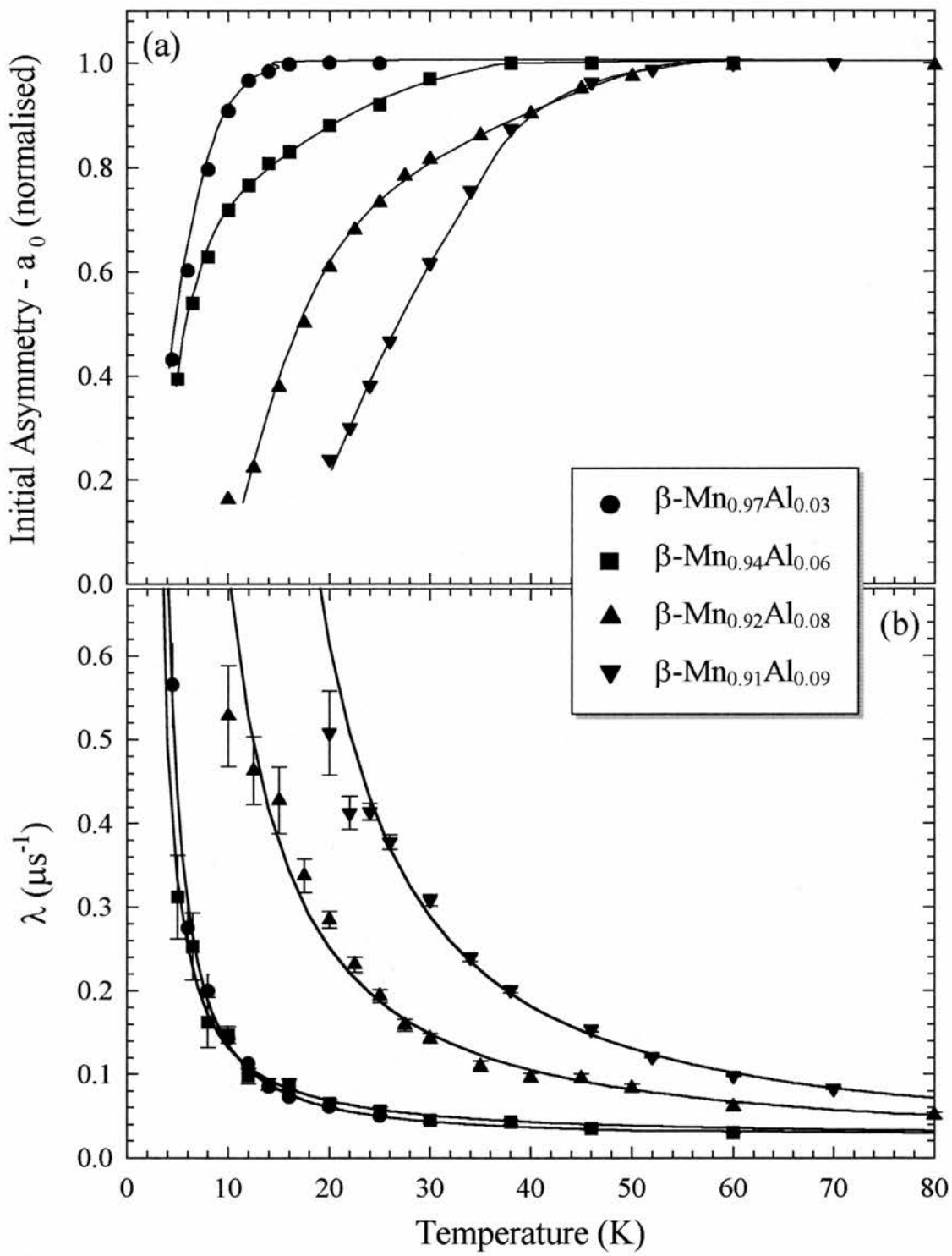

Figure 6.20

The temperature dependence of, a) the initial asymmetry a_0 and b) the muon depolarisation rate λ for β-$Mn_{1-x}Al_x$ with x=0.03, 0.06, 0.08 and 0.09. Solid lines in a) are guides to the eye and in b) are fits to the data of the critical form given in eq. (6.42)

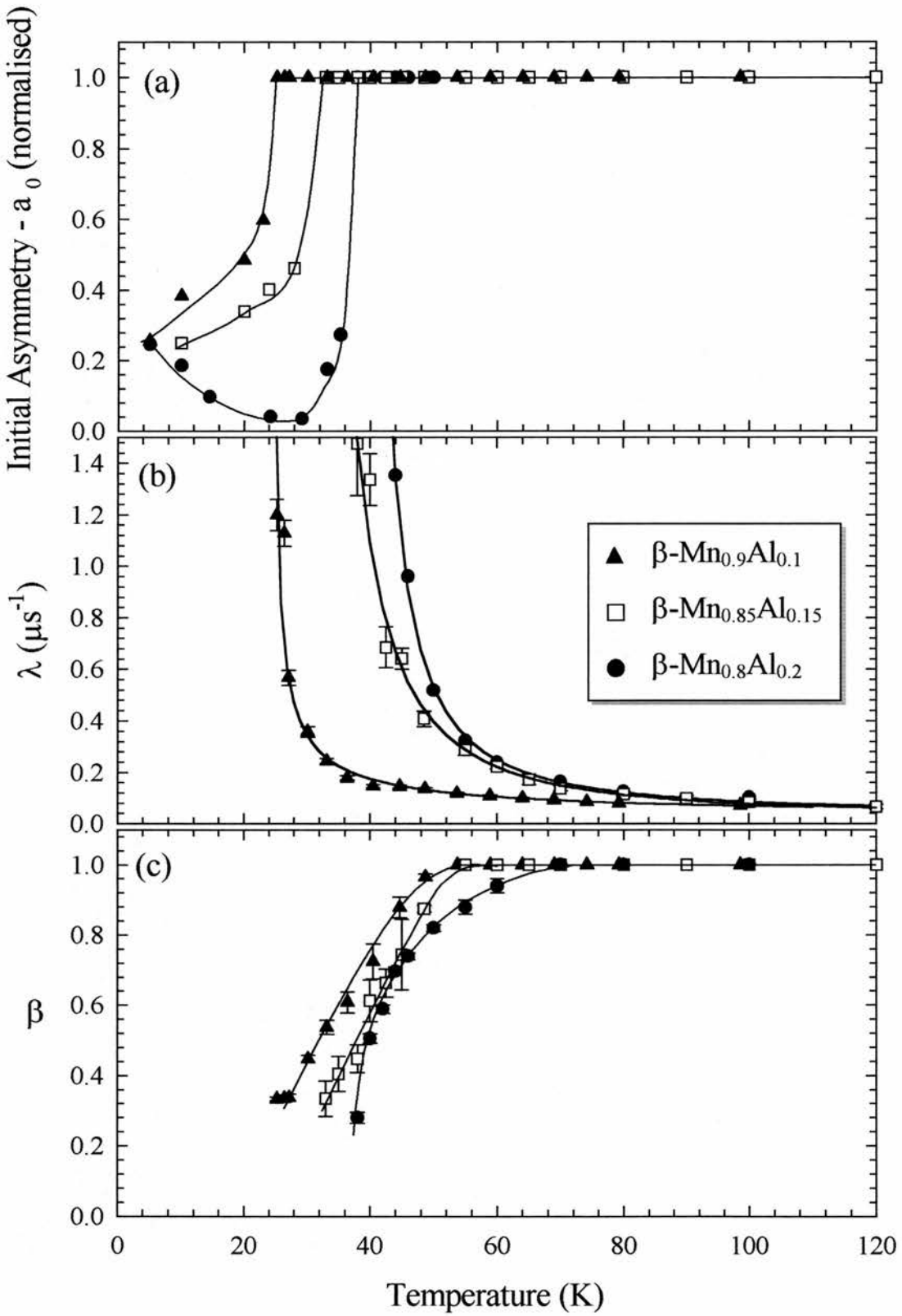

Figure 6.21

The temperature dependence of, a) the initial asymmetry a_0, b) the atomic depolarisation rate λ and c) the stretch exponent β, for β-$Mn_{1-x}Al_x$ with x=0.1, 0.15 and 0.2. Solid lines in a) and c) are guides to the eye, and in b) are fits to the data of the critical form given in eq. (6.42)

It has been possible to fit the critical form

$$\lambda(T)=\lambda_o\left(\frac{T_c}{T-T_c}\right)^{\gamma}, \qquad (6.42)$$

to the temperature dependence of λ, as shown by the solid lines in figure 6.20. Although at present we attach little physical significance either to such critical scaling or to the critical exponent itself, eq. (6.42) is useful in allowing the magnetic transition to be parameterised consistently. For all β-$Mn_{1-x}Al_x$ alloys with $x \leq 0.09$ we find an intrinsic depolarisation rate of $\lambda_o \sim 0.02\mu s^{-1}$. Significantly this value is close to that of the temperature independent magnetic depolarisation rate found for pure β-Mn. The critical temperature, T_c, increases slightly with concentration from 1.5K for x=0.03 to 6.4K for x=0.09. γ remains relatively independent of concentration taking values in the range 1.1 to 1.4. A summary of the fitted parameters is given in table 6.1.

Table 6.1 Nuclear depolarisation rate, σ, and the fitting parameters, T_c, λ_0 and γ from eq. (6.42) for β-$Mn_{1-x}Al_x$.

Al conc. (at%)	σ (μs^{-1})	T_c (K)	λ_0 (μs^{-1})	γ
0	0.371(5)	0		
3	0.362(5)	1.78(5)	0.023(1)	1.37(2)
6	0.356(5)	1.76(5)	0.023(1)	1.12(2)
8	0.345(5)	2.42(5)	0.014(1)	1.27(2)
9	0.347(5)	6.40(5)	0.017(1)	1.43(2)
10	0.321(5)	24.4(5)	0.020(1)	0.74(2)
15	0.317(5)	30.8(5)	0.022(1)	1.25(2)
20	0.318(5)	37.9(5)	0.026(1)	1.42(2)

B. β-$Mn_{1-x}Al_x$ with $0.09 < x \leq 0.2$

There is an abrupt change in the nature of the spin fluctuation spectrum of β-$Mn_{1-x}Al_x$ between concentrations of x=0.09 and x=0.1 with the muon spin relaxation exhibiting a sudden transition from simple exponential to stretched exponential behaviour. The exponent β in eq. (6.39) is no longer temperature independent, but is now found to decrease from unity at high temperatures to a value close to 1/3 at the transition temperature, as shown in figure 6.21c. Moreover the initial asymmetry exhibits a relatively sharp magnetic transition (figure 6.21a), although there remains some

evidence of residual spin fluctuations below the transition temperature. The temperature dependence of λ is not significantly different from that observed at lower concentrations: its divergence towards the magnetic transition is still well described by the critical form of eq. (6.42) and the intrinsic depolarisation rate, λ_o, remains close to $0.02\mu s^{-1}$. However, the transition temperatures associated with the critical divergence are now significantly higher in these more concentrated alloys, rising from 24.4K for β-$Mn_{0.9}Al_{0.1}$ to 37.9K for β-$Mn_{0.8}Al_{0.2}$. These transition temperatures are in close agreement with the values obtained from the magnetisation measurements described in chapters 1 and 4. The parameters obtained from the fitting procedure are given in Table 6.1.

6.4 Discussion

Our μSR measurements have highlighted a remarkable evolution of atomic spin fluctuations with increasing Al concentration in β-$Mn_{1-x}Al_x$. Three distinct regimes have been identified.

Firstly, in pure β-Mn we observe simple exponential relaxation, implying a single spin fluctuation frequency. The muon spin relaxation rate, λ, is found to be small and independent of temperature. This result is in marked contrast to the observed $\sqrt{T}$ dependence of the nuclear relaxation rate $1/T_1$ measured by NMR as shown in chapter 1 [24,25]. In situations where the muon relaxation is dominated by the Fermi contact field at the muon site $1/T_1$ and λ are expected to scale according to the relation

$$\lambda\left(\gamma_n^{Mn} A_{hf}^{Mn}\right) = \frac{1}{T_1}\left(\gamma_\mu A_{hf}^{\mu}\right), \qquad (6.43)$$

where A_{hf}^{μ} and A_{hf}^{Mn} are the hyperfine coupling constants for the interstitial muon and the Mn atom respectively. The breakdown of this scaling indicates a significant fluctuating atomic dipolar contribution to the muon relaxation which is at least comparable with any Fermi-contact field contribution. At the Mn nuclear site, it is assumed that the Fermi-contact field is the dominant contribution to the nuclear relaxation, and indeed the SCR theory prediction of a $\sqrt{T}$ dependence in $1/T_1$ assumes this [26]. However, for antiferromagnetically correlated spins, the electron spin-density

at the interstitial muon site may be extremely small, effectively eliminating any Fermi-contact contribution, and allowing the dipolar contribution to dominate the muon depolarisation [27]. The temperature independence of λ in pure β-Mn is therefore suggestive of a system of antiferromagnetically correlated, longitudinally fluctuating atomic moments, in the extreme motional narrowing limit.

Secondly, for β-$Mn_{1-x}Al_x$ with $0.03 \leq x \leq 0.09$, we still observe simple exponential relaxation. However the muon depolarisation rate λ diverges at low temperatures, accompanied by a gradual drop in the initial asymmetry indicative of the formation of a static magnetic ground state. In general, such a static magnetic ground state with randomly oriented internal fields, will result in a time independent muon asymmetry of exactly 1/3 of its high temperature value, since 1/3 of the muon ensemble remains polarised along the static field direction, while fields orthogonal to the muon spin direction will immediately depolarise the remaining 2/3. A fall in a_0 to <u>below</u> 1/3 of its high temperature value implies a residual fluctuating field component at the muon site in these alloys, at low temperatures. In addition, the gradual decrease a_0 with decreasing temperature indicates a steady statistical growth of strongly depolarising regions within the sample, rather than a critical phase transition at a well defined temperature. However, the observation of a divergent muon depolarisation rate λ in these alloys is an indication that a truly static field component is formed at the muon site at low temperatures, and that Al concentrations of as little as 3at% are sufficient to dampen the zero-point spin fluctuations in β-Mn.

Thirdly, for β-$Mn_{1-x}Al_x$ with $x \geq 0.1$, we observe stretched exponential relaxation, generally associated with spin glass order. The initial asymmetry a_0 falls sharply at the magnetic transition temperature in contrast to the more gradual decrease in a_0 observed in the dilute alloys. The critical form of $\lambda(T)$ is very similar to that observed in dilute β-$Mn_{1-x}Al_x$ alloys.

The most striking difference between the dilute β-$Mn_{1-x}Al_x$ alloys with $x \leq 0.09$, and the more concentrated alloys, is an abrupt rise in transition temperature, along with a concomitant change in the nature of the spin dynamics from a simple to a stretched exponential form. This is depicted in figure 6.22 which shows the magnetic phase diagram of β-$Mn_{1-x}Al_x$ system determined by these μSR measurements.

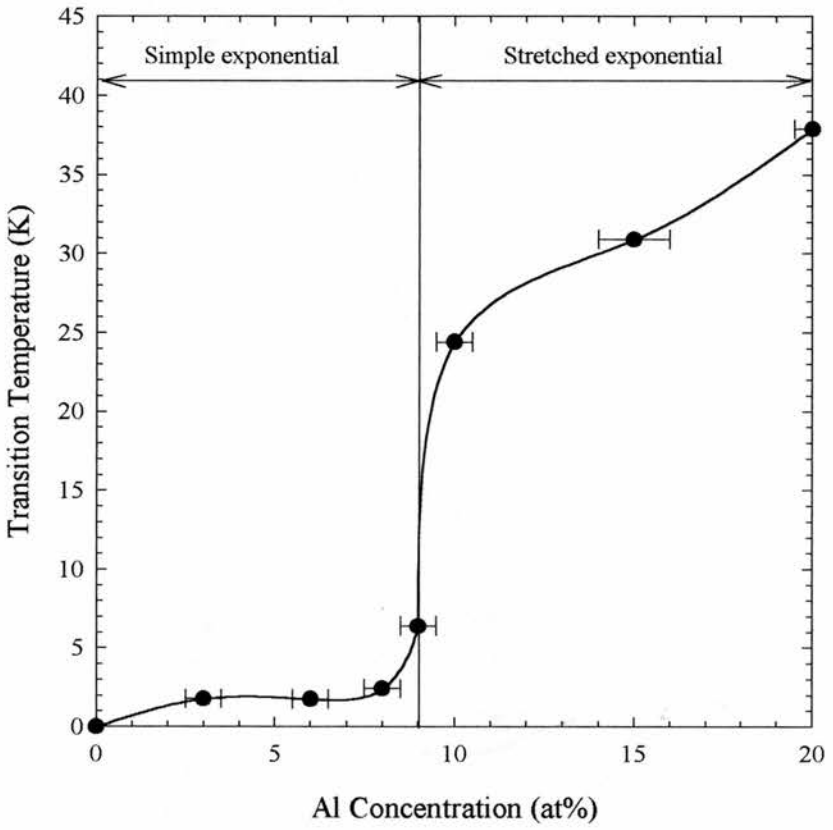

Figure 6.22

Magnetic phase diagram of the β-$Mn_{1-x}Al_x$ system. The regions of simple and stretched exponential relaxation are shown.

6.5 Conclusion

We have undertaken a muon spin relaxation study of β-$Mn_{1-x}Al_x$. We have identified the interstitial muon site in the material and have observed a nuclear contribution to the muon relaxation function which is consistent with a non-Gaussian distribution of nuclear dipolar fields at the muon site.

We have provided a systematic account of the dynamical magnetic behaviour in β-$Mn_{1-x}Al_x$ for $0 \leq x \leq 0.2$. These measurements have provided the first published phase diagram of the β-MnAl system and have revealed a remarkable change in the nature of the spin dynamics at Al concentrations of greater than 9at%. This spin dynamical behaviour has been interpreted in terms of both amplitude spin fluctuations and transverse spin fluctuations arising from the band nature of the magnetic correlations in β-Mn and local moment characteristics promoted by the introduction of Al. The process of increasing Mn moment localisation as the Al substitution increases has been attributed to lattice expansion, local magnetic disorder and a reduction in the degree of magnetic frustration present in the β-Mn matrix.

6.6 References

[1] R Cywinski and B D Rainford, Hyp. Int. **85** (1994) 215

[2] M T F Telling, *Muon Studies of Paramagnetic Spin Fluctuations*, PhD Thesis, University of Reading (1997)

[3] S H Kilcoyne, *The Muon Data Analysis Program "RUMDA"*, Rutherford Appleton Laboratory Report **RAL-94-080** (1994)

[4] A Schenck, *Muon Spin Rotation Spectroscopy*, Adam Hilger (1985)

[5] R S Hayano, Y J Uemura, J Imazato, N Nishida, T Yamazaki and R Kubo, Phys. Rev **B20** (1979) 850

[6] R Kubo, J. Phys. Soc. Japan **9** (1954) 935

[7] A Keren, Phys. Rev. **B50** (1994) 10039

[8] T Yamazaki, Nucl. Inst. Meth. Phys. Res. **199** (1982) 133

[9] A Abragam, *The Principles of Nuclear Magnetism*, Oxford University Press (1961)

[10] see for instance, Y J Uemura, Hyp. Int. **8** (1981) 739

[11] Y J Uemura, T Yamazaki, D R Harshman, M Senba and E J Ansaldo, Phys. Rev **B31** (1985) 546

[12] R I Bewley and R Cywinski, submitted to Phys. Rev **B**, May 1998

[13] A T Ogielski, Phys. Rev **B32** (1985) 7384

[14] I A Campbell, A Amato, F N Gygax, D Herlach, A Schenck, R Cywinski and S H Kilcoyne, Phys. Rev. Lett. **72** (1994) 1291

[15] A D Hillier, J R Stewart, M T F Telling, R I Bewley, Z-P Han, S L Lee and R Cywinski, J. Mag. Magn. Mater. **177** (1998) 1111

[16] P Dalmas de Roetier, PhD Thesis

[17] M R Crook and R Cywinski, J. Phys. Cond. Mater. **9** (1997) 1149

[18] E Holzschuh and P F Meier, Phys. Rev. B **29** (1984) 1129

[19] see for example, R Kadono, J Imazato, K Nishiyama, K Nagamine, T Yamasaki, D Richter and J-M Welter, Phys. Lett. **107A** (1985) 279

[20] S F J Cox, J. Phys. C **20** (1987) 3187

[21] M Camani, F N Gygax, W Rüegg, A Schenck and H Schilling, Phys. Rev. Lett. **39** (1977) 836

[22] F Perrot and M Rasolt, Phys. Rev. B **23** (1981) 6534

[23] T Matsuzaki, K Nishiyama, K Nagamine, T Yamazaki, M Senba, J M Bailey and J H Brewer, Phys. Lett. A **123** (1987) 91

[24] S Akimoto, T Kohara and K Asayama, Solid State Comm. **16** (1975) 1227

[25] M Katayama, S Akimoto and K Asayama, J. Phys. Soc. Japan **42** (1977) 97

[26] T Moriya, *Spin Fluctuations in Itinerant Electron Magnetism*, Springer-Verlag (1985), pp 99-101

[27] R S Hayano, Y J Uemura, J Imazato, N Nishida, K Nagamine, T Yamazaki, Y Ishikawa and H Yasuoka, J. Phys. Soc. Japan **49** (1980) 1773

7 A Neutron Polarisation Analysis Study of β-MnAl

7.1 Introduction

A diffuse neutron scattering experiment in which the incident neutron beam is polarised and the scattered neutrons are analysed for their final spin state, is a powerful tool for the analysis of both nuclear and magnetic short-range order in antiferromagnetically correlated systems. Analysis of the x, y and z components of the neutron spin-dependent scattering allows total and unambiguous separation of the nuclear and magnetic contributions to the differential scattering cross-section. In this chapter we present an XYZ neutron polarisation analysis study of β-$Mn_{1-x}Al_x$ alloys with x = 0.03, 0.06, 0.1 and 0.2. This experiment was undertaken in order to gain information on the nature of the magnetic correlations between Mn atoms in the β-MnAl system, taking into account the rôle played by any possible nuclear short-range order between the Al impurity atoms in the β-Mn matrix.

7.2 Theory of XYZ Neutron Polarisation Analysis

The theory of the XYZ difference method of neutron polarisation analysis has been presented by Schärpf and Capellmann [1] and will be briefly summarised here.

We start with the expression for the neutron partial differential cross-section given by equation (3.5). For magnetic scattering, we can define an interaction potential V in eq. (3.5) which describes the interaction of the electron magnetisation density M(**r**) and the magnetic dipole moment of the neutron as,

$$V = \frac{1}{4\pi\varepsilon_0}\mathbf{M}(r).\mathbf{B}_n(r), \tag{7.1}$$

where $B_n(r)$ is the magnetic dipole field of the neutron,

$$\mathbf{B}_n(r) = \nabla_r \wedge \left[\nabla_r \wedge \frac{\mu_n}{|\mathbf{r}-\mathbf{r}_n|}\right], \tag{7.2}$$

and $|\mu_n| = \gamma\mu_N$ is the magnetic dipole moment of the neutron. To obtain the magnetic cross-section we need to evaluate the matrix element <k`|V|k> in eq. (3.5). Defining the wavevector transfer $\mathbf{Q} = \mathbf{k}` - \mathbf{k}$, we can write,

$$\langle k'|V|k\rangle = \langle k'|\mathbf{M}(r).\mathbf{B}_n(r)|k\rangle = \mathbf{M}(r).\left[\frac{\mathbf{Q}}{|Q|}\wedge\left(\mu_n\wedge\frac{\mathbf{Q}}{|Q|}\right)e^{iQ.r}\right] = \mathbf{M}(r).\mu_{n\perp}e^{iQ.r}. \qquad (7.3)$$

where $\mu_{N\perp}$ is the component if the neutron spin perpendicular to **Q** [1].

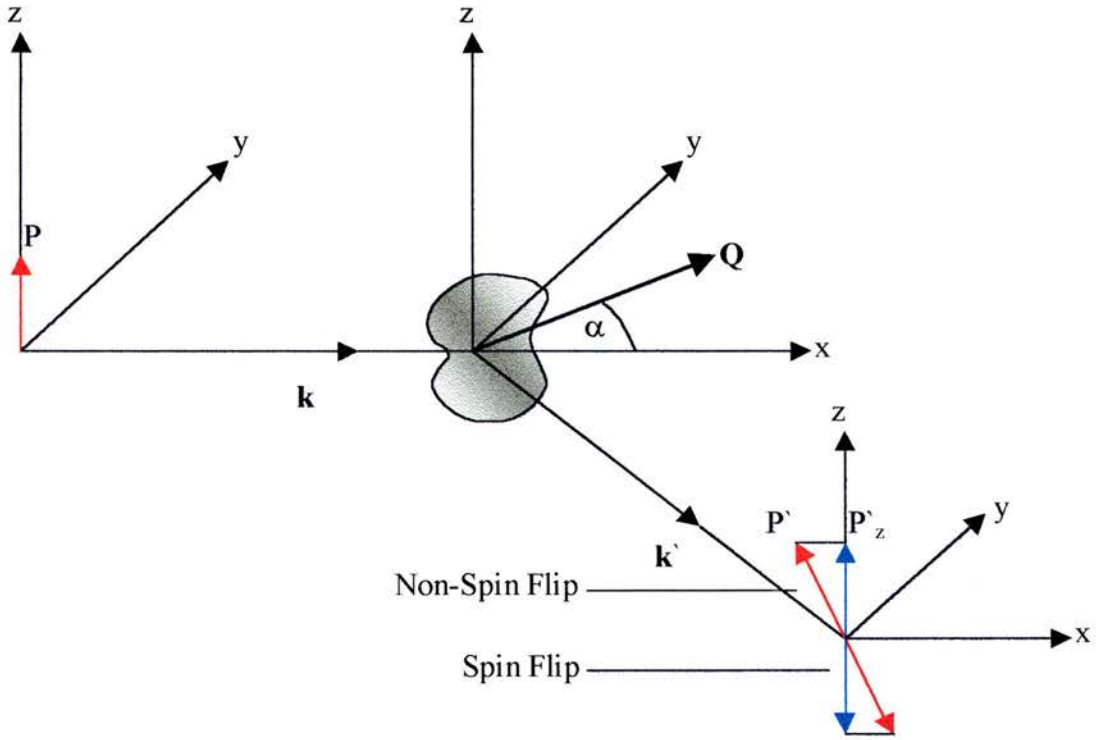

Figure 7.1

The geometry of an XYZ neutron polarisation analysis experiment with initial polarisation in the z-direction.

If we choose the geometry of our neutron scattering instrument so that **Q** is always in the x-y plane as shown in figure 7.1, each detector will lie at an angle α with respect to the x-axis in the direction,

$$\frac{\mathbf{Q}}{|Q|} = (\cos\alpha, \sin\alpha, 0). \qquad (7.4)$$

We can then write the magnetic interaction matrix element given by eq. (7.3) as,

$$\begin{aligned}\mathbf{M}.\mu_{n\perp} &= \mu_x(M_x\sin^2\alpha - M_y\sin\alpha\cos\alpha) + \mu_y(M_y\cos^2\alpha - M_x\sin\alpha\cos\alpha) - \mu_z M_z \\ &= \mathbf{M}_\perp.\mu_n\end{aligned} \qquad (7.5)$$

where M_x, M_y and M_z are the components of the magnetisation density, $\mu_n = -\gamma\mu_N\sigma_n$ is the spin dependent magnetic moment of the neutron and σ_n are the Pauli spin matrices for the neutron spin [2]. Equation (7.5) highlights the well known result that only those components of the magnetisation perpendicular to the wavevector transfer **Q** will be effective in scattering the neutrons [3,4].

We now need to include the nuclear contribution to the interaction potential V, in which the spin-dependent nuclear scattering lengths must be taken into account (see section 3.2 1). The total interaction is then described by,

$$\langle k`|V|k\rangle = \frac{2\pi\hbar^2}{m_n}\left[e^{iQ.(r-R)}(b^2{}_{coh} + B\xi.\sigma_n) + \left(\frac{r_o\gamma}{2}\right)\mathbf{M}(r).\sigma_{n\perp}e^{iQ.r}\right], \qquad (7.6)$$

where b_{coh} is the coherent nuclear scattering length, $B\xi$ is the nuclear spin-dependent scattering length and **R** is the position vector of the nucleus. Using the properties of the Pauli spin matrices in the x, y and z directions,

$$\sigma_x = \begin{pmatrix} 0 & 1 \\ 1 & 0 \end{pmatrix}, \quad \sigma_y = \begin{pmatrix} 0 & -i \\ i & 0 \end{pmatrix}, \quad \text{and } \sigma_z = \begin{pmatrix} 1 & 0 \\ 0 & -1 \end{pmatrix}, \qquad (7.7)$$

it can be shown that the total cross-section given by eq. (3.5) with the interaction potential given by eq (7.6), for a power diffraction measurement, can be separated into the following partial differential cross-sections [1,2].

$$\begin{aligned}
\left(\frac{d^2\sigma}{d\Omega dE}\right)^Z_{SF} &= \frac{2}{3}\left(\frac{d^2\sigma}{d\Omega dE}\right)_{SI} + \frac{1}{2}\left(\frac{d^2\sigma}{d\Omega dE}\right)_{MAG} \\
\left(\frac{d^2\sigma}{d\Omega dE}\right)^Z_{NSF} &= \frac{1}{3}\left(\frac{d^2\sigma}{d\Omega dE}\right)_{SI} + \frac{1}{2}\left(\frac{d^2\sigma}{d\Omega dE}\right)_{MAG} + \left(\frac{d^2\sigma}{d\Omega dE}\right)_{NUC} + \left(\frac{d^2\sigma}{d\Omega dE}\right)_{II} \\
\left(\frac{d^2\sigma}{d\Omega dE}\right)^Y_{SF} &= \frac{2}{3}\left(\frac{d^2\sigma}{d\Omega dE}\right)_{SI} + (1+\sin^2\alpha)\frac{1}{2}\left(\frac{d^2\sigma}{d\Omega dE}\right)_{MAG} \\
\left(\frac{d^2\sigma}{d\Omega dE}\right)^Y_{NSF} &= \frac{1}{3}\left(\frac{d^2\sigma}{d\Omega dE}\right)_{SI} + (\cos^2\alpha)\frac{1}{2}\left(\frac{d^2\sigma}{d\Omega dE}\right)_{MAG} + \left(\frac{d^2\sigma}{d\Omega dE}\right)_{NUC} + \left(\frac{d^2\sigma}{d\Omega dE}\right)_{II} \\
\left(\frac{d^2\sigma}{d\Omega dE}\right)^X_{SF} &= \frac{2}{3}\left(\frac{d^2\sigma}{d\Omega dE}\right)_{SI} + (1+\cos^2\alpha)\frac{1}{2}\left(\frac{d^2\sigma}{d\Omega dE}\right)_{MAG} \\
\left(\frac{d^2\sigma}{d\Omega dE}\right)^X_{NSF} &= \frac{1}{3}\left(\frac{d^2\sigma}{d\Omega dE}\right)_{SI} + (\sin^2\alpha)\frac{1}{2}\left(\frac{d^2\sigma}{d\Omega dE}\right)_{MAG} + \left(\frac{d^2\sigma}{d\Omega dE}\right)_{NUC} + \left(\frac{d^2\sigma}{d\Omega dE}\right)_{II}
\end{aligned} \qquad (7.8)$$

The subscripts SF and NSF in eqs (7.8) signify spin flip or non-spin flip scattering cross sections in the directions indicated. Referring to figure 7.1, the polarisation component $P`_z$ of the neutron spin will either be in the same direction as the incident neutron polarisation P, and hence contribute to the NSF partial differential cross-section in the z-direction, or $P`_z$ will be in the opposite direction to P having been spin flipped by the sample, therefore contributing to the SF partial differential cross-section in the z-direction. The contributions to the total cross-section in eq (7.8) have the following definitions.

The *nuclear coherent* partial differential cross-section is given by,

$$\left(\frac{d^2\sigma}{d\Omega dE}\right)_{NUC} = \frac{k`}{k} b^2 S(Q,\omega). \tag{7.9}$$

The *spin incoherent* partial differential cross-section is given by,

$$\left(\frac{d^2\sigma}{d\Omega dE}\right)_{SI} = \frac{k`}{k} B^2 S_{SI}(Q,\omega). \tag{7.10}$$

The *isotope incoherent* partial differential cross-section is given by,

$$\left(\frac{d^2\sigma}{d\Omega dE}\right)_{II} = \frac{k`}{k}(\overline{b^2} - (\bar{b})^2) S_{II}(Q,\omega). \tag{7.11}$$

The *magnetic* partial differential cross-section is given by.

$$\left(\frac{d^2\sigma}{d\Omega dE}\right)_{MAG} = \frac{k`}{k}\frac{2}{3}\left(\frac{r_0\gamma}{2}\right)^2 |f(Q)|^2 M^2(Q,\omega), \tag{7.12}$$

where $M^2(Q,\omega)$ is the Fourier transform of the spatial magnetisation density.

By combining the measured partial differential cross-sections given by eq. (7.8) one can separate out the different contributions from one another, with the exception that the isotope incoherent cross-section cannot be distinguished from the nuclear coherent cross-section. Once the spin incoherent cross-section is found via,

$$\left(\frac{d^2\sigma}{d\Omega dE}\right)_{SI} = \frac{3}{2}\left[3\left(\frac{d^2\sigma}{d\Omega dE}\right)_{SF}^{Z} - \left(\frac{d^2\sigma}{d\Omega dE}\right)_{SF}^{X} - \left(\frac{d^2\sigma}{d\Omega dE}\right)_{SF}^{Y}\right], \tag{7.13}$$

we obtain the nuclear coherent (neglecting the isotope incoherent contribution) and magnetic cross sections using the equations,

$$\left(\frac{d^2\sigma}{d\Omega dE}\right)_{NUC} = \left(\frac{d^2\sigma}{d\Omega dE}\right)^{Z}_{NSF} - \left(\frac{d^2\sigma}{d\Omega dE}\right)^{Z}_{SF} + \frac{1}{3}\left(\frac{d^2\sigma}{d\Omega dE}\right)_{SI}$$
$$\left(\frac{d^2\sigma}{d\Omega dE}\right)_{MAG} = 2\left[\left(\frac{d^2\sigma}{d\Omega dE}\right)^{Z}_{SF} - \frac{2}{3}\left(\frac{d^2\sigma}{d\Omega dE}\right)_{SI}\right] \quad , \qquad (7.14)$$

A full derivation of these equations is given in references [1] and [2].

7.3 The Polarised Neutron Spectrometer, D7

7.3.1 Layout of D7

Our neutron polarisation analysis measurements were performed on the polarised neutron spectrometer D7 at the Institut Laue-Langevin (ILL) in Grenoble. The layout of D7 is shown in figures 7.2, 7.3 and 7.4. D7 is a general-purpose long wavelength multidetector spectrometer. The neutron polariser and analysers can be removed if desired to facilitate conventional diffraction measurements. The inclusion of a neutron chopper enables energy analysis of the scattered neutrons by the time-of-flight method (see section 8.2.1). Our measurements of β-MnAl were performed using D7 in diffraction mode, with the chopper removed. Neutrons from the H15 cold neutron source at the ILL are monochromated by a focusing graphite monochromator crystal. The take-off angle from the monochromator crystal defines the incident neutron wavelength. The three wavelengths available on D7 are, λ = 3.1Å, 4.8Å or 5.7Å. The neutrons pass through a beryllium filter which removes higher orders of the incident wavelength, λ/n where n = 2, 3, ... etc. The neutrons are then polarised by a supermirror polariser (see figure 7.5) and pass through a Mezei π spin flipper which is turned on when measuring the SF cross-section and turned off when measuring the NSF cross-section. The neutron polarisation, which is in the z-direction, is maintained by a neutron guide field of around 1mT. The neutrons pass through the sample which in our measurements was situated in an ILL "Orange" Cryostat, placed in the centre of 3 orthogonal Helmholtz coils, known as the *spin turn coils*. These coils rotate the initial neutron polarisation by $\pi/2$ from the z-direction onto the x- or y-direction before hitting the sample and then rotate the scattered neutrons back by $-\pi/2$. This allows the sequential measurement of the SF and NSF cross-section in each direction.

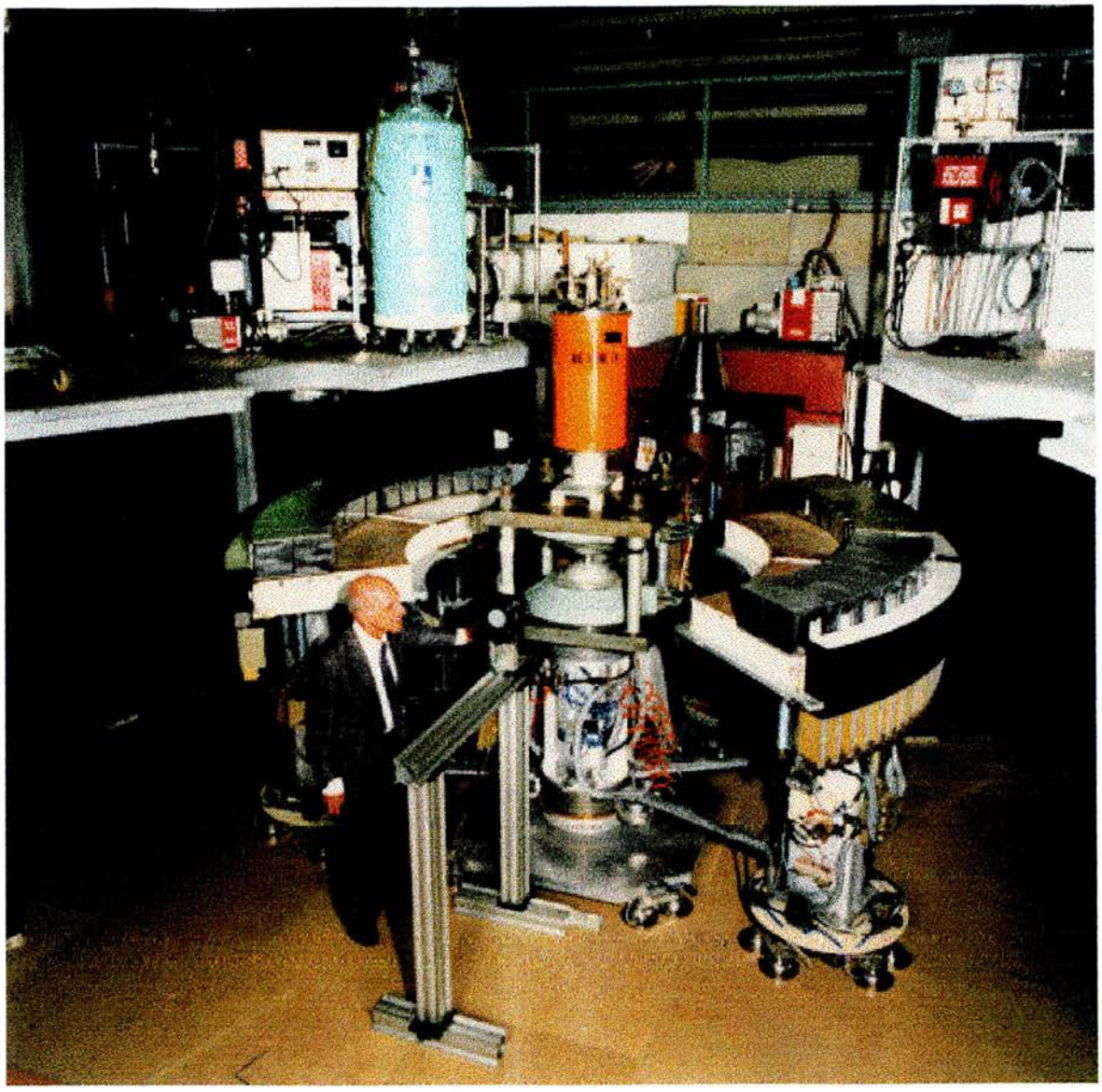

Figure 7.2

Otto Schärpf with the D7 polarised neutron spectrometer [5].

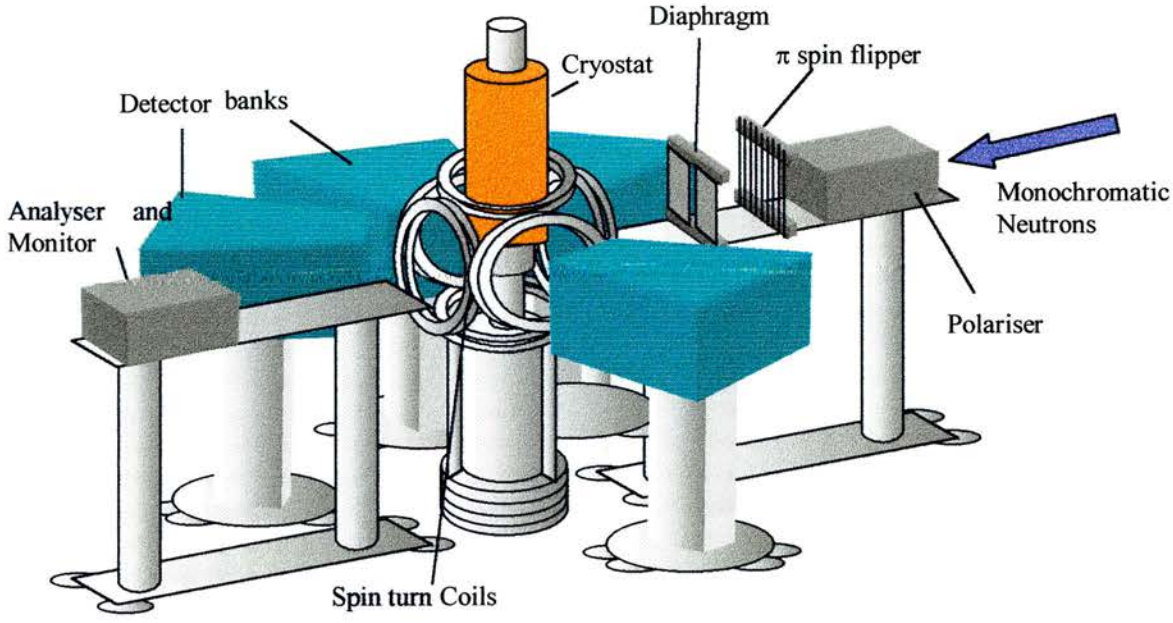

Figure 7.3

Schematic diagram of D7. Three 45 degree detector banks are placed on one side of the instrument, with the 4th bank positioned to cover the blind spot created by the spin turn coils. The neutrons arrive at the polariser via a graphite monochromator and a beryllium filter.

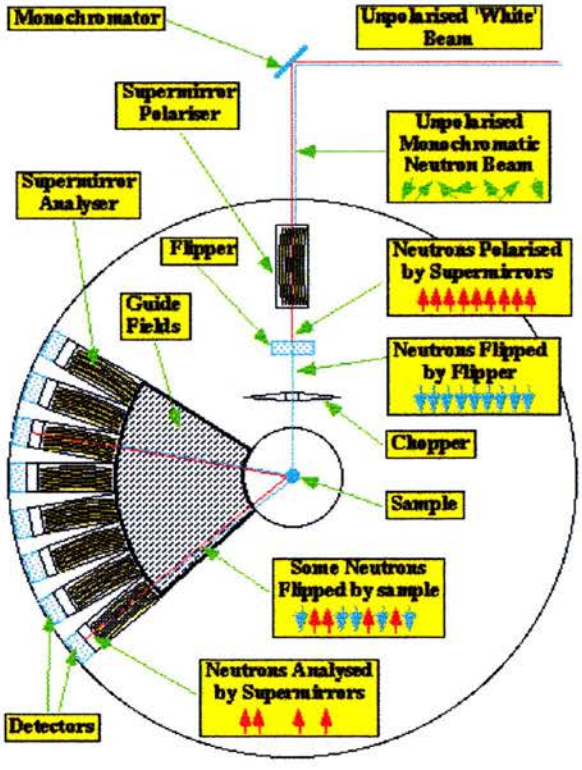

Figure 7.4

Aerial view of the D7 spectrometer layout [6]

The neutrons then enter the detector banks, each of which consists of a neutron guide field, 8 removable supermirror analysers and 16 ^{3}He detector tubes (see figure 7.4). With the supermirror analysers in place only 8 detectors are used in each bank. The 8 detectors are placed 6 degrees apart, each bank subtending an angle of 45 degrees. With four identical banks, there are in total over 6000 supermirrors on D7. The banks can be placed on either side of the instrument and can cover scattering angles from $2\theta = 7°$ to 160°. Figure 7.5 shows the supermirror polariser/analyser used on D7.

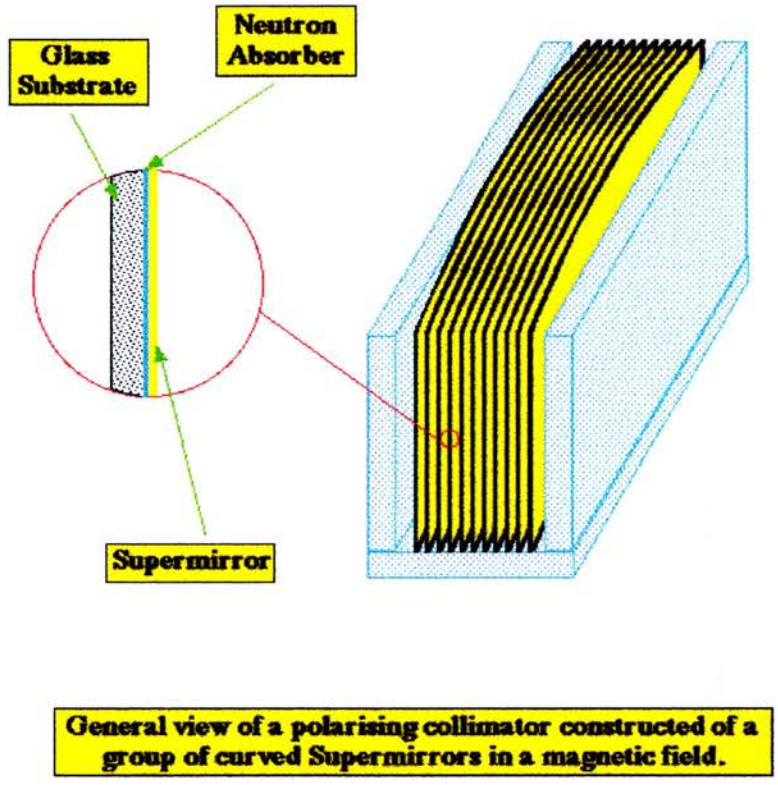

Figure 7.5

The supermirror polariser/analyser used on D7 [7]

A polarising supermirror consists of alternate nonmagnetic and magnetic Ni layers, the latter being magnetised in plane by permanent magnets situated above and below the layers. Since the scattering potential of the magnetised Ni layers depends on the direction of the spin of the incident neutron, neutrons of one spin state are reflected by the supermirror at the Bragg angle which corresponds to the layer thickness, while all the other neutrons are transmitted by the Ni layers and then absorbed by a suitable substrate on the non magnetic layers. By selecting a suitable range of layer thicknesses

it is possible to extend the wavelength range of total reflection for one spin state while almost completely suppressing the other spin state. The neutron supermirror polariser comprises a number of such individual supermirrors in the form of a collimator. The supermirrors are curved to ensure that all neutrons are reflected at least once on a mirror surface.

The transmission of the supermirror polariser and analysers is dependent on the incident wavelength used in the measurement. Figure 7.6 shows the wavelength dependent transmission of the supermirrors used on D7.

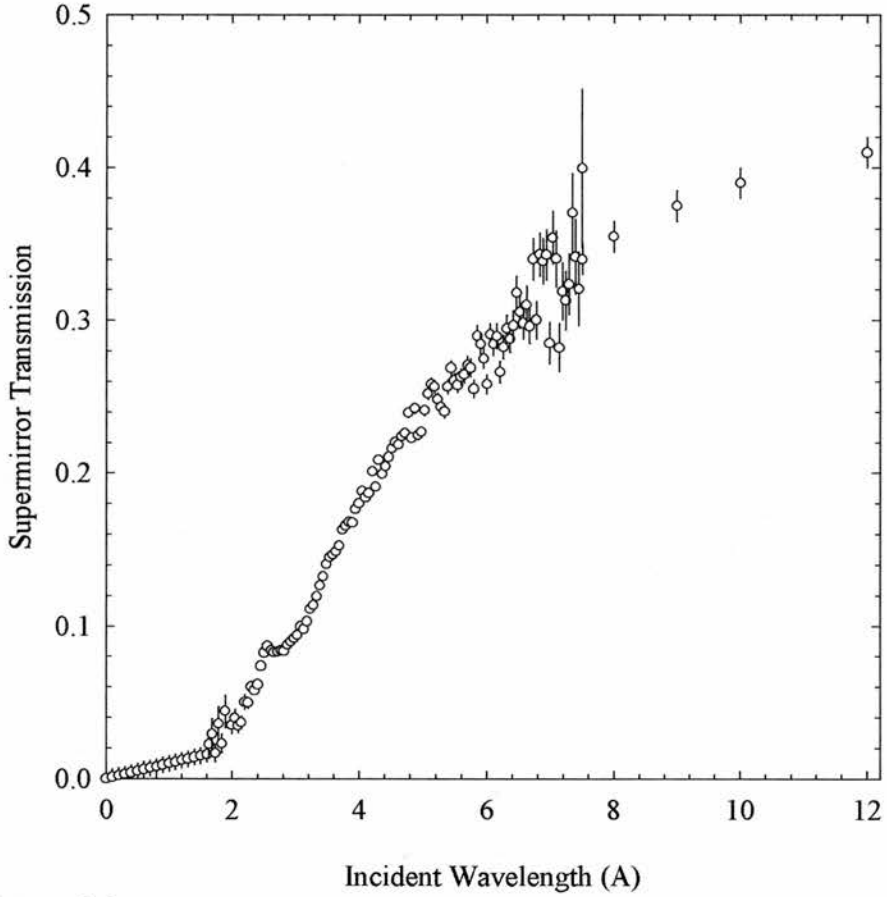

Figure 7.6

Wavelength dependence of the supermirror transmission on D7 [8]

In our measurements of β-MnAl the incident wavelength used was 3.02Å. Using this fact and the above wavelength dependence of the supermirror analysers, we can extract the energy window over which we are integrating eq.(7.8) to extract the differential cross-sections in this measurement. Figure 7.7 shows the supermirror analyser transmission as a function of neutron energy transfer, where we have used the equation,

$$\Delta E = E - E' = 81.72\left(\frac{1}{(3.02)^2} - \frac{1}{\lambda^2}\right), \qquad (7.15)$$

where E and E` are in incident and scattered neutron energies respectively.

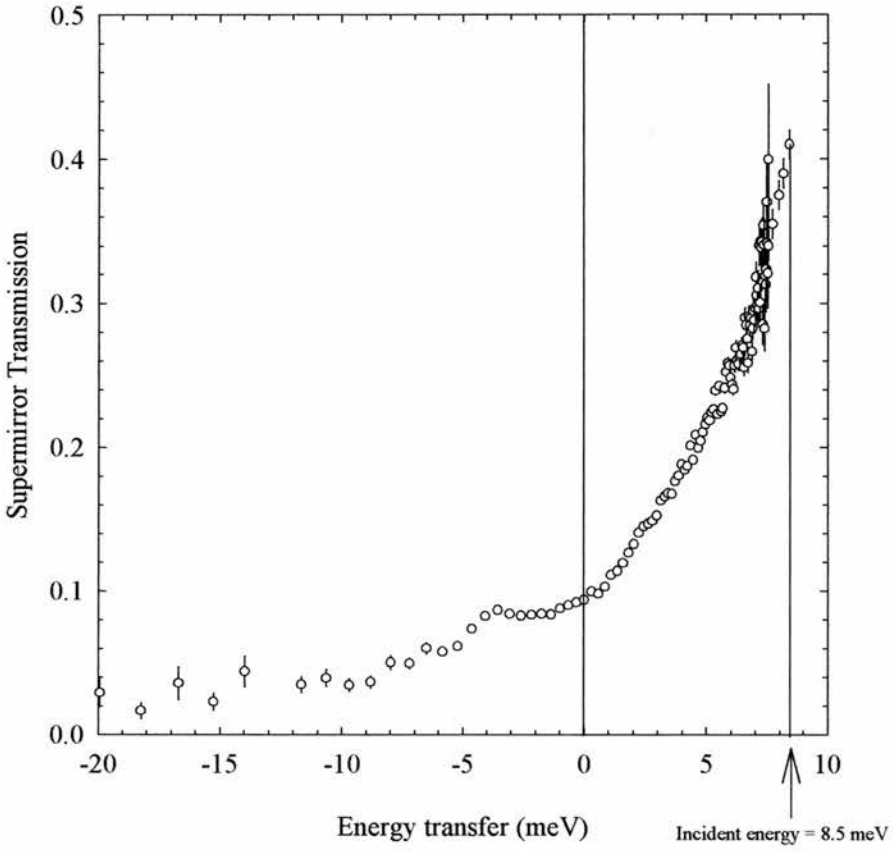

Figure 7.7

The transmission of the supermirror analysers as a function of energy transfer with incident wavelength λ=3.02Å. This represents the energy window of the experiment over which eqs. (7.8) are integrated. The upper limit of the energy window is given by the incident energy of the experiment.

Figure 7.7 demonstrates that the available energy window is extremely narrow on D7. Consequently, measurements of the magnetic cross-section on D7 should only be attempted for static magnetic materials. In view of this fact, our measurements of β-MnAl were all taken at the lowest possible temperature of 1.2K, where our μSR measurements had indicated a transition to a largely static magnetic ground state. Since pure β-Mn does not show a transition to a static magnetic ground state at low temperatures, measurement of the magnetic cross-section of β-Mn was not attempted.

7.3.2 Operation of D7

All of the supermirror analysers on D7 are arranged to transmit neutron spins in the positive z-direction. Therefore, in order to measure the SF cross-sections in eq. (7.8) the spins are flipped by a Mezei π spin flipper so that only neutrons that have been spin flipped by the sample will be counted (see figure 7.4). The operation of the π spin flipper is depicted in figure 7.8.

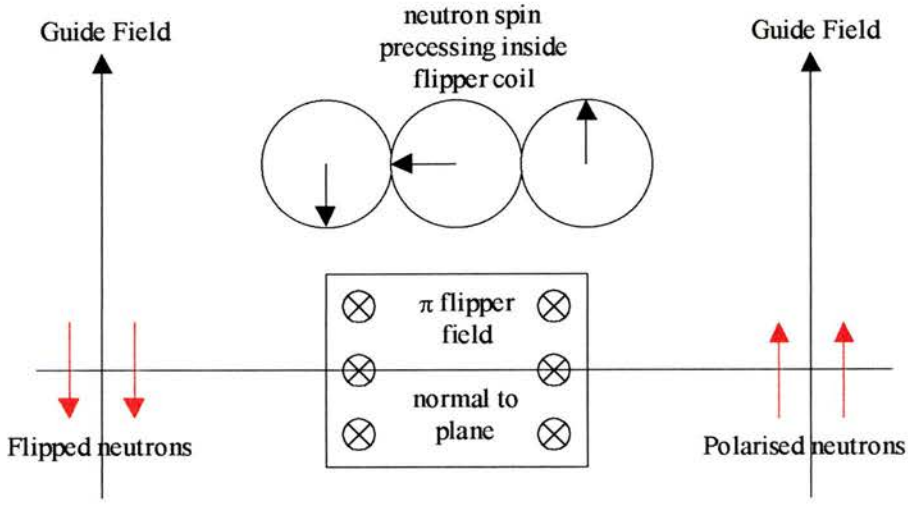

Figure 7.8

The operation of a π spin flipper [2]

The neutron is flipped in a flipper field H_π as a result of a classical Larmor rotation. The transition from the neutron guide field to the flipper field is sudden, corresponding to an adiabatic change in field, ensuring that the neutron energy state is unchanged during the flipping process. Before a neutron polarisation analysis experiment, the current in the π spin flipper coil is adjusted until the field in the coils is given by,

$$H = H_\pi = \frac{67.825}{\lambda L}, \tag{7.16}$$

where λ is the neutron wavelength in Å and L is the coil width in cm [2].

In practice, after the flipper current has been set to the current given by eq. (7.16) a correction coil must be included in the spin flipper to compensate for the neutron guide field. The correction current is adjusted until the transmission of the analyser in front of the transmission monitor is a minimum, corresponding to the maximum number of

spin flipped neutrons. After setting the flipper currents, the typical flipping ratio in the transmission monitor is,

$$FR_T = \frac{\text{transmitted neutron counts/incident neutron counts with flipper off}}{\text{transmitted neutron counts/incident neutron counts with flipper on}} \approx 35-40.$$

In order to obtain finer coverage of the available angular range on D7 it is possible to successively step the detector banks by an angle during the measurement. In our measurements the detector banks were each stepped in 5 one degree increments so that each measurement consisted of $4\times8\times5 = 160$ data points between $10° < 2\theta < 170°$.

In addition to full XYZ polarisation analysis, D7 may also be operated in *z-up/z-down* mode, in which the spin turn coils are removed from the instrument and the SF and NSF cross-sections are measured in the z-direction only. Full separation of the nuclear and magnetic cross-sections can now be performed only if the spin incoherent cross-section is known in advance. In our measurements the spin incoherent cross-section was found for β-$Mn_{0.8}Al_{0.2}$ using full XYZ polarisation analysis. Thereafter our measurements were performed in z-up/z-down mode. Performing measurements in z-up/z-down mode reduces counting time in a typical experiment by a factor of 2.

7.4 Corrections to the Raw Data

In order to obtain the absolute cross-section from the raw number of neutron counts, the following corrections must be applied.

i) The relative detector efficiency correction
ii) The supermirror analyser transmission correction
iii) The background scattering correction
iv) The sample self-attenuation correction
v) The absolute scale of cross-section

7.4.1 The Relative Detector Efficiency Correction

In order to correct the data for detector efficiencies, a measurement of the total (SF plus NSF) differential cross-section of vanadium is performed. Vanadium has the property

that the total neutron scattering cross section is almost 100% spin incoherent. Since the scattering is incoherent, V scatters isotropically over 4π steradians. The number of neutron counts in each detector should therefore be the same if all of the detectors are equally efficient. The measured V counts, having been corrected for self-attenuation (see section 7.4.4) and background scattering (see section 7.4.3), therefore give the relative efficiencies of each detector assuming that a full integration over energy has been performed. This is quite a good assumption on D7, since the total cross-section of V is largely elastic with inelastic phonon contributions to the scattering being small. The measured neutron counts are therefore divided by the corrected vanadium integrals in order to correct the raw data for relative detector efficiency

7.4.2 The Supermirror Analyser Transmission Correction

In order to ensure an accurate separation of the SF and NSF cross-sections, the flipping ratios of each of the supermirror analysers has to be measured. Variations in the flipping ratios of the analysers will occur since a finite number of neutrons of the wrong spin state will be incorrectly transmitted.

In order to measure the flipping ratios of each supermirror analyser, the SF and NSF cross-sections of amorphous quartz are measured in each direction. The cross-section of quartz (SiO_2) is entirely non-spin flip. The flipping ratio for each detector is then defined as,

$$FR = \frac{\text{normalised NSF cross-section}}{\text{normalised SF cross-section}}. \qquad (7.18)$$

In order to obtain similar statistical counting errors in the NSF and SF cross-sections, the SF cross-section is usually measured for between 15 and 20 times longer than the NSF cross-section.

Once the flipping ratios for each detector are obtained, neutron counts are swapped between the measured SF and NSF channels in proportion to the flipping ratio of each detector.

7.4.3 The Background Scattering Correction

The total background scattering in a neutron experiment arises from scattering from the cryostat and sample holder, scattering from parts of the instrumentation and air scattering. We can separate the total background scattering into two components.

- B_1 This term represents background scattering from neutrons which have passed through the sample position.
- B_2 This term represents background scattering from neutrons which have not passed through the sample position.

We can therefore write the relation,

$$I_{sample} = (T(\theta)_{sample} \times I) + (T(\theta)_{sample} \times B_1) + B_2, \quad (7.19)$$

where I_{sample} is the measured neutron counts, $T(\theta)_{sample}$ is the angle dependent transmission coefficient of the sample and I is the corrected number of counts. The definition of $T(\theta)_{sample}$ will be given in section 7.4.4. In order to find the background terms B_1 and B_2 two measurements need to be performed. Firstly, the scattering from an empty sample holder, I_{empty} is measured. I_{empty} will include both background contributions which allows us to write,

$$I_{empty} = B_1 + B_2. \quad (7.20)$$

Secondly, the scattering from a sheet of cadmium in place of the sample is measured. Cd is opaque to neutrons at the energies available on D7, and therefore the measured Cd counts, I_{cd} will only include the second background term,

$$I_{cd} = B_2. \quad (7.21)$$

Combining eqs. (7.19), (7.20) and (7.21) we arrive at the expression for the background subtracted counts,

$$I = T^{-1}(\theta)_{sample} \times (I_{sample} - I_{cd}) - (I_{empty} - I_{cd}). \quad (7.22)$$

7.4.4 The Sample Self-Attenuation Correction

The angle dependent transmission coefficient of a cylindrical sample is given by the Blech-Averbach formula [9],

$$T(\theta) = \exp[-(a_1 + b_1 \sin^2\theta)(\mu R) - (a_2 + b_2 \sin^2\theta)(\mu R)^2], \quad (7.23)$$

where the coefficients a_1, a_2, b_1 and b_2 are,

$a_1 = 1.7133$ $\quad$ $a_2 = -0.0927$

$b_1 = -0.0368$ $\quad$ $b_2 = -0.3750$,

and where $\mu = N\sigma_{tot}$ is the linear absorption coefficient and R is the radius of the cylindrical sample. μR may be calculated from the equation

$$\frac{I_{sample}}{I_{empty}} = \exp(-2\mu R), \tag{7.24}$$

where I_{sample} and I_{empty} are the measured counts in the transmission monitor with the neutrons passing through a very thin slit formed with cadmium metal in front of the sample can. The cadmium slit ensures that the counted neutrons have passed through a thickness of sample equal to the sample diameter.

7.4.5 The Absolute Scale of the Cross-Section

In order to obtain the absolute differential cross-section in units of barns st^{-1} $atom^{-1}$. We need to normalise I given by eq. (7.22) by the number of atoms in the sample. The absolute scale is obtained from the measured vanadium intensity. Vanadium has a well known differential cross-section of 5.07 barns $atom^{-1}$. We can therefore write,

$$\frac{I_{vanadium}}{N_{vanadium}} = \frac{5.07}{4\pi} \text{ (barns st}^{-1}\text{atom}^{-1)}. \tag{7.25}$$

The absolute differential cross-section is then given by,

$$\frac{d\sigma}{d\Omega} = \frac{5.07}{4\pi} \frac{I/N_{sample}}{I_{vanadium}/N_{vanadium}}. \tag{7.26}$$

7.5 XYZ Neutron Polarisation Analysis of β-$Mn_{0.8}Al_{0.2}$

Fully corrected magnetic, nuclear and spin incoherent cross-sections of β-$Mn_{0.8}Al_{0.2}$ obtained from the x, y and z SF and NSF cross-sections using eqs. (7.13) and (7.14) are shown in figure 7.9.

Figure 7.9a shows a strong magnetic response in β-$Mn_{0.8}Al_{0.2}$ peaked at $Q \sim 1.4\text{Å}^{-1}$. This data is very similar to the graph of the Q-dependence of $f^2(Q)M^2(Q)$ measured by Shiga and co-workers, shown in figure 1.14 [10]. The nuclear cross-section shown in figure 7.9b shows the (1 1 0), (2 2 1) and (3 2 1) nuclear Bragg peaks.

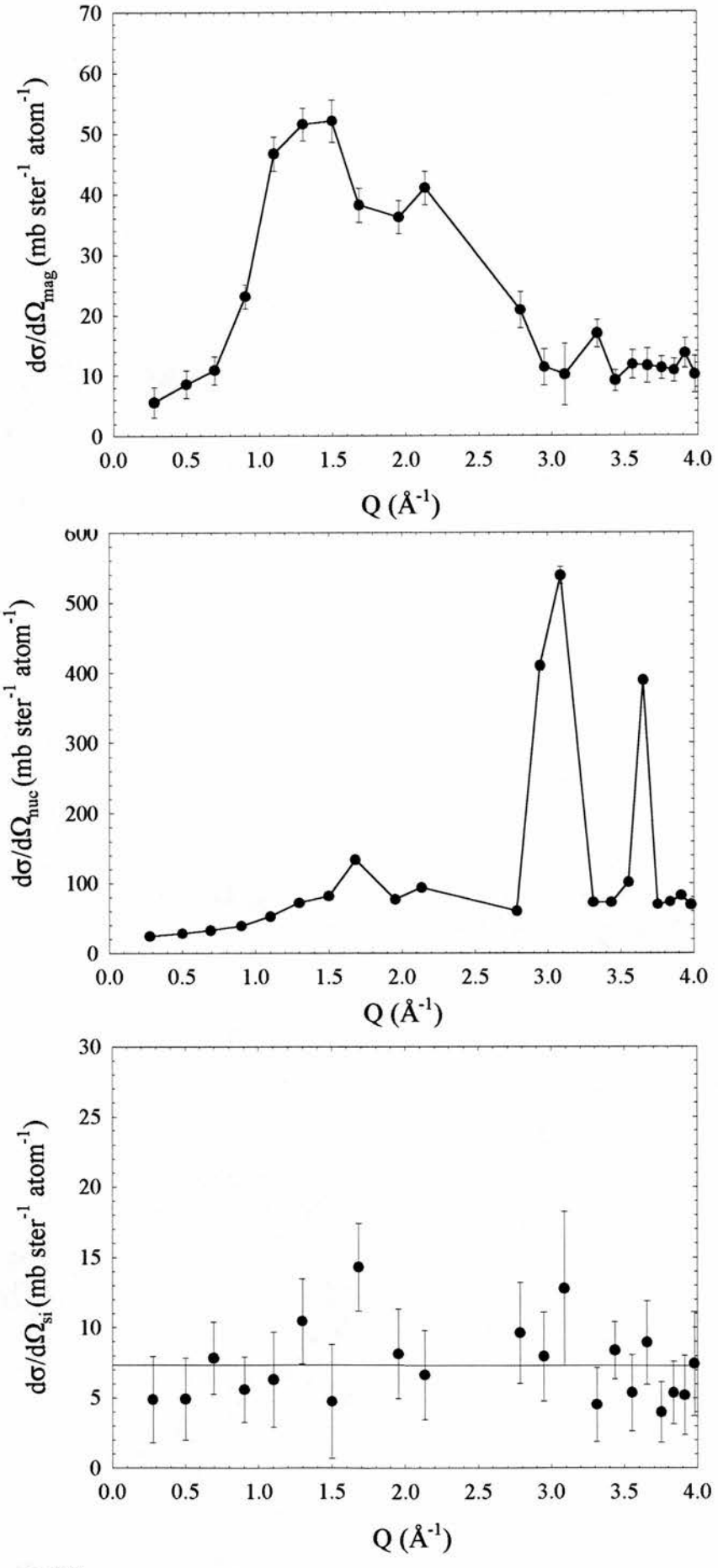

Figure 7.9

The a) magnetic, b) nuclear and c) spin incoherent cross-sections obtained for β-$Mn_{0.8}Al_{0.2}$.

There is also an indication of a diffuse peak in the nuclear cross-section centred at Q ~ 1.6Å^{-1}. This implies short-range substitutional order between the Al impurities in β-$Mn_{0.8}Al_{0.2}$. The spin incoherent cross-section of Mn shown in figure 7.9c was found to be,

$$\left(\frac{d\sigma}{d\Omega}\right)_{SI} = 7.3 \pm 0.3 \text{ mb st}^{-1} \text{ Mn atom}^{-1}. \qquad (7.27)$$

This result is in agreement with the previously reported value measured using pure β-Mn by Davis and Hicks [11] of 9 ± 5 mb st^{-1} Mn atom^{-1}. Their result is slightly higher due to the fact that they assumed that the magnetic scattering of pure β-Mn would be negligible. This is in fact not the case, even at the elastic line, as will be shown in chapter 8.

The XYZ neutron polarisation analysis data taken for β-$Mn_{0.8}Al_{0.2}$ allow us to draw several useful conclusions. The magnetic scattering is strong and approaches zero at Q = 0Å^{-1}, the nuclear cross-section displays nuclear substitutional short-range order, and the spin incoherent cross-section is small for β-$Mn_{0.8}Al_{0.2}$. Since the spin incoherent cross-section is small, it was decided that the remainder of the experiment would be conducted in z-up/z-down mode. The value of the spin incoherent cross-section needed to isolate the magnetic and nuclear scattering using eq. (7.14) was hereafter estimated to be the value required to reduce the magnetic cross-section to zero at Q = 0Å^{-1}. From eq.(7.14) this means that the background level of the SF cross-section was assumed to be 2/3 of the spin-incoherent cross-section. Since the spin-incoherent cross-section measured for β-$Mn_{0.8}Al_{0.2}$ is small compared to the magnetic cross-section, it was concluded that any error in the estimation of the spin-incoherent cross-section would not significantly affect the extracted magnetic scattering. The significant advantage of measuring the samples in z-up/z-down mode was that the counting time need for equivalent statistical errors in the data was halved. This allowed us to obtain more data points in the measured spectra by stepping the detector banks in 1° steps as described in section 7.3.2.

7.6 *Nuclear Short-Range Order in β-MnAl*

7.6.1 Theory of Nuclear Short-Range Order

For a binary alloy of the form $A_{1-c}B_c$, the nuclear disorder cross-section may written as,

$$\left(\frac{d\sigma}{d\Omega}\right)_{NUC} = LS(\mathbf{Q}), \tag{7.28}$$

where L is defined as,

$$L = c(1-c)(b_B - b_A)^2, \tag{7.29}$$

and where b_A and b_B are the scattering lengths of the A and B nuclei. $S(\mathbf{Q})$ is the structure factor of the nuclear disorder scattering and manifests itself as a modulation to and otherwise isotropic background. If the binary alloy forms a random solid solution, there being no nuclear short-range correlations, $S(\mathbf{Q}) = 1$ and eq. (7.28) represents the well known *Laue scattering*. In the mean-field approach suggested by Moss and Walker [12] $S(\mathbf{Q})$ can be written as,

$$S(\mathbf{Q}) \approx (1 + V(\mathbf{Q}))^{-1}, \tag{7.30}$$

where $V(\mathbf{Q})$ is the Fourier transform of the *pair interaction potential*,

$$V(\mathbf{Q}) = \sum_{\mathbf{R}_n} V'(\mathbf{R}_n) e^{i\mathbf{Q}\cdot\mathbf{R}_n}. \tag{7.31}$$

The pair interaction potential $V`(\mathbf{R}_n)$ is proportional to the interaction between a nucleus at an arbitrary origin and a nucleus of the same type at position vector $\mathbf{R}_n$. In the limit of small $V(\mathbf{Q})$ we can make the approximation,

$$\left(\frac{d\sigma}{d\Omega}\right)_{NUC} \approx L(1 - V(Q) + V^2(Q) - V^3(Q) + ...), \tag{7.32}$$

where we have assumed that terms in $V^4(\mathbf{Q})$ and higher are negligible. If one further assumes that first near neighbour interactions are dominant, eq.(7.32) can in principle be spherically averaged to produce an expression for the nuclear disorder cross-section appropriate to a powder measurement [13]. This calculation is however impractical for β-Mn.

Although the underlying symmetry of β-Mn is simple cubic, the point group symmetry is non-centrosymmetric. This means that if we take an arbitrary origin in the β-Mn matrix, the near neighbour nuclei do not fall into well defined nuclear shells with well defined coordinations. To illustrate this point: if we assume that substitutional disorder

will be restricted to the site II sublattice in β-Mn since the Al nuclei show a strong occupational preference for site II in the β-Mn matrix (see chapter 5), we can calculate the site II near neighbour shells around an arbitrary Al atom. Table 7.1 shows the first 25 neighbouring shells around an arbitrary site II origin in pure β-Mn.

Table 7.1 The first 24 neighbouring shell coordination numbers and shell distances of an arbitrary site II nucleus in the pure β-Mn matrix.

n	Z_n	R_n (Å)
1	6	2.6557
2	2	3.2675
3	2	3.8958
4	4	4.3696
5	2	4.4259
6	4	4.5555
7	4	4.6312
8	4	5.1505
9	4	5.1982
10	2	5.2646
11	4	5.7698
12	4	6.2506
13	6	6.3200
14	8	6.3816
15	2	6.5248
16	4	6.5715
17	4	6.7700
18	4	6.8190
19	4	6.9892
20	4	7.2984
21	4	7.3773
22	2	7.4241
23	4	7.6188
24	2	7.7155

Table 7.1 shows that the near neighbour shells around site II in β-Mn are extremely tightly spaced. For instance, shells 8, 9 and 10 have almost the same radial distance from the origin. In consequence, consideration of the first 24 near neighbour shells only covers a radial distance of 7.7155Å. Another consequence of the non-

centrosymmetric point group is the that the coordination numbers of the shells do not increase with increasing radial distance.

The calculation of the radial average eq. (7.32) is therefore extremely complicated due to the complex β-Mn crystal structure and would probably need to include many terms in R_n to cover the required radial correlation distance.

7.6.2 The Warren-Cowley Formalism

According to the formalism of Cowley [14] the nuclear disorder structure factor may be expressed as,

$$S(\mathbf{Q}) = \sum_N \alpha_{0N} e^{i\mathbf{Q}\cdot\mathbf{R}_{0N}}, \tag{7.33}$$

where the sum is over all atomic sites N at position vectors R_{0N}. α_{0N} is the Warren-Cowley (WC) parameter for site N, which is defined using the conditional probabilities $P_{0N}{}^{\nu\mu}$ of finding a μ nucleus at site N if a ν nucleus is at the origin, i.e.,

$$\alpha_{0N} = 1 - \frac{P_{0N}{}^{BA}}{c} = \frac{P_{0N}{}^{BB} - c}{1-c}, \tag{7.34}$$

where c is the concentration of the B nucleus. Factorising eq.(7.33) to obtain the Warren-Cowley parameters for near neighbour shells, and taking the polycrystalline average we obtain the expression,

$$S(Q) = \sum_n \alpha_{0n} Z_n \frac{\sin(QR_n)}{QR_n}, \tag{7.35}$$

where the sum is over n near neighbour shells of radial distance R_n from the origin each with coordination number Z_n. Combining eqs. (7.28) and (7.35), the nuclear disorder cross-section can then be written as,

$$\left(\frac{d\sigma}{d\Omega}\right)_{NUC} = c(1-c)(b_B - b_A)^2 \left[1 + \alpha_{01} Z_1 \frac{\sin(QR_1)}{QR_1} + \alpha_{02} Z_2 \frac{\sin(QR_2)}{QR_2} + \ldots\ldots\right], \tag{7.36}$$

where we have used the result that $\alpha_{00} = 1$. Notice that in a randomly substituted binary alloy, the conditional probability of finding a B nucleus is the concentration c, ensuring that the Warren-Cowley parameters are equal to zero as required. The sum in eq. (7.36) should be performed over sufficient nuclear shells so that the short-range correlation length is less than the radius of the largest shell considered.

Attempts at a least-squares fit of eq. (7.36) to our nuclear diffuse scattering data over the β-Mn nuclear shells proved to be fruitless. The first difficulty is that the shells are extremely close packed and contain relatively few nuclei. One is therefore forced to include a very large number of terms in the sum of eq. (7.36), with each fitted WC parameter having extremely little statistical significance in the fit. The second difficulty is that in attempting to fit eq.(7.36) to the data with a predetermined number of WC parameters, one is forcing the inclusion of Fourier components in the sum which may not be physically consistent with each other.

In order to extract physically meaningful WC parameters from the measured nuclear diffuse cross-section, we have developed a Reverse Monté-Carlo algorithm which calculates eq.(7.36) from first principles and iteratively compares the calculated cross-section to the measured cross-section.

7.6.3 RMC Modelling of Nuclear Disorder Scattering

A full listing of the RMC nuclear disorder modelling program "INTA" is given in appendix A.

In our program a β-Mn lattice of 4×4×4 unit cells with periodic boundary conditions is generated. Since we are assuming that the nuclear disorder resides completely on site II, we have 12 atoms per unit cell giving 4×4×4×12 = 768 nuclei in the simulation. The impurity concentration and the Laue scattering level, L (eq. (7.29)) are input by the user. The program then randomly assigns Al atoms to lattice positions until the desired concentration level is reached. Alternatively, the user can specify the Al positions by using a nuclear position file, previously generated by the program. The program then calculates the conditional probabilities of finding an Al atom in the nth near neighbour shell with each Al atom in turn taken as the origin. The probabilities are then summed and averaged, and the WC parameters calculated from eq (7.34). The cross-section is calculated, summing over the first 24 near neighbour shells, and the calculated cross-section is compared to the measured cross-section. The goodness of the fit of the calculated cross-section to the data is given by the usual definition of χ^2 [16],

$$\chi^2 = \frac{\sum_D w\left(\left.\frac{d\sigma(Q_D)}{d\Omega}\right|_{cal} - \left.\frac{d\sigma(Q_D)}{d\Omega}\right|_{exp}\right)^2}{D}, \qquad (7.37)$$

where D is the number of experimental data points and where w is the weighting factor, defined as,

$$w = \frac{1}{(E_{exp}(Q_D))^2}, \qquad (7.38)$$

where $E_{exp}(Q_D)$ is the experimental error of the Dth data point.

After the initial calculation of χ^2 up to 5 Al nuclei atoms are swapped randomly with Mn nuclei and the cross-section is recalculated. If the value of χ^2 is less than the original value then the moves are accepted. The process is then repeated with moves only being accepted if χ^2 is less than the previously accepted χ^2 value. Each time a move is accepted, the program outputs files containing the calculated fit to the data, the conditional probabilities for each shell and the Mn and Al nuclear position file, enabling the progress of the program to be monitored without interruption. The program continues until a tolerance value of χ^2 input by the user is achieved. The program was found to achieve a reasonable fit to the data in about 30 minutes, corresponding to around 2000 moves. The program was run in two stages with 5 Al nuclei initially swapped with Mn nuclei per move, followed by only 1 swap per move as the value of χ^2 became smaller.

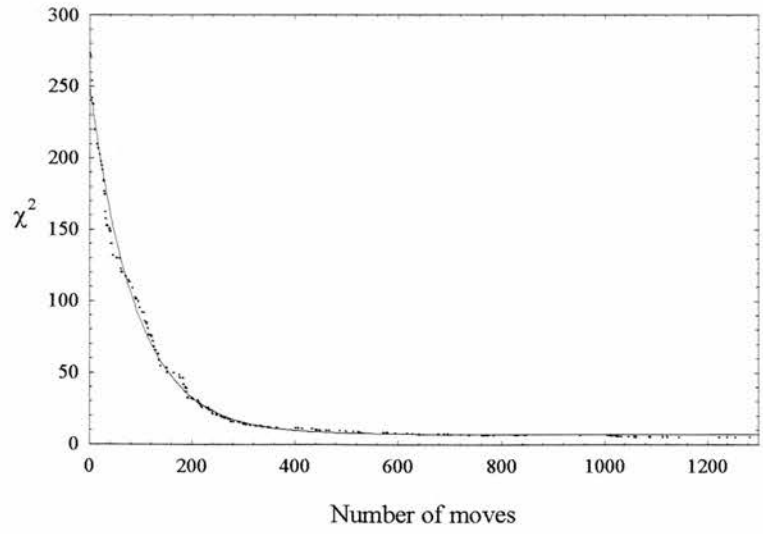

Figure 7.10

Plot of χ^2 versus the number of moves for a typical run of the RMC modelling program "INTA". The solid line demonstrates that χ^2 decreases exponentially.

The variation of χ^2 with the number of moves for a typical program run is shown in figure 7.10. The solid line in figure 7.10 indicates that χ^2 decreases exponentially with the number of moves. INTA was run several times with different initial random configurations. The results, within statistical accuracy were the same.

Extracting the WC parameters from the measured data in this manner has several advantages over a straightforward least-squares fitting procedure:

i) No assumptions are made as to the shell sizes and coordinations.

ii) The WC parameters obtained are physically consistent with one another.

iii) The procedure automatically produces a table of the Mn and Al nuclear positions.

iv) The WC parameters are automatically constrained to lie within the limits;

$$\alpha_{min} = -c/(1-c) \quad \rightarrow \quad \alpha_{max} = 1.$$

7.6.4 Results

The measured nuclear cross-sections of β-$Mn_{0.97}Al_{0.03}$, β-$Mn_{0.94}Al_{0.06}$, β-$Mn_{0.9}Al_{0.1}$ and β-$Mn_{0.8}Al_{0.2}$ measured using z-up/z-down neutron polarisation analysis is shown in figure 7.11. The nuclear Bragg peaks have been removed from the raw data. Figure 7.11 shows that the experimental cross-sections are extremely well represented by the simulation output. The pair probabilities P_n^{BB}, and corresponding WC parameters α_n calculated using eq (7.34), for each of the alloys studied, are given in table 7.2. The pair probabilities are plotted as a function of radial distance in figure 7.12.

The dependence of P_n^{BB} on radial distance was parameterised using a damped cosine function, shown as a solid line in figure 7.12. The errors shown in figure 7.12 and given in table 7.2 are the standard errors calculated from variance of the distributions of the pair probabilities for each of the 24 shells used to generate the calculated cross-section using eq. (7.36). The standard procedure for extracting errors in the fitting parameters associated with a least-squares fitting procedure (see, for example [16]) is inappropriate here, since in our RMC procedure the pair probabilities are not arbitrarily adjusted fitting parameters. They are ab-initio values calculated from the modelled crystal lattice, and therefore are inter-dependent. Errors associated with the χ^2 fit could therefore not be extracted from our simulations.

Table 7.2 Warren Cowley parameters and corresponding pair probabilities of the first14 near neighbour shells from the "INTA" simulation program for the alloys shown.

	β-$Mn_{0.97}Al_{0.03}$			β-$Mn_{0.94}Al_{0.06}$			β-$Mn_{0.9}Al_{0.1}$			β-$Mn_{0.8}Al_{0.2}$		
n	R_n	α_n	P_n^{BB}	R_n	α_n	P_n^{BB}	R_n	α_n	P_n^{BB}	R_n	α_n	P_n^{BB}
1	2.6599	-0.02(1)	0.03(1)	2.6620	-0.05(1)	0.05(1)	2.6687	-0.08(1)	0.10(1)	2.6830	-0.14(2)	0.24(1)
2	3.2726	-0.05(1)	0.000(1)	3.2753	-0.11(1)	0.000(1)	3.2835	-0.19(1)	0.01(1)	3.3011	-0.29(2)	0.14(2)
3	3.9018	-0.02(2)	0.03(2)	3.9050	-0.04(2)	0.07(2)	3.9149	0.0(3)	0.16(2)	3.9358	0.16(3)	0.44(2)
4	4.3771	0.01(2)	0.07(2)	4.3800	0.13(3)	0.22(2)	4.3911	0.10(2)	0.25(2)	4.4146	0.10(2)	0.40(1)
5	4.4329	0.08(4)	0.13(3)	4.4364	0.03(3)	0.13(3)	4.4476	0.12(4)	0.27(3)	4.4714	0.08(3)	0.39(2)
6	4.5627	0.0(2)	0.05(2)	4.5663	0.01(2)	0.11(2)	4.5778	0.08(2)	0.23(2)	4.6023	0.06(2)	0.38(1)
7	4.6380	-0.01(2)	0.04(1)	4.6422	0.06(2)	0.15(2)	4.6539	0.02(2)	0.18(2)	4.6788	0.05(2)	0.37(1)
8	5.1587	0.02(2)	0.07(2)	5.1627	-0.08(1)	0.02(1)	5.1758	-0.11(1)	0.07(1)	5.2035	-0.04(2)	0.30(1)
9	5.2064	0.02(2)	0.07(2)	5.2105	-0.07(1)	0.04(1)	5.2237	-0.06(2)	0.11(1)	5.2517	-0.11(2)	0.26(1)
10	5.2729	0.0(3)	0.05(2)	5.2771	-0.01(2)	0.09(2)	5.2904	-0.05(2)	0.12(2)	5.3187	0.02(3)	0.35(2)
11	5.7787	-0.01(2)	0.04(1)	5.7835	0.05(2)	0.14((2)	5.7981	0.05(2)	0.21(2)	5.8292	0.06(2)	0.38(2)
12	6.2604	0.0(2)	0.05(2)	6.2654	0.01(2)	0.11(2)	6.2812	0.07(2)	0.23(2)	6.3149	-0.01(2)	0.33(1)
13	6.3300	0.03(2)	0.08(2)	6.3350	0.05(2)	0.15(2)	6.3510	0.03(2)	0.19(1)	6.3850	0.05(2)	0.37(1)
14	6.3914	-0.03(1)	0.02(1)	6.3967	0.0(1)	0.10(1)	6.4129	0.0(1)	0.17(1)	6.4472	-0.06(1)	0.29(1)

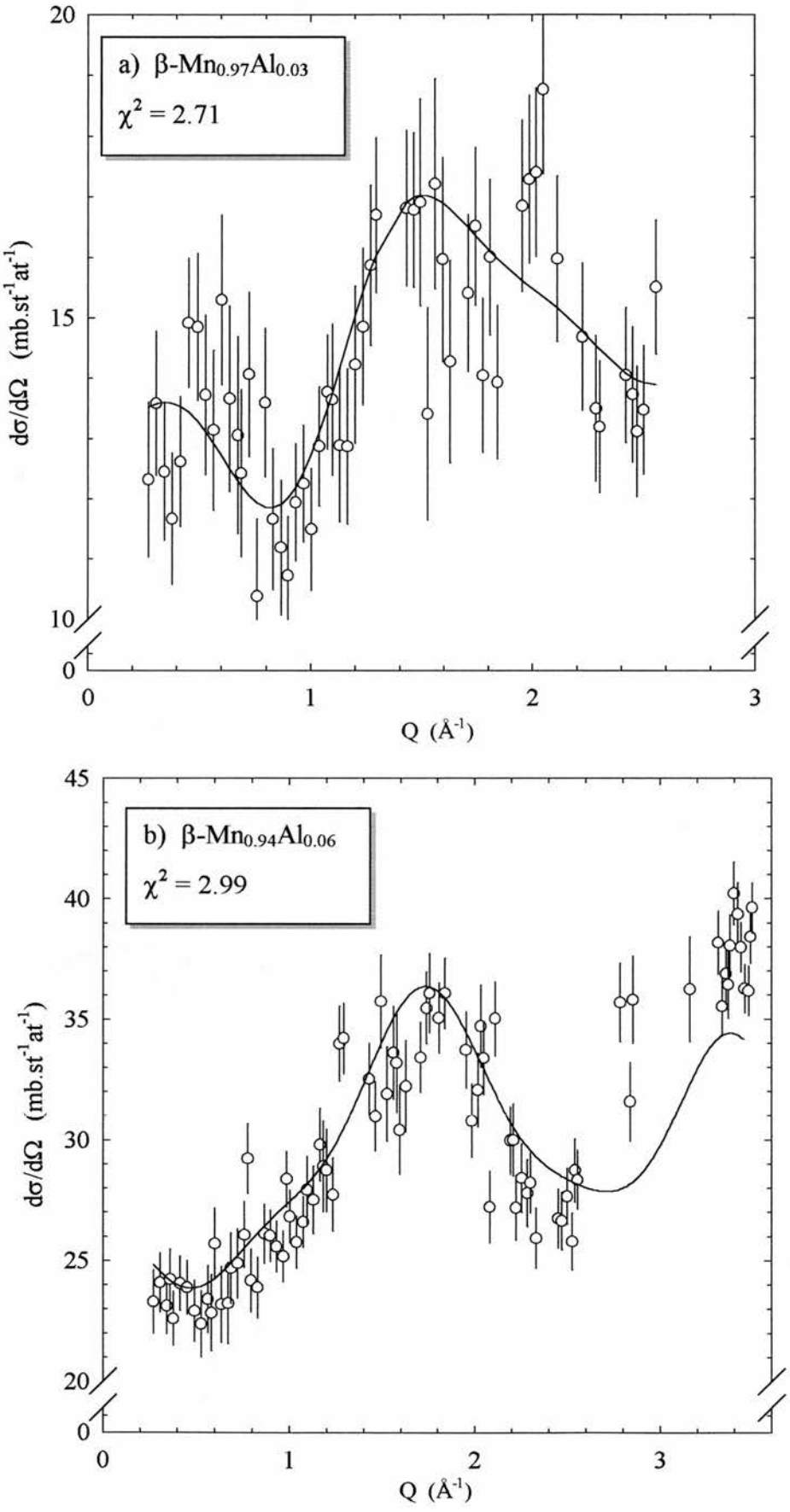

Figure 7.11

Nuclear cross-sections of a) β-$Mn_{0.97}Al_{0.03}$ and b)β-$Mn_{0.94}Al_{0.06}$ with nuclear Bragg peaks removed. Solid line is simulated cross-section from "INTA".

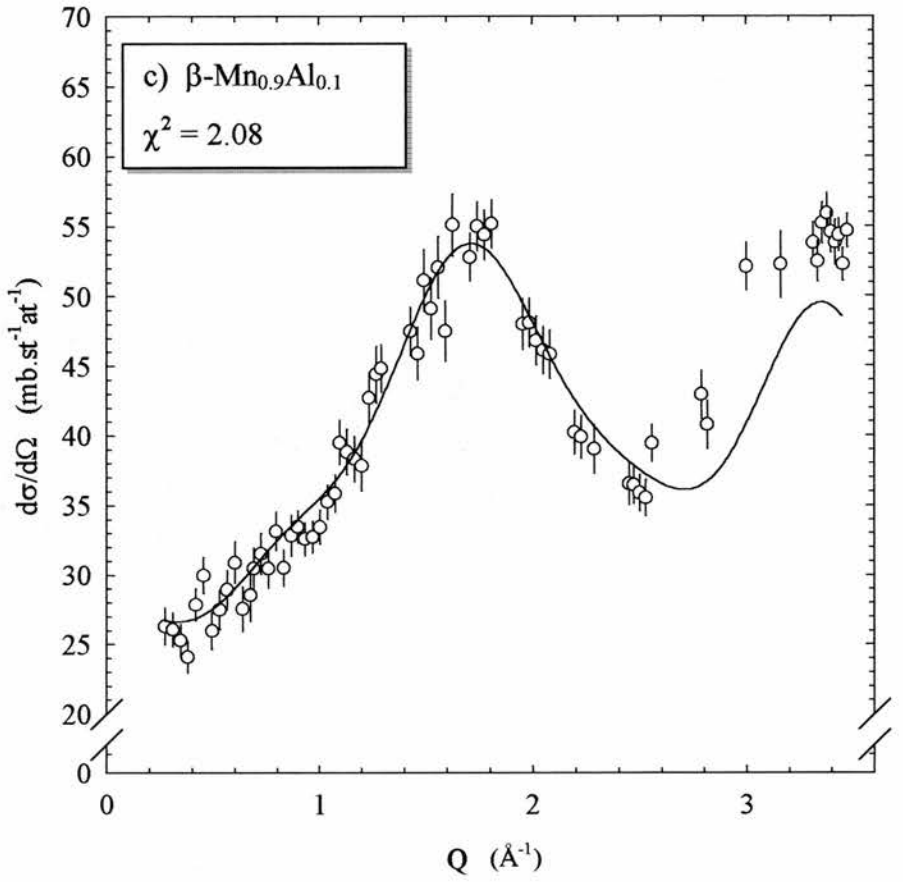

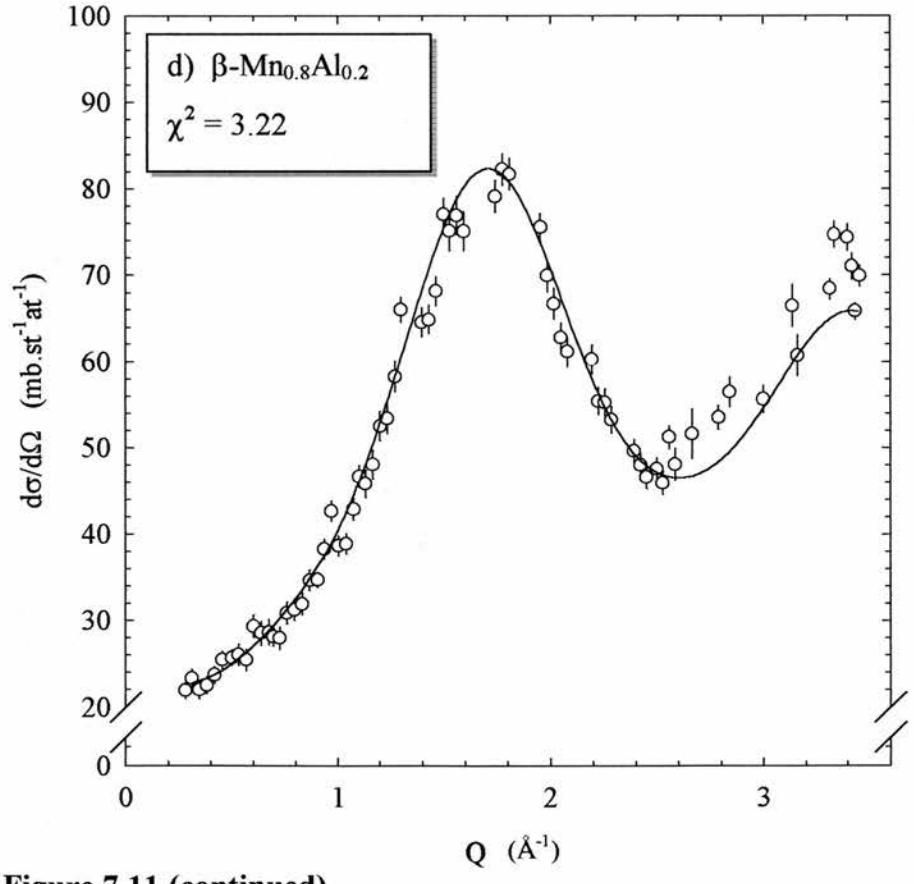

Figure 7.11 (continued)

Nuclear cross-sections of c) β-$Mn_{0.9}Al_{0.1}$ and d) β-$Mn_{0.8}Al_{0.2}$ with nuclear Bragg peaks removed. Solid line is simulated cross-section from "INTA".

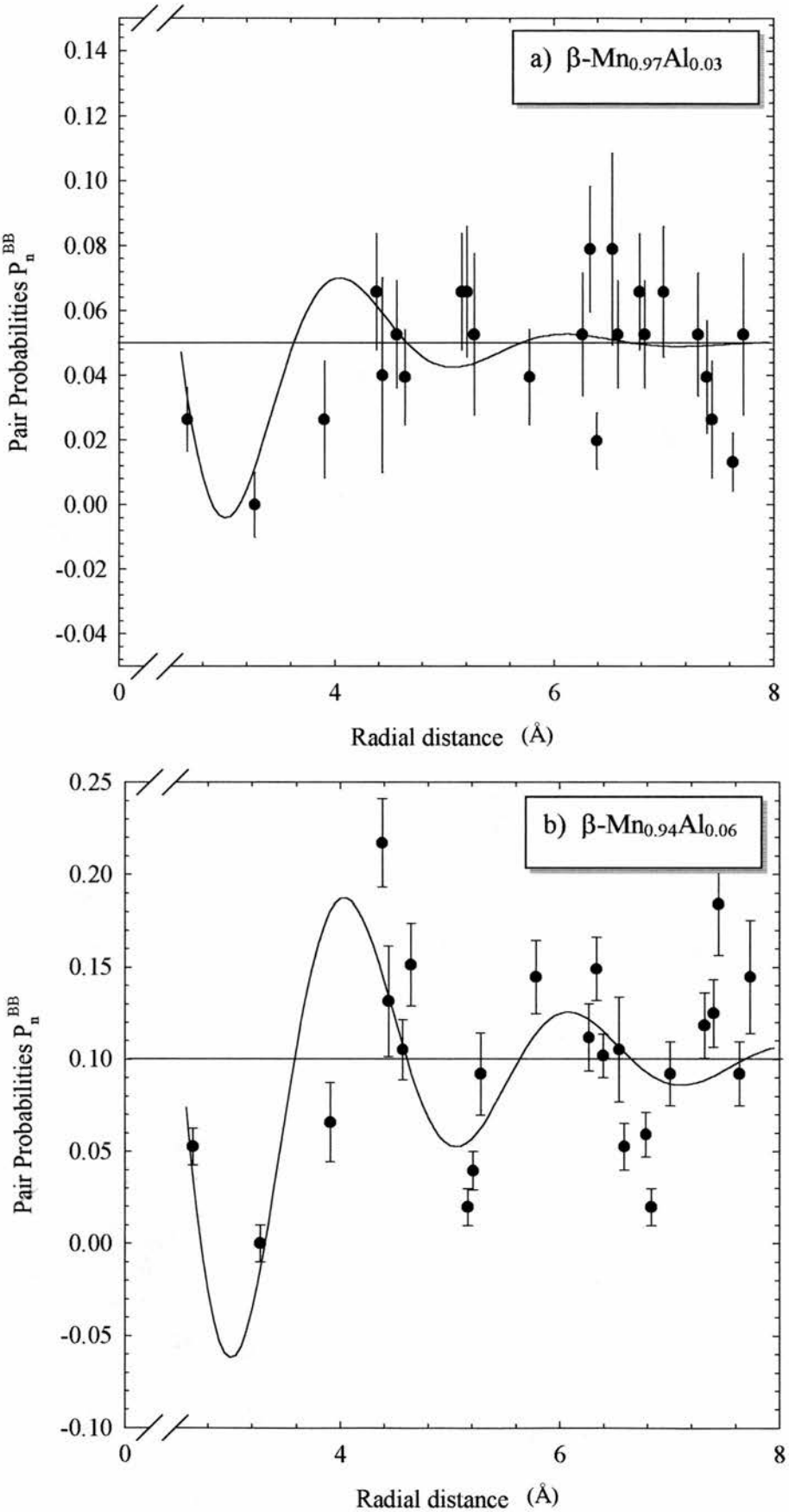

Figure 7.12

Pair probabilities P_n^{BB} from "INTA" simulation of a) β-$Mn_{0.97}Al_{0.03}$ and b) β-$Mn_{0.94}Al_{0.06}$. The solid lines shown are fits to a damped cosine curve. The straight line indicates the probability level expected for a random substitution.

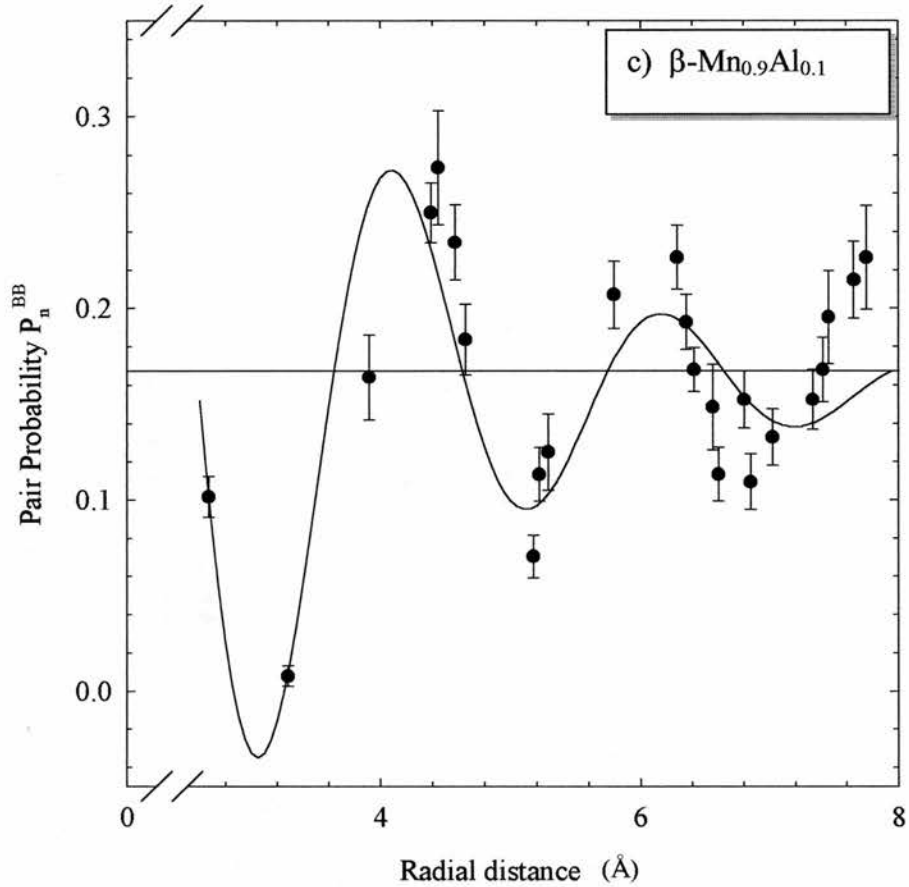

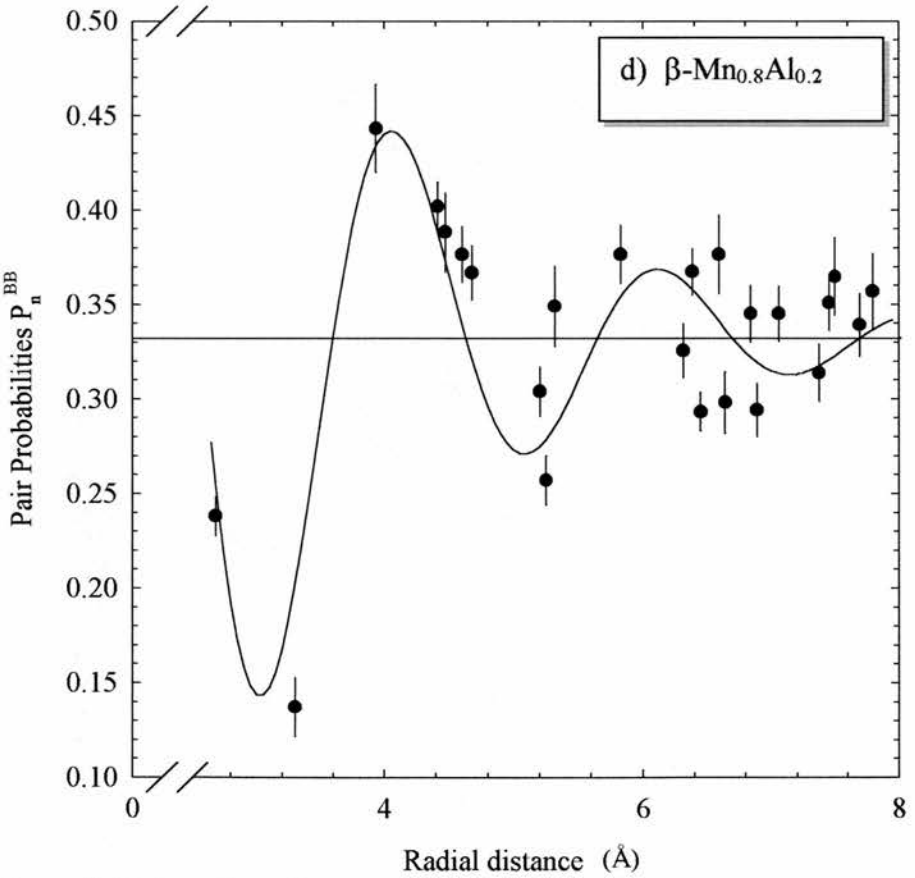

Figure 7.12 (continued)

Pair probabilities P_n^{BB} from "INTA" simulation of c) β-$Mn_{0.9}Al_{0.1}$ and d) β-$Mn_{0.8}Al_{0.2}$. The solid lines shown are fits to a damped cosine curve. The straight line indicates the probability level expected for a random substitution.

The graphs of the dependence of the pair probabilities on radial distance all display the same frequency of oscillation around $P_n^{BB} = c$ where c is the Al concentration, with the first peak in the curve coming at around R = 4Å. This corresponds to a Q of ~1.6Å^{-1} which is the position of the first maximum in the nuclear cross-section for all the alloys studied. The parameters obtained from a fit to a damped cosine function of the form,

$$\alpha_n(R) = \cos(-kR)\exp(-dR), \qquad (7.40)$$

are given in table 7.3.

Table 7.3 Laue scattering level and parameters obtained from eq. (7.40) for the concentrations shown.

	Laue scattering (mb st^{-1} atom^{-1})	k (Å^{-1})	d (Å^{-1})
β-$Mn_{0.97}Al_{0.03}$	15	3.03±0.06	0.95±0.2
β-$Mn_{0.94}Al_{0.06}$	29	3.07±0.02	0.64±0.04
β-$Mn_{0.9}Al_{0.1}$	43	3.03±0.02	0.53±0.03
β-$Mn_{0.8}Al_{0.2}$	68	3.05±0.02	0.54±0.04

While the frequency of oscillation remains constant throughout the concentration range studied, the damping of the nuclear correlations decreases as the Al concentration increases, implying that the correlation length of the nuclear disorder increases with increasing Al concentration.

In conclusion, we have isolated the nuclear disorder cross-section of β-$Mn_{1-x}Al_x$ with x=0.03, 0.06, 0.1 and 0.2, and extracted the short-range Warren-Cowley parameters using an RMC algorithm. Al impurities display a tendency to anti-cluster in the β-Mn site II sublattice with the first maximum in the nuclear disorder cross-section appearing at Q ~ 4Å^{-1}. The range of the short-range nuclear correlations increases with increasing Al concentration whereas the frequency of oscillation of the WC parameters remains unchanged, implying that the effective pair interaction potentials between Al impurities in the β-Mn matrix are independent of Al concentration. Figure 7.13 shows the output positions of Mn and Al nuclei in β-$Mn_{0.8}Al_{0.2}$ generated by "INTA".

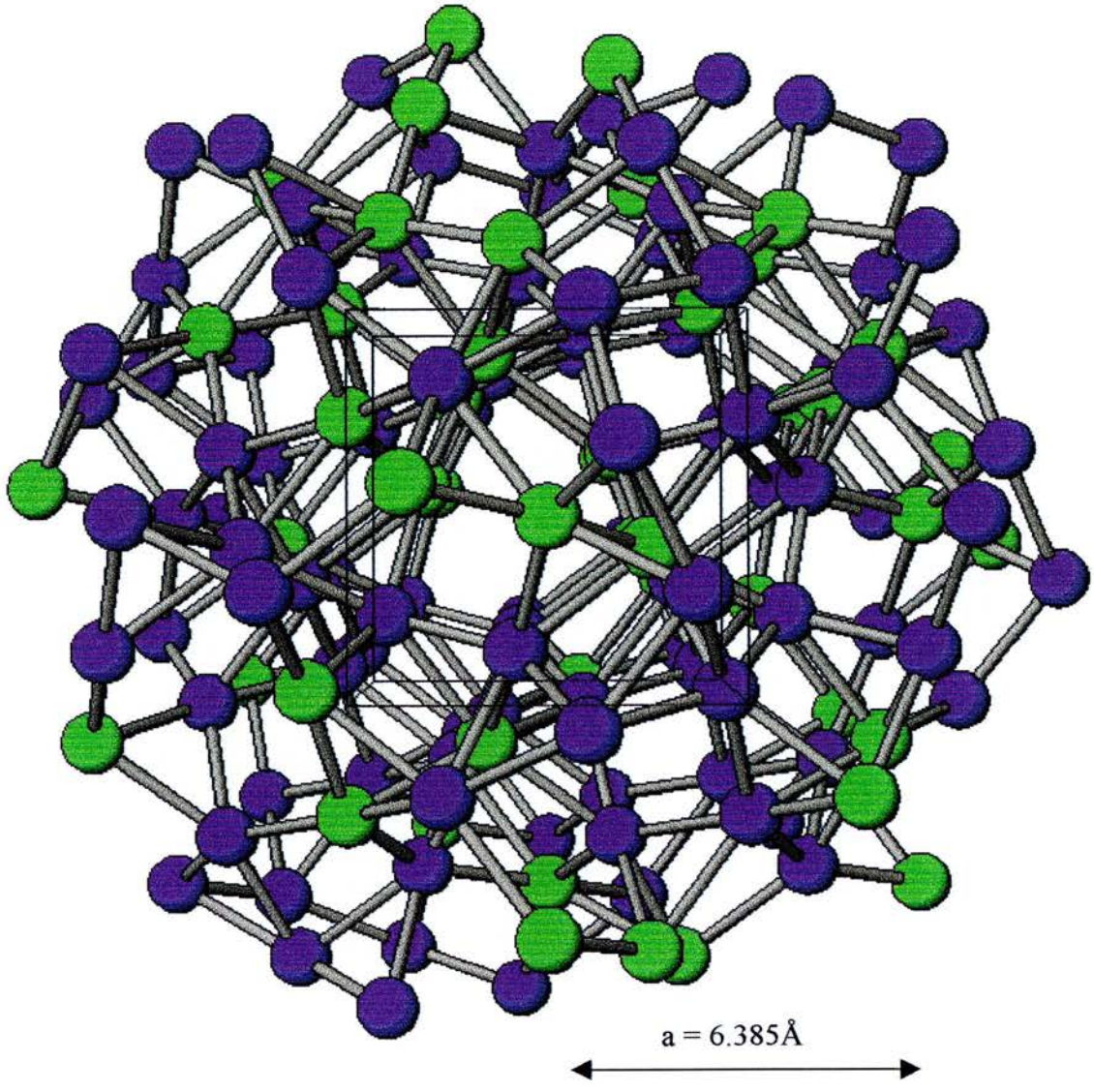

Figure 7.13

Depiction of the site β-Mn sublattice of β-$Mn_{0.8}Al_{0.2}$ using the nuclear position file generated by "INTA". Mn atoms are shown in blue and Al atoms in green. The β-Mn unit cell is shown in the centre. The triangular coordination of the Mn atoms is clearly seen to be disrupted by the introduction of Al, supporting the assertion that relief of geometrical frustration occurs in the β-Mn structure when Al is added.

7.7 Magnetic Short-Range Order in β-MnAl

7.7.1 Theory of Magnetic Short-Range Order

The expression for the magnetic differential cross-section is obtained by integrating eq. (7.12) to obtain

$$\left(\frac{d\sigma}{d\Omega}\right)_{MAG} = \frac{2}{3}\left(\frac{r_0\gamma}{2}\right)^2 |f(\mathbf{Q})|^2 S(\mathbf{Q}) M^2(\mathbf{Q}), \qquad (7.41)$$

where $M(\mathbf{Q})$ is the Fourier transform of the spatially dependent magnetisation density $M(\mathbf{r})$. $M^2(\mathbf{Q})$ can be written as,

$$M^2(\mathbf{Q}) = g_s{}^2 S(S+1) \sum_N \frac{\mathbf{S}_0.\mathbf{S}_N}{S(S+1)} \exp^{i\mathbf{Q}.\mathbf{R}_N}, \qquad (7.42)$$

where $\mathbf{S}_0$ and $\mathbf{S}_N$ are the atomic spin vectors at an arbitrary origin and the Nth atom respectively. S(S+1) is the self correlation term. Factorising eq. (7.42) into near neighbour shells and taking a polycrystalline average we obtain the expression [15],

$$\left(\frac{d\sigma}{d\Omega}\right)_{MAG} = \frac{2}{3}\left(\frac{r_0\gamma}{2}\right)^2 |f(Q)|^2 g_s{}^2 S(S+1)\left[1 + \frac{\langle \mathbf{S}_0.\mathbf{S}_1 \rangle}{S(S+1)} N_1 \frac{\sin(QR_1)}{QR_1} + \ldots\ldots\right], \qquad (7.43)$$

where the factor $2/3(r_0\gamma/2)^2 = 0.049$ barns, $g_s{}^2 = 4$ for Mn atoms and R_n and N_n are the radii and coordination numbers of the nth near neighbour shells respectively, and where we have assumed that there are no concentration driven variations in the magnetic moment distribution arising from nuclear short-range order, so that $S(\mathbf{Q}) = 1$ in eq (7.41). However, we know from the previous section that there is marked nuclear short-range order present in the Mn site II sublattice. The possibility of nuclear short-range order affecting the moment distribution is therefore extremely likely to affect the measured magnetic cross-section in this experiment. In order to obtain an expression for the magnetic differential cross-section therefore, we have to perform a spherical average of $f^2(\mathbf{Q})S(\mathbf{Q})M^2(\mathbf{Q})$.

In practice, this calculation is extremely complicated, especially for the complex β-Mn structure. We have therefore used a further reverse Monté-Carlo algorithm to model the magnetic moment distribution in β-MnAl.

7.7.2 RMC Modelling of Magnetic Diffuse Scattering

The RMC program "MAG" for the modelling of our experimental magnetic neutron scattering data was based on the program "INTA" described in section 7.6.3. A full listing of the program "MAG" is given in appendix B.

In our magnetic diffuse scattering RMC modelling program "MAG", the nuclear positions and species are defined by the nuclear position file which is output from the program "INTA", with periodic boundary conditions being defined as before. Magnetic Heisenberg spins of unit length are then assigned to each Mn atom in the matrix and are oriented randomly. Alternatively, the spin directions and nuclear positions can be read from a previously generated magnetic position file. The value of the β-MnAl lattice constant and the estimated value of S(S+1) is input by the user. The fact that the spins have unit length satisfies the requirement that,

$$\frac{\langle \mathbf{S}_0 . \mathbf{S}_n \rangle}{S(S+1)} = \langle \hat{\mathbf{S}}_0 . \hat{\mathbf{S}}_n \rangle . \qquad (7.44)$$

The magnetic short-range correlations are therefore calculated by taking the dot product of each Mn spin with each other Mn spin taken as the origin in turn. The magnetic correlation parameters are then summed and averaged for each shell, and the cross-section is calculated from eq. (7.43) where the sum is performed over the first 24 near neighbour shells. Since eq. (7.43) is calculated over a lattice where the Al positions are known, the nuclear short-range order structure factor S(Q) is automatically taken into account. The calculated cross-section is compared to the fully corrected experimental data in the same way as in the program "INTA". Up to 5 Mn spins are rotated at random and the cross-section is recalculated and compared with the data. Any move in which the value of χ^2 is less than the value found in the last accepted move is accepted. In addition, the value of S(S+1) may be varied in "MAG" using a traditional gradient search of the best fit value [16]. Each time a move is accepted output files containing the calculated cross-section, magnetic spin configuration and the magnetic short-range correlation parameters for each of the first 24 near neighbour shells are generated. The program is executed until a tolerance level input by the user has been satisfied as before.

"MAG" takes very much longer to converge than "INTA", as there are many more degrees of freedom in the direction of a spin vector, than in the occupation of a nuclear

site by Mn or Al nuclei. Good agreement between the calculated cross-section and the data for all of the β-MnAl alloys studied was found after approximately 30,000 moves in the program (between 12 and 24 hours CPU time depending on the number of Mn spins in the model). MAG was run several times with different initial random configurations. The results, within statistical accuracy were the same.

This approach to the modelling of magnetic short-range order in β-MnAl relies on two assumptions.

i) Only site II Mn atoms carry a magnetic moment. This observation has been borne out by NMR and Mössbauer studies as well as theoretical band structure calculations (see chapter 1).

ii) The value of the Mn moment is constant throughout the lattice. We need to make this assumption in order to assert that the magnetic short-range correlations are merely dependent on the angle between the Mn spins. This assumption may be justified by the fact that the magnetic moment carried by Mn atoms in the β-Mn matrix is determined by the details of the band rather than the local magnetic environment. It will be shown in chapter 8, that while β-MnAl adopts characteristics consistent with partial moment localisation, it remains essentially an itinerant system.

7.7.3 Results

The fully corrected measured magnetic differential cross-sections of β-$Mn_{0.97}Al_{0.03}$, β-$Mn_{0.94}Al_{0.06}$, β-$Mn_{0.9}Al_{0.1}$ and β-$Mn_{0.8}Al_{0.2}$ are presented in figure 7.14. These cross-sections were extracted from the measured z-up/z-down cross-sections using eq. (7.14), with the value of the spin incoherent cross-section obtained as described in section 7.5. The simulated magnetic cross-section produced by "MAG" is shown to provide an excellent description of the magnetic data. The extracted magnetic short-range correlations for each of the first 24 near neighbour shells as a function of radial distance are shown in figure 7.15 and tabulated in table 7.4.

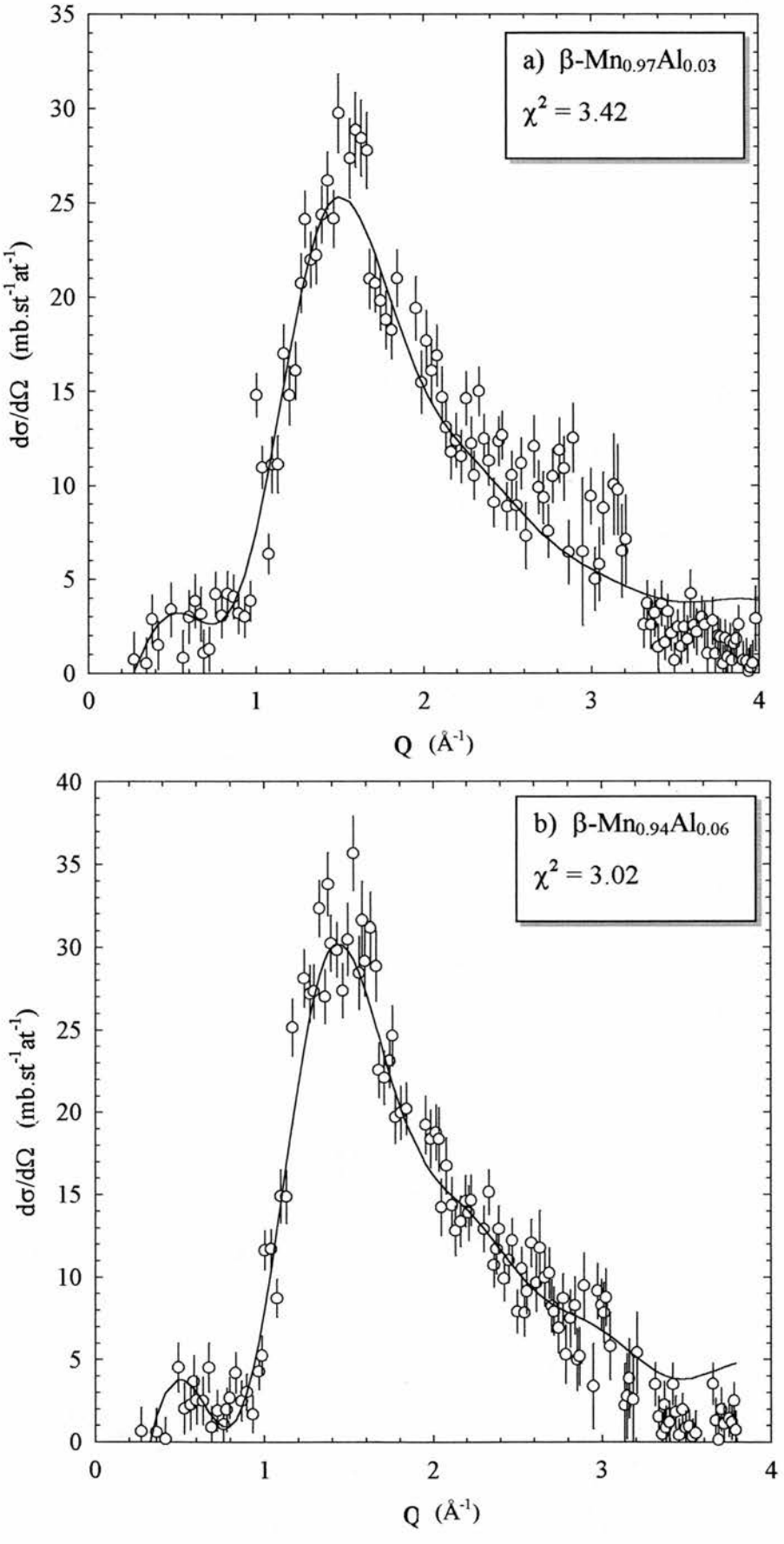

Figure 7.14

Magnetic cross-section of a) β-$Mn_{0.97}Al_{0.03}$ and b) β-$Mn_{0.94}Al_{0.06}$. The solid line is the calculated magnetic cross-section produced by the program "MAG".

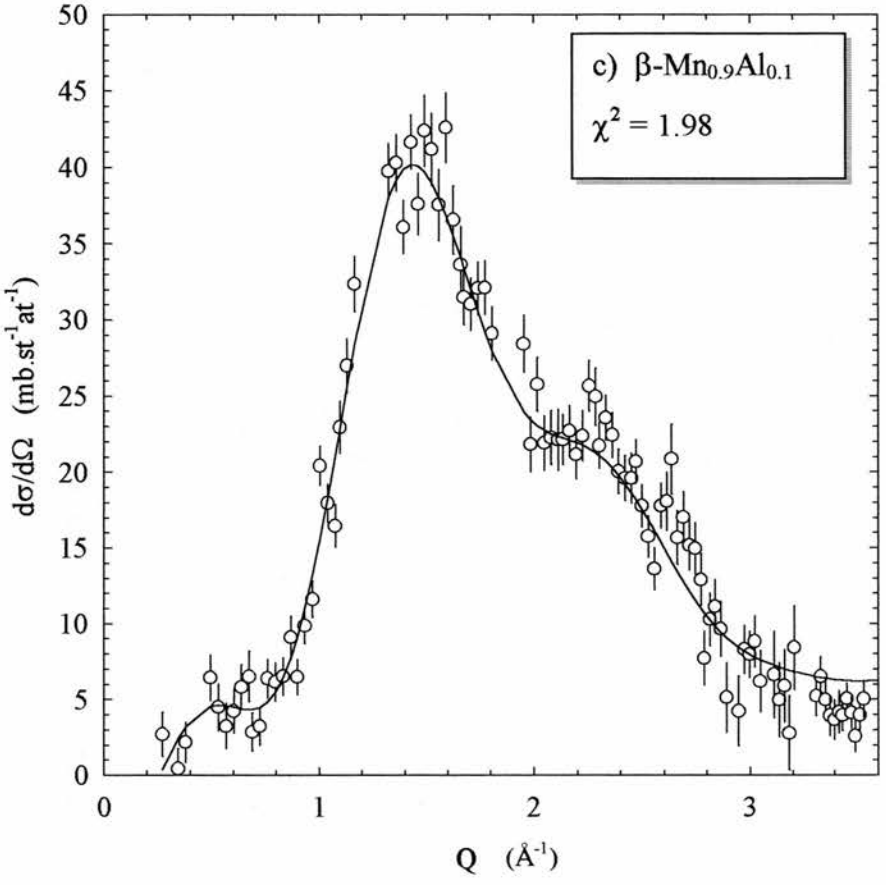

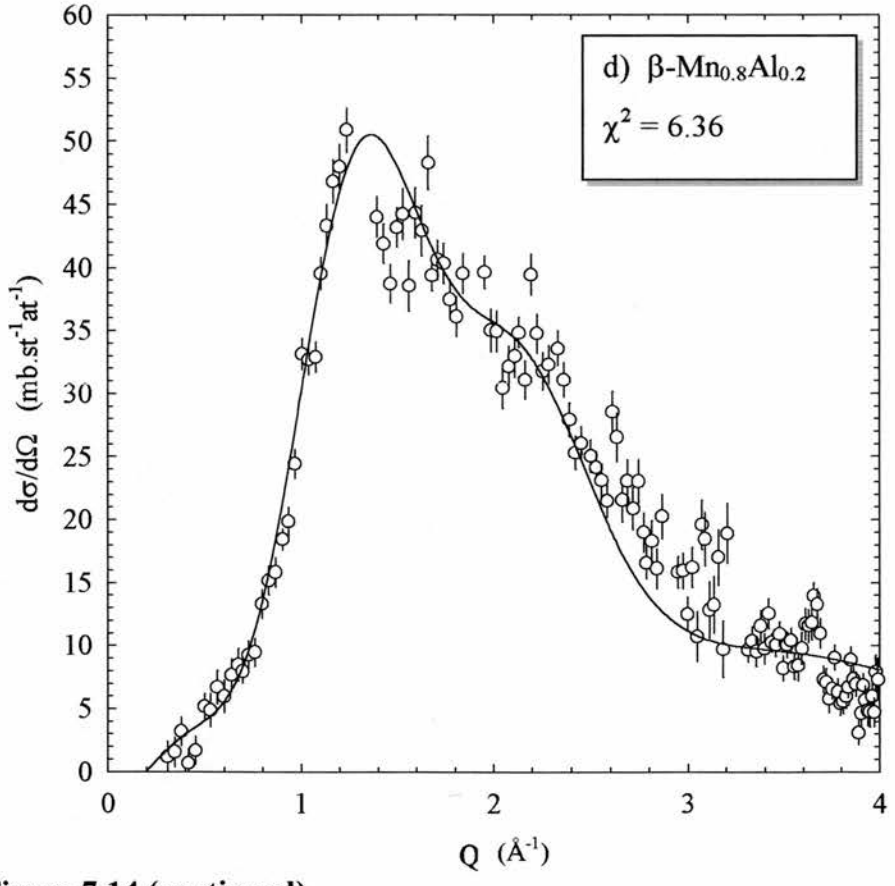

Figure 7.14 (continued)

Magnetic cross-section of c) β-$Mn_{0.9}Al_{0.1}$ and d) β-$Mn_{0.8}Al_{0.2}$. The solid line is the calculated magnetic cross-section produced by the program "MAG".

Table 7.4 magnetic short-range order correlation parameters from the "MAG" simulation program for the β-MnAl alloys shown

	β-$Mn_{0.97}Al_{0.03}$		β-$Mn_{0.94}Al_{0.06}$		β-$Mn_{0.9}Al_{0.1}$		β-$Mn_{0.8}Al_{0.2}$	
n	R_n	$<S_0,S_n>$	R_n	$<S_0,S_n>$	R_n	$<S_0,S_n>$	R_n	$<S_0,S_n>$
1	2.659	-0.33(1)	2.662	-0.30(1)	2.668	-0.33(1)	2.683	-0.31(1)
2	3.272	0.28(1)	3.275	0.15(2)	3.283	0.47(2)	3.301	0.49(2)
3	3.901	-0.21(1)	3.905	-0.10(2)	3.914	-0.28(2)	3.935	-0.28(2)
4	4.376	-0.02(1)	4.380	-0.17(1)	4.391	0.00(1)	4.414	0.03(2)
5	4.432	0.08(2)	4.436	0.04(2)	4.447	0.08(2)	4.471	0.0(2)
6	4.562	0.04(1)	4.566	0.02(1)	4.577	-0.07(1)	4.602	-0.02(2)
7	4.638	0.03(1)	4.642	0.08(1)	4.653	-0.08(1)	4.678	-0.03(2)
8	5.158	0.23(1)	5.162	0.24(1)	5.175	0.21(1)	5.203	0.02(2)
9	5.206	0.01(1)	5.210	0.14(1)	5.223	0.08(1)	5.251	-0.02(2)
10	5.272	0.16(2)	5.277	0.20(1)	5.290	0.16(2)	5.318	0.04(2)
11	5.779	-0.15(1)	5.783	-0.18(1)	5.798	-0.07(1)	5.829	0.10(2)
12	6.260	0.09(1)	6.265	-0.05(1)	6.281	0.13(1)	6.314	0.13(2)
13	6.330	0.07(1)	6.335	0.07(1)	6.351	0.08(1)	6.385	0.01(1)
14	6.391	-0.03(1)	6.396	0.01(1)	6.412	-0.02(1)	6.447	0.00(1)
15	6.535	-0.07(1)	6.540	-0.10(2)	6.556	-0.03(2)	6.591	0.02(2)
16	6.581	0.00(1)	6.587	0.06(1)	6.603	0.00(1)	6.639	0.02(2)
17	6.780	-0.03(1)	6.786	0.06(1)	6.803	-0.07(1)	6.839	-0.08(2)
18	6.829	0.06(1)	6.835	0.12(1)	6.852	0.01(1)	6.889	-0.06(2)
19	7.000	-0.09(1)	7.005	-0.01(1)	7.023	-0.04(1)	7.061	-0.01(2)
20	7.309	-0.11(1)	7.315	-0.18(1)	7.334	-0.13(1)	7.373	0.01(2)
21	7.389	0.00(1)	7.394	-0.12(1)	7.413	-0.05(1)	7.453	0.10(2)
22	7.435	-0.08(1)	7.441	-0.04(1)	7.460	-0.07(1)	7.500	0.05(2)
23	7.630	0.02(1)	7.636	-0.03(2)	7.656	0.05(2)	7.697	-0.10(2)
24	7.727	-0.01(1)	7.733	-0.13(1)	7.753	-0.01(1)	7.794	-0.05(2)

The errors in the magnetic correlation parameters listed in table 7.4 and shown in figure 7.15 were produced in the same manner as the errors in the pair probabilities (see section 7.6.4). The oscillation observed in the magnetic correlation parameters could not be parameterised by a damped cosine function.

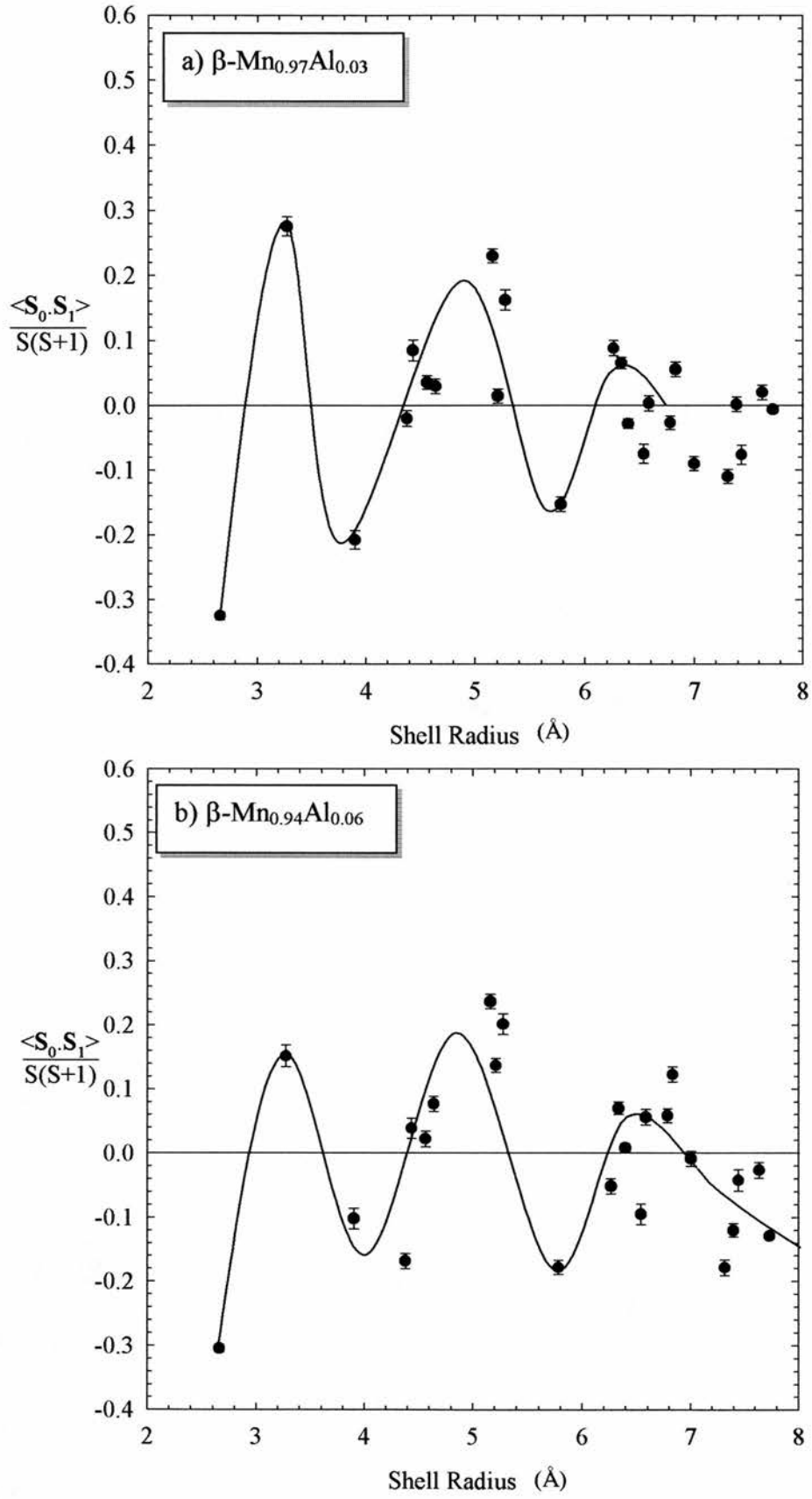

Figure 7.15

Magnetic correlation parameters extracted from "MAG" as a function of shell radius, for a) β-$Mn_{0.97}Al_{0.03}$ and b) β-$Mn_{0.94}Al_{0.06}$. The solid lines are guides to the eye.

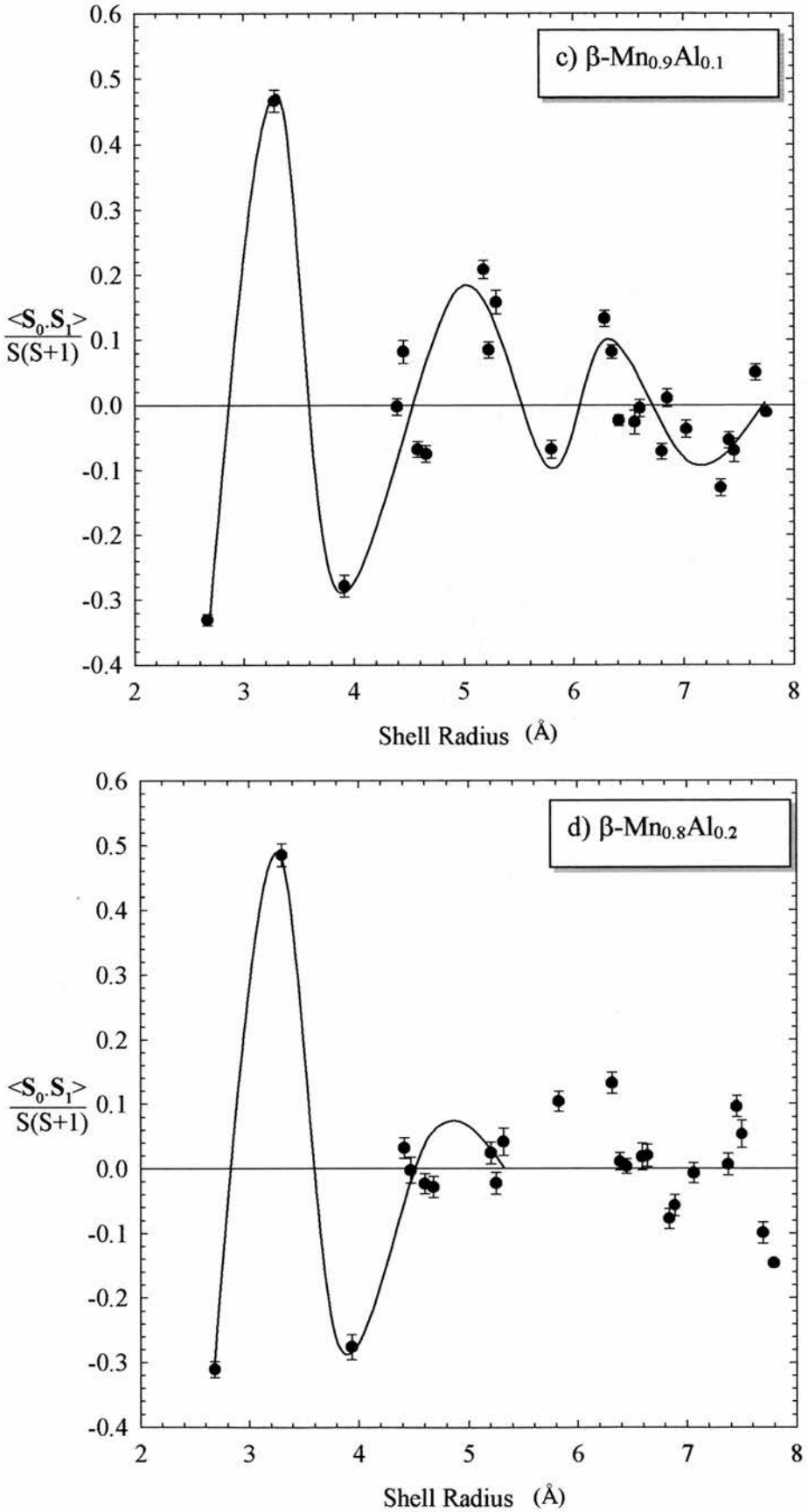

Figure 7.15 (continued)

Magnetic correlation parameters extracted from "MAG" as a function of shell radius, for c) β-$Mn_{0.9}Al_{0.1}$ and d) β-$Mn_{0.8}Al_{0.2}$. The solid lines are guides to the eye.

The oscillatory behaviour of the magnetic correlation parameters is very similar in all four β-MnAl compositions studied, with the 1st and 3rd near neighbour shells strongly antiferromagnetically correlated, and the 2nd near neighbour shell strongly ferromagnetically correlated. The radius of the second shell (between 3.27Å and 3.30Å) corresponds to $Q \sim 1.9Å^{-1}$, where we see a small peak in the experimental cross-section. A broad region of ferromagnetic correlations is observed centred at around R = 5.2Å corresponding to $Q \sim 1.2Å^{-1}$. This peak in the magnetic correlation parameters falls steadily with increasing Al concentration, from around 0.23±0.13 for β-$Mn_{0.97}Al_{0.03}$ to 0.02±0.05 for β-$Mn_{0.8}Al_{0.2}$. This indicates that the correlations are of longer range in the more dilute β-MnAl alloys, and is borne out by the fact that the magnetic cross-section becomes increasingly broad as the Al concentration increases. However, figure 7.15 shows that the magnetic correlations in the first 3 shells increase as the Al concentration increases. This may be due to the fact that the frustration inherent in the β-Mn matrix is being disrupted by the introduction of Al atoms, therefore facilitating the alignment of the neighbouring Mn spins.

It is instructive to investigate how the magnetic correlations between individual atoms in each shell are distributed around the mean value. An average correlation of $\langle \mathbf{S}_0.\mathbf{S}_n \rangle = 0$ may either imply an even distribution of spins around 4π steradians (and therefore a total absence of correlations), or a sharp distribution of spins oriented at π/2 radians to one another. The analysis of each individual distribution of magnetic correlations will also allows us to analyse the errors inherent in the calculation of the mean magnetic correlation of the each distribution.

The normalised distributions of the magnetic correlations for the first 6 near neighbour shells are shown in figure 7.16. The errors shown are the statistical errors based on the size of each distribution sample. Notice that the errors in shells 2 and 3, each with a coordination number of 2, are considerably larger than those on shell 1 which has a coordination number of 6. These distributions clearly demonstrate the rapid fall-off in magnetic correlations with radial distance in each of the compositions studied with the distribution of magnetic correlations for shell 6 being almost flat. The distributions for shells 9-24 are all more or less flat.

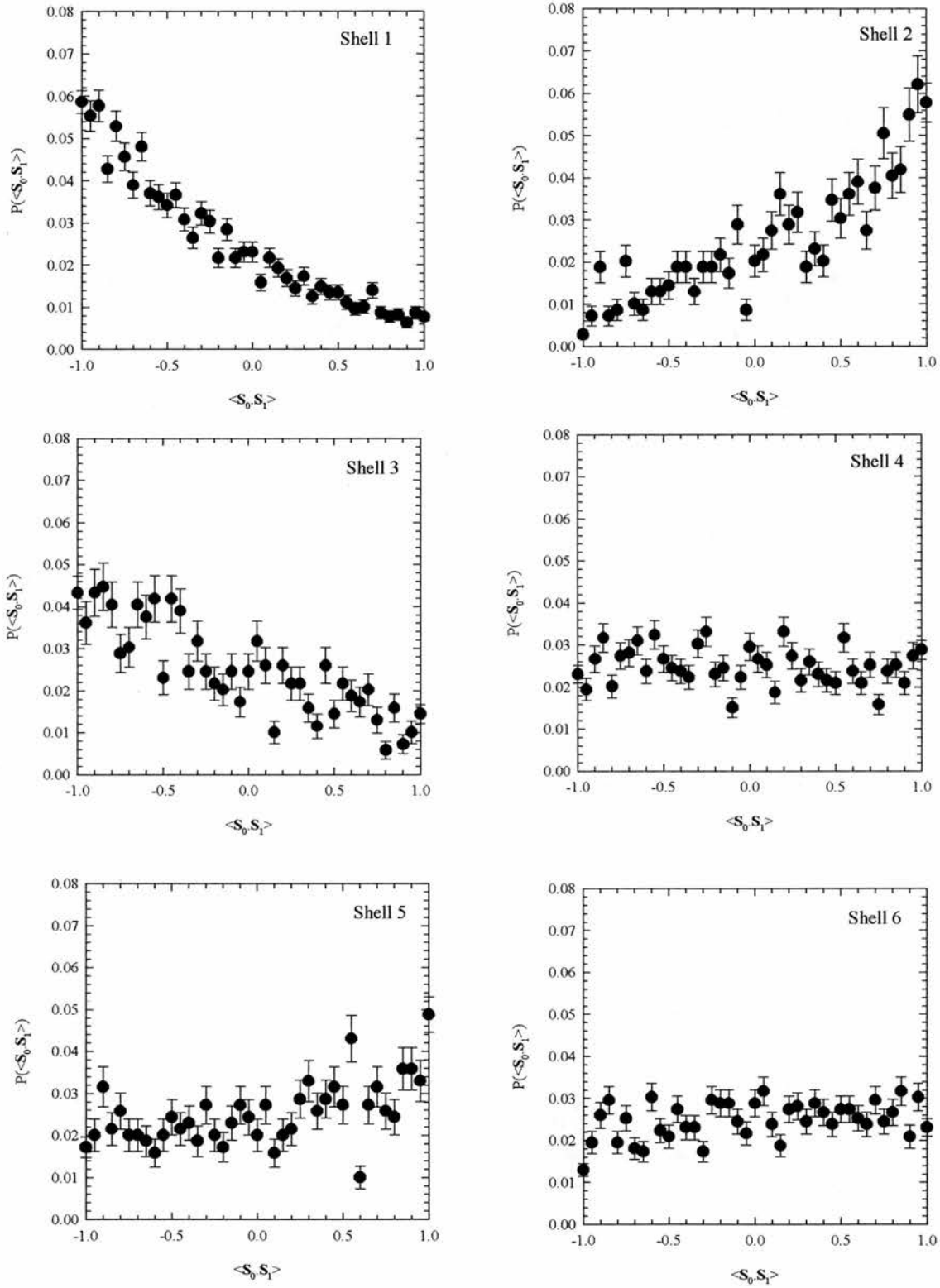

Figure 7.16a

Distributions of magnetic correlations in β-$Mn_{0.97}Al_{0.03}$ for near neighbour shells 1 –6.

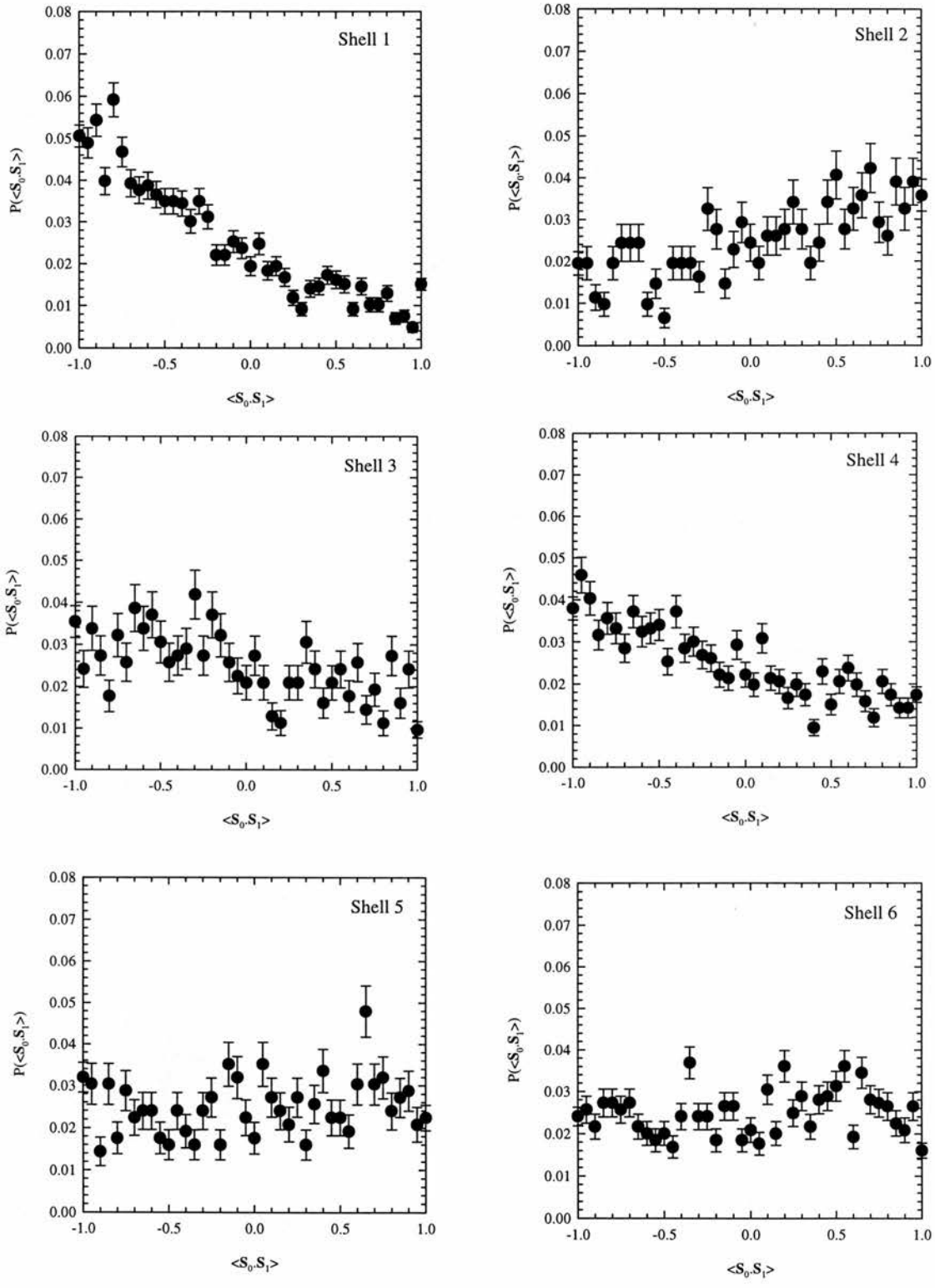

Figure 7.16b

Distributions of magnetic correlations in β-$Mn_{0.94}Al_{0.06}$ for near neighbour shells 1 –6.

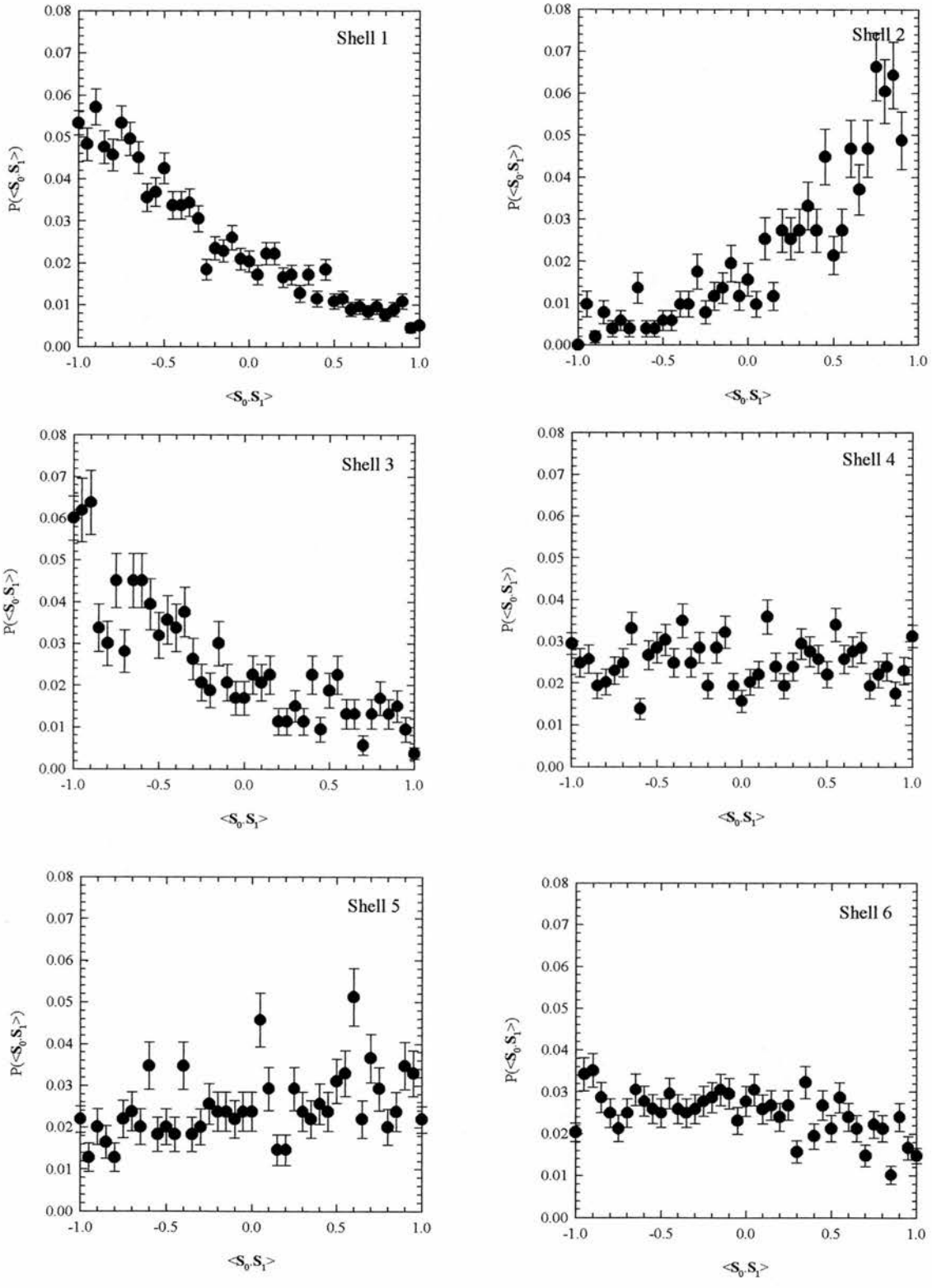

Figure 7.16c

Distributions of magnetic correlations in β-$Mn_{0.9}Al_{0.1}$ for near neighbour shells 1 –6.

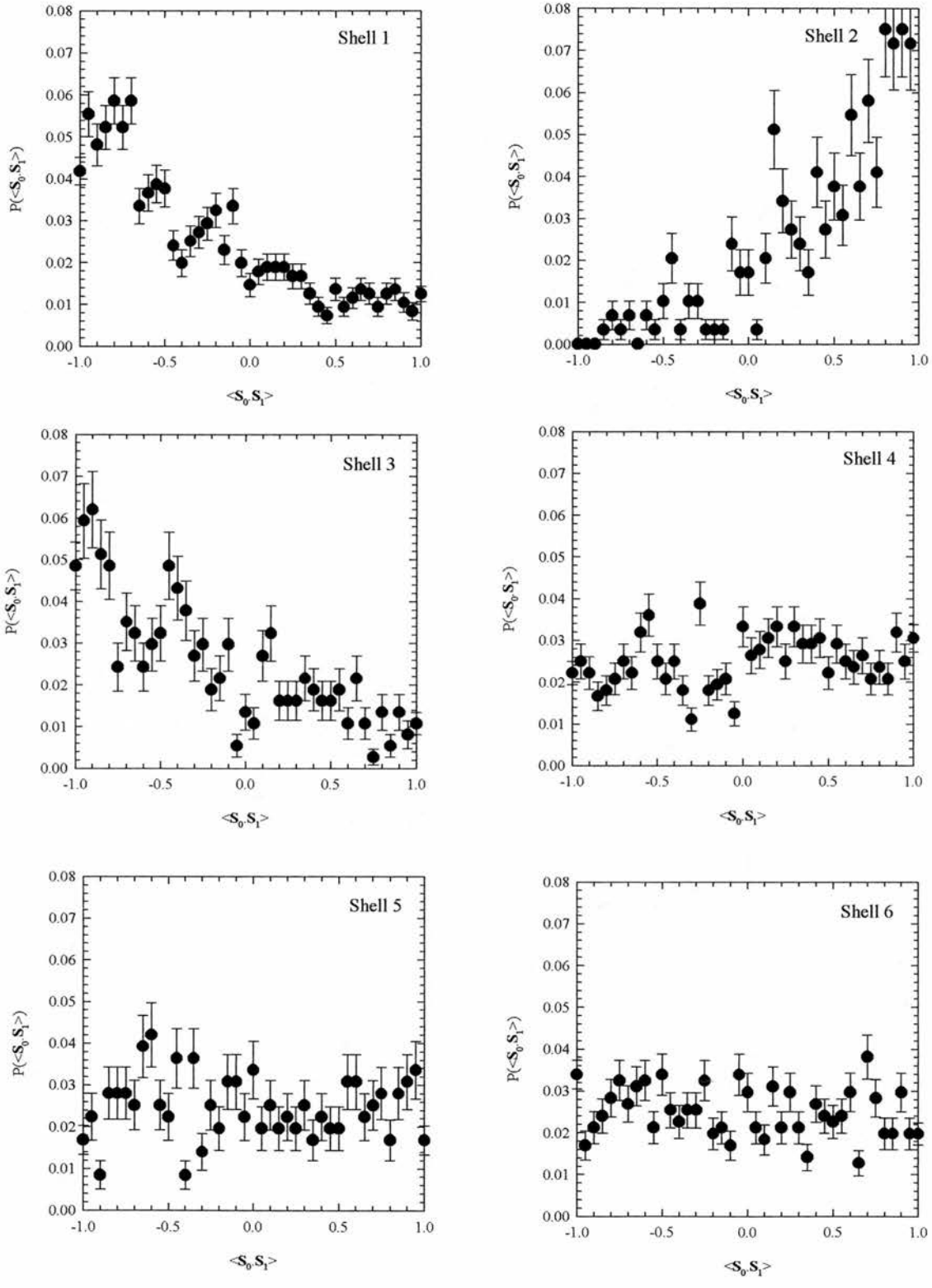

Figure 7.16d

Distributions of magnetic correlations in β-$Mn_{0.8}Al_{0.2}$ for near neighbour shells 1 –6.

7.8 Discussion

While the magnetic correlations extracted from the measured magnetic cross-sections do not change dramatically with Al concentration in β-MnAl, the measured Mn spin number changes significantly. Figure 7.17 shows a plot of the Al concentration dependence of S(S+1) for the four β-MnAl samples studied in this investigation.

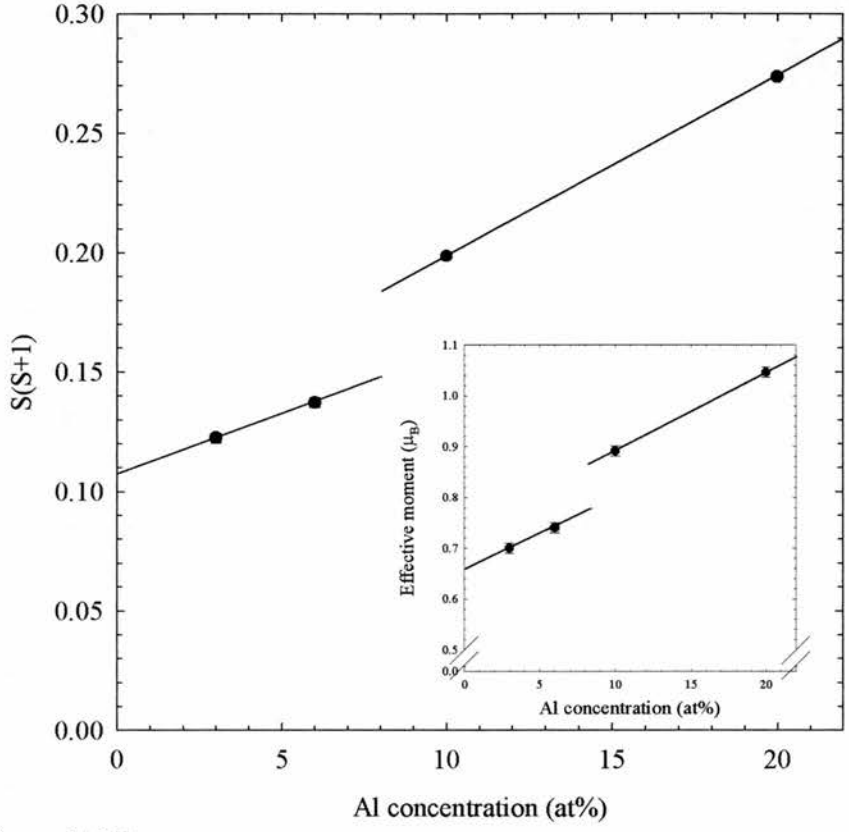

Figure 7.17

The quantum mechanical square of the spin quantum number S as a function of Al concentration. The inset shows the concentration dependence of the effective Bohr magneton number. The lines shown are guides to the eye.

Figure 7.17 shows that S(S+1) rises with Al concentration from 0.122±0.002 for β-$Mn_{0.97}Al_{0.03}$ to 0.274±0.001 for β-$Mn_{0.8}Al_{0.2}$. This corresponds to a rise in effective Mn moment from 0.70±0.02 μ_B in β-$Mn_{0.97}Al_{0.03}$ to 1.04±0.02μ_B in β-$Mn_{0.8}Al_{0.2}$, as shown in the inset of figure 7.17. From figure 7.17 there appears to be a discontinuity in the observed increase of S(S+1) with increasing Al concentration between β-$Mn_{0.94}Al_{0.06}$ and β-$Mn_{0.9}Al_{0.1}$. It is tempting to associate this discontinuity with the sudden change of spin dynamical behaviour and increase of magnetic transition temperature observed between Al concentrations of 9at% and 10at% observed in our μSR study presented in chapter 6 (see figure 6.22). The most likely explanation for the observation of a

decrease in the effective moment with decreasing Al concentration is that there are residual dynamic spin fluctuations present in the more dilute β-MnAl compositions which reduce the magnetic intensity around the elastic line and contribute to the magnetic intensity lying outside the available energy window. Our inelastic neutron scattering measurements presented in chapter 8 will show that there are considerable spin-fluctuations persisting down to low temperatures in both pure β-Mn and β-$Mn_{0.8}Al_{0.2}$, despite the observation of a critical divergence in λ observed in our μSR measurements. The values of the effective moment of the Mn spins in the β-Mn alloys studied in this experiment should therefore not be considered as accurate. However, the overall shape and nature of the nuclear and magnetic short-range correlations have been successfully analysed both qualitatively and quantitatively.

7.9 Conclusions

We have used neutron polarisation analysis to investigate both nuclear and magnetic short-range order in β-MnAl. We have developed a reverse Monté-Carlo modelling algorithm to extract the Warren-Cowley nuclear short-range order parameters and the magnetic correlations in the material.

- We have observed strong short-range order scattering due to Al nuclei anticlustering on the site II β-Mn sublattice.
- We have found that the sudden change in the spin dynamics of β-MnAl between 9at% and 10at% Al observed by μSR does not result in a dramatic change in the nature of the antiferromagnetic spin correlations.
- Our RMC modelling programs have allowed us to analyse the magnetic correlations in β-MnAl while automatically accounting for the effects of the observed nuclear short-range order. The measured magnetic cross-sections suggest strong antiferromagnetic coupling of neighbouring site II Mn spins over the first 3 near neighbour shells. For dilute β-MnAl alloys there is a small peak in the magnetic correlations at R =~5.1Å, which dies away as the Al concentration increases. This indicates that the correlations in dilute β-MnAl are of longer range than those in the more concentrated alloys. However, no evidence of long-range antiferromagnetic order has been found in any of the β-MnAl alloys.

7.10 References

[1] O Schärpf and H Capellmann, Phys. Stat. Sol. **A135** (1993) 359

[2] O Schärpf, *The Spin of the Neutron as a Measuring Probe*, (Institut Laue-Langevin 1996)

[3] RM Moon, T Riste and W C Koehler, Phys. Rev. **181** (1969) 920

[4] O Halpern and M R Johnson, Phys. Rev. **55** (1939) 898

[5] http://www.ill.fr/YellowBook/D7/EDIT94/d7_p1.gif

[6] http://www.ill.fr/YellowBook/D7/layout.gif

[7] http://www.ill.fr/YellowBook/D7/EDIT94/d7_f3.gif

[8] K H Andersen, private communication

[9] Blech and Averbach, Phys. Rev. **137** (1965) 1115

[10] M Shiga, H Nakamura, M Nishi and K Kakurai, J. Phys. Soc. Japan **63** (1994) 1656

[11] J R Davis and T J Hicks, J. Phys. C: Solid State Phys. **8** (1976) L177

[12] S C Moss and R H Walker, J. Appl. Cryst. **8** (1975) 96

[13] for a derivation of the spherical average of $d\sigma/d\Omega$ assuming a simple bcc structure see; R Cywinski and T J Hicks, J. Phys. F: Metal Phys. **10** (1980) 693

[14] J M Cowley, J. Appl. Phys **21** (1950) 24
J M Cowley, Phys. Rev, **77** (1950) 669

[15] R Cywinski, S H Kilcoyne, S F J Cox, C A Scott and O Schärpf, Hyp. Int., **64** (1990), 427

[16] P R Bevington, *Data Reduction and Error Analysis for the Physical Sciences*, (1969)

8 An Inelastic Neutron Scattering Study of β-MnAl

8.1 Introduction

The inelastic polarised neutron scattering study of pure β-Mn and β-$Mn_{0.9}Al_{0.1}$ by Shiga and co-workers [1] presented in chapter 1, showed that the introduction of Al into the β-Mn matrix significantly reduces the spectral width of the spin fluctuations present in the pure metal. This observation, which has been supported by our own μSR study of β-MnAl alloys presented in chapter 6, has led Shiga to characterise the transition from the dynamic magnetic ground state of pure β-Mn to the largely static magnetic ground state of β-$Mn_{0.9}Al_{0.1}$ as a quantum spin liquid (QSL) to spin glass transition. However, Shiga's measurement of the inelastic linewidth was performed at an incident neutron energy of 34meV and consisted of only 11 data points per measurement with rather large error bars (see figure 1.15). Shiga's measurement of the magnetisation density in β-Mn and β-$Mn_{0.9}Al_{0.1}$ suffered from the same problem as the measurements taken on D7 presented in chapter 7 of this thesis; namely that the differential magnetic cross-section was not integrated over all energies, therefore underestimating the calculated values of the mean Mn moment.

In order to expand and improve on Shiga's original study, we have used inelastic neutron scattering to study the spin dynamics and magnetic ground states of pure β-Mn and β-$Mn_{0.8}Al_{0.2}$. Our measurements were performed at an incident energy of E_i = 100meV ensuring that a broad range of spin fluctuation energies was observable. The staggered magnetic susceptibility has been extracted from these measurements (see eqs. (2.53) and (3.26)) via a full energy integration of the data. Finally, we have interpreted our results in terms of the self consistent renormalisation (SCR) theory of spin fluctuations described in chapter 2.

8.2 *Inelastic Neutron Scattering*

8.2.1 Time of Flight Inelastic Neutron Scattering

In a time of flight inelastic neutron scattering experiment, we wish to measure both the incident and scattered neutron energies and wavevectors. In a neutron scattering experiment, the neutron energy $\hbar\omega$ and the wavevector transfer **Q** abide by the conservation laws,

$$\mathbf{Q} = \mathbf{k}_i - \mathbf{k}', \tag{8.1}$$

and

$$\hbar\omega = \frac{\hbar^2}{2m}\left(k_i^{\,2} - k'^{2}\right). \tag{8.2}$$

The momentum conservation defines the scattering triangle of the scattering event. On a pulsed neutron source the neutron time of flight is used to determine either k_i or k'. In a *direct geometry* spectrometer, the incident neutron wavevector k_i is known and the scattered wavevector k' is determined by measuring the time of flight of the neutron over the scattered flight path L_1, thus defining the neutron velocity,

$$\mathbf{v}' = \frac{L_1}{t} = \frac{\hbar\mathbf{k}'}{m}. \tag{8.3}$$

The layout of a direct geometry inelastic spectrometer and the range of scattering triangles available to a single detector at angle 2θ is shown in figure 8.1

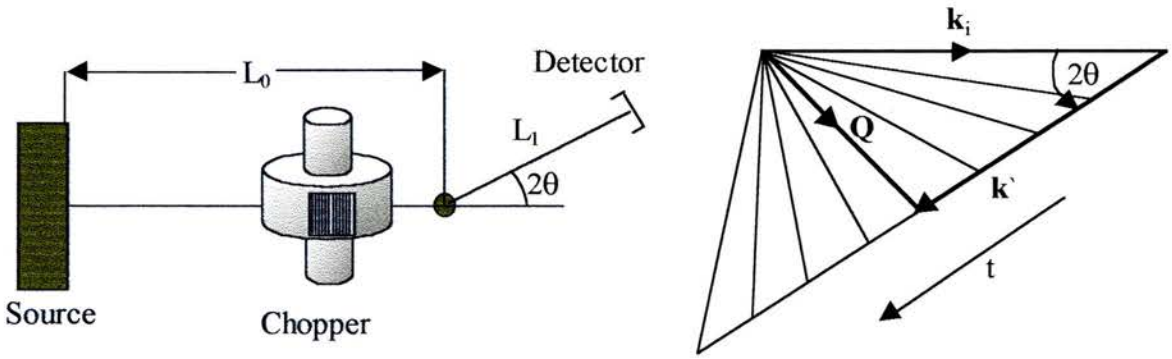

Figure 8.1

Layout of a direct geometry inelastic neutron spectrometer on a pulsed source. The incident wavevector is fixed by a Fermi neutron chopper. Also shown is the range of scattering triangles available to each detector at angle 2θ which is scanned by analysing the neutron time of flight.

The kinematical constraints of the conservation laws restrict the available range of Q-ω space observable in an inelastic neutron experiment. Applying the cosine rule to eq. (8.1) we obtain,

$$|\mathbf{Q}|^2 = |\mathbf{k_i}|^2 + |\mathbf{k`}|^2 - 2|\mathbf{k_i}||\mathbf{k`}|\cos(2\theta). \qquad (8.4)$$

Rewriting this equation in terms of the incident energy $E_i = \hbar^2|\mathbf{k_i}|^2/2m$, and the energy transfer $\hbar\omega$ given by eq. (8.2) we obtain the Q-ω trajectory for a single detector at scattering angle 2θ as,

$$\frac{\hbar^2|\mathbf{Q}|^2}{2m} = 2E_i - \hbar\omega - 2\cos(2\theta)\left[E_i(E_i - \hbar\omega)\right]^{1/2}. \qquad (8.5)$$

A graph of the region of Q-ω space available from eq. (8.5) for an incident energy of E_i = 100meV on the HET spectrometer used in this study is shown in figure 8.2.

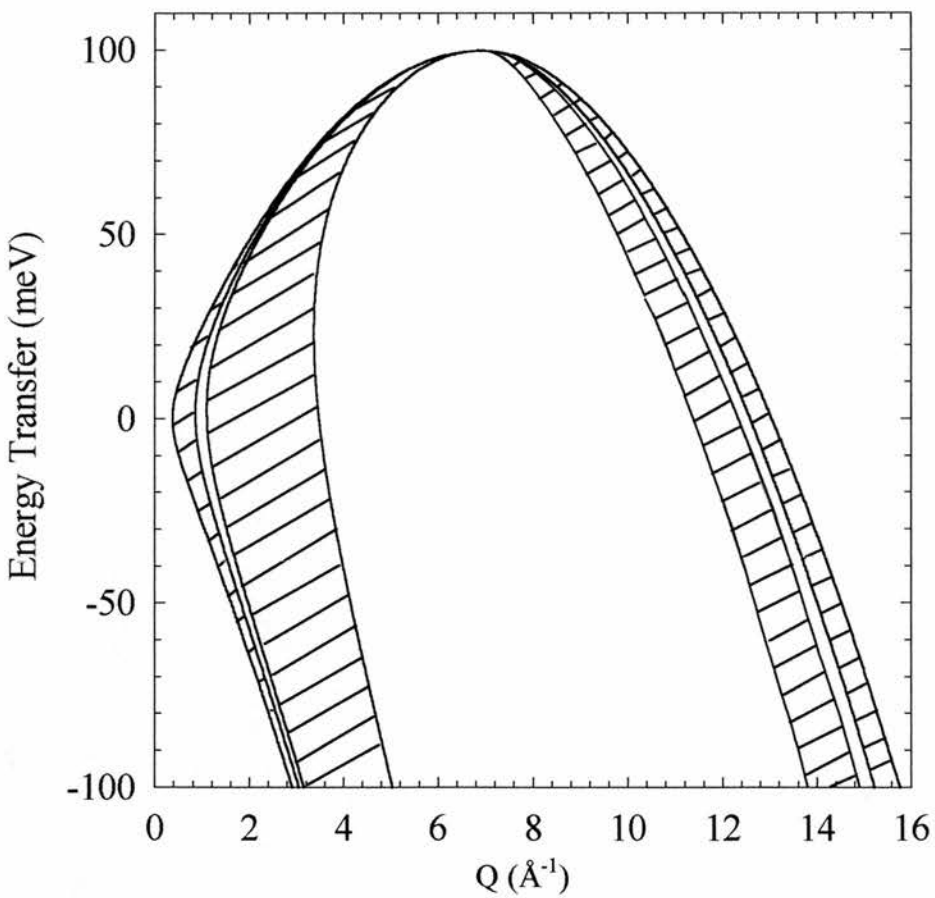

Figure 8.2

The region of Q-ω space available on the HET spectrometer at an incident energy of 100meV. The shaded regions represent the four detector banks present on the HET spectrometer.

Figure 8.2 shows the region over which the dynamical structure factor $S(Q,\omega)$ can be extracted from the measured partial differential cross-section using eq. (3.19).

8.2.2 The HET (High Energy Transfer) Spectrometer

The High Energy Transfer (HET) neutron spectrometer is a direct geometry time of flight instrument at the ISIS pulsed spallation neutron facility at the Rutherford Appleton Laboratory. A schematic diagram of the HET spectrometer is shown in figure 8.3.

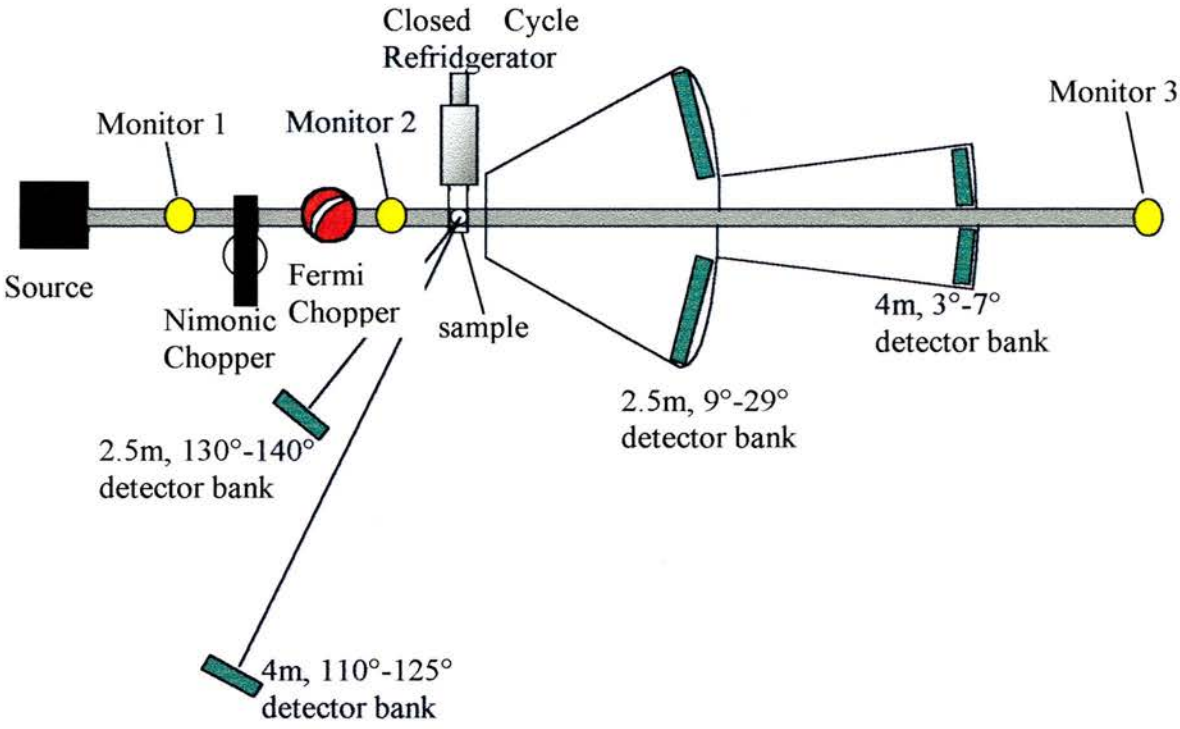

Figure 8.3

The HET spectrometer at the ISIS pulsed neutron source.

A pulse of neutrons from the source arrives at the HET spectrometer after having been collimated to reduce beam divergence. The presence of a nimonic chopper rotating at the incident neutron pulse frequency of 50Hz removes unmoderated fast neutrons and gamma-rays produced by the proton target station. A particular neutron energy is then selected from the incident pulse using a curved-slit Fermi chopper shown in figure 8.4.

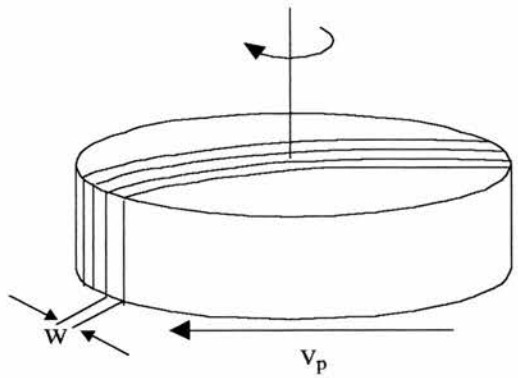

Figure 8.4

A curved-slit Fermi chopper with slit width w and peripheral speed v_p [2].

The Fermi chopper allows the passage of neutrons of pulse width Δt around the incident time of flight t_i given by [2],

$$\Delta t = \frac{w}{2v_p} + \frac{\alpha}{2\pi f}, \tag{8.6}$$

where w is the slit width, v_p is the peripheral chopper speed, f is the frequency of rotation and α is the angular collimation of the incident beam. The incident time of flight is selected by applying a suitable phase shift to the chopper rotation. The curvature of the slits accounts for the fact that the neutrons have finite velocity v_0. The radius of curvature of the slits will be given by [2],

$$R = \frac{v_0}{4\pi f}. \tag{8.7}$$

From eq. (8.6) the resolution $\Delta t/t_i$ will be improved as the rotation frequency is increased in multiples of the incident neutron pulse frequency (50Hz).

There are 4 choppers available on HET which have different radii of curvature and slit widths optimised for various incident energies and resolutions. In this measurement, the HET "sloppy" chopper was used. This chopper has relaxed resolution and is optimised for maximum incident neutron flux. At the incident energy of 100meV used in this measurement the sloppy chopper provided a resolution of ΔE_{res} = 4.43meV and an incident neutron flux of 14,400 neutrons/cm^2/sec.

Neutrons scattered by the sample are detected by four detector banks covering the scattering angles, 3°-7°, 9°-29°, 110°-125° and 130°-140°, as shown in figure 8.3. The range of Q-ω space covered by these detector banks is shown in figure 8.2.

8.3 Experimental Results

8.3.1 Introduction

Powdered β-Mn and β-$Mn_{0.8}Al_{0.2}$ samples were mounted as flat plates of typical dimensions, 4.5cm × 4.5cm × 0.5cm, sandwiched between thin layers of Al foil. Approximately 50g of powder was used in each case. The samples were placed in a top loading closed cycle refridgerator (CCR) enabling temperature coverage from 15K to 300K. The measured spectra were corrected for energy dependent detector efficiency and sample absorption, and converted to absolute cross-section units using the LEONARDO inelastic neutron scattering analysis package. Constant Q cuts of the measured spectra were also obtained using the LEONARDO package.

Typical inelastic neutron spectra obtained for β-Mn and β-$Mn_{0.8}Al_{0.2}$ are shown in figures 8.5 and 8.6 in the form of contour plots of the partial differential cross-section $\partial^2\sigma/\partial\Omega\partial E$ as a function of both the modulus of the wavevector transfer $|\mathbf{Q}|$ and the energy transfer ΔE. The shape of the spin fluctuation response observed in both pure β-Mn and β-$Mn_{0.8}Al_{0.2}$ is very similar and appears not to change greatly with temperature, except for the effects of detailed balance which suppresses the neutron energy gain ($\Delta E < 0$) response at low temperatures (see section 3.2.3). A peak in the magnetic response is observed at around Q ~1.4Å^{-1} in both β-Mn and β-$Mn_{0.8}Al_{0.2}$. The phonon response which dominates the scattering at high Q, where the magnetic response is reduced almost to zero due to the magnetic form factor, can clearly be seen in the high angle bank data shown in figure 8.6.

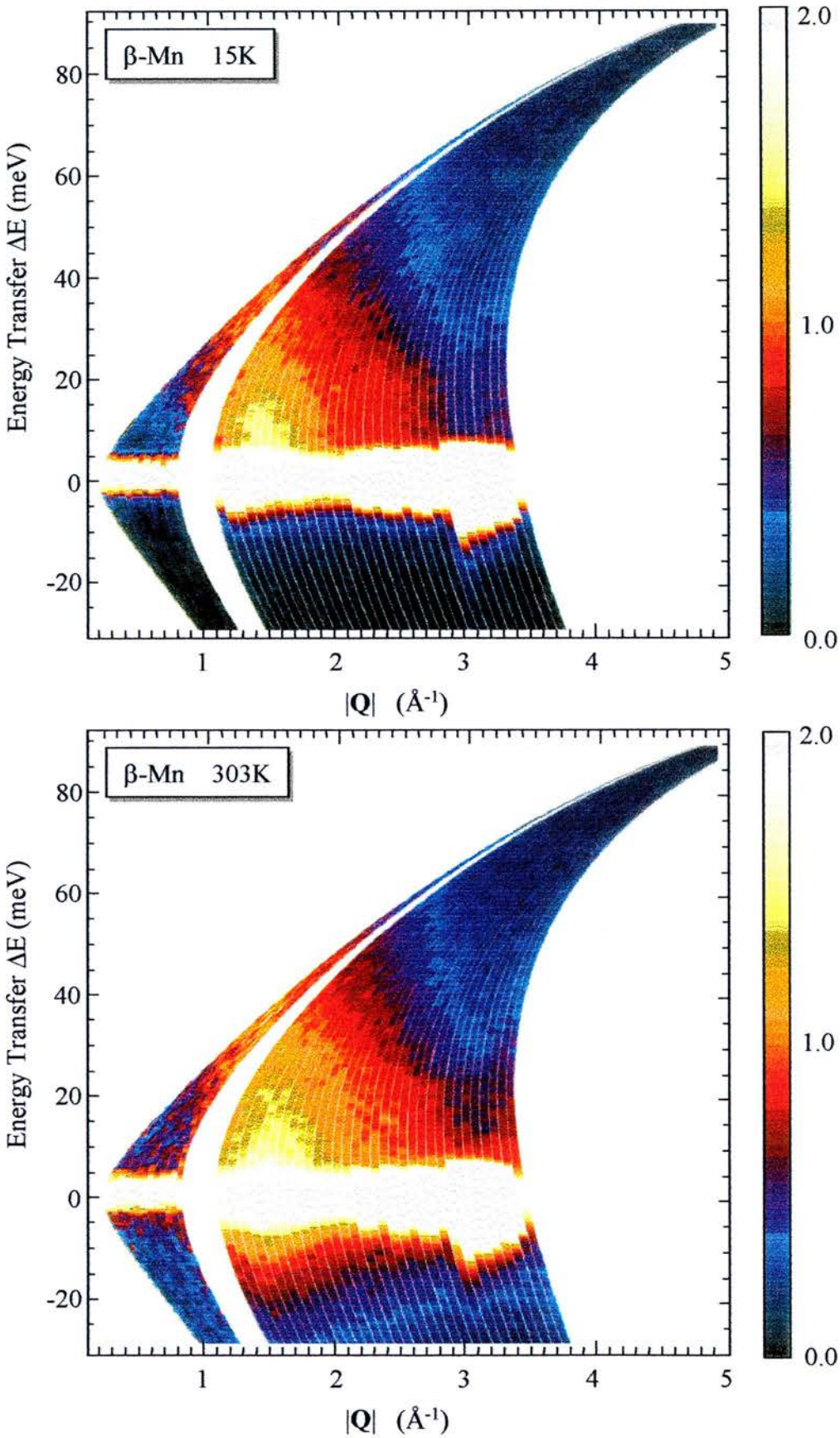

Figure 8.5

Contour plots of $\partial^2\sigma/\partial\Omega\partial E$ for pure β-Mn at 15K and 303K. The quasi-elastic spin fluctuation response is clearly visible, peaked around $Q = 1.4\text{Å}^{-1}$. The spin fluctuation response is extremely broad extending out beyond 40meV, and changes little with temperature, apart from the effects of detailed balance.

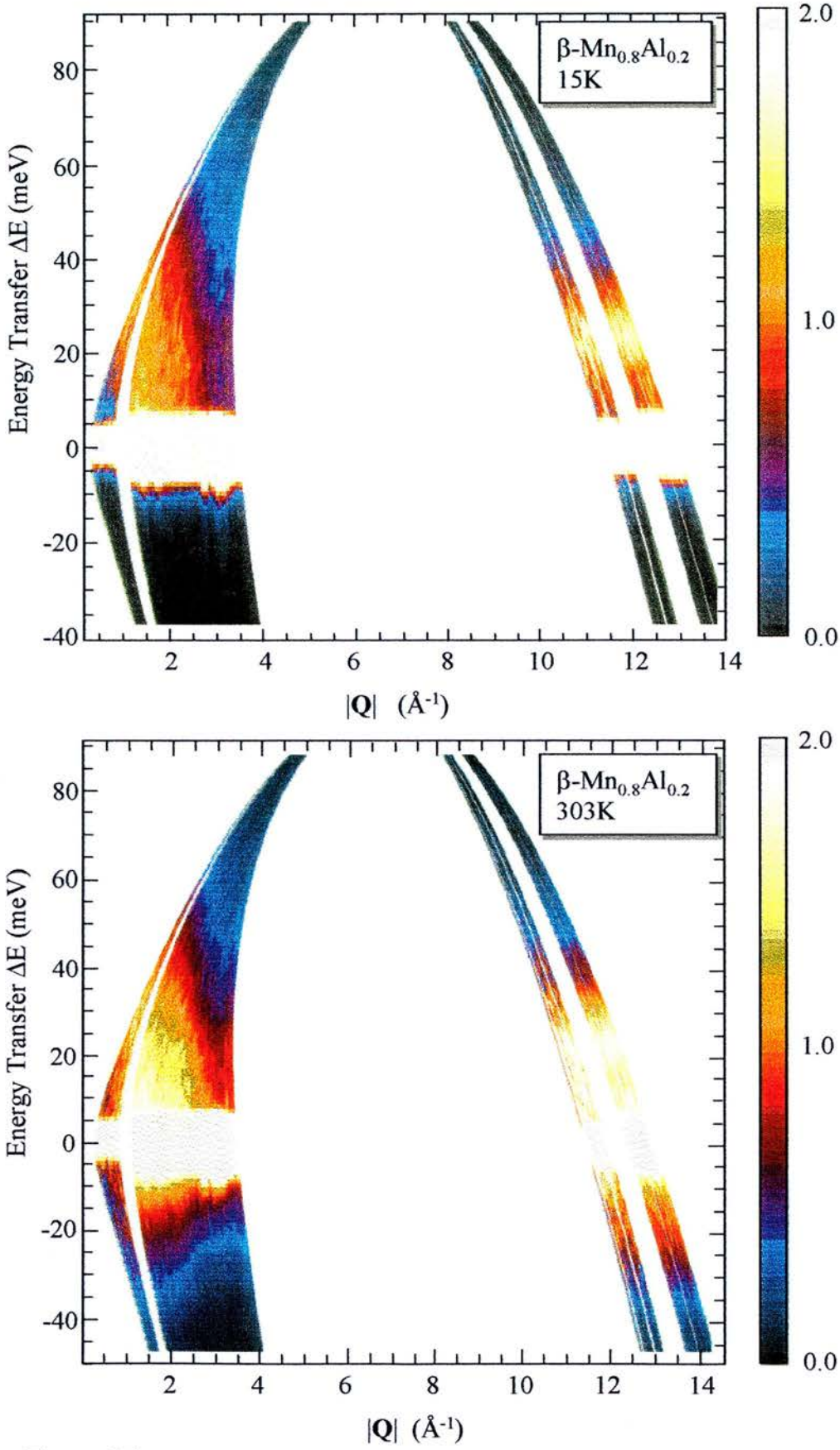

Figure 8.6

Contour plots of $\partial^2\sigma/\partial\Omega\partial E$ for β-$Mn_{0.8}Al_{0.2}$ at 15K and 303K. The high angle data are shown with the coherent phonon excitations clearly visible around $\Delta E = 20meV$. The spin fluctuation response is very similar to that observed in pure β-Mn, and depends little on temperature.

8.3.2 Subtraction of the Phonon Response

In the absence of neutron polarisation analysis it is impossible to separate the magnetic and phonon contributions to the measured inelastic partial differential cross-section. Often, the phonon scattering can be measured using a non-magnetic "blank" sample with the same structure as the sample under investigation. For example, the magnetic rare-earth ions in intermetallic compounds may be replaced by non-magnetic lanthanum ions to produce a non-magnetic version of the parent compound. However, this technique is unsuitable for the study of β-Mn alloys as no other metal forms with the β-Mn structure.

8.3.2.1 Measurement of the Phonon Response

The magnetic contribution to the measured partial differential cross-section in a neutron scattering experiment decreases as a function of the square of the magnetic form factor as discussed in section 3.2.2. If the Mn^{2+} form factor is assumed, then at $Q = 5Å^{-1}$ the magnetic cross-section is reduced to 5.7% of its $Q = 0Å^{-1}$ value, and falls to 0.01% of its $Q = 0Å^{-1}$ value at $Q = 9Å^{-1}$ (see figure 3.3). However, the phonon contribution to the partial differential cross-section rises quadratically with increasing Q and may be approximated by [3],

$$d^2\sigma/d\Omega dE_{phonon} \sim A(\omega) + B(\omega)Q^2, \qquad (8.8)$$

where $B(\omega)$ is the contribution from single phonon scattering events in which one or more phonons are created, and $A(\omega)$ is the contribution from multiple phonon scattering events in which one or more phonons are created more than once by the same neutron.

The form of the phonon cross-section as observed in the high angle detector banks on HET, is such that

$$B(\omega) \propto \frac{Z(\omega)[1 + n(\omega)]}{\omega}, \qquad (8.9)$$

where $Z(\omega)$ is the generalised phonon density of states (PDOS) and $[1 + n(\omega)]$ is the detailed balance factor.

The form of B(ω) for β-Mn was parameterised by fitting three Gaussian lineshapes to the energy loss side of the spectrum obtained from the 135° detector bank on HET as shown in figure 8.7. The contribution to $d^2\sigma/d\Omega dE$ from the elastic line and the multiple scattering tail above ΔE = 40meV has been subtracted from the fit shown.

At low energy transfers the phonon spectrum may be described by the Debye approximation in which the longitudinal and transverse phonon modes are approximated by the linear dispersion relationship [4],

$$\omega = c \times Q, \tag{8.10}$$

where c is a constant. Therefore, at temperatures less than the Debye temperature, the single phonon density of states can be written,

$$Z(\omega) = \alpha \times \omega^2, \tag{8.11}$$

where α is a constant. Z(ω) is, therefore, obtained from the parameterised form of B(ω) using eq. (8.9), and is then adjusted so that the low energy transfer region (ΔE < 5meV) is quadratic in ω. Finally, Z(ω) is normalised to unit area. The final form of the single phonon density of states of pure β-Mn is shown in figure 8.8.

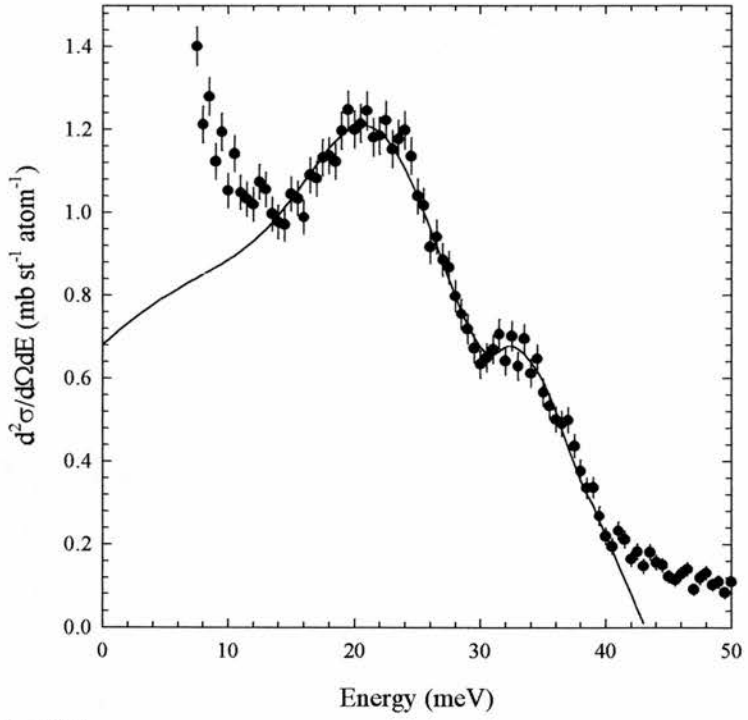

Figure 8.7

The form of B(ω) of pure β-Mn parameterised by fitting the neutron energy loss response of the high angle (135°) bank data to three Gaussian lineshapes, shown as a solid line. This measurement was taken at a temperature of 109K. The multiple scattering contribution above 40meV and the elastic line contribution have been excluded from the fit.

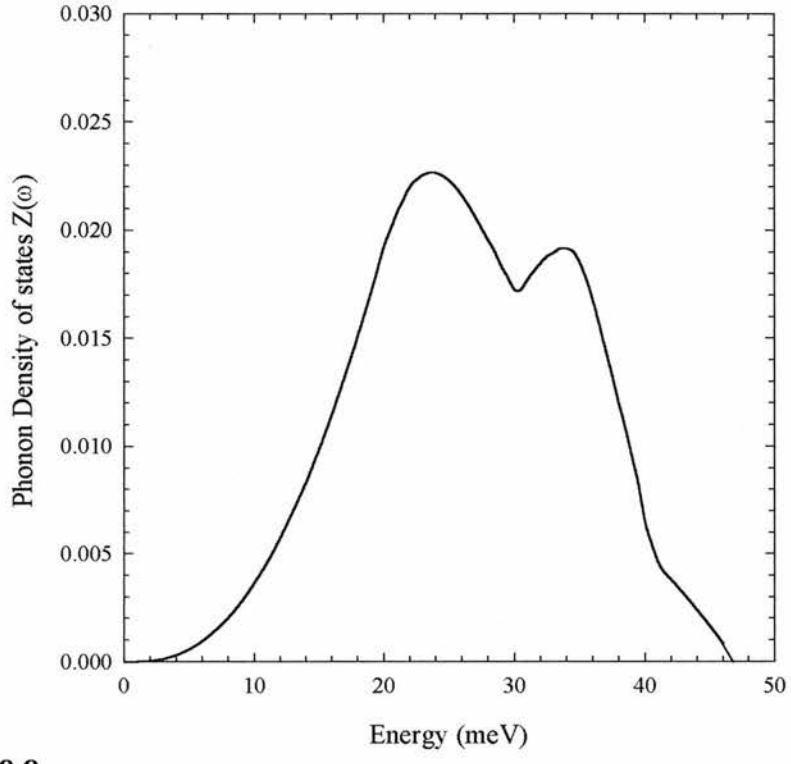

Figure 8.8

The single phonon density of states, Z(ω) for pure β-Mn, derived from the parameterised form of B(ω) shown in figure 8.7 using eqs. (8.9) and (8.11) and normalised to unit area.

8.3.2.2 Monté-Carlo Phonon Simulations

The calculated form of Z(ω) may be used as input to a Monté-Carlo phonon simulation program called "DISCUS" written by M W Johnson [5]. The simulation output produces the phonon scattering cross-section as a function of energy transfer at a constant scattering angle input by the user, fully corrected for temperature and neutron absorption. The phonon simulation was performed for sixteen different scattering angles corresponding to specific detectors on HET. A simulation was also obtained for the 135° detector bank so that the simulated phonon cross-section could be compared with the experimental phonon cross-section used to calculate the phonon density of states. This provided a check on the internal consistency of the simulation procedure. The output phonon simulations as a function of energy transfer at constant scattering angle were converted to functions of both ΔE and Q using eq. (8.5) to produce a grid of the simulated phonon cross-section. Cuts at constant energy transfer ΔE were then extracted from the simulated $d^2\sigma/d\Omega dE_{phonon}$ grid and eq. (8.8) was fitted to these constant ΔE cuts. In this way the A(ω) and B(ω) contributions to the phonon cross-section were extracted and the entire $d^2\sigma/d\Omega dE_{phonon}$ grid was calculated.

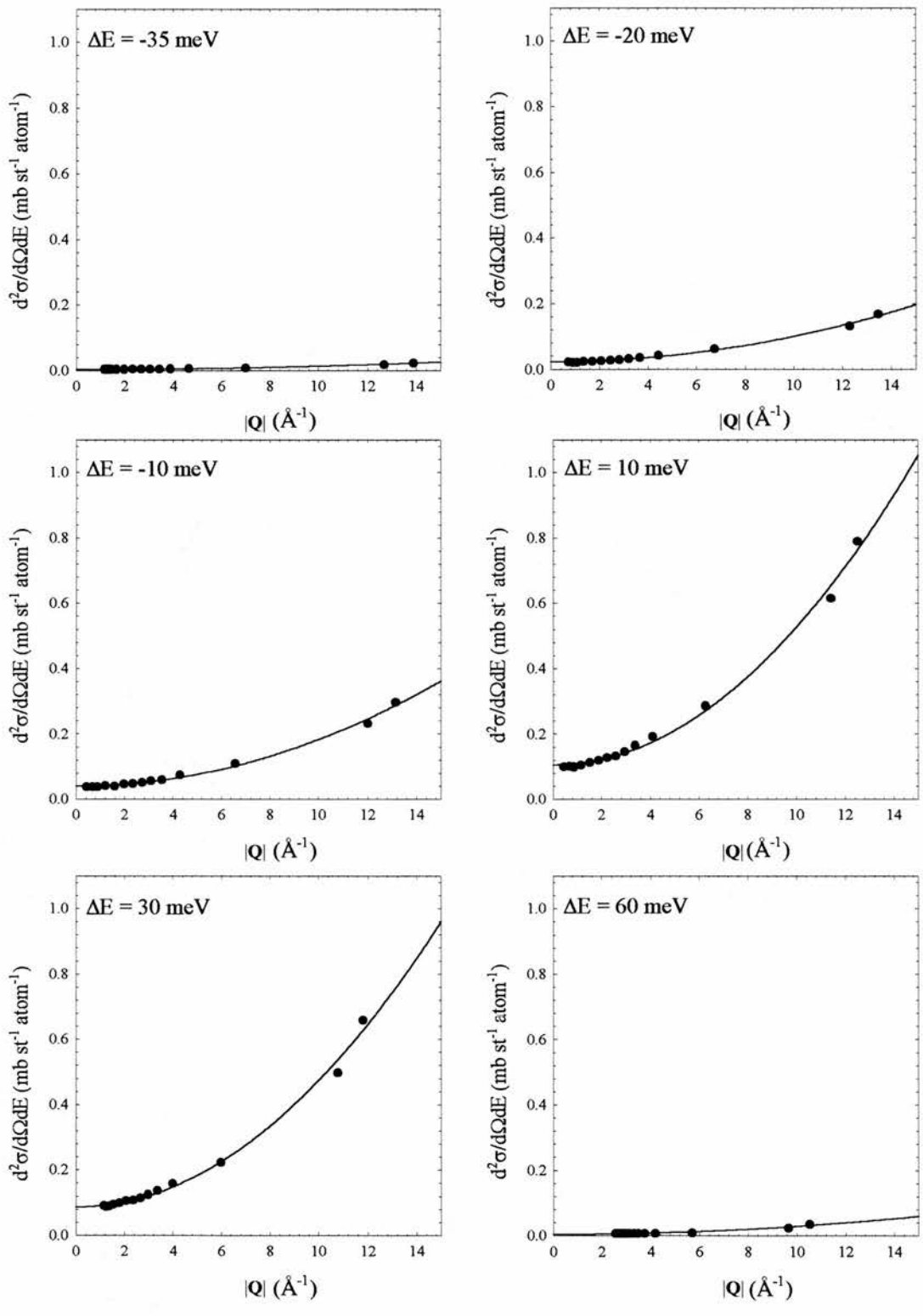

Figure 8.9

Constant energy transfer cuts through the total phonon cross-section of pure β-Mn at 109K simulated using the "DISCUS" Monté-Carlo program. The observed Q dependence was fitted using eq. (8.8) to the parameters A(ω) and B(ω). The fits are shown as solid lines in the diagrams.

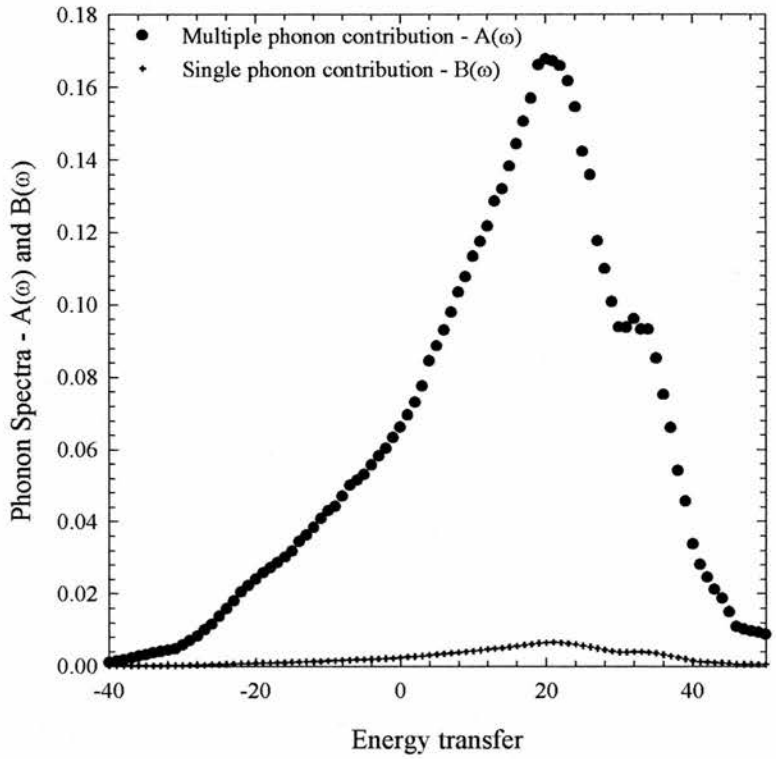

Figure 8.10

The single phonon and multiple phonon contributions B(ω) and A(ω) extracted from fitting eq. (8.8) to the constant energy transfer cuts of the simulated phonon cross-section of pure β-Mn at 109K shown in figure 8.9.

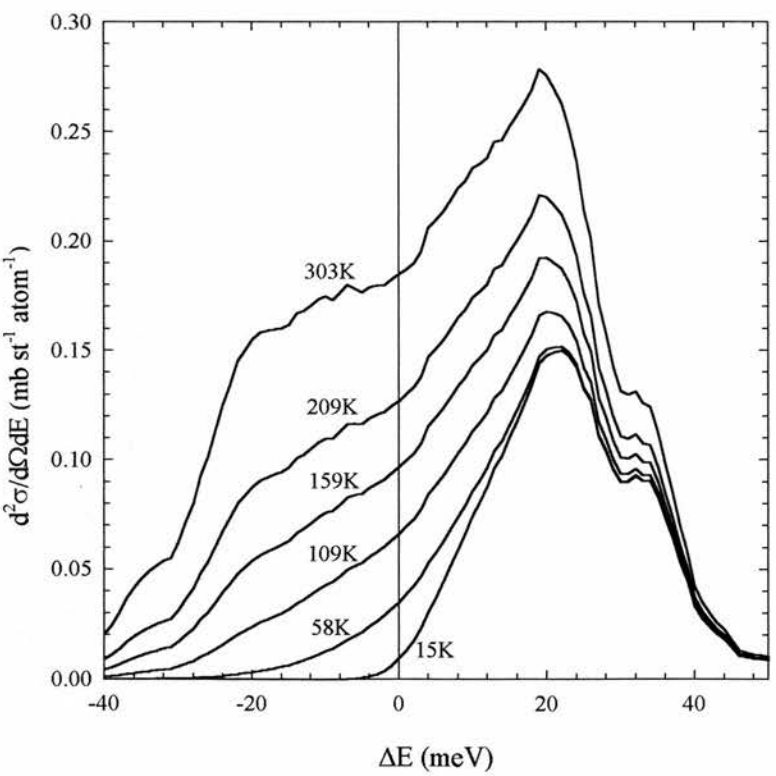

Figure 8.11

Temperature dependence of the phonon cross-section $d^2\sigma/d\Omega dE_{phonon}$ for pure β-Mn derived from A(ω) and B(ω) using eq. (8.8). The data for each temperature was derived by multiplying the 109K data by the relevant ratio of detailed balance factors.

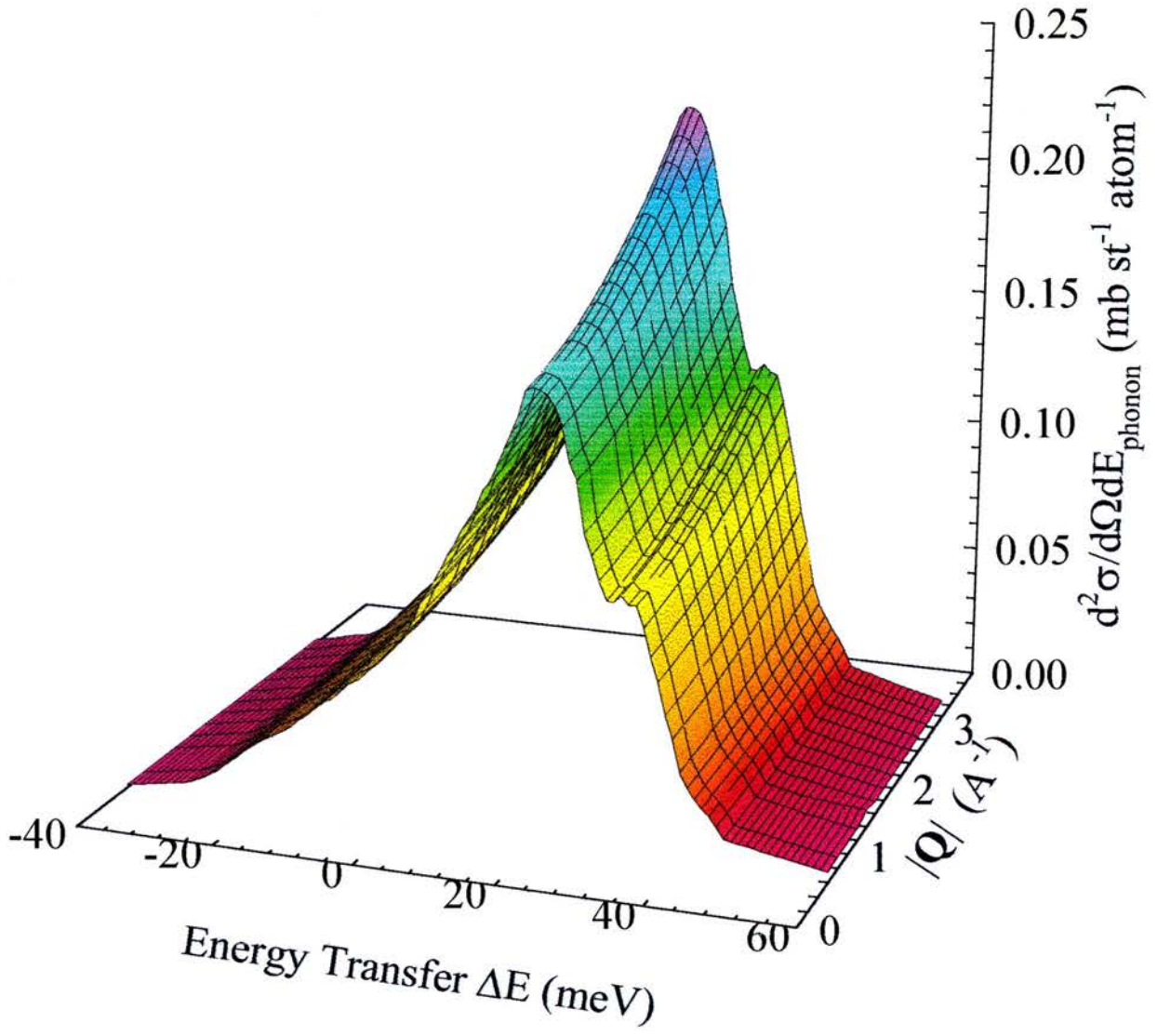

Figure 8.12

The simulated phonon cross-section of pure β-Mn at 109K at low Q from 0.8A^{-1} to 3.2A^{-1}. This region covers the low angle detector banks on HET at an incident energy of 100meV.

Figure 8.9 shows six constant energy cuts through the simulated $d^2\sigma/d\Omega dE_{phonon}$ grid fitted to eq. (8.8). The form of $A(\omega)$ and $B(\omega)$ extracted from these fits is shown in figure 8.10. Figure 8.11 shows the phonon scattering at a constant wavevector transfer of 1.4Å^{-1} calculated from the values of $A(\omega)$ and $B(\omega)$ using eq. (8.8). The response at each temperature was found by multiplying the simulated response at 109K by a ratio of detailed balance factors,

$$\left.\frac{d^2\sigma}{d\Omega dE}\right|_T = \left.\frac{d^2\sigma}{d\Omega dE}\right|_{109K} \times \frac{[1+n_T(\omega)]}{[1+n_{109K}(\omega)]}. \qquad (8.12)$$

The values of $d^2\sigma/d\Omega dE_{phonon}$ at each temperature found in this way were found to agree well with the measured phonon response at high angles. Finally, the $d^2\sigma/d\Omega dE_{phonon}$ grid calculated from these simulations is shown in figure 8.12. The Q range shown in figure 8.12 of $0.6 \leq Q \leq 3.2$ corresponds to the Q range of the low angle detector banks on HET at the incident energy used in this experiment (100meV).

After subtracting the calculated phonon cross-section from low angle data, the magnetic response remains, isolated from the total scattering. The form of the phonon cross-section calculated for pure β-Mn was found to scale well with the measured phonon response in $\beta\text{-}Mn_{0.8}Al_{0.2}$ at high angles. Therefore, in order to isolate the magnetic scattering from the total scattering for $\beta\text{-}Mn_{0.8}Al_{0.2}$, the calculated $d^2\sigma/d\Omega dE_{phonon}$ grid was scaled to the experimental data at high Q before subtraction.

8.3.3 Analysis of Results

8.3.3.1 Modelling of the Inelastic Cross-section at Constant Q.

It was shown in section 3.2.3 that the magnetic partial differential cross-section can be written as,

$$\left.\frac{d^2\sigma}{d\Omega dE}\right|_{magnetic} = \frac{k`}{k_i}\frac{(\gamma r_0)^2}{\hbar}\left[\frac{1}{2}g_s f(Q)\right]^2 S(Q,\omega), \qquad (8.13)$$

where the structure factor $S(Q,\omega)$ can be related to the imaginary part of the dynamical susceptibility of the system using the fluctuation-dissipation theorem [6],

$$S(Q,\omega) = \frac{N\hbar}{(g_s\mu_B)^2}[1+n(\omega)]\frac{1}{\pi}\chi''(Q,\omega), \qquad (8.14)$$

where the symbols have their usual meanings. In section 2.3.3 it was shown that the ω-dependence of the dynamical susceptibility was Lorentzian in form with,

$$\chi''(Q,\omega) = \frac{\omega\chi(Q)\Gamma(Q)}{\Gamma(Q)^2 + \omega^2}. \qquad (8.15)$$

Therefore, combining equations (8.13), (8.14) and (8.15) we can write the magnetic partial differential cross-section as,

$$\left.\frac{d^2\sigma}{d\Omega dE}\right|_{magnetic} = \frac{k`}{k_i}\frac{N(\gamma r_0)^2}{\pi(2\mu_B)^2}|f(Q)|^2[1+n(\omega)]\frac{\omega\chi(Q)\Gamma(Q)}{\Gamma(Q)^2+\omega^2}, \qquad (8.16)$$

where we have assumed that $g_s = 2$. The partial differential cross-section at a constant Q is then given by a Lorentzian lineshape of width Γ multiplied by ω, with an area proportional to the Q-dependent magnetic susceptibility χ(Q) of the system.

The measured, phonon subtracted, spectra at constant Q cuts through the measured inelastic response were modelled by eq. (8.16) convoluted with the spectrometer resolution which was measured using pure vanadium and taken to be a Gaussian with a FWHM of 3.66meV. The elastic contribution to the scattering was simultaneously fitted to an Ikeda-Carpenter function (see section 5.3).

Fits of eq. (8.16) plus an elastic lineshape to the measured response in β-Mn and β-$Mn_{0.8}Al_{0.2}$ at Q = 1.4Å^{-1} are presented in figures 8.13 and 8.14 for various sample temperatures.

The fitting parameters used to model the observed constant Q cuts of the inelastic response were as follows.

a) The Ikeda-Carpenter function used to fit the elastic line was determined by three parameters; the elastic integrated intensity, H_{el}, the exponential damping coefficient, λ_{el} and the elastic linewidth Γ_{el}. Both λ_{el} and Γ_{el} were found to be independent of temperature and wavevector Q, with $\lambda_{el} \sim 3.4$meV and $\Gamma_{el} \sim 1.7$meV for pure β-Mn and $\lambda_{el} \sim 2.7$meV and $\Gamma_{el} \sim 2.7$meV for β-$Mn_{0.8}Al_{0.2}$.

b) Equation (8.16) used to model the magnetic quasi-elastic response was determined by two parameters; the inelastic linewidth Γ_{inel} and the inelastic intensity H_{inel} which is directly proportional to the wavevector dependent susceptibility χ(Q).

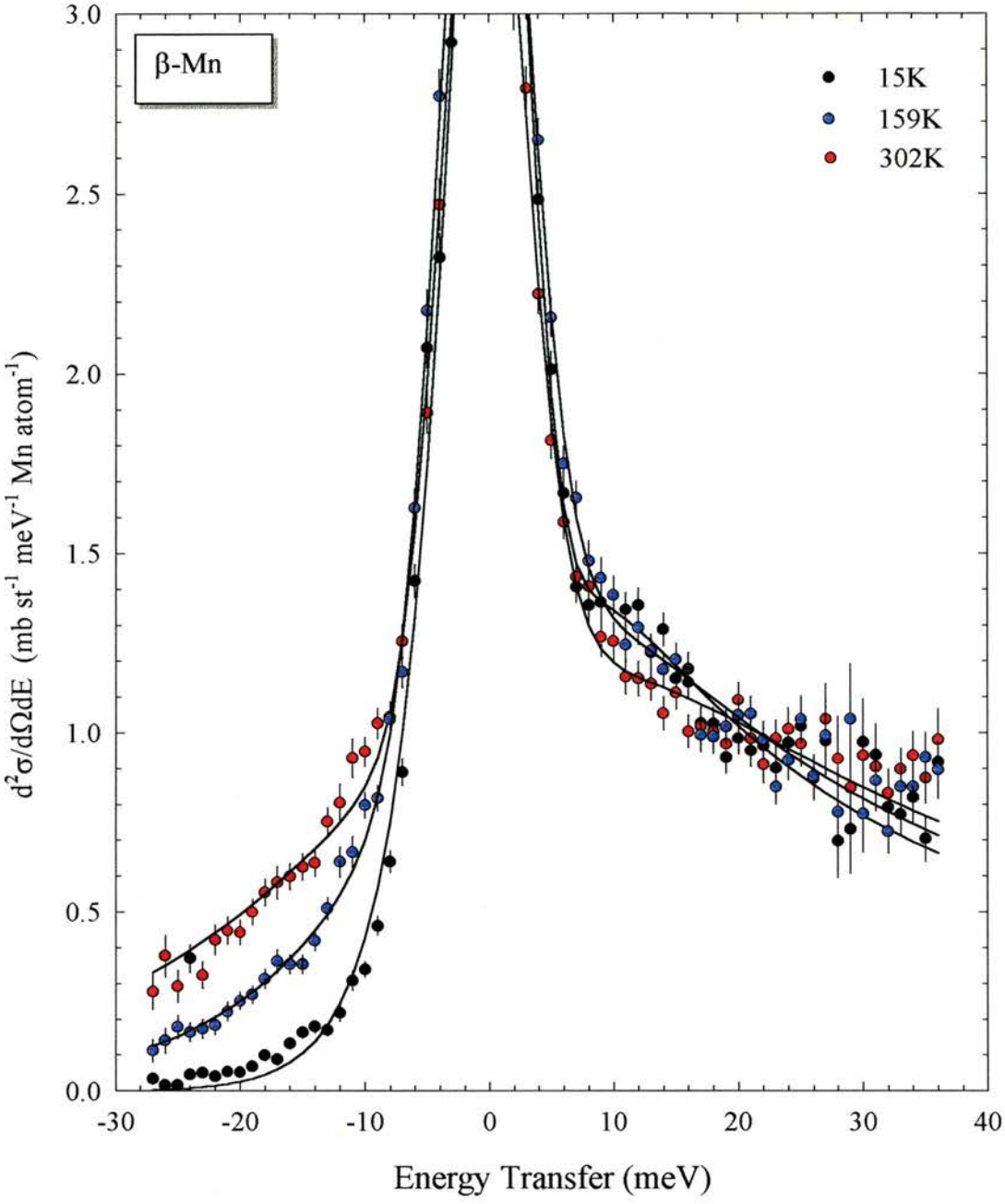

Figure 8.13

The partial differential cross-section of pure β-Mn at $Q = 1.4\text{Å}^{-1}$ at T = 15K, 159K and 303K. The solid lines are fits of eq. (8.16) plus an elastic lineshape given by an Ikeda-Carpenter function all convoluted with the instrumental resolution function. The energy gain side ($\Delta E < 0$) illustrates the effects of detailed balance, while the energy loss side of the spectra shows remarkably little temperature dependence.

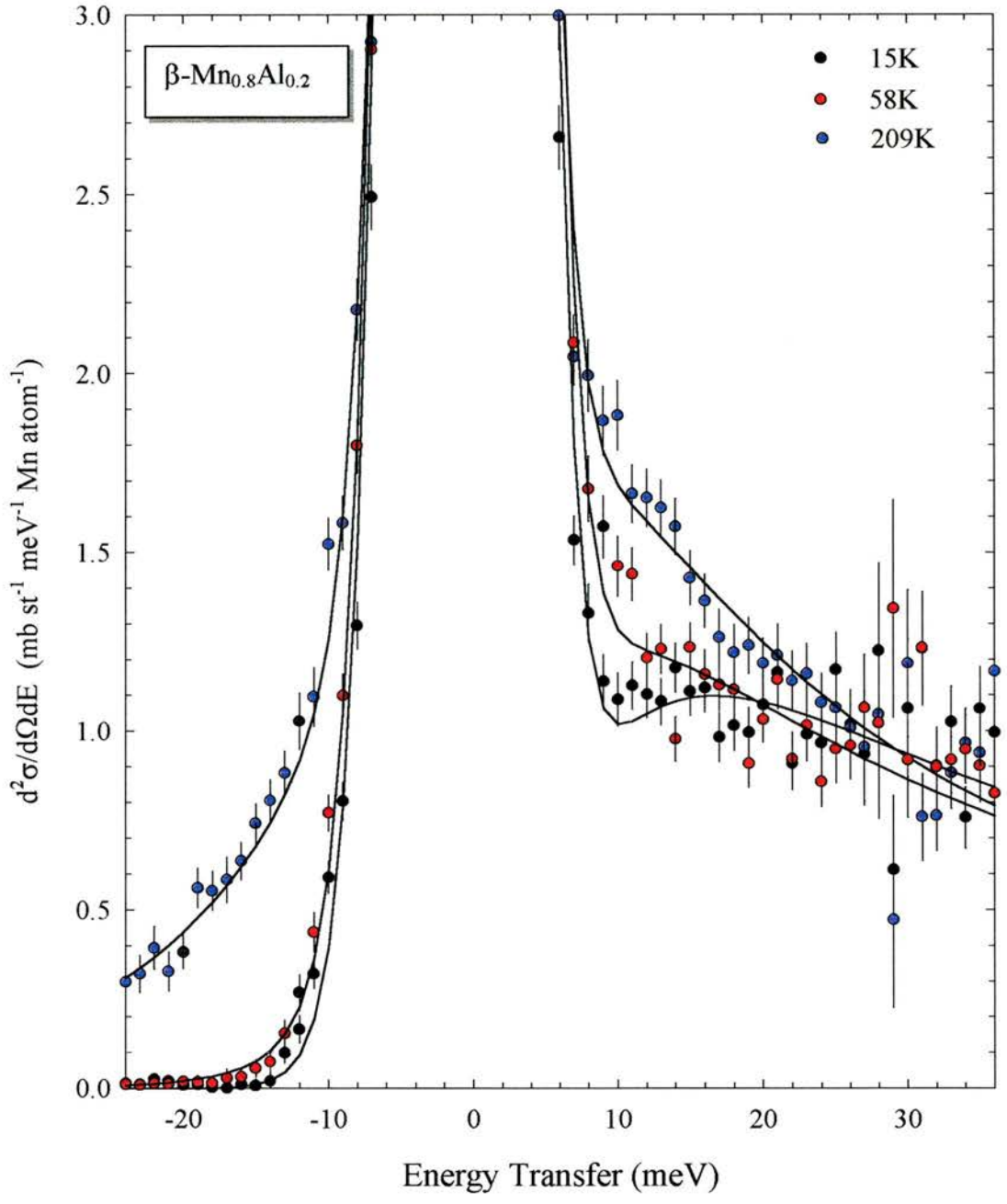

Figure 8.14

The partial differential cross-section of β-$Mn_{0.8}Al_{0.2}$ at $Q = 1.4Å^{-1}$ at $T = 15K$, 58K and 209K. The solid lines are fits of eq. (8.16) plus an elastic lineshape given by an Ikeda-Carpenter function all convoluted with the instrumental resolution function. The energy loss side of the spectra now displays strong temperature dependence.

The parameters derived from the fits of the Q = 1.4Å^{-1} data shown in figures 8.13 and 8.14 are presented in tables 8.1 and 8.2 and figures 8.15 and 8.16. Since the value of Q = 1.4Å^{-1} corresponds to the peak in the magnetic response observed in figures 8.5 and 8.6, the measured wavevector dependent susceptibility $\chi(Q)$ at Q = 1.4Å^{-1} corresponds to the staggered susceptibility χ_s of both β-Mn and β-$Mn_{0.8}Al_{0.2}$, as defined in section 2.3.2.3.

Table 8.1: Fitting parameters derived from the partial differential cross-section of pure β-Mn at Q = 1.4Å^{-1}. Plots of these parameters are shown in figure 8.15

Temp (K)	H_{el} (mb st^{-1} Mn atom^{-1})	H_{inel} (mb st^{-1} Mn atom^{-1})	Γ_{inel} (meV)	χ(Q=1.4Å^{-1}) (μ_B^2 meV^{-1} Mn atom^{-1})	1/χ(Q=1.4Å^{-1}) (meV Mn atom μ_B^{-2})
15	33.8	4.3	8.3	0.061	16.5
58	30.2	12.3	12.0	0.045	22.1
109	27.1	19.1	14.9	0.037	26.9
159	25.9	22.5	18.8	0.030	33.1
209	23.6	27.1	23.1	0.028	36.3
302	21.6	30.9	27.9	0.022	46.2

Table 8.2: Fitting parameters derived from the partial differential cross-section of β-$Mn_{0.8}Al_{0.2}$ at Q = 1.4Å^{-1}. Plots of these parameters are shown in figure 8.16

Temp (K)	H_{el} (mb st^{-1} Mn atom^{-1})	H_{inel} (mb st^{-1} Mn atom^{-1})	Γ_{inel} (meV)	χ(Q=1.4Å^{-1}) (μ_B^2 meV^{-1} Mn atom^{-1})	1/χ(Q=1.4Å^{-1}) (meV Mn atom μ_B^{-2})
15	188.0	2.9400	16.6	0.049	20.2
58	177.7	11.7000	13.8	0.055	18.1
109	156.8	22.5500	13.9	0.057	17.7
159	146.3	28.9100	16.7	0.050	20.1
209	139.2	31.2600	18.4	0.041	24.4
302	135.2	37.0600	29.7	0.033	29.9

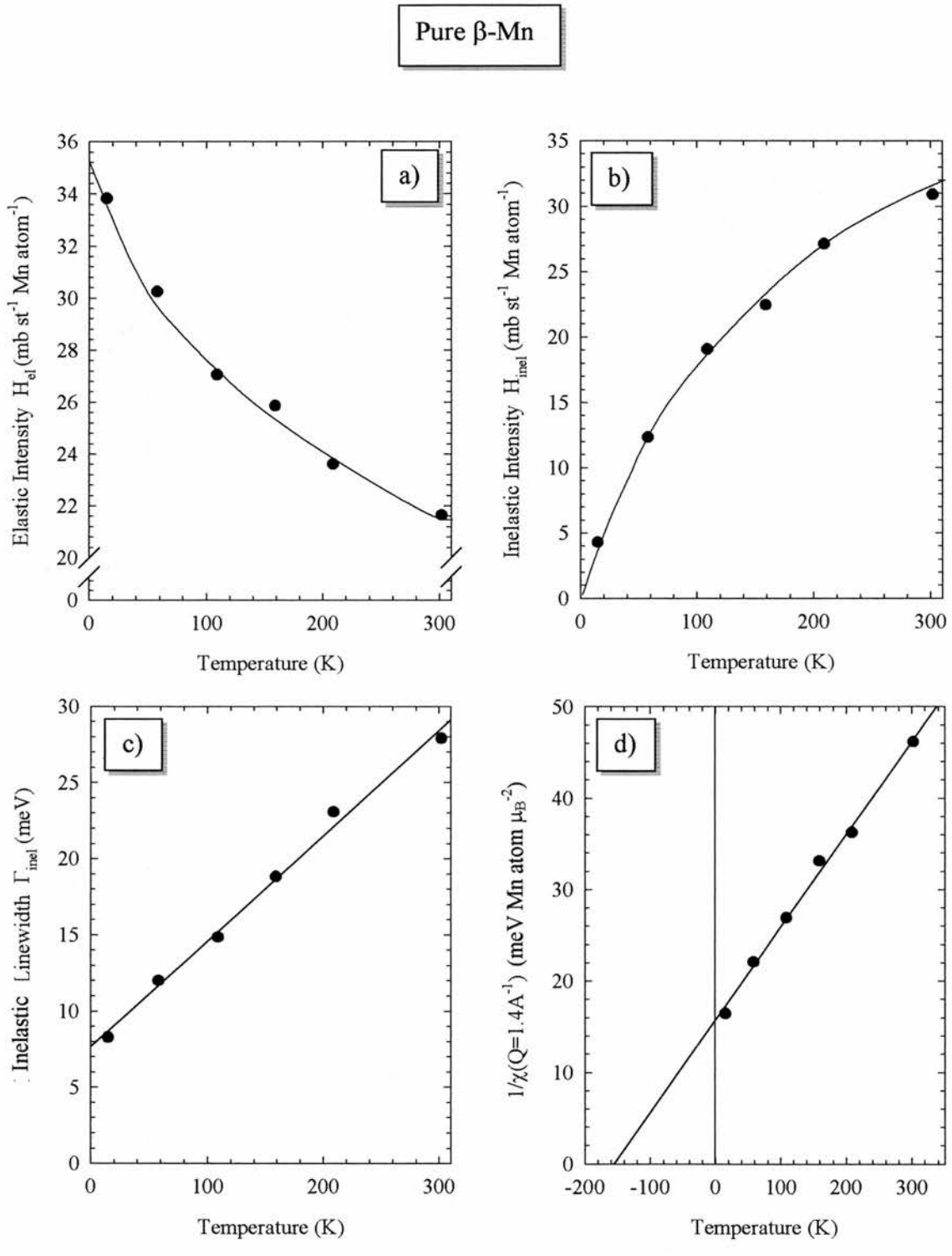

Figure 8.15

Plots of the temperature dependence of the fitting parameters of the inelastic partial differential cross-section of pure β-Mn at $Q = 1.4\text{Å}^{-1}$. a) Shows a steady increase in the intensity of the elastic line with decreasing temperature, while b) shows a concomitant decrease in the inelastic scattering intensity. c) shows that the inelastic linewidth Γ_{inel} decreases linearly with decreasing temperature. d) Shows that the staggered susceptibility derived from the inelastic intensity follows a Curie-Weiss law, in accordance with the predictions of the SCR theory. The lines shown are guides to the eye.

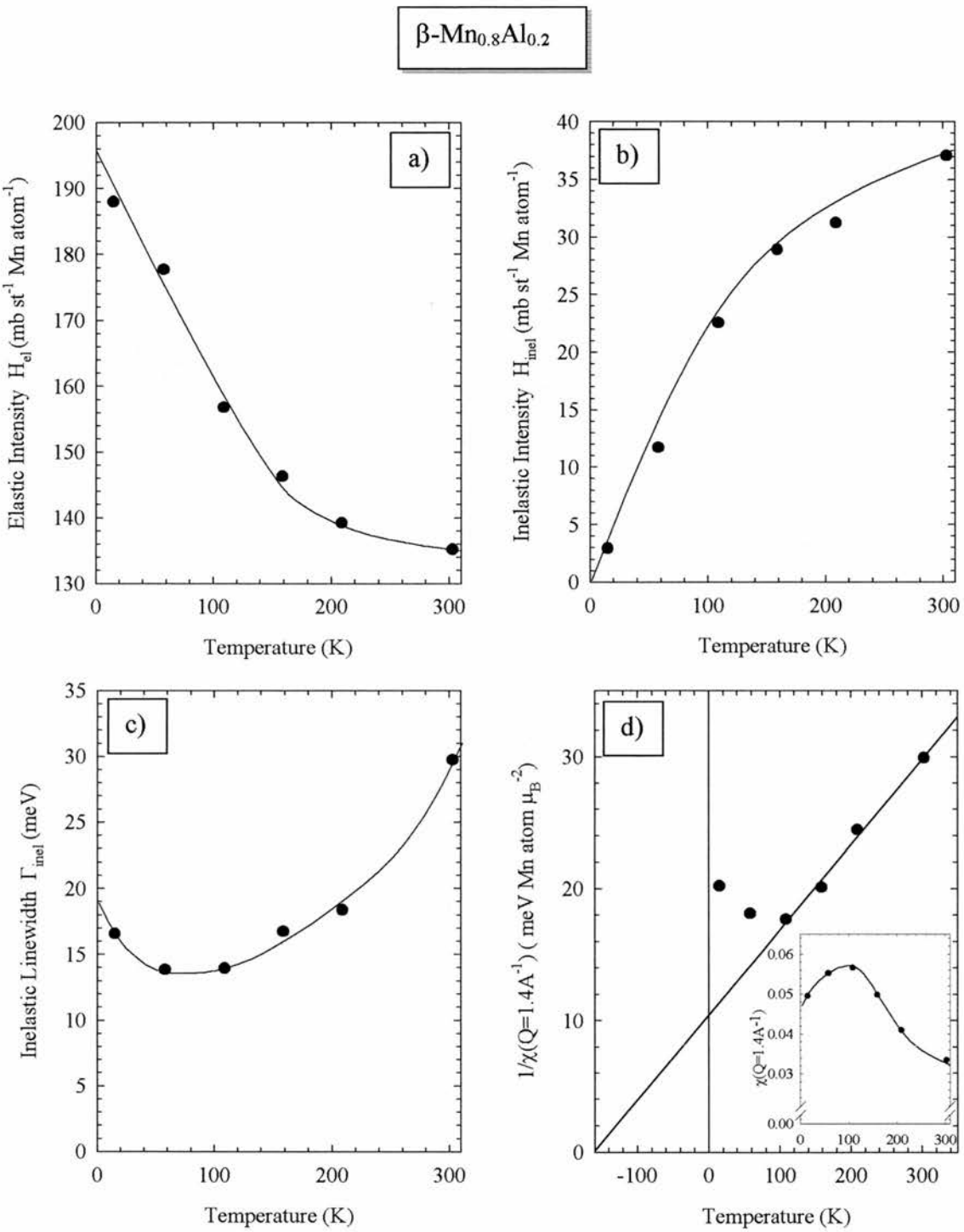

Figure 8.16

Plots of the temperature dependence of the fitting parameters of the inelastic partial differential cross-section of β-$Mn_{0.8}Al_{0.2}$ at $Q = 1.4Å^{-1}$. a) and b) show similar behaviour for the elastic and inelastic intensity as was found in pure β-Mn. The inelastic linewidth Γ_{inel} shown in c) displays a minimum at T ~70K. The staggered susceptibility shown in the inset of d) reaches a maximum at T ~ 70K coincident with the minimum observed in the temperature dependence of Γ_{inel}. The inverse staggered susceptibility is shown to follow a Curie-Weiss law for temperatures above the peak position. The lines shown are guides to the eye.

In pure β-Mn, the integrated intensity of the elastic line is found to increase steadily with decreasing temperature as shown in figure 8.15a while the inelastic intensity is shown in figure 8.15b to fall sharply with decreasing temperature. Figure 8.15c shows that the inelastic spin fluctuation linewidth Γ_{inel} is directly proportional to the temperature. The form of the staggered susceptibility is shown in figure 8.15d to obey a Curie-Weiss law in accordance with the predictions of the SCR theory for nearly and weakly antiferromagnetic metals (see section 2.4.1.2). The observation of temperature independence on the energy loss side of the β-Mn spectrum has also been observed in the Kondo lattice system UCu_4Pd_1 [7], where this behaviour was interpreted as an indication of non-Fermi liquid scaling of the dynamical susceptibility.

While the temperature dependence of the elastic and inelastic integrated intensities found in β-$Mn_{0.8}Al_{0.2}$ is very similar to that observed in pure β-Mn, figures 8.16c and 8.16d reveal striking differences in the form of both the inelastic linewidth and the staggered susceptibility. Γ_{inel} no longer displays Korringa-like behaviour, but passes through a minimum at $T \sim 70K$ and then increases with decreasing temperature tending towards a value of $\Gamma_{inel}(T=0K) \sim 18meV$. A peak is observed in the temperature dependence of the staggered susceptibility χ_s at $T \sim 70K$. Above this temperature, χ_s is found to obey a Curie-Weiss law. The observed peak in $\chi_s(T)$ is somewhat reminiscent of the peak observed in the magnetisation measurements performed on β-$Mn_{0.8}Al_{0.2}$ (see figure 4.4). Both pure β-Mn and β-$Mn_{0.8}Al_{0.2}$ have large inelastic linewidths at the lowest temperatures studied, indicating the presence of strong zero-point spin fluctuations. The Curie-Weiss nature of the staggered susceptibility will be discussed in section 8.3.3.4.

8.3.3.2 Analysis of the Wavevector Dependent Susceptibility

The values of $\chi(Q)f^2(Q)$ for β-Mn and β-$Mn_{0.8}Al_{0.2}$ extracted from the integrated inelastic intensity of constant Q cuts through the inelastic cross-section using eq. (8.16) are plotted in figures 8.17 and 8.18.

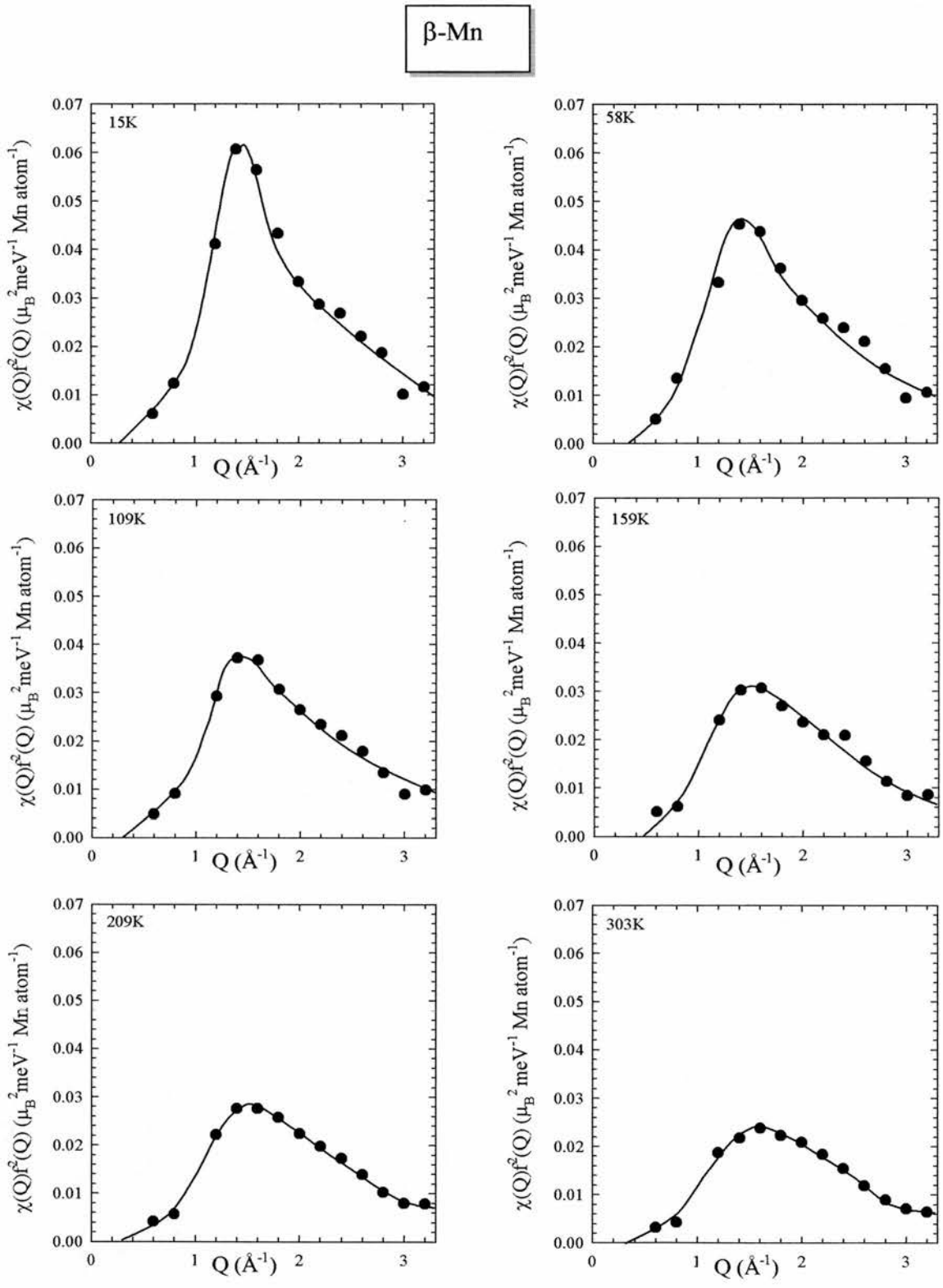

Figure 8.17

The wavevector dependent susceptibility of pure β-Mn derived from the integrated inelastic intensity of the magnetic cross-section at constant Q using equation (8.16). The solid lines are guides to the eye.

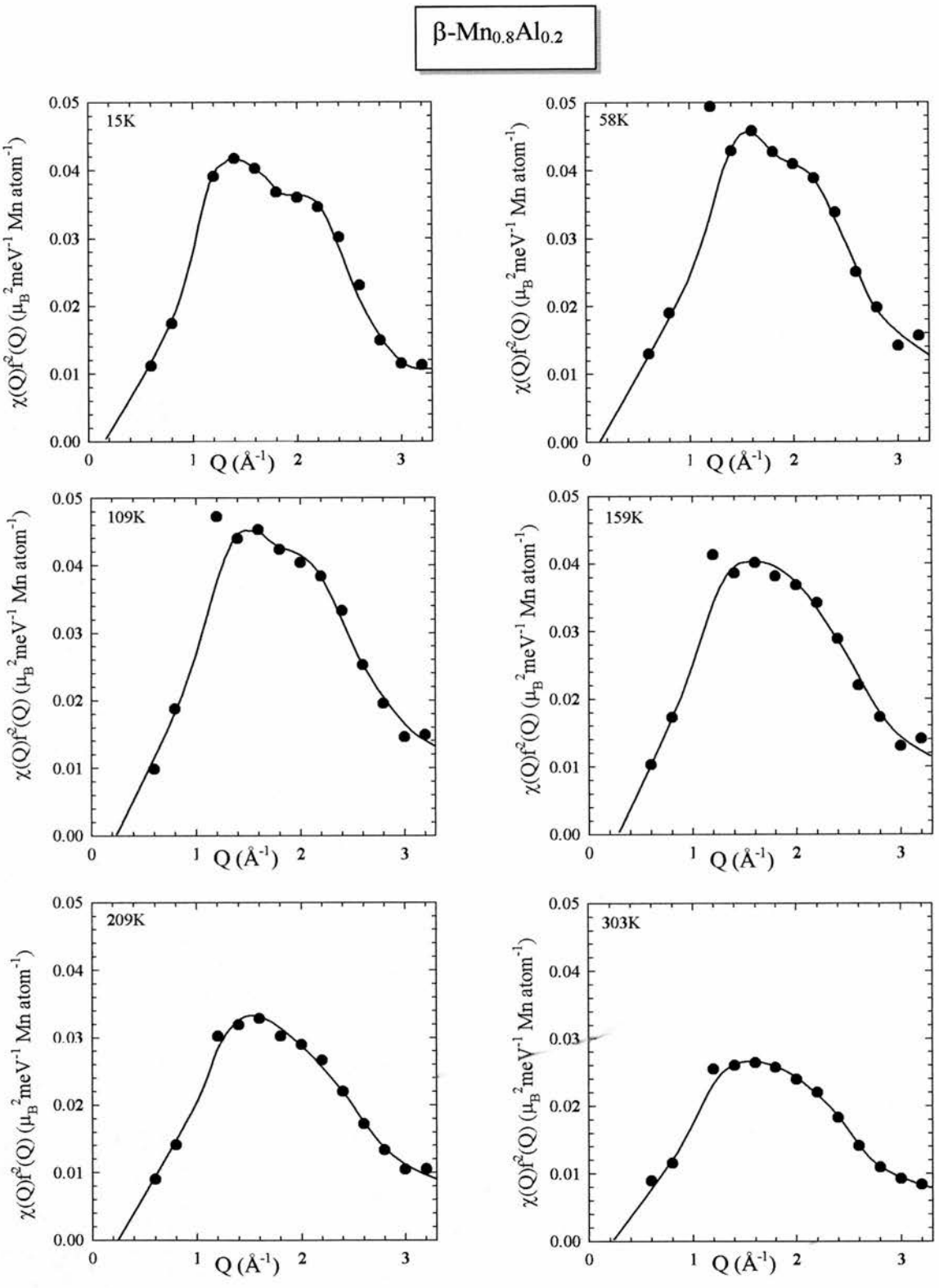

Figure 8.18

The wavevector dependent susceptibility of β-$Mn_{0.8}Al_{0.2}$ derived from the integrated inelastic intensity of the magnetic cross-section at constant Q using equation (8.16). The solid lines are guides to the eye.

The Q-dependence of $\chi(Q)f^2(Q)$ illustrated in figures 8.17 and 8.18 is very similar to the Q-dependence of the elastic magnetic cross-section of the β-$Mn_{1-x}Al_x$ alloys presented in the neutron polarisation analysis study presented in chapter 7 (see figure 7.14).

In pure β-Mn, $\chi(Q)f^2(Q)$ is peaked around $Q = 1.4\text{Å}^{-1}$ at all temperatures. $\chi(Q)f^2(Q)$ is sharply peaked around $Q = 1.4\text{Å}^{-1}$ at $T = 15K$. At higher temperatures, the peak in $\chi(Q)f^2(Q)$ broadens and reduces in intensity with increasing temperature. In β-$Mn_{0.8}Al_{0.2}$, the peak in $\chi(Q)f^2(Q)$ is much broader at low temperatures, and a second peak is observed at approximately $Q = 2.0\text{Å}^{-1}$. This second peak in $\chi(Q)f^2(Q)$ disappears at $T \geq 159K$, above which the form of $\chi(Q)f^2(Q)$ is very similar to that observed for pure β-Mn.

The observation of a magnetic response which is sharply peaked around $Q = 1.4\text{Å}^{-1}$ in pure β-Mn and more broadly peaked in β-$Mn_{0.8}Al_{0.2}$, and the appearance of a second peak in the susceptibility at around $Q = 2.0\text{Å}^{-1}$ in β-$Mn_{0.8}Al_{0.2}$, is fully consistent with our observations of the elastic magnetic scattering presented in chapter 7 (see section 7.7.3). This behaviour indicates that the magnetic correlations are of longer range in pure β-Mn and dilute β-MnAl alloys, than in the more concentrated alloys. However, figures 8.17 and 8.18 show that the intensity of the magnetic response integrated over all energies changes little between pure β-Mn and β-$Mn_{0.8}Al_{0.2}$, in contrast to our observation of increasing elastic magnetic intensity in β-MnAl alloys as the Al concentration increases. This implies that the apparent reduction in the Mn moment in dilute β-MnAl alloys observed in our neutron polarisation analysis study (see figure 7.17) is due to an increasingly inelastic component of the magnetic scattering, which is not observable on D7 due to the narrow energy window available (see figure 7.7).

8.3.3.3 The Local Susceptibility χ_L

The local susceptibility at each Mn atom in β-Mn and β-$Mn_{0.8}Al_{0.2}$ is derived by integrating the wavevector dependent susceptibility over Q, as given by equation (2.40). Defining $\langle\chi(Q)\rangle_{Qm}$ to be the sum over $\chi(Q)$ up to a maximum value of $Q = Q_m$, we have,

$$<\chi(\mathbf{Q})>_{Qm} = \frac{\int_0^{Qm} \chi(\mathbf{Q})d\mathbf{Q}}{\frac{4}{3}\pi Q_m^{\ 3}}. \qquad (8.17)$$

To facilitate this calculation, eq. (8.18) was approximated to a form based on the modulus of the wavevector transfer [8],

$$<\chi(Q)>_{Qm} = \frac{\sum_{i=1}^{m} \chi(Q_i)Q_i^{\ 2}}{\sum_{i=1}^{m} Q_i^{\ 2}}. \qquad (8.18)$$

The value of $<\chi(Q)>_{Qm}$ as a function of Q_m is found to increase from zero wavevector transfer, and then to oscillate about a constant value as Q_m increases. This constant value is taken to be the local susceptibility χ_L since the oscillation ensures that an integration over an adequate Q range has been performed. An example of the Q_m dependence of $<\chi(Q)>_{Qm}$ is shown in figure 8.19. The limit of Q_m in the low angle bank on HET at E_i = 100meV is 3.2Å^{-1}, which is only enough to observe the first maximum in the oscillation of $<\chi(Q)>_{Qm}$.

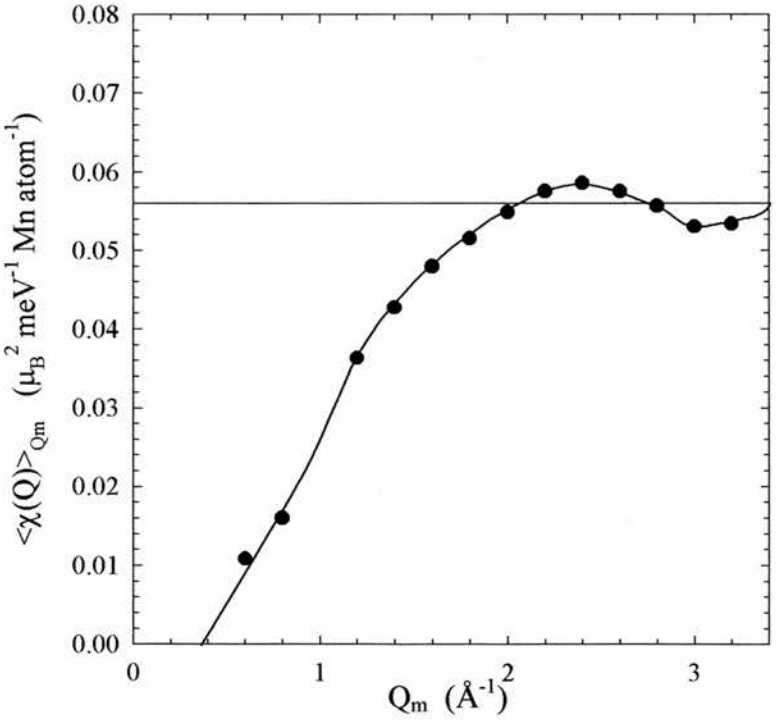

Figure 8.19

The values of $<\chi(Q)>_{Qm}$ shown as a function of Q_m for β-$Mn_{0.8}Al_{0.2}$ at a temperature of 159K. The value of the local susceptibility χ_L is taken to be the level at which $<\chi(Q)>_{Qm}$ oscillates at high wavevector transfers.

The temperature dependence of the inverse of the local susceptibility $1/\chi_L$ thus derived for β-Mn and β-$Mn_{0.8}Al_{0.2}$ is shown in figure 8.20. The error associated with the determination of χ_L was typically around 10%, or $\pm$ 0.05 μ_B^2 meV^{-1} Mn $atom^{-1}$.

Figure 8.20 shows that the form of χ_L is Curie-Weiss like at all temperatures in β-Mn and for T > 70K for β-$Mn_{0.8}Al_{0.2}$. Fitting $1/\chi_L$ to a straight line of the form,

$$\frac{1}{\chi_L} = \frac{1}{C}(T - \theta_{cw}), \tag{8.19}$$

we can calculate the mean Mn moment per atom via eq. (2.3),

$$\frac{C}{\mu_B^{\,2}} = \frac{g_s^{\,2} S(S+1)}{3k_B}, \tag{8.20}$$

where

$$\mu_{mean} = g_s S \mu_B. \tag{8.21}$$

Taking $g_s = 2$ for Mn, we obtain S = 0.68 $\pm$ 0.01 giving μ_{mean} = 1.36 $\pm$ 0.02μ_B per Mn atom in β-Mn, and S = 0.72 $\pm$ 0.02 giving μ_{mean} = 1.44 $\pm$ 0.04μ_B per Mn atom in β-$Mn_{0.8}Al_{0.2}$. The value of the Curie-Weiss constant determined from fitting eq. (8.19) to the data was θ_{CW} = 295 $\pm$ 2K for β-Mn and θ_{CW} = 136 $\pm$ 3K for β-$Mn_{0.8}Al_{0.2}$.

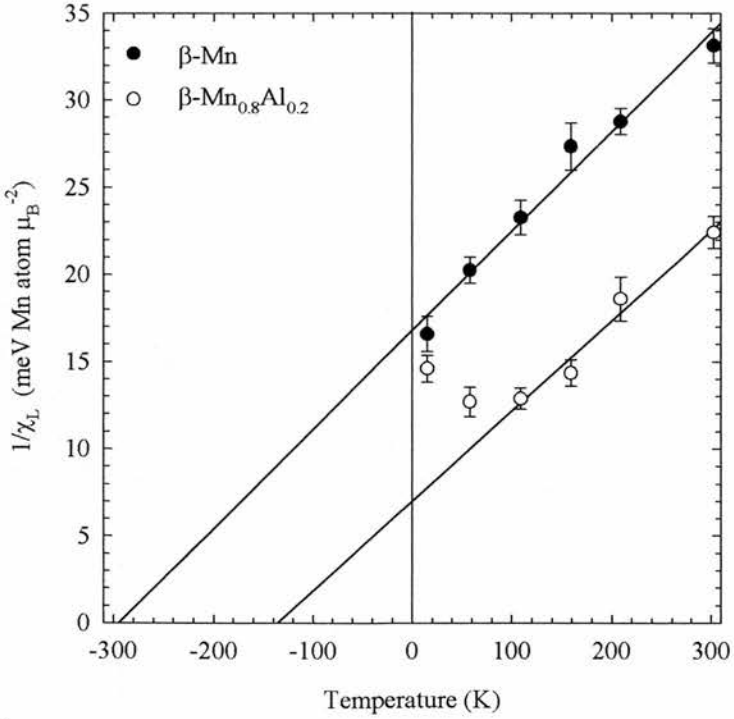

Figure 8.20

The Curie-Weiss temperature dependence of $1/\chi_L$. The solid lines are fits to eq. (8.19).

The value of the $\mu_{mean} = 1.44 \pm 0.04\mu_B$ for β-$Mn_{0.8}Al_{0.2}$ is in close agreement with the value reported by Nakamura and co-workers [9] of $\mu_{mean} = 1.5 \pm 0.2\mu_B$. However, the foregoing analysis assumes that there is a well defined localised paramagnetic moment in β-Mn and β-$Mn_{0.8}Al_{0.2}$. While β-$Mn_{0.8}Al_{0.2}$ displays certain characteristics of local moment formation, as indicated by our magnetisation (chapter 4) and μSR (chapter 6) studies, it is likely that both β-Mn and β-$Mn_{0.8}Al_{0.2}$ are essentially itinerant in nature. A more valid approach to the analysis of the local susceptibility χ_L and staggered susceptibility χ_s, is provided by the SCR theory introduced in chapter 2.

2.1.1.1 Analysis of χ_L and χ_s Using SCR Theory

It was shown in section 2.4.1.1 that the local susceptibility χ_L is related to the square of the thermal average of the longitudinal and transverse local spin fluctuation amplitude $\langle S_L \rangle^2$ [10] by the equation,

$$\chi_L(T) = \frac{N g_s^2 \mu_B^2 \langle S_L \rangle^2}{3 k_B T}. \qquad (8.22)$$

If $\langle S_L \rangle^2$ is independent of temperature, then eq. (8.22) is of the form of the Curie Law [eq. (2.2)]. The observation of a Curie-Weiss dependence of $\chi_L(T)$ in itinerant electron systems can only be described by eq. (8.22) with a temperature dependent spin fluctuation amplitude $\langle S_L(T) \rangle^2$. Values of $\langle S_L(T) \rangle^2$ calculated using eq. (8.22) for β-Mn and β-$Mn_{0.8}Al_{0.2}$ are plotted in figure 8.21. The solid lines in figure 8.21 are guides to the eye.

The temperature dependence of $\langle S_L(T) \rangle^2$ changes dramatically from pure β-Mn to β-$Mn_{0.8}Al_{0.2}$. In pure β-Mn, $\langle S_L(T) \rangle^2$ increases linearly with increasing temperature, which from figure 2.12 is indicative of a nearly antiferromagnetic metal with a small longitudinal stiffness constant (see section 2.4.3.2). In β-$Mn_{0.8}Al_{0.2}$, $\langle S_L(T) \rangle^2$ increases more rapidly than for β-Mn, and then shows a tendency to saturate at a value of approximately $\langle S_L \rangle^2 \sim 0.33$. This behaviour is characteristic of temperature dependent local moment formation, discussed in section 2.4.3.2, and suggests that the Mn moments in β-$Mn_{0.8}Al_{0.2}$ are partially localised due to an increased longitudinal stiffness constant.

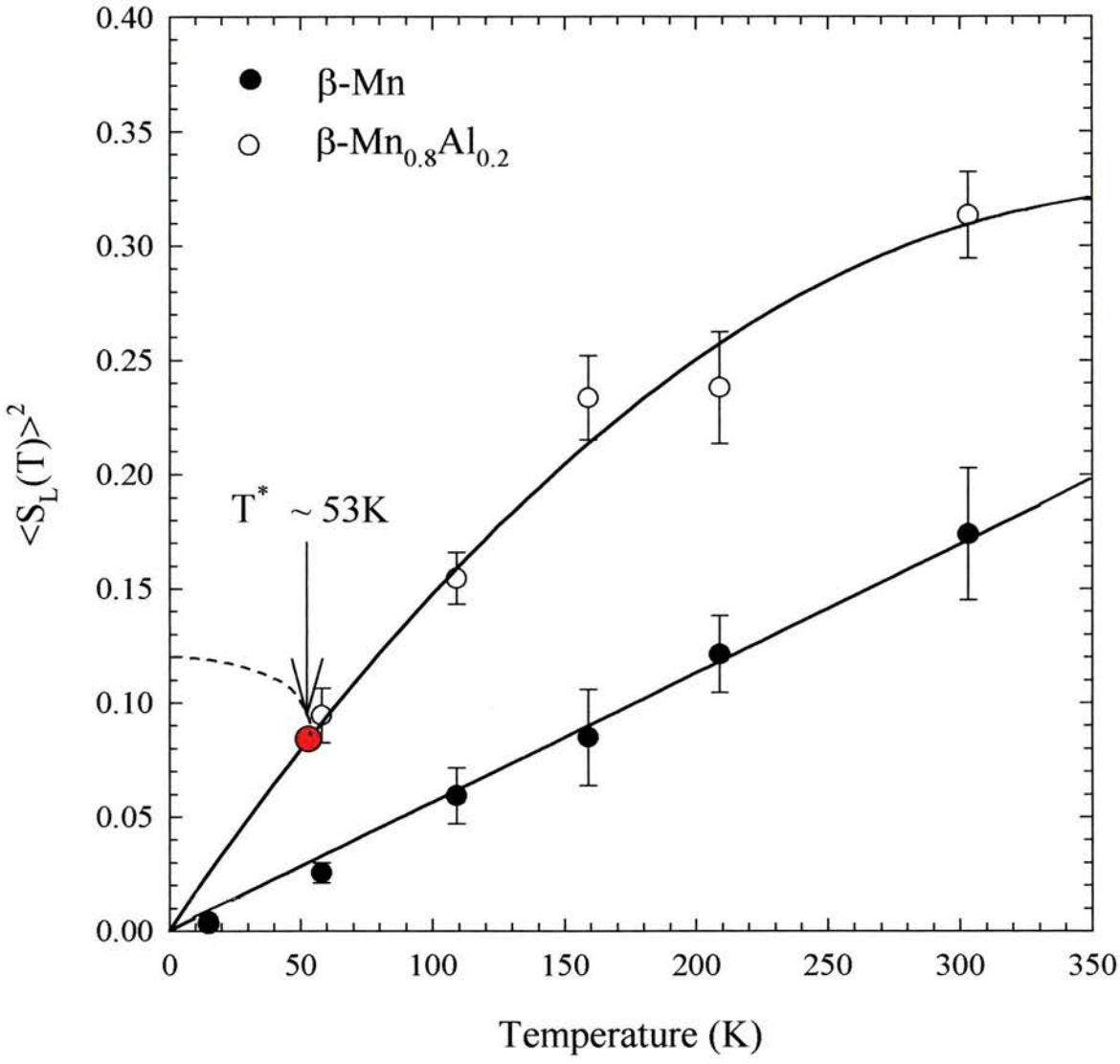

Figure 8.21

The temperature dependence of the square of the thermal average of the longitudinal and transverse local spin fluctuation amplitude $\langle S_L(T)\rangle^2$ for pure β-Mn and β-$Mn_{0.8}Al_{0.2}$. The form of $\langle S_L(T)\rangle^2$ indicates the presence of purely itinerant Mn moments in pure β-Mn and the partial localisation of the Mn moments in β-$Mn_{0.8}Al_{0.2}$. The point shown in red indicates the magnetic transition temperature of β-$Mn_{0.8}Al_{0.2}$ given by eq. (8.25) The dotted line indicates the expected temperature dependence of $\langle S_L(T)\rangle^2$ of an antiferromagnet below the transition temperature.

The value of the saturation moment indicated by the saturation amplitude of $\langle S_L \rangle^2 \sim 0.33$ for β-$Mn_{0.8}Al_{0.2}$ is $\mu \sim 1.15\mu_B$. This value is in broad agreement with both the value of $\mu = 1.5 \pm 0.2\mu_B$ obtained by Nakamura et. al., and the value of $\mu = 1.44 \pm 0.04\mu_B$ obtained from a conventional fit of the local susceptibility to a Curie-Weiss law.

The fact that the values of the Mn moment in β-$Mn_{0.8}Al_{0.2}$ calculated using conventional local moment theory and SCR theory are of the same order, is suggestive of the increasing local moment nature of β-MnAl alloys with high Al concentrations. However, a Curie-Weiss analysis of the local susceptibility of β-MnAl alloys is clearly an inadequate description of the data, due to the variation of the Mn spin fluctuation amplitude with temperature shown in figure 8.21.

Having obtained the form of the temperature dependence of the local Mn spin fluctuation amplitude, we can now use eq. (2.45) to parameterise the observed staggered susceptibility at $Q = 1.4\text{Å}^{-1}$ in terms of the mode-mode coupling constant F_s, the square of the staggered spin magnetisation per Mn atom at T = 0K, $M_s^2(0)$ and the non-interacting Hartree-Fock contribution to the susceptibility $\chi_{HF}(q)$, where q is the antiferromagnetic wavevector, via

$$\frac{1}{\chi_s} = F_s\left[\frac{5}{3}\langle S_L \rangle^2 + \frac{1}{F_s\chi_{HF}(q)} + M_s^2(0)\right]. \qquad (8.23)$$

In order to fit the observed temperature dependence of the staggered susceptibility of β-Mn and β-$Mn_{0.8}Al_{0.2}$ (see figures 8.15 and 8.16) to eq. (8.23), the temperature dependence of $\langle S_L \rangle^2$ shown in figure 8.21 was parameterised by fitting a straight line in the case of pure β-Mn and a quadratic in the case of β-$Mn_{0.8}Al_{0.2}$.

Figure 8.22 shows the temperature dependence of the inverse staggered susceptibility of β-Mn and β-$Mn_{0.8}Al_{0.2}$ fitted to eq. (8.23). The values of F_s and $[1/F_s\chi_{HF}(q) + M_s^2(0)]$ obtained from the fits are shown in the figure. Since eq. (8.23) is defined only for the paramagnetic regime, the fit of the β-$Mn_{0.8}Al_{0.2}$ data is shown above the position of the peak in χ_s at T ~ 70K (see figure 8.16d).

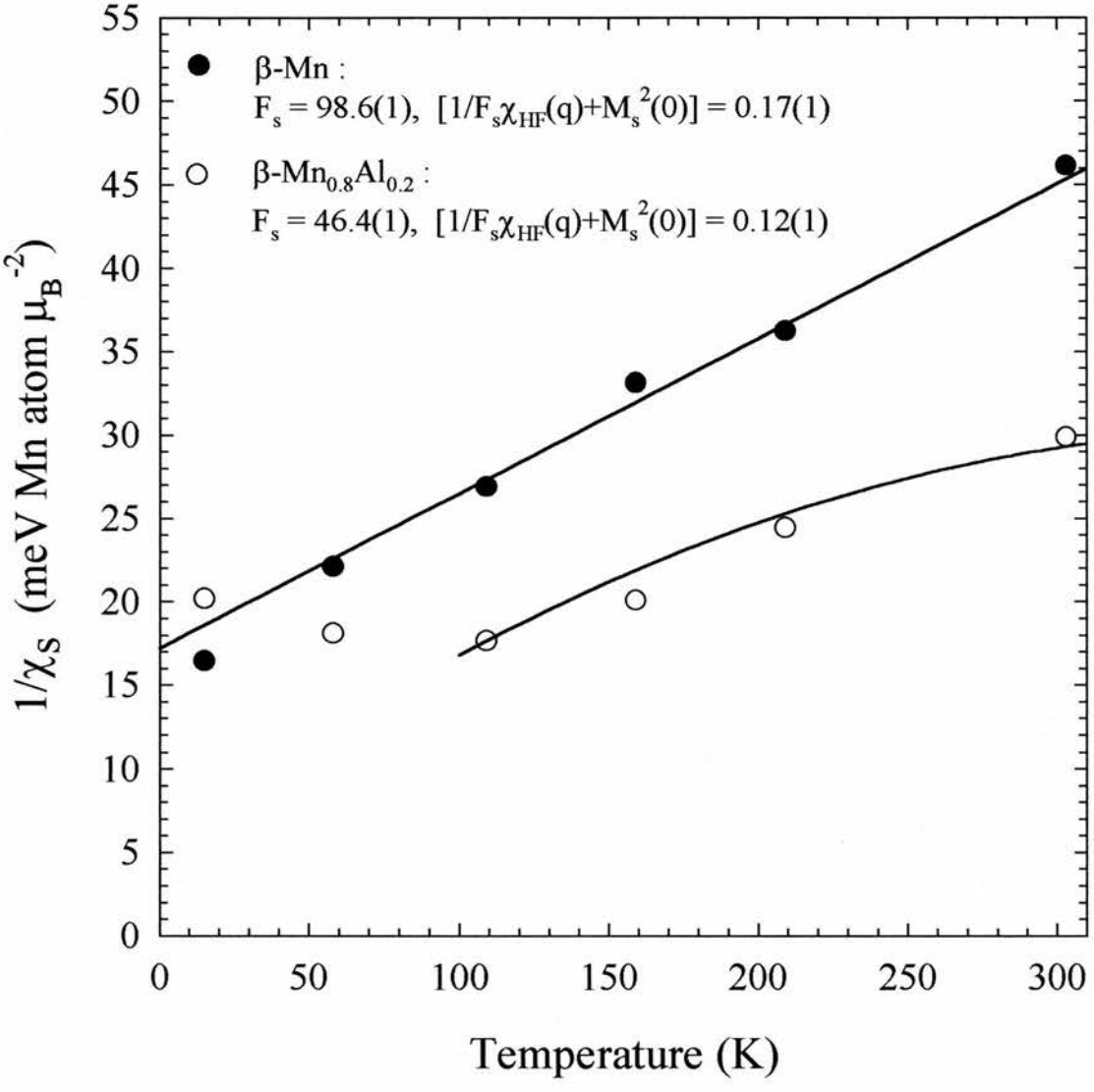

Figure 8.22

The temperature dependence of the inverse staggered susceptibility $1/\chi_s$ of β-Mn and β-$Mn_{0.8}Al_{0.2}$ fitted to eq. (8.24). The parameters F_s and $[1/F_s\chi_{HF}(q) + M_s^2(0)]$ for each fit are shown.

Taking the value of the ordered Mn moment of $\mu \sim 1.05\mu_B$/Mn atom for β-$Mn_{0.8}Al_{0.2}$ obtained from our neutron polarisation analysis study (see figure 7.17), the value of $M_s^2(0)$ in β-$Mn_{0.8}Al_{0.2}$ is approximately ~0.275 /Mn atom. Therefore, from the value of $[1/F_s\chi_{HF}(q) + M_s^2(0)] = 0.12 \pm 0.01\mu_B^2$ obtained from the fit of eq. (8.24) to $1/\chi_s$ shown in figure 8.22, we can infer that,

$$1/\chi_{HF}(q) \sim -7.192 \text{ meV Mn atom } \mu_B^{-2}.$$

From eq. (2.30), a negative value of $1/\chi_{HF}(q)$ indicates that the Stoner condition for the appearance of magnetic order, $\alpha\chi_0 > 1$, is satisfied in β-$Mn_{0.8}Al_{0.2}$.

Since the magnetic transition temperature is defined as the point at which $1/\chi_s = 0$, we can rearrange eq. (8.24) to obtain,

$$S_L^2(T^*) = 3/5[1/F_s\chi_{HF}(q) + M_s^2(0)], \qquad (8.24)$$
$$= 0.072 \pm 004 \text{ for } \beta\text{-}Mn_{0.8}Al_{0.2}.$$

where T^* is the transition temperature predicted by SCR theory. This is shown as the red point in figure 8.21, and indicates a transition temperature of $T^* \sim 53K$ for β-$Mn_{0.8}Al_{0.2}$. This value of the transition temperature is higher than that obtained from our magnetisation ($T_g = 34K$) and μSR ($T_g = 38K$) measurements. This discrepancy is accounted for by the fact that the SCR theory does not take the effects of moment frustration into account, which will inevitably depress the magnetic transition temperature of the system. The SCR prediction of the temperature dependence of $\langle S_L \rangle^2$ below the magnetic transition temperature is shown as the dotted line in figure 8.21.

For pure β-Mn we can assume that there is zero ordered moment per Mn atom at $T = 0K$. Therefore, the non interacting Hartree-Fock susceptibility in pure β-Mn is given by,

$$1/\chi_{HF} = 16.762 \ \mu_B^2 \text{ mev}^{-1} \text{ Mn atom}^{-1},$$

which is the intercept on the $1/\chi_s$ axis at $T = 0K$.

8.4 Discussion

The inelastic polarised neutron scattering study of Shiga et. al. [1] presented in chapter 1 indicated that the introduction of Al into the β-Mn lattice resulted in a significant reduction in the Mn spin fluctuation spectral width, from 20meV at 7K in pure β-Mn to 0.7meV at 7K in β-$Mn_{0.9}Al_{0.1}$. This observation led Shiga to characterise the transition from the dynamic β-Mn ground state to the largely static β-$Mn_{0.9}Al_{0.1}$ ground state as a quantum spin liquid (QSL) to spin glass transition. Our measurements, however, indicate that the spectral width of the spin fluctuations in β-Mn is not reduced by the introduction of Al. We do, however, observe a sharp reduction in the inelastic intensity of both β-Mn and β-$Mn_{0.8}Al_{0.2}$ together with a concomitant rise in the elastic intensity as the temperature decreases.

The observation of a persistent dynamic component in β-$Mn_{0.8}Al_{0.2}$ is consistent with our μSR measurements (see chapter 6). Figure 6.21a shows that the initial muon asymmetry $a_0(T)$ in β-$Mn_{0.8}Al_{0.2}$ recovers to 1/3 of its high temperature value at T ~ 5K, indicating a truly static magnetic ground state only at that temperature. The lowest available temperature in our inelastic neutron study was 15K, at which point the initial muon asymmetry lies well below 1/3 of its high temperature value, indicating residual spin dynamics below the observed magnetic transition temperature of T_g = 38K.

The most striking difference between pure β-Mn and β-$Mn_{0.8}Al_{0.2}$ is the change in the nature of the staggered susceptibility χ_s and the local Mn spin fluctuation amplitude $\langle S_L \rangle^2$. The forms of the temperature dependence of χ_s, χ_L and $\langle S_L \rangle^2$ in both β-Mn and β-$Mn_{0.8}Al_{0.2}$ are in extremely good agreement with the theoretical predictions of the SCR theory of nearly and weakly antiferromagnetic metals. The form of the temperature dependence of $\langle S_L \rangle^2$ indicates that β-Mn is an archetypal itinerant electron, nearly antiferromagnetic metal, with $\langle S_L \rangle^2$ increasing linearly with temperature. $\langle S_L \rangle^2$ in β-$Mn_{0.8}Al_{0.2}$ displays a tendency to saturate at high temperatures, thus displaying both itinerant and local moment characteristics in accord with Moriya's unified theory [10].

8.5 Conclusions

We have undertaken an inelastic neutron scattering study of β-Mn and β-$Mn_{0.8}Al_{0.2}$. We have shown that the large zero-point spin fluctuation spectral width of pure β-Mn is not greatly reduced by the introduction of Al. Our measurements do not, therefore, support the notion of a dynamic QSL to static spin glass phase transition.

The form of the magnetic scattering obtained by integrating over the entire inelastic linewidth agrees well with the form of elastic magnetic scattering observed in our neutron polarisation analysis study (chapter 7). The intensity of the magnetic scattering is found not to vary greatly between β-Mn and β-$Mn_{0.8}Al_{0.2}$, indicating that the loss in magnetic intensity observed in our neutron polarisation analysis study is due to an increasingly inelastic component of the scattering cross-section.

The temperature dependence of the staggered susceptibility is found to be Curie-Weiss like in the paramagnetic regime for both β-Mn and β-$Mn_{0.8}Al_{0.2}$ as predicted by the SCR theory. The form of the observed temperature dependence of the local Mn spin fluctuation amplitude indicates the presence of purely itinerant moments in β-Mn and partially localised moments in β-$Mn_{0.8}Al_{0.2}$.

8.6 References

[1] M Shiga, H Nakamura, M Nishi and K Kakurai, J. Phys. Soc. Japan **63** (1994) 1656

[2] C G Windsor, *Pulsed Neutron Scattering*, (Taylor and Francis, 1981)

[3] A P Murani, Phys. Rev. **B47** (1993) 14280

B D Rainford, private communication

[4] C Kittel, *Introduction to Solid State Physics*, (Wiley, 6th ed., 1986)

[5] M W Johnson, *DISCUS, A Computer Program for the Calculation of Multiple Scattering Effects in Inelastic Neutron Scattering*, (UKAEA Harwell Report AERE-R7682, 1974)

[6] P M Chaikin and T C Lubensky, *Principles of Condensed Matter Physics*, (Cambridge University Press, 1995), chapter 7

[7] M C Aronson, R Osborn, R A Robinson, J W Lynn, R Chau, C L Seaman and M B Maple, Phys. Rev. Lett. **75** (1995) 725

[8] S J Dakin, *Spin Fluctuations in Metallic Magnets*, PhD Thesis, University of Southampton, 1992

[9] H Nakamura, K Yoshimoto, M Shiga, M Nishi and K Kakurai, J. Phys. Cond. Matter **9** (1997) 4701

[10] T Moriya, *Spin Fluctuations in Itinerant Electron Magnetism*, (Springer-Verlag, 1985)

9 Conclusions and Further Studies

In this thesis, I have characterised the magnetic and structural properties of pure β-Mn and β-$Mn_{1-x}Al_x$ alloys with concentrations in the range $0 < x \leq 0.2$, using a combination of experimental techniques. I have attempted to describe the mechanism by which the inclusion of non magnetic Al impurities in the non-magnetic β-Mn lattice results in the stabilisation of short-range magnetic order, and to characterise the nature of the spin dynamics and the magnetic ground states of the β-$Mn_{1-x}Al_x$ series.

9.1 Structural Properties

We have demonstrated that the formation of β-Mn from α-Mn results in a close packed crystal structure in which there is geometrical frustration between the triangularly coordinated site II Mn moments. Al impurities display a strong preference for the site II crystallographic position in the β-Mn matrix, lending support to the contention that the introduction of Al impurities in β-Mn disrupts the spin configurational degeneracy associated with the site II sublattice. We have also shown that there exists short-range order of the Al impurities on the site II β-Mn sublattice, with the Al nuclei displaying anticlustering behaviour.

9.2 Magnetic Properties

9.2.1 In-house Characterisation

Magnetisation studies of β-$Mn_{1-x}Al_x$ reveal spin glass like behaviour for concentrations $x > 0.1$. The observation of a temperature dependent bulk susceptibility in β-$Mn_{1-x}Al_x$ alloys with $x \geq 0.1$ in contrast to the weak temperature dependence observed in pure β-Mn indicates partial moment localisation in the concentrated alloys.

We have observed non-Fermi Liquid scaling properties of the electrical resistivity of pure β-Mn with $\rho(T) \propto T^{3/2}$ at low temperatures, in accordance with the SCR prediction for nearly antiferromagnetic metals.

9.2.2 μSR Measurements

From our muon spin relaxation (μSR) studies, we have obtained the first published [1] magnetic phase diagram of the β-$Mn_{1-x}Al_x$ series (figure 6.22). This phase diagram reveals an abrupt rise in the transition temperature of β-$Mn_{1-x}Al_x$ alloys at a concentration of x = 0.09, which is accompanied by a change in the nature of the spin dynamics from simple exponential to stretched exponential, indicating spin glass-like magnetic relaxation in the paramagnetic state of the more concentrated alloys.

It is tempting to interpret this remarkable behaviour in terms of a quantum spin liquid to spin glass phase transition. Nakamura and co-workers [2] have observed magnetic ordering in β-$Mn_{1-x}Al_x$ for $x \geq 0.05$, using NMR, and have attributed this magnetic order to just such a transition process. Their observations of the temperature dependence of the nuclear relaxation rate $1/T_1$ show a $\sqrt{T}$ dependence for β-$Mn_{0.97}Al_{0.03}$ going over to a critical divergence in $1/T_1$ vs. T for β-$Mn_{0.9}Al_{0.1}$ (see chapter 1). It would be instructive to investigate whether this change in the temperature dependence of the nuclear relaxation rate in β-MnAl occurs at Al concentrations between 9at% and 10at%, where we observe the crossover from simple to stretched exponential spin dynamics. However, our results are in broad agreement with those of Nakamura, in that spin glass like magnetic behaviour is only observed in β-$Mn_{1-x}Al_x$ alloys with $x \geq 0.1$, the NMR signal for alloys with $x < 0.1$ being too weak to observe.

The question remains as to what precipitates this extraordinarily abrupt crossover region in the β-MnAl phase diagram at an Al concentration between 9at% and 10at%. One can identify three main mechanisms which will affect the degree of local moment formation and the nature of the spin dynamics in β-MnAl.

a) *Lattice expansion*

As the β-Mn lattice expands with increasing Al substitution, the intersite electron hopping rate will decrease (see section 2.4.3.1), leading to a narrowing of the spin fluctuation spectral width. However, neutron diffraction studies of the β-MnAl series presented in chapter 5 reveal no discontinuity in the lattice constant at the crossover concentration.

b) *Local environment*

The substitution of non-magnetic Al atoms onto the magnetic site II β-Mn sublattice introduces a degree of disorder into the matrix, and disrupts the magnetic exchange between the magnetic site II Mn atoms.

c) *Spin configurational degeneracy*

Recent work by Asada [3] has shown a high degree of spin configurational degeneracy in β-Mn, brought about by geometrical frustration in the site II β-Mn sublattice. We believe that substitution of non-magnetic Al atoms into this sublattice reduces this frustration and, at least partially, lifts the spin-configurational degeneracy, thereby reducing the spectral width of the spin fluctuations in the manner suggested by Pinettes and Lacroix [4].

The indication of a unique spin relaxation time in dilute β-$Mn_{1-x}Al_x$ alloys provided by our μSR measurements implies that the nature of the spin relaxation in these alloys is determined by the details of the 3d electron band, where itinerant moments, forming on site II Mn atoms, do so uniformly throughout the lattice, as determined by the density of 3d electron states at the Fermi energy. The sudden appearance of a broad distribution of spin relaxation times in β-$Mn_{1-x}Al_x$ alloys with $x > 0.09$, indicated by the stretched exponential form of the muon relaxation function, implies that the spin dynamics in this regime are determined by a wide range of local magnetic environments over the site II Mn atoms, as the degree of local magnetic disorder increases. The muon therefore, becomes increasingly sensitive to localised transverse spin fluctuations, characterised by a broad distribution of relaxation times. The reduction in the muon initial asymmetry to well below 1/3 of its high temperature value indicates that while these transverse spin

fluctuations effectively "freeze", longitudinal (amplitude) spin fluctuations still persist to very low temperatures.

9.2.3 Neutron Polarisation Analysis Studies

Analysis of the magnetic short-range order in β-MnAl alloys at low temperature using a novel Monté-Carlo procedure shows that the nature of the magnetic correlations in β-MnAl changes little throughout the series. The strength of the magnetic correlations increases but extend over a shorter range as the Al concentration increases. This concentration dependence of the magnetic correlations is consistent with a system in which long-range antiferromagnetic order is disrupted by geometrical frustration of the Mn spins at the dilute end of the series and local chemical disorder at the concentrated end of the series. However, since the magnetic correlations are similar in form throughout the β-MnAl concentration range, the abrupt nature of the crossover region in the μSR phase diagram should not necessarily be interpreted as a transition between magnetic ground states at a critical Al concentration, but rather as a consequence of a sudden change in the nature of the fundamental spin dynamics.

9.2.4 Inelastic Neutron Scattering Studies

Inelastic neutron scattering studies of pure β-Mn and β-$Mn_{0.8}Al_{0.2}$ reveal that the wide spin fluctuation spectral width at low temperatures in pure β-Mn is not significantly reduced by the introduction of Al, and that there remains a significant dynamic component to the magnetic ground state at low temperatures. This observation is in full agreement with our μSR measurements. However, the magnetic ground state of β-$Mn_{0.8}Al_{0.2}$ is observed to be largely static at low temperatures. Analysis of the integrated magnetic intensity reveals that our polarised neutron scattering experiment measured only the dominant elastic contribution to the magnetic cross-section at these temperatures. The observed decrease in the static Mn moment with decreasing Al concentration is, therefore, assumed to be due to an increasingly large contribution to the magnetic response from residual dynamical spin fluctuations at low temperatures.

The staggered susceptibility of both β-Mn and β-$Mn_{0.8}Al_{0.2}$ displays Curie-Weiss behaviour in the paramagnetic regime in full agreement with the predictions of the SCR theory. The origin of the Curie-Weiss temperature dependence is interpreted in terms of the temperature dependence of the thermal average of the local spin fluctuation amplitude, which indicates purely itinerant moments in pure β-Mn and partially localised moments in β-$Mn_{0.8}Al_{0.2}$.

9.2.5 Comparison of μSR and Inelastic Neutron Measurements

It has been shown [5,6] that in the case of a Lorentzian spin fluctuation lineshape, the muon spin relaxation rate λ is related to the Q-dependent susceptibility and linewidth according to the relation,

$$\lambda_n = \left(\frac{BT}{N}\right)\sum_Q \frac{\chi(Q)}{\Gamma(Q)}, \qquad (9.1)$$

where B is a coupling constant and the subscript n signifies that λ is determined from neutron measurements. In practice we do not have detailed information about Γ(Q), since we are measuring the powder averaged Γ(|**Q**|) over a small Q-range. However, it would appear from our inelastic neutron data that the Q-dependence of Γ(Q) is weak. We may therefore write eq. (9.1) as [6],

$$\lambda_n = \frac{BT\chi_L}{\Gamma}. \qquad (9.2)$$

Thus, the functional form of λ(T) measured in a μSR experiment may be derived from the inelastic linewidth and local susceptibility measured in an inelastic neutron experiment. It has recently been shown that this relationship holds extremely well for the C15 laves phase compounds, YMn_2 and $Y(Mn_{0.9}Al_{0.1})_2$ [6].

Figure 9.1 shows the form of the muon depolarisation rate derived from our inelastic neutron scattering data (λ_n) for β-Mn and β-$Mn_{0.8}Al_{0.2}$, compared with the measured muon depolarisation rate from our μSR study ($\lambda_{\mu SR}$) scaled to the data at high temperatures by the coupling constant B. Figure 9.1 shows that eq. (9.2) does not hold for either β-Mn or β-$Mn_{0.8}Al_{0.2}$. In fact, the form of $\lambda_n(T)$ is much more reminiscent of the temperature dependence of the NMR relaxation rate $1/T_1$ shown in figure 1.12.

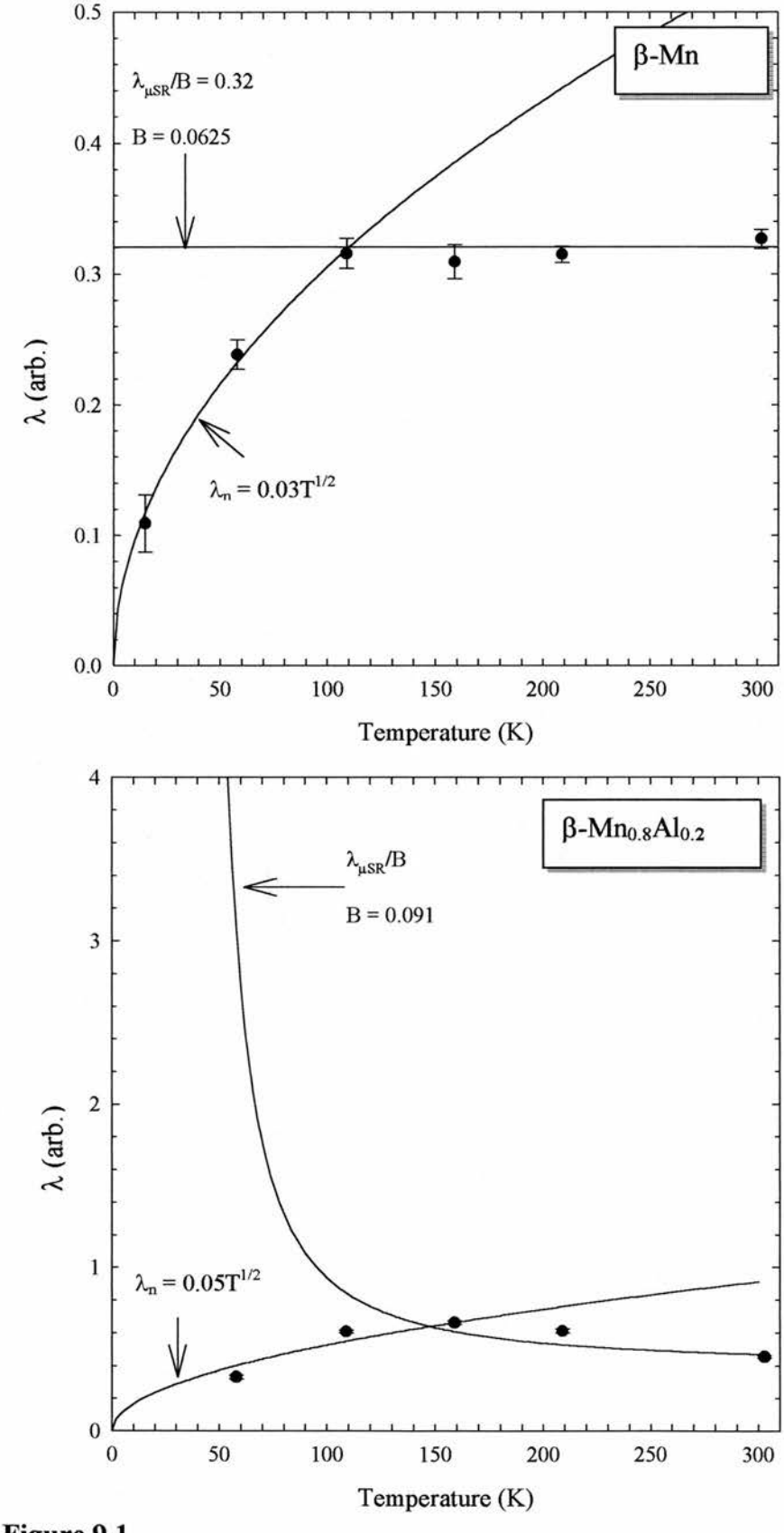

Figure 9.1

The muon depolarisation rate λ_n of β-Mn and β-$Mn_{0.8}Al_{0.2}$ derived from our inelastic neutron data using eq. (9.2) compared to the measured muon depolarisation rate $\lambda_{\mu SR}$ scaled to the data at high temperatures using the value of B shown. $\lambda_n(T)$ is shown to follow a $T^{1/2}$ temperature dependence in common with the NMR relaxation rate $1/T_1$.

Figure 9.1 shows that the paramagnetic low temperature region of $\lambda_n(T)$ approximately follows a $T^{1/2}$ dependence, in common with $1/T_1$.

This observation leads one to conclude that the muon and inelastic neutron data do not scale according to eq. (9.2) for the same reason as the muon and NMR relaxation rates are found not to scale according to eq. (6.43) (see section 6.4). Namely, that the muon and nuclear and atomic spins are sensitive to different local environments and relaxation rates.

As discussed in section 6.4, the Fermi contact contribution to the spin relaxation rate at the interstitial muon site may be greatly reduced if the system is antiferromagnetically correlated. Therefore, while the NMR and inelastic neutron measurements are sensitive to the intrinsic spin relaxation rate, the muon relaxation rate is determined only by the fluctuating dipolar fields at the muon site. One would therefore expect that the NMR and neutron data would scale with each other according to eq. (9.2) but not necessarily scale with the muon data. In contrast, the temperature dependence of both the inelastic neutron linewidth and the muon depolarisation rate in YMn_2 and $Y(Mn_{1-x}Al_x)_2$ is found to follow an Arrhenius law of the form, $\lambda = \lambda_0 \exp^{-E/kT}$ and $\Gamma = \Gamma_0 \exp^{E/kT}$ [6]. Therefore, while antiferromagnetic correlations prevail in these systems, the Fermi contact interaction does not determine the spin relaxation and the conflict between the μSR and NMR relaxation rates is avoided.

9.3 Classification of β-MnAl

In this thesis we have shown that β-Mn is an archetypal nearly antiferromagnetic metal. The measured temperature dependence of the NMR $1/T_1$, the specific heat, the resistivity and the staggered susceptibility χ_s all follow the functional forms predicted by the SCR theory of nearly antiferromagnetic metals. We have demonstrated that the addition of Al to β-Mn results in the formation of partially localised magnetic moments and a spin glass-like magnetic ground state at low temperatures. Between 9at% and 10at% we have observed an abrupt change in the nature of the fundamental spin dynamics of β-MnAl from simple to stretched exponential.

Referring to Moriya's classification diagram (figure 2.10), the increased amplitude of the spin fluctuations and the observation of partially localised moments allows us to characterise β-$Mn_{0.8}Al_{0.2}$ as an intermediate system at the centre of the diagram. On the evidence of our magnetisation and inelastic neutron scattering experiments, one might expect that the route followed by the β-$Mn_{1-x}Al_x$ series across the classification diagram shown in figure 9.2 would be given by a smooth transition from pure β-Mn to β-$Mn_{0.8}Al_{0.2}$ involving a gradual process of moment localisation and a gradual increase in the spin fluctuation amplitude. The precise route across the Moriya classification diagram will be determined by further inelastic neutron scattering studies of intermediate β-$Mn_{1-x}Al_x$ concentrations, scheduled on HET.

The most likely origin of the abrupt increase in the observed transition temperatures of β-$Mn_{1-x}Al_x$, is the sudden lifting of the degeneracy of the Mn spin configurations, and the creation of a unique local spin configuration, caused by the reduction in the topological frustration of the Mn moments. This reduction in frustration will suddenly decrease the spectral width of the amplitude spin fluctuations, allowing the spin dynamics to become dominated by the transverse spin fluctuations associated with ever more localised Mn moments in the system.

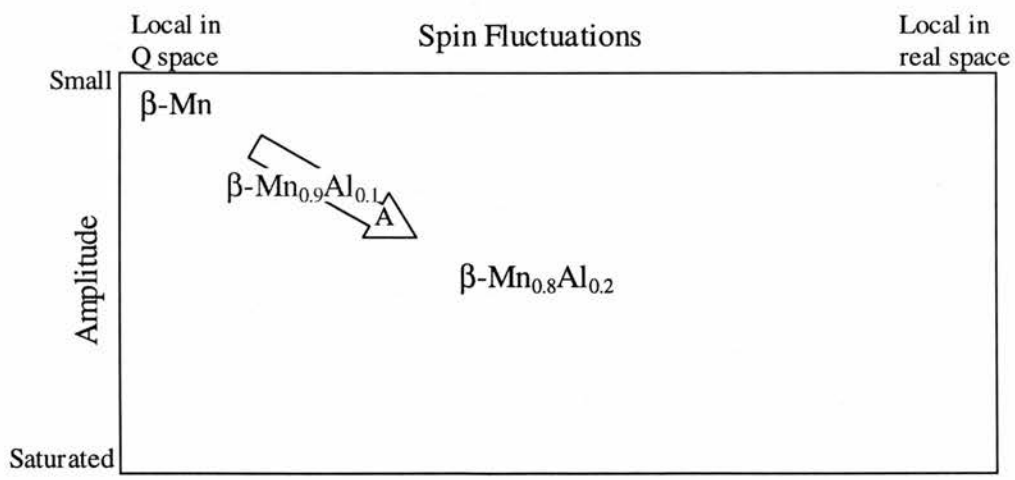

Figure 9.2

The positions of β-Mn and β-$Mn_{0.8}Al_{0.2}$ on Moriya's classification diagram estimated from our inelastic neutron scattering and μSR studies.

It is clear from this study that the characterisation of the transition from β-Mn to β-$Mn_{0.8}Al_{0.2}$ as a quantum spin liquid to spin glass transition [2] is an oversimplification of the problem. Our studies show that while we see a well defined magnetic transition temperature in the more concentrated β-MnAl alloys, there remains a residual spin dynamical component of the magnetic ground state. This indicates that, while the transverse spin fluctuations associated with partially localised moments may be critically damped, some amplitude spin fluctuations remain.

9.4 Suggestions for Further Study

As a further investigation of the magnetic properties of the β-MnAl system, we shall be undertaking a comprehensive study of the pressure dependence of the electrical resistivity. Such studies have provided valuable insight into the rôle played by spin fluctuations in the laves phase compounds YMn_2 and YCo_2 [7]. Analysis of the pressure dependence of ρ(T) will allow us to characterise the magnetic properties of the β-MnAl series as a function of lattice constant alone in alloys with fixed chemical disorder.

The analysis of the magnetic diffuse scattering of β-MnAl using Monté-Carlo modelling has proved a very successful method of analysing magnetic short-range order in powdered samples, while simultaneously taking nuclear short-range correlations into account. Having established the basic framework for this type of analysis, there is a great deal of scope for future work.

Investigations of β-MnFe and β-MnCo alloys are also planned, in which the formation of a magnetic ground state is related to 3d electron donation (see sections 1.3.2 and 1.3.3), and in which the substituent atoms reside on the site I β-Mn sublattice (see chapter 5). It will be instructive to classify these alloys in terms of their moment localisation and spin dynamical properties.

9.5 References

[1] J R Stewart, A D Hillier, S H Kilcoyne, P Manuel, M T F Telling and R Cywinski, J. Mag. Magn. Mater. **177** (1998) 602

[2] H Nakamura, K Yoshimoto, M Shiga, M Nishi and K Kakurai, J Phys. Condens. Matter **9** (1997) 4701

[3] T Asada, J Mag. Magn. Mater. **140-144** (1995) 47

[4] C Pinettes and C Lacroix, J. Phys. Cond. Mater. **6** (1994) 10093

[5] S W Lovesey, A Cuccoli and V Tognetti, Hyp. Int. **64** (1990) 321

[6] B D Rainford, R Cywinski and S J Dakin, J. Mag. Magn. Mater. **140-144** (1995) 805

[7] R Hauser, E Bauer and E Gratz, Phys. Rev **B57** (1998) 13929

R Hauser, A Indinger, E Bauer and E Gratz, J. Mag. Magn. Mater **144** (1995) 799

Appendix A

The code of the Reverse-Monté-Carlo program "INTA" used to model the nuclear diffuse scattering in β-MnAl alloys in chapter 7 is here annotated and listed.

The program was compiled and run on a Digital VMS Alpha computer. The intrinsic function "RAN(I)" is specific to VMS FORTRAN 77 and generates an random number between 0 and 1 from the integer seed I.

```
C
C Reverse Monte-Carlo program to model nuclear disorder scattering in
C a binary alloy.
C
      PROGRAM INTA
C
C     ROSS STEWART: CREATED 12/5/98
C                   LAST MODIFIED 22/5/98
C
      IMPLICIT NONE
C
      INTEGER X2(1000),Y2(1000),Z2(1000)
      INTEGER X3(1000),Y3(1000),Z3(1000)
      INTEGER XSEP,YSEP,ZSEP,CURR,ACOUNT,SNUM
      REAL TOLL,SUMDSQ,OLDDSQ,STEP,STAR,SUMDSQ1(10),LAUT(10)
      REAL A,CONC,LS,SDIST(30),DIST(1000),RAN,DIST2(1000),LATT
      REAL QD(200),COD(200),ERRD(200),WC,PROB,RES(200),SUMSINC(200)
      REAL SINCF(30,200),CAL(200),LAUE,CHISQ(90000),GRACHI(10)
      INTEGER HOLD,NUMD,PFLAG,HOLDX,HOLDY,HOLDZ,F
      INTEGER LOOP,COUNT,NX,NY,NZ,MX,MY,MZ,N,YES(30),ITER,RSHELL,NMN
      INTEGER NAL,HIT,I,HITS(1000),AL(1000),MAIN,C(100),HOLDAL
      INTEGER FIRST,LAST,INDCENT,CENT,COORD(30),SHELL,NUM,SH,NAT(30)
      INTEGER SWAP(10),MISS(1000),ARSE,MCOUNT,GOODAL(1000),SENT
      INTEGER COUNTAL,COUNTMN,NINSH,PAV(30),G,L,SCOORD(30),SUMS
      LOGICAL SORTED
      CHARACTER*60 TITLE
      CHARACTER*8 DFILE,PFILE,UFILE
      CHARACTER*33 DAFILE,PAFILE,CHIFILE
      CHARACTER*30 PARFILE
      CHARACTER*1 ANS
C
C  Title
C
      PRINT*, ' '
      PRINT*, '              ****************************************'
      PRINT*, '              *   IIIIII NN     NN  TTTTTTTT   AA     *'
      PRINT*, '              *     II   NNN    NN     TT     AAAA    *'
      PRINT*, '              *     II   NNNN   NN     TT    AA  AA   *'
      PRINT*, '              *     II   NN NN  NN     TT    AAAAAA   *'
      PRINT*, '              *     II   NN  NN NN     TT    AA  AA   *'
      PRINT*, '              *     II   NN   NNNN     TT    AA  AA   *'
      PRINT*, '              *   IIIIII NN    NNN     TT    AA  AA   *'
      PRINT*, '              ****************************************'
      PRINT*, ' '
      PRINT*, '            RMC Modelling of Nuclear Diffuse Scattering'
```

```
      PRINT*, '                              by Ross Stewart'
      PRINT*, ' '
      PRINT*, '                    University of St Andrews, May 1998'
      PRINT*, ' '
      PRINT*, ' '
C
C  Parameters
C
      I=9762
      PARFILE='MUSER1:[JRS2.NUC_SIM]PAR.DAT'
C
      F=8
      OPEN (UNIT=F,FILE=PARFILE,STATUS='OLD')
      PRINT*, ' Input Data File (.DAT assumed) ----  '
      READ(F,73) DFILE
      DAFILE='MUSER1;[JRS2.NUC_SIM]'//DFILE//'.DAT'
      PRINT*, ' Generate Random substitution (R) or '
      PRINT*, ' read positions from "pos" file? (P) ----  '
      READ(F,72) ANS
      IF(ANS.EQ.'P'.OR.ANS.EQ.'p') THEN
        PFLAG=1
      ELSE
        PFLAG=0
      END IF
      PRINT*, ' Input impurity concentration ----  '
      READ(F,*) CONC
      PRINT*, ' Input Laue Scattering level (barns/st/atom) ---  '
      READ(F,*) LAUE
      PRINT*, ' Input Lattice constant (A) ----  '
      READ(F,*) LATT
      PRINT*, ' Input tolerence level ----  '
      READ(F,*) TOLL
      PRINT*, ' Input number of swaps per iteration (max 5) ----  '
      READ(F,*) SNUM
      PRINT*, ' Input name for output files ----  '
      READ(F,73) UFILE
C
      A=LATT*1E-04
C
C Format Statements
C
71    FORMAT(A60)
72    FORMAT(A1)
73    FORMAT(A8)
C
C  Read in data
C
      OPEN(1,FILE=DAFILE,STATUS='OLD')
      READ(1,71)TITLE
      READ(1,*)NUMD
      DO L=1,NUMD
        READ(1,*) QD(L),COD(L),ERRD(L)
      END DO
      CLOSE(1)
C
      IF(PFLAG.EQ.1) GO TO 222
C
C Coordinates for Site II nuclei
C
      X2(1)=3750
      Y2(1)=7965
```

```
      Z2(1)=9535
      X2(2)=9535
      Y2(2)=3750
      Z2(2)=7965
      X2(3)=7965
      Y2(3)=9535
      Z2(3)=3750
      X2(4)=8750
      Y2(4)=7035
      Z2(4)=465
      X2(5)=4535
      Y2(5)=1250
      Z2(5)=2035
      X2(6)=2965
      Y2(6)=5465
      Z2(6)=6250
      X2(7)=6250
      Y2(7)=2965
      Z2(7)=5465
      X2(8)=465
      Y2(8)=8750
      Z2(8)=7035
      X2(9)=2035
      Y2(9)=4535
      Z2(9)=1250
      X2(10)=1250
      Y2(10)=2035
      Z2(10)=4535
      X2(11)=5465
      Y2(11)=6250
      Z2(11)=2965
      X2(12)=7035
      Y2(12)=465
      Z2(12)=8750
C
C Generate two unit cells in X,Y, and Z directions IN FIRST QUADRANT
C
      COUNT=0
      DO NX=0,1
        DO NY=0,1
          DO NZ=0,1
            CALL UNITGEN(X2,Y2,Z2,NX,NY,NZ,COUNT)
          END DO
        END  DO
      END DO
      COUNT=0
C
C Transform nuclei in first quadrant onto other seven quadrants
C
      MX=-2
      MY=0
      MZ=0
40    CALL QUADGEN(X2,Y2,Z2,MX,MY,MZ,COUNT)
      IF (COUNT.EQ.1) THEN
        MX=-2
        MY=-2
        MZ=0
        GO TO 40
      END IF
      IF (COUNT.EQ.2) THEN
        MX=0
```

```
        MY=-2
        MZ=0
        GO TO 40
      END IF
      IF (COUNT.EQ.3) THEN
        MX=0
        MY=0
        MZ=-2
        GO TO 40
      END IF
      IF (COUNT.EQ.4) THEN
        MX=-2
        MY=0
        MZ=-2
        GO TO 40
      END IF
      IF (COUNT.EQ.5) THEN
        MX=-2
        MY=-2
        MZ=-2
        GO TO 40
      END IF
      IF (COUNT.EQ.6) THEN
        MX=0
        MY=-2
        MZ=-2
        GO TO 40
      END IF
      IF (COUNT.EQ.7) THEN
        COUNT=0
      END IF
C
      N=768
C
C Number of Al nuclei in matix
      IF (CONC.EQ.0) THEN
        NAL=0
      ELSE
        NAL=N*CONC
      END IF
      NMN=N-NAL
C
C Set all nuclei to be Mn
C
      DO LOOP=1,N
        AL(LOOP)=0
      END DO
C
C Randomly assign the Al nuclei
C
      COUNT=1
      IF (NAL.GT.0) THEN
        DO LOOP=1,NAL
200       LS=RAN(I)
          HIT=INT(LS*N)
          DO L=1,COUNT-1
            IF(HIT.EQ.HITS(L)) GO TO 200
          END DO
          IF (HIT.EQ.0) GO TO 200
          HITS(COUNT)=HIT
          COUNT=COUNT+1
```

```
          AL(HIT)=1
        END DO
      END IF
      PRINT*, 'THERE ARE ',COUNT-1,' AL ATOMS'
      GO TO 223
C
C Read Al and Mn nuclear positions from a previously generated
C input file
C
222   PRINT*, ' Input position file (.POS assumed) ----  '
      READ(F,73) PFILE
      PAFILE='MUSER1:[JRS2.NUC_SIM]'//PFILE//'.POS'
      N=768
      OPEN(12,FILE=PAFILE,STATUS='OLD')
      DO LOOP=1,N
        READ(12,*) X2(LOOP), Y2(LOOP), Z2(LOOP), AL(LOOP)
      END DO
      CLOSE(12)
      CLOSE(F)
C
C Count Al and Mn nuclei
C
223   COUNT=1
      ACOUNT=1
      DO LOOP=1,N
        IF(AL(LOOP).EQ.0) THEN
          MISS(COUNT)=LOOP
          COUNT=COUNT+1
        ELSE
          HITS(ACOUNT)=LOOP
          ACOUNT=ACOUNT+1
        END IF
      END DO
      IF(PFLAG.EQ.1) THEN
        PRINT*, 'THERE ARE ',ACOUNT-1,' AL NUCLEI'
        NAL=ACOUNT-1
        NMN=N-NAL
      END IF
C
      MCOUNT=0
C
C*********************************************************************
C
C Work out shell transformations
C
       SENT=5
       DO LOOP=1,N
         XSEP=X2(LOOP)-X2(SENT)
         YSEP=Y2(LOOP)-Y2(SENT)
         ZSEP=Z2(LOOP)-Z2(SENT)
         DIST(LOOP)=SQRT(REAL(XSEP**2)
     +                  +REAL(YSEP**2)
     +                  +REAL(ZSEP**2))
       END DO
C
C Sort DISTANCE and separation arrays into ascending distance order
C
      SORTED=.FALSE.
      FIRST=1
      LAST=N-1
80    IF (.NOT.SORTED) THEN
```

```
        SORTED=.TRUE.
C
        DO 90 LOOP=FIRST,LAST
          IF (DIST(LOOP).GT.DIST(LOOP+1)) THEN
            HOLD=DIST(LOOP)
            HOLDAL=AL(LOOP)
            HOLDX=X2(LOOP)
            HOLDY=Y2(LOOP)
            HOLDZ=Z2(LOOP)
            DIST(LOOP)=DIST(LOOP+1)
            AL(LOOP)=AL(LOOP+1)
            X2(LOOP)=X2(LOOP+1)
            Y2(LOOP)=Y2(LOOP+1)
            Z2(LOOP)=Z2(LOOP+1)
            DIST(LOOP+1)=HOLD
            AL(LOOP+1)=HOLDAL
            X2(LOOP+1)=HOLDX
            Y2(LOOP+1)=HOLDY
            Z2(LOOP+1)=HOLDZ
            SORTED=.FALSE.
          END IF
90      CONTINUE
        LAST=LAST-1
        GO TO 80
      END IF
C
C  Ignore shells greater than 8 angstroms away
C
      DO 120 LOOP=1,N
        DIST(LOOP)=DIST(LOOP)*A
        IF (DIST(LOOP).GT.8.0) THEN
          NINSH=LOOP-1
          GO TO 12
        END IF
120   CONTINUE
C
C  Sort nuclei into shells
C
12    NUM=1
      SHELL=0
      DO 110 LOOP=1,NINSH
        IF ((DIST(LOOP+1)-DIST(LOOP)).LT.0.001) THEN
          NUM=NUM+1
        ELSE
          COORD(SHELL+1)=NUM
          SDIST(SHELL+1)=DIST(LOOP)
          SHELL=SHELL+1
          NUM=1
        END IF
110   CONTINUE
C
      RSHELL=SHELL-1
C
C Reinspect spins and assign
C
      COUNTAL=1
      COUNTMN=1
      DO LOOP=1,N
        IF(AL(LOOP).EQ.1) THEN
          HITS(COUNTAL)=LOOP
          COUNTAL=COUNTAL+1
```

```
        ELSE
          MISS(COUNTMN)=LOOP
          COUNTMN=COUNTMN+1
        END IF
      END DO
C
C Check on internal consistency
C
      IF(COUNTMN-1.NE.NMN.OR.COUNTAL-1.NE.NAL) GO TO 876
C
C Initialise arrays
C
      DO LOOP=1,RSHELL
        YES(LOOP)=0
        NAT(LOOP)=0
      END DO
C
C*********************************************************************
C Start of main Loop
C
999   CONTINUE
C
C     calulate sum of probability of each shell
C
      DO L=1,NAL
        CENT=HITS(L)
        IF(AL(CENT).NE.1) THEN
           PRINT*, 'MISTAKE AT ',ITER,CENT,AL(CENT)
        END IF
C
C Transform to neighbours and apply boundary conditions
C Identify and add AL
C
        DO LOOP=1,N
          XSEP=X2(LOOP)-X2(CENT)
          YSEP=Y2(LOOP)-Y2(CENT)
          ZSEP=Z2(LOOP)-Z2(CENT)
          X3(LOOP)=X2(LOOP)
          Y3(LOOP)=Y2(LOOP)
          Z3(LOOP)=Z2(LOOP)
          IF(XSEP.GT.20000) X3(LOOP)=X2(LOOP)-40000
          IF(YSEP.GT.20000) Y3(LOOP)=Y2(LOOP)-40000
          IF(ZSEP.GT.20000) Z3(LOOP)=Z2(LOOP)-40000
          IF(XSEP.LT.-20000) X3(LOOP)=X2(LOOP)+40000
          IF(YSEP.LT.-20000) Y3(LOOP)=Y2(LOOP)+40000
          IF(ZSEP.LT.-20000) Z3(LOOP)=Z2(LOOP)+40000
          XSEP=X3(LOOP)-X2(CENT)
          YSEP=Y3(LOOP)-Y2(CENT)
          ZSEP=Z3(LOOP)-Z2(CENT)
          DIST2(LOOP)=SQRT(REAL(XSEP**2)+REAL(YSEP**2)
     +                                   +REAL(ZSEP**2))*A
          DO ITER=2,RSHELL
            IF(ABS(DIST2(LOOP)-SDIST(ITER)).LT.0.001) THEN
              IF(AL(LOOP).EQ.1) YES(ITER-1)=YES(ITER-1)+1
              NAT(ITER)=NAT(ITER)+1
            END IF
          END DO
        END DO
      END DO
C
C Re-initialise arrays
```

```
C
      DO LOOP=1,RSHELL-1
          PAV(LOOP)=YES(LOOP)
          NAT(LOOP)=0
          YES(LOOP)=0
      END DO
C
C     compare simulation with experimental data
C
      SUMDSQ=0.0
      DO L=1,NUMD
        SUMSINC(L)=0.0
      END DO
C
C Calculate pair probabilities and Warren-Cowley parameters
C Calculate simulated cross-section
C
      DO LOOP=1,RSHELL-1
        PROB=REAL(PAV(LOOP))/(NAL*COORD(LOOP+1))
        WC=1.0+((PROB-1.0)/(1.0-CONC))
        DO L=1,NUMD
          SINCF(LOOP,L)=REAL(COORD(LOOP+1))*WC
     +                 *SIN(QD(L)*SDIST(LOOP+1))/(QD(L)*SDIST(LOOP+1))
          SUMSINC(L)=SUMSINC(L)+SINCF(LOOP,L)
        END DO
      END DO
C
C Calculate ChiSq
C
      DO L=1,NUMD
        CAL(L)=LAUE*(1+SUMSINC(L))
        RES(L)=(COD(L)-CAL(L))/ERRD(L)
        SUMDSQ=SUMDSQ+(RES(L)**2)
      END DO
      SUMDSQ=SUMDSQ/FLOAT(NUMD)
C
C  Is tolerance satisfied
C
      IF (SUMDSQ.LT.TOLL) THEN
        CALL ACCEPT(AL,GOODAL)
        CHISQ(MCOUNT)=SUMDSQ
        GO TO 666
      END IF
C
66    FORMAT('  CHISQ =',F8.4,2X,'---  compared with ',F8.4,
     +'   MOVE',I5,' ACCEPTED')
67    FORMAT('  CHISQ =',F8.4,2x,'---  compared with ',F8.4,
     +'   MOVE',I5,' REJECTED')
C
C Accept first move
C
      IF(MCOUNT.EQ.0) THEN
        CALL ACCEPT(AL,GOODAL)
        CHISQ(MCOUNT)=SUMDSQ
        OLDDSQ=SUMDSQ
        CALL OUT(X2,Y2,Z2,SDIST,PAV,RSHELL,GOODAL,NUMD,QD,COD,CAL,ERRD
     +           ,UFILE)
        GO TO 333
      END IF
C
C  Allow moves which minimise SUMDSQ
```

```
C
      IF(SUMDSQ.LT.OLDDSQ) THEN
        CALL ACCEPT(AL,GOODAL)
        CALL OUT(X2,Y2,Z2,SDIST,PAV,RSHELL,GOODAL,NUMD,QD,COD,CAL,ERRD
     +           ,UFILE)
        WRITE(*,66)SUMDSQ,OLDDSQ,MCOUNT
        CHISQ(MCOUNT)=SUMDSQ
        OLDDSQ=SUMDSQ
      ELSE
        WRITE(*,67)SUMDSQ,OLDDSQ,MCOUNT
      END IF
      DO LOOP=1,N
        AL(LOOP)=GOODAL(LOOP)
      END DO
C
C  Swap 5 Al atoms with Mn
C
333   SWAP(1)=HITS(INT(RAN(I)*REAL(NAL))+1)
      SWAP(2)=HITS(INT(RAN(I)*REAL(NAL))+1)
      SWAP(3)=HITS(INT(RAN(I)*REAL(NAL))+1)
      SWAP(4)=HITS(INT(RAN(I)*REAL(NAL))+1)
      SWAP(5)=HITS(INT(RAN(I)*REAL(NAL))+1)
      SWAP(6)=MISS(INT(RAN(I)*REAL(NMN))+1)
      SWAP(7)=MISS(INT(RAN(I)*REAL(NMN))+1)
      SWAP(8)=MISS(INT(RAN(I)*REAL(NMN))+1)
      SWAP(9)=MISS(INT(RAN(I)*REAL(NMN))+1)
      SWAP(10)=MISS(INT(RAN(I)*REAL(NMN))+1)
C
C Check nuclear type
C
      DO LOOP=1,5
        IF(AL(SWAP(LOOP)).NE.1) GO TO 333
        IF(AL(SWAP(LOOP+5)).NE.0) GO TO 333
      END DO
C
      DO LOOP=1,10
        DO L=1,10
          IF(SWAP(L).EQ.SWAP(LOOP).AND.L.NE.LOOP) GO TO 333
        END DO
      END DO
C
      DO LOOP=1,SNUM
        AL(SWAP(LOOP))=0
        AL(SWAP(LOOP+5))=1
      END DO
C
C Re-inspect spins and assign
C
      COUNTAL=1
      COUNTMN=1
      DO LOOP=1,N
        IF(AL(LOOP).EQ.1) THEN
          HITS(COUNTAL)=LOOP
          COUNTAL=COUNTAL+1
        ELSE
          MISS(COUNTMN)=LOOP
          COUNTMN=COUNTMN+1
        END IF
      END DO
      IF(COUNTMN-1.NE.NMN.OR.COUNTAL-1.NE.NAL) GO TO 876
C
```

```
      PRINT*,' '
C
      MCOUNT=MCOUNT+1
      GO TO 999
C
C End of main loop
C**********************************************************************
C
666   PRINT*, 'Tolerance achieved'
      PRINT*, 'END'
      PRINT*,' '
      CHIFILE='MUSER1:[JRS2.NUC_SIM]'//UFILE//'.CHI'
      OPEN (3,FILE=CHIFILE,STATUS='UNKNOWN')
      DO LOOP=1,MCOUNT
         WRITE(3,*) LOOP,CHISQ(LOOP)
      END DO
      CLOSE(3)
      CALL OUT(X2,Y2,Z2,SDIST,PAV,RSHELL,GOODAL,NUMD,QD,COD,CAL,ERRD
     +         ,UFILE)
      GO TO 101
C
C  Consistency check failed
C
876   PRINT*, 'ERROR - FAILED CONSISTENCY CHECK'
C
101   END
C
C**********************************************************************
C
      SUBROUTINE UNITGEN(X2,Y2,Z2,NX,NY,NZ,COUNT)
C
      INTEGER X2(1000),Y2(1000),Z2(1000)
      INTEGER NX,NY,NZ,COUNT,LOOP
      IF (NX.EQ.0.AND.NY.EQ.0.AND.NZ.EQ.0) THEN
        RETURN
      END IF
      DO 101 LOOP=1,12
        X2(12+(COUNT*12)+LOOP)=X2(LOOP)+(NX*10000)
        Y2(12+(COUNT*12)+LOOP)=Y2(LOOP)+(NY*10000)
        Z2(12+(COUNT*12)+LOOP)=Z2(LOOP)+(NZ*10000)
101   CONTINUE
      COUNT=COUNT+1
C
      RETURN
      END
C
C**********************************************************************
C
      SUBROUTINE QUADGEN(X2,Y2,Z2,MX,MY,MZ,COUNT)
C
      INTEGER X2(1000),Y2(1000),Z2(1000)
      INTEGER MX,MY,MZ,COUNT,LOOP,B
      B=96
      DO 100 LOOP=1,B
        X2(B+(COUNT*B)+LOOP)=X2(LOOP)+(MX*10000)
        Y2(B+(COUNT*B)+LOOP)=Y2(LOOP)+(MY*10000)
        Z2(B+(COUNT*B)+LOOP)=Z2(LOOP)+(MZ*10000)
100   CONTINUE
      COUNT=COUNT+1
C
      RETURN
```

```
      END
C
C*********************************************************************
C
      SUBROUTINE ACCEPT(AL,GOODAL)
C
      INTEGER AL(1000), GOODAL(1000)
C
      N=768
      DO LOOP=1,N
        GOODAL(LOOP)=AL(LOOP)
      END DO
C
      RETURN
      END
C
C*********************************************************************
C
      SUBROUTINE
     +OUT(X2,Y2,Z2,SDIST,PAV,RSHELL,GOODAL,NUMD,QD,COD,CAL,ERRD
     +,UFILE)
C
      INTEGER X2(1000),Y2(1000),Z2(1000),PAV(30),GOODAL(1000),NUMD
      INTEGER LOOP, RSHELL
      REAL SDIST(30),LAUE
      REAL COD(200),CAL(200),ERRD(200),QD(200)
      CHARACTER*8 UFILE
      CHARACTER*33 OFILE, PFILE, RFILE, FFILE
C
      OFILE='MUSER1:[JRS2.NUC_SIM]'//UFILE//'.OUT'
      PFILE='MUSER1:[JRS2.NUC_SIM]'//UFILE//'.POS'
      RFILE='MUSER1:[JRS2.NUC_SIM]'//UFILE//'.RAW'
      FFILE='MUSER1:[JRS2.NUC_SIM]'//UFILE//'.FIT'

      OPEN(1,FILE=OFILE,STATUS='UNKNOWN')
      DO LOOP=1,RSHELL-1
        WRITE(1,*) SDIST(LOOP+1),PAV(LOOP),0.0
      END DO
      CLOSE(1)
      OPEN(2,FILE=PFILE,STATUS='UNKNOWN')
      DO LOOP=1,768
        WRITE(2,*) X2(LOOP), Y2(LOOP), Z2(LOOP), GOODAL(LOOP)
      END DO
      CLOSE(2)
      OPEN(3,FILE=RFILE,STATUS='UNKNOWN')
      DO LOOP=1,NUMD
        WRITE(3,*) QD(LOOP),COD(LOOP),ERRD(LOOP)
      END DO
      CLOSE(3)
      OPEN(4,FILE=FFILE,STATUS='UNKNOWN')
      DO LOOP=1,NUMD
        WRITE(4,*) QD(LOOP), CAL(LOOP), 0.0
      END DO
      CLOSE(4)
C
      RETURN
      END
C
C
C*********************************************************************
```

Appendix B

The code of the Reverse-Monté-Carlo program "MAG" used to model the magnetic diffuse scattering in β-MnAl alloys in chapter 7 is here annotated and listed.

The program was compiled and run on a Digital VMS Alpha computer. The intrinsic function "RAN(I)" is specific to VMS FORTRAN 77 and generates an random number between 0 and 1 from the integer seed I.

```
C
C  Reverse Monte-Carlo program to model magnetic disorder scattering in
C  a binary alloy.
C
      PROGRAM INTMAG
C
C     ROSS STEWART: CREATED 20/5/98
C                   LAST MODIFIED 22/5/98
C
      IMPLICIT NONE
C
      INTEGER X2(1000),Y2(1000),Z2(1000)
      INTEGER X3(1000),Y3(1000),Z3(1000)
      INTEGER X4(1000),Y4(1000),Z4(1000)
      INTEGER XSEP,YSEP,ZSEP,HOLDX,HOLDY,HOLDZ
      REAL TOLL,SUMDSQ,OLDDSQ,DUM,THETA,THI,MUX(1000),MUY(1000)
      REAL MUZ(1000),PI,YES(30),PAV(30),FFS(200),PLIER,SELF
      REAL A,CONC,LS,SDIST(30),DIST(1000),RAN,DIST2(1000)
      REAL QD(200),COD(200),ERRD(200),WC,PROB,RES(200),SUMSINC(200)
      REAL SINCF(30,200),CAL(200),LAUE,FF1,FF2,FF3,LATT
      REAL GMUX(1000),GMUY(1000),GMUZ(1000),SUMDSQ1(10)
      REAL CHISQ(90000),STEP,STAR,SELT(10),GRACHI(10)
      INTEGER HOLD,NUMD,PFLAG,IPRINT
      INTEGER LOOP,COUNT,N,ITER,RSHELL,NMN,CURR
      INTEGER NAL,HIT,I,HITS(1000),AL(1000),MAIN,C(100),HOLDAL
      INTEGER FIRST,LAST,INDCENT,CENT,COORD(30),SHELL,NUM,SH
      INTEGER SWAP(10),MISS(1000),ARSE,MCOUNT,SENT,VFLAG,NAT(30)
      INTEGER COUNTAL,COUNTMN,NINSH,G,L,SUMS,SNUM,F
      LOGICAL SORTED
      CHARACTER*60 TITLE
      CHARACTER*8 DFILE, PFILE, UFILE, MPFILE
      CHARACTER*33 DAFILE, PAFILE, MPAFILE,CFILE
      CHARACTER*1 ANS
      CHARACTER*31 PARFIL
C
C  User input
C
      PRINT*, '             ******************************'
      PRINT*, '             *  MM    MM     AA    GGGGGG  *'
      PRINT*, '             *  MMM MMM    AAAA   GG      *'
      PRINT*, '             *  MM M MM   AA  AA  GG GGG  *'
      PRINT*, '             *  MM    MM  AAAAAA  GG  GG  *'
      PRINT*, '             *  MM    MM  AA  AA  GGGGGG  *'
      PRINT*, '             ******************************'
```

```
      PRINT*, ' '
      PRINT*, '      RMC Modelling of Magnetic Diffuse Scattering'
      PRINT*, ' '
      PRINT*, '                    by  Ross Stewart'
      PRINT*, '           University of St Andrews, May 1998'
      PRINT*, ' '
      PRINT*, ' '
C
C  Input Parameters
C
      I=9762
      IPRINT=0
      F=8
      PARFIL='MUSER1:[JRS2.NUC_SIM]MAGPAR.DAT'
      OPEN(UNIT=F,FILE=PARFIL,STATUS='OLD')
C
      PRINT*, ' Input data file (.DAT assumed) ----  '
      READ(F,73) DFILE
      DAFILE='MUSER1:[JRS2.NUC_SIM]'//DFILE//'.DAT'
      PRINT*, ' Input position file from INTA (.POS) ----  '
      READ(F,73) PFILE
      PAFILE='MUSER1:[JRS2.NUC_SIM]'//PFILE//'.POS'
      PRINT*, ' Generate random spins (R) or '
      PRINT*, ' read from magnetic position file (P)? ----  '
      READ(F,72) ANS
      IF(ANS.EQ.'P'.OR.ANS.EQ.'p') THEN
        PFLAG=1
      ELSE
        PFLAG=0
      END IF
      PRINT*, ' Input S(S+1) ----  '
      READ(F,*) SELF
      PRINT*, ' Do you want to vary (V) or fix (F) S(S+1)? ----  '
      READ(F,72) ANS
      IF(ANS.EQ.'V'.OR.ANS.EQ.'v') THEN
        VFLAG=1
        PRINT*, ' Look for hits? ----  '
        READ(F,72) ANS
        IF(ANS.EQ.'Y'.OR.ANS.EQ.'y') IPRINT=1
        PRINT*, ' Input Stepsize ----  '
        READ(F,*) STEP
        STAR=5.0*STEP
      ELSE
        VFLAG=0
      END IF
      PRINT*, ' Input Lattice constant (A) ----  '
      READ(F,*) LATT
      A=LATT*1E-04
      PRINT*, ' Input number of spin rotations (max 5) ----  '
      READ(F,*) SNUM
      PRINT*, ' Input Tolerance level ----  '
      READ(F,*) TOLL
      PRINT*, ' Input name for output files ----  '
      READ(F,73) UFILE
C
      N=768
      PI=3.1415927
C
C  Format statements
C
71    FORMAT(A60)
```

```
72    FORMAT(A1)
73    FORMAT(A8)
C
C  Read in data
C
      OPEN(1,FILE=DAFILE,STATUS='OLD')
      READ(1,71)TITLE
      READ(1,*)NUMD
      DO L=1,NUMD
        READ(1,*) QD(L),COD(L),ERRD(L)
      END DO
      CLOSE(1)
C
C  Calculate Free Mn form factor
C
      DO LOOP=1,NUMD
        FF1=0.2438*EXP(-24.963*((QD(LOOP)/12.566)**2))
        FF2=0.1472*EXP(-15.673*((QD(LOOP)/12.566)**2))
        FF3=(0.6189*EXP(-6.54*((QD(LOOP)/12.566)**2)))-0.0105
        FFS(LOOP)=(FF1+FF2+FF3)**2
      END DO
C
C  "Plier" is (gamma*ro)**2
C
      PLIER=0.1936807
C
C Read in Mn and Al atomic position file
C
      OPEN(2,FILE=PAFILE,STATUS='OLD')
      DO LOOP=1,N
        READ(2,*) X2(LOOP),Y2(LOOP),Z2(LOOP),AL(LOOP)
      END DO
C
C*****************************************************************
C
C Sort out neighbouring shells and coordinations
C
      SENT=5
      DO LOOP=1,N
             XSEP=X2(LOOP)-X2(SENT)
             YSEP=Y2(LOOP)-Y2(SENT)
             ZSEP=Z2(LOOP)-Z2(SENT)
             DIST(LOOP)=SQRT(REAL(XSEP**2)
     +                  +REAL(YSEP**2)
     +                  +REAL(ZSEP**2))
      END DO
C
C Sort DISTANCE and separation arrays into ascending distance order
C
      SORTED=.FALSE.
      FIRST=1
      LAST=N-1
80    IF (.NOT.SORTED) THEN
        SORTED=.TRUE.
C
        DO 90 LOOP=FIRST,LAST
          IF (DIST(LOOP).GT.DIST(LOOP+1)) THEN
            HOLD=DIST(LOOP)
            HOLDAL=AL(LOOP)
            HOLDX=X2(LOOP)
            HOLDY=Y2(LOOP)
```

```
            HOLDZ=Z2(LOOP)
            DIST(LOOP)=DIST(LOOP+1)
            AL(LOOP)=AL(LOOP+1)
            X2(LOOP)=X2(LOOP+1)
            Y2(LOOP)=Y2(LOOP+1)
            Z2(LOOP)=Z2(LOOP+1)
            DIST(LOOP+1)=HOLD
            AL(LOOP+1)=HOLDAL
            X2(LOOP+1)=HOLDX
            Y2(LOOP+1)=HOLDY
            Z2(LOOP+1)=HOLDZ
            SORTED=.FALSE.
          END IF
90      CONTINUE
        LAST=LAST-1
        GO TO 80
      END IF
C
C  Ignore shells greater than 8 angstroms away
C
      DO 120 LOOP=1,N
        DIST(LOOP)=DIST(LOOP)*A
        IF (DIST(LOOP).GT.8.0) THEN
           NINSH=LOOP-1
           GO TO 12
        END IF
120   CONTINUE
C
C  Sort into shells
C
12    NUM=1
      SHELL=0
      DO 110 LOOP=1,NINSH
        IF ((DIST(LOOP+1)-DIST(LOOP)).LT.0.001) THEN
           NUM=NUM+1
        ELSE
           COORD(SHELL+1)=NUM
           SDIST(SHELL+1)=DIST(LOOP)
           SHELL=SHELL+1
           NUM=1
        END IF
110   CONTINUE
C
      RSHELL=SHELL-1
C
C inspect spins and assign
C
      COUNTAL=1
      COUNTMN=1
      DO LOOP=1,N
        IF(AL(LOOP).EQ.1) THEN
          HITS(COUNTAL)=LOOP
          COUNTAL=COUNTAL+1
        ELSE
          MISS(COUNTMN)=LOOP
          COUNTMN=COUNTMN+1
        END IF
      END DO
      NAL=COUNTAL-1
      NMN=COUNTMN-1
      IF(NAL+NMN.NE.N) GO TO 876
```

```
      CONC=REAL(NAL)/REAL(N)
      PRINT*,' Input file consistent with a ',CONC,'% concentration'
C
C  Assign spin directions randomly or read from file
C
      IF(PFLAG.EQ.1) THEN
        PRINT*,'Input magnetic position file (.MOS assumed) ----  '
        READ(F,73) MPFILE
        MPAFILE='MUSER1:[JRS2.NUC_SIM]'//MPFILE//'.MOS'
        OPEN(4,FILE=MPAFILE,STATUS='OLD')
      END IF
      COUNT=1
      DO LOOP=1,N
        IF(AL(LOOP).EQ.0) THEN
          IF(PFLAG.EQ.0) THEN
             X3(COUNT)=X2(LOOP)
             Y3(COUNT)=Y2(LOOP)
             Z3(COUNT)=Z2(LOOP)
33           DUM=RAN(I)*PI
             IF (RAN(I).GT.SIN(DUM)) THEN
               GOTO 33
             END IF
             THETA=DUM
             THI=RAN(I)*2.0*PI
             MUX(COUNT)=SIN(THETA)*COS(THI)
             MUY(COUNT)=SIN(THETA)*SIN(THI)
             MUZ(COUNT)=COS(THETA)
          ELSE
             READ(4,*) X3(COUNT),Y3(COUNT),Z3(COUNT),
     +                 MUX(COUNT),MUY(COUNT),MUZ(COUNT)
          END IF
          COUNT=COUNT+1
        END IF
      END DO
C
      IF(PFLAG.EQ.1) CLOSE(4)
      CLOSE(F)
C
C  initialise arrays
C
      DO LOOP=1,RSHELL
        YES(LOOP)=0
        NAT(LOOP)=0
      END DO
C
      MCOUNT=0
C
C ********************START OF MAIN LOOP*************************
C
999   CONTINUE
C
C  calculate sum of each shell
C
      DO L=1,NMN
        CENT=L
C
C  Find neighbours, calculate total dot product of each shell
C  for all Mn atoms
C
        DO LOOP=1,NMN
          XSEP=X3(LOOP)-X3(CENT)
```

```
          YSEP=Y3(LOOP)-Y3(CENT)
          ZSEP=Z3(LOOP)-Z3(CENT)
          X4(LOOP)=X3(LOOP)
          Y4(LOOP)=Y3(LOOP)
          Z4(LOOP)=Z3(LOOP)
C
C  Boundary Conditions
C
          IF(XSEP.GT.20000) X4(LOOP)=X3(LOOP)-40000
          IF(YSEP.GT.20000) Y4(LOOP)=Y3(LOOP)-40000
          IF(ZSEP.GT.20000) Z4(LOOP)=Z3(LOOP)-40000
          IF(XSEP.LT.-20000) X4(LOOP)=X3(LOOP)+40000
          IF(YSEP.LT.-20000) Y4(LOOP)=Y3(LOOP)+40000
          IF(ZSEP.LT.-20000) Z4(LOOP)=Z3(LOOP)+40000
          XSEP=X4(LOOP)-X3(CENT)
          YSEP=Y4(LOOP)-Y3(CENT)
          ZSEP=Z4(LOOP)-Z3(CENT)
          DIST2(LOOP)=SQRT(REAL(XSEP**2)+REAL(YSEP**2)
     +                                  +REAL(ZSEP**2))*A
          DO ITER=2,RSHELL
            IF(ABS(DIST2(LOOP)-SDIST(ITER)).LT.0.001) THEN
               YES(ITER-1)=YES(ITER-1)+(MUX(CENT)*MUX(LOOP))+
     +                                  (MUY(CENT)*MUY(LOOP))+
     +                                  (MUZ(CENT)*MUZ(LOOP))
               NAT(ITER-1)=NAT(ITER-1)+1
            END IF
          END DO
        END DO
      END DO
C
C  Convert to <So.S1> values
C
      DO LOOP=1,RSHELL-1
        PAV(LOOP)=YES(LOOP)/REAL(NAT(LOOP))
        NAT(LOOP)=0
        YES(LOOP)=0.0
      END DO
C
C     Calculate theoretical cross-section
C
      SUMDSQ=0.0
      DO L=1,NUMD
        SUMSINC(L)=0.0
      END DO
C
      DO LOOP=1,RSHELL-1
        DO L=1,NUMD
          SINCF(LOOP,L)=REAL(COORD(LOOP+1))*PAV(LOOP)
     +              *SIN(QD(L)*SDIST(LOOP+1))/(QD(L)*SDIST(LOOP+1))
          SUMSINC(L)=SUMSINC(L)+SINCF(LOOP,L)
        END DO
      END DO
C
C     Compare with experimental cross-section data and obtain ChiSq
C
      IF(VFLAG.EQ.1) THEN
        DO CURR=1,10
          SELT(CURR)=SELF-STAR+(CURR*STEP)
          DO L=1,NUMD
            CAL(L)=FFS(L)*SELT(CURR)*PLIER*(1+SUMSINC(L))
            RES(L)=(COD(L)-CAL(L))/ERRD(L)
```

```
            SUMDSQ1(CURR)=SUMDSQ1(CURR)+(RES(L)**2)
          END DO
          SUMDSQ1(CURR)=SUMDSQ1(CURR)/FLOAT(NUMD)
        END DO
C
C  Test dShiSq/d(s(s+1)) and to adjust S(S+1) value (if desired)
C
        DO CURR=2,10
          GRACHI(CURR)=(SUMDSQ1(CURR)-SUMDSQ1(CURR-1))/STEP
          IF(IPRINT.EQ.1) PRINT*, SELT(CURR),GRACHI(CURR)
          IF(GRACHI(CURR).LT.0.0.AND.GRACHI(CURR-1).GT.0.0) THEN
            SELF=SELT(CURR)-(STEP/2)
            IF(IPRINT.EQ.1) PRINT*, 'GOTCHA1'
          END IF
          IF(GRACHI(CURR).GT.0.0.AND.GRACHI(CURR-1).LT.0.0) THEN
            SELF=SELT(CURR)-(STEP/2)
            IF(IPRINT.EQ.1) PRINT*, 'GOTCHA2'
          END IF
        END DO
      END IF
C
C     Calculate final ChiSq
C     SUMDSQ is normalised ChiSq
C
      DO L=1,NUMD
        CAL(L)=FFS(L)*SELF*PLIER*(1+SUMSINC(L))
        RES(L)=(COD(L)-CAL(L))/ERRD(L)
        SUMDSQ=SUMDSQ+(RES(L)**2)
      END DO
      SUMDSQ=SUMDSQ/FLOAT(NUMD)
C
C  Is tolerance satisfied?
C
      IF (SUMDSQ.LT.TOLL) THEN
        CALL ACCEPT(NMN,MUX,MUY,MUZ,GMUX,GMUY,GMUZ)
        CHISQ(MCOUNT)=SUMDSQ
        GO TO 666
      END IF
C
66    FORMAT('  CHISQ =',F8.4,2X,'---  compared with ',F8.4,
     +'   MOVE',I5,' ACCEPTED')
67    FORMAT('  CHISQ =',F8.4,2x,'---  compared with ',F8.4,
     +'   MOVE',I5,' REJECTED')
C
C     Accept first calculated spin configuration
C
      IF(MCOUNT.EQ.0) THEN
        CALL ACCEPT(NMN,MUX,MUY,MUZ,GMUX,GMUY,GMUZ)
        CHISQ(MCOUNT)=SUMDSQ
        OLDDSQ=SUMDSQ
        CALL OUT(X3,Y3,Z3,SDIST,PAV,RSHELL,NUMD,QD,COD,CAL,ERRD
     +           ,GMUX,GMUY,GMUZ,SELF,NMN,UFILE)
        GO TO 333
      END IF
C
C     Allow spin re-orientations which reduce SUMDSQ
C
      IF(SUMDSQ.LT.OLDDSQ) THEN
        CALL ACCEPT(NMN,MUX,MUY,MUZ,GMUX,GMUY,GMUZ)
        CALL OUT(X3,Y3,Z3,SDIST,PAV,RSHELL,NUMD,QD,COD,CAL,ERRD
     +           ,GMUX,GMUY,GMUZ,SELF,NMN,UFILE)
```

```
        WRITE(*,66)SUMDSQ,OLDDSQ,MCOUNT
        CHISQ(MCOUNT)=SUMDSQ
        OLDDSQ=SUMDSQ
      ELSE
        WRITE(*,67)SUMDSQ,OLDDSQ,MCOUNT
      END IF
      DO LOOP=1,NMN
        MUX(LOOP)=GMUX(LOOP)
        MUY(LOOP)=GMUY(LOOP)
        MUZ(LOOP)=GMUZ(LOOP)
      END DO
C
C     Rotate up to 5 spins at random
C
333   SWAP(1)=INT(RAN(I)*REAL(NMN))+1
      SWAP(2)=INT(RAN(I)*REAL(NMN))+1
      SWAP(3)=INT(RAN(I)*REAL(NMN))+1
      SWAP(4)=INT(RAN(I)*REAL(NMN))+1
      SWAP(5)=INT(RAN(I)*REAL(NMN))+1
      DO LOOP=1,5
           DO L=1,5
          IF(SWAP(L).EQ.SWAP(LOOP).AND.L.NE.LOOP) GO TO 333
        END DO
      END DO
C
      DO LOOP=1,SNUM
34      DUM=RAN(I)*PI
        IF (RAN(I).GT.SIN(DUM)) THEN
        GOTO 34
        ENDIF
        THETA=DUM
        THI=RAN(I)*2.0*PI
        MUX(SWAP(LOOP))=SIN(THETA)*COS(THI)
        MUY(SWAP(LOOP))=SIN(THETA)*SIN(THI)
        MUZ(SWAP(LOOP))=COS(THETA)
      END DO
C
      PRINT*,' '
C
      MCOUNT=MCOUNT+1
      GO TO 999
C
C************************END OF MAIN LOOP**************************
C
666   PRINT*, 'Tolerance acheived'
      PRINT*, 'END'
      PRINT*,' '
      CFILE='MUSER1:[JRS2.NUC_SIM]'//UFILE//'.CHI'
      OPEN (3,FILE=CFILE,STATUS='UNKNOWN')
      DO LOOP=1,MCOUNT
         WRITE(3,*) LOOP,CHISQ(LOOP)
      END DO
      CLOSE(3)
      CALL OUT(X3,Y3,Z3,SDIST,PAV,RSHELL,NUMD,QD,COD,CAL,ERRD
     +        ,GMUX,GMUY,GMUZ,SELF,NMN,UFILE)
      GO TO 101
C
C  Consistency check failed
C
876   PRINT*, 'ERROR - FAILED CONSISTENCY CHECK'
C
```

```
101   END
C
C*****************************************************************
C
      SUBROUTINE ACCEPT(NMN,MUX,MUY,MUZ,GMUX,GMUY,GMUZ)
C
      REAL MUX(1000),MUY(1000),MUZ(1000),GMUX(1000),GMUY(1000)
      REAL GMUZ(1000)
      INTEGER NMN
C
      DO LOOP=1,NMN
      GMUX(LOOP)=MUX(LOOP)
        GMUY(LOOP)=MUY(LOOP)
        GMUZ(LOOP)=MUZ(LOOP)
      END DO
C
      RETURN
      END
C
C*****************************************************************
C
      SUBROUTINE OUT(X3,Y3,Z3,SDIST,PAV,RSHELL,
     +          NUMD,QD,COD,CAL,ERRD,GMUX,GMUY,GMUZ,SELF,NMN,UFILE)
C
      INTEGER X3(1000),Y3(1000),Z3(1000),NUMD,NMN
      REAL PAV(30),GMUX(1000),GMUY(1000),GMUZ(1000)
      INTEGER LOOP, RSHELL
      REAL SDIST(30),SELF
      REAL COD(200),CAL(200),ERRD(200),QD(200)
      CHARACTER*8 UFILE
      CHARACTER*33, OFILE, PFILE, RFILE, FFILE
C
      OFILE='MUSER1:[JRS2.NUC_SIM]'//UFILE//'.OUT'
      PFILE='MUSER1:[JRS2.NUC_SIM]'//UFILE//'.MOS'
      RFILE='MUSER1:[JRS2.NUC_SIM]'//UFILE//'.RAW'
      FFILE='MUSER1:[JRS2.NUC_SIM]'//UFILE//'.FIT'
C
C     Output <S0.S1> file in "genie" format
C
      OPEN(1,FILE=OFILE,STATUS='UNKNOWN')
      WRITE(1,*) SELF
      DO LOOP=1,RSHELL-1
        WRITE(1,*) SDIST(LOOP+1),PAV(LOOP),0.0
      END DO
      CLOSE(1)
C
C     Atomic position and magnetic configuration file
C
      OPEN(2,FILE=PFILE,STATUS='UNKNOWN')
      DO LOOP=1,NMN
        WRITE(2,*) X3(LOOP),Y3(LOOP),Z3(LOOP),GMUX(LOOP),GMUY(LOOP)
     +             ,GMUZ(LOOP)
      END DO
      CLOSE(2)
C
C     Raw data file in "genie" format
C
      OPEN(3,FILE=RFILE,STATUS='UNKNOWN')
      DO LOOP=1,NUMD
        WRITE(3,*) QD(LOOP),COD(LOOP),ERRD(LOOP)
      END DO
```

```
      CLOSE(3)
C
C     Calculated cross-section in "genie" format
C
      OPEN(4,FILE=FFILE,STATUS='UNKNOWN')
      DO LOOP=1,NUMD
        WRITE(4,*) QD(LOOP), CAL(LOOP), 0.0
      END DO
      CLOSE(4)
C
      RETURN
      END
C
C
C*********************************************************************
```